

NUMERICAL SIMULATION OF THE HYDRODYNAMIC PROCESSES IN THE RED SEA REGION

Dissertation

zur Erlangung des Doktorgrades

der Mathematisch-Naturwissenschaftlichen Fakultät

der Christian-Albrechts-Universität zu Kiel

vorgelegt von

Fawaz Madah

Kiel

December 2016

Referent: Prof. Dr. Roberto Mayerle
Koreferent: Prof. Dr. Thomas Pohlmann
Tag der mündlichen Prüfung: 16. March 2017
Zum Druck genehmigt: Kiel, March 2017
Der Dekan: Prof. Dr. Wolfgang J. Duschl

Acknowledgements

First of all, I would like to thank GOD for giving me the health, discernment and blessings to study and complete my PhD studies in a different country and culture. Secondly, the production of this work would have been impossible without the support and participation of several people. Therefore, it is a great pleasure for me to thank and express my appreciation to those persons who helped me in the preparation of this dissertation and my doctorate studies either directly or indirectly.

In the first place I would like to express my deepest gratitude to my supervisor, Prof. Dr. Roberto Mayerle for his concern, constructive comments, encouragement, active involvement in the thesis and guidance throughout the working stages of this study. My sincere thanks also go to my dissertation advisory Prof. Dr. Thomas Pohlman for his valuable comments towards improving the work. Special acknowledgments are due to Dr. Peter Weppen for his assist since my arrival in Germany (Kiel) and continuously throughout the academic years.

I would like to thank CORELAB-FTZ at the University of Kiel for the unlimited support in terms of computing resources. My sincere thanks go to all colleagues in the CORELAB for their friendship and assist during the period of my studies. Collective acknowledgments are owed also to all my professors and colleagues in the Department of Marine Physics, King Abdul-Aziz University for their continuous support. I must not forget to thank also the Saudi ARAMCO Oil Company, Department of marine physics at Faculty of Marine Science at King Abdul-Aziz University, Saudi Arabia, Sea Level Center at University of Hawaii for supplying the water level data.

Words fail me when it comes to acknowledge my soul mate; I am deeply indebted to my wife Ohoud Hijazi for her unlimited encouragement, support and patience being abroad throughout my stay in Germany and also for the lovely times we spend together with our wonderful kids Samaa and Abdulwahab.

Last, but not least, I would like to thank my mother for her love, support and unlimited encouragement. I pray to God to keep her in a good health and wellness. My indebtedness is also extended to my dearest brothers and sisters for their endless endorsement.

Kiel, March 2017
Fawaz Madah

Notation

Symbol	Definition	Unit
H_n	Amplitude of tidal constituents	[m]
ω_n	Angular speed	[deg/s]
g_n	Phase lag of tidal constituents	[°]
T_z	Time zone	[--]
τ	Wind stress vector	[m.s ⁻¹]
ρ	Density of air	[kg.m ⁻³]
K_1	luni-solar diurnal constituent	[°/hour]
O_1	lunar diurnal constituent	[°/hour]
M_2	principal lunar semidiurnal constituent	[°/hour]
S_2	principal solar semidiurnal constituent	[°/hour]
Δt	Computational time step	[s]
Δx	The length of the grid cells in x –direction	[m]
Δy	The length of the grid cells in y-direction	[m]
Δz	The length of the grid cells in z-direction	[m]
u	Current velocity component in x-direction	[m.s ⁻¹]
v	Current velocity component in y-direction	[m.s ⁻¹]
w	Current velocity component in z-direction	[m.s ⁻¹]
f	Coriolis parameter	[Hz, 1/S]
g	Gravitational acceleration	[m.s ⁻²]
h	total water depth	[m]
ρ_o	Density of water	[kg.m ⁻³]
C_z	Che'zy Coefficient	[m ^{1/2} /s]
t_d	Wind duration	[s]
u	Wind velocity	[m.s ⁻¹]
C_r	Courant Number	[---]
d	water depth below horizontal plane of reference	[m]
ζ	Surface elevation above horizontal plane of reference	[m]
ξ	Horizontal coordinate	[m]
η	Horizontal coordinate	[m]
Q	discharge of water	[---]
E	evaporation	[m.y ⁻¹]
P	precipitation	[m.s ⁻¹]
q_{in}	Local source of water per unit of volume	[1/s]
q_{out}	Local sink of water per unit of volume	[1/s]
P_x	Horizontal pressure	[kg.m ⁻² .s ⁻²]
P_y	Horizontal pressure	[kg.m ⁻² .s ⁻²]
F_x	Horizontal eddy viscosity	[m ² /s]
v_V	Vertical eddy viscosity	[m ² /s]
M_x	External momentum in x-direction	[m/s ²]

M_y	External momentum in y-direction	[m/s ²]
C	concentration of dissolved substances	[---]
D_H	Horizontal eddy diffusivity	[m ² s ⁻¹]
Q_{tot}	The net heat flux	[W/m ²]
Q_{sn}	The net incident solar radiation (short wave)	[W/m ²]
Q_{an}	The net incident atmospheric radiation	[W/m ²]
Q_{br}	The back radiation (long wave)	[W/m ²]
Q_{ev}	The evaporative heat flux (latent heat)	[W/m ²]
Q_{co}	The convective heat flux (sensible heat)	[W/m ²]
ρ_ω	The specific density of water	[kg/m ³]
c_p	The specific heat capacity of sea water	[m ² (s ² °C)]
Δz_s	Thickness of the top layer	[m]
c_h	The Stanton number	[--]
c_e	The Dalton number	[--]
TCM	Turbulence Closure Model	[---]
Z	z-coordinate system	[---]
σ	σ -coordinate system	[---]
ρ	Isopycnal coordinate system	[---]
BC	Boundary Conditions	[---]
ME	Mean Error	[m]
RS-Model	Red Sea Model	[---]
MAE	Mean Absolute Error	[m]
MAD	Mean Absolute difference	[m]
RMAE	Relative Mean Absolute Error	[m]
RMAD	Relative Mean Absolute difference	[m]
THC	Thermohaline Circulation	
QuikSCAT	Quick Scatterometer satellite	
WOA01	World Ocean Atlas Data-2001	
DWD	Deutscher Wetterdienst	
SLA	Sea Level Anomaly	
RSOW	Red Sea outflow water	
RSSW	Red Sea Surface water	
GASW	Gulf of Aden Surface Water	
GAIW	Gulf of Aden Intermediate water	
SST	Sea surface Temperature	
SSS	Sea Surface Salinity	
SODA	Simple Ocean Data Assimilation	

Abstract

Marginal seas (semi-enclosed basin) have drawn the attention of the oceanographic scientists for many decades. They have been of such interest because in the majority of cases, they play a significant role socially, environmentally and economically. The semi-enclosed Red Sea basin presents a unique large marine ecosystem. Therefore it deserves scientific attention. Beside its extraordinary biotic richness, the Red Sea is an important international shipping path connecting eastern and southern Asia with the Middle East and Europe. In spite of its economic and environmental importance, very few studies of the hydrodynamic processes inside the Red Sea domain were carried out. During the last century, most of the previous studies focused in the vicinity of the Strait of Bab el Mandeb aiming at understanding the exchange between the Red Sea and Gulf of Aden and the spreading of the Red Sea outflow into the Gulf of Aden. Accordingly, the main concern of this work is to study the hydrodynamic processes and improve our understanding about physical processes inside the Red Sea domain.

The processes under concern are studied using a combination of very few available observations (water levels and oceanographic data), remotely sensed data as well as numerical modelling approach. The numerical simulations are performed using the three-dimensional modeling system Delft3D, developed by WL | Delft Hydraulics. The computational domain is configured to include the entire basin of the Red Sea; the two Gulfs located in the northern end and part of the Gulf of Aden. The Red Sea Model (hereafter RS-Model) with high grid resolution of 5 km and 30 vertical layers has been forced by the main eight semidiurnal and diurnal tidal constituents, used to compute the tidal elevations at the boundary of the computational domain. Besides that, transport forcing of salinity (S) and temperature (T) were prescribed along the open boundary sections. The surface boundary of the model is forced by realistic high-frequency atmospheric forcing. The RS-Model was initialized with Simple Ocean Data Assimilation (SODA).

Sensitivity analyses of the numerical and physical parameters were carried out with the aim of understanding the overall behavior of the model and its response to changes in the physical and numerical parameters adopted. An assessment of the model predictions was carried out using available sea level observations, CDT measurements, remotely sensed SST (AVHRR / Pathfinder) and on the basis of results of previous work. The model performance is found capable of adequately reproducing the tidal conditions in the region, the stratification characteristics observed in the summer field; in addition to the reversal processes of the seasonal exchange flow system existing at the strait of Bab el Mandeb.

The first part of the present thesis investigates the tidal characteristics in the Red Sea. The RS-Model suggests that the dominant pattern in the region is primarily semidiurnal with the

appearance of diurnal character at places where amphidromic systems are established. Major semidiurnal and diurnal tidal constituents are M_2 , S_2 , N_2 and K_1 . The former have three anticlockwise amphidromic systems that are located north of the strait ($\sim 13.5^\circ\text{N}$), in the central part of the Red Sea (19.5°N) and in the entrance of the Gulf of Suez, respectively. The latter have only a single amphidromic point centred around 15.5°N . Tidal hydrodynamic simulations predicted tidal flows of ~ 0.5 m/s at the strait of Bab el Mandeb, about 0.3 m/s at the Gulf of Suez and currents in the range of 0.1 m/s are prevalent inside the Red Sea domain.

The second part of the thesis concerns the seasonal circulation patterns and thermohaline structure in the Red Sea. The simulation results revealed several interesting features of the circulation in the region. The model results indicate that the Red Sea basin shares several aspects with other semi-enclosed marginal seas such as the Mediterranean Sea, where the general circulation is a result of combined effect of the wind-driven and thermohaline-driven flow, complex mesoscale eddy fields and water exchange with the open ocean. The simulation results show that the circulation structure in the Red Sea is complex.

The major features predicted by the RS-Model include the existence of several cyclonic and anticyclonic gyres; small eddies as well as intensified boundary currents at both boundaries. The model suggests that under combined wind-stresses and thermohaline forcing, the summer circulation pattern is characterized by a series of organized energetic anticyclonic eddies. In contrast, during winter months the circulation consists of alternating cyclones and anticyclones eddies. The most important feature during winter period is eddies activities located in the northern part of the Red Sea that contributes significantly to the formation of the Red Sea Outflow Water (RSOW).

The main site, period and mechanisms involved in the formation of RSOW are investigated in detail. The results suggest that the northern part of the Red Sea is the dominant formation site where baroclinic instability mechanism controls the formation process. The convection events include periods of 3-months (January-March) where three convective chimneys are formed. The results show that the formation process does not involve deep penetrative convection and the maximum depth of convection is about 150 m. A number of eddies produce intensified southward currents along the western boundary in addition to cross-basin westward currents in the middle of the basin to carry the formed RSOW towards Bab el Mandeb strait. High-frequency atmospheric forcing is observed as an important approach in studying the circulation in the Red Sea region.

In the third part of the thesis, the relative importance of wind and thermohaline forcing on the key circulation features is investigated through additional numerical experiments. The numerical experiments showed that the wind-driven circulation is stronger and dominates the thermohaline driven-circulation. The results suggest also that the wind-stress forcing reinforces the anticyclonic features and the inflow of water in the southern part of the basin while cyclonic circulation is mainly thermohaline-driven.

Keywords: *Red Sea, Delft3D modeling system, Amphidromic system, wind and thermohaline forcing, wind and thermohaline circulation, water mass formation, open-ocean convection*

Zusammenfassung

Randmeere (teilweise abgeschlossene Becken) haben die Aufmerksamkeit der ozeanographischen Wissenschaftler seit vielen Jahrzehnten angezogen. Sie sind von solchem Interesse weil sie in der Mehrheit der Fälle eine wichtige Rolle spielen, gesellschaftlich, ökologisch und ökonomisch. Das halbgeschlossene Becken des Roten Meeres (RS) stellt ein einzigartiges großes marines Ökosystem dar, deshalb verdient es die Aufmerksamkeit der Wissenschaft. Neben seiner ausserordentlichen biologischen Vielfalt stellt das Rote Meer eine bedeutsame internationale Wasserstrasse dar, die das östliche und südliche Asien mit dem Nahen Osten und Europa verbindet. Trotz seiner Bedeutung für Ökonomie und Umwelt wurden nur sehr wenige Studien der hydrodynamischen Prozesse im Gebiet des Roten Meeres ausgeführt. Im letzten Jahrhundert wurden die meisten der vorangegangenen Untersuchungen in der Umgebung der Strasse von *Bab el Mandeb* ausgeführt, die auf ein Verständnis der Austauschprozesse zwischen dem Roten Meer und dem Golf von Aden und auf die Ausbreitung des Ausstromes aus dem Roten Meer in den Golf von Aden zielten. Folgerichtiger Weise ist das Hauptanliegen dieser Arbeit die hydrodynamischen Prozesse zu untersuchen und unser Verständnis für physikalische Vorgänge innerhalb des Gebietes des Roten Meeres zu verbessern.

Die interessierenden Prozesse werden mithilfe einer Kombination aus sehr wenigen verfügbaren Beobachtungen (Wasserstände und ozeanographische Daten), mit Daten aus der Fernerkundung sowie mit einem numerischen Modellierungsansatz studiert. Die numerischen Simulationen werden mithilfe des dreidimensionalen Modellierungssystems Delft3D, das von *WL/Delft Hydraulics* entwickelt wurde, durchgeführt. Die im Computer berechnete Domäne ist so konfiguriert, dass das gesamte Becken des Roten Meeres enthalten ist; die beiden am nördlichen Ende befindlichen Meeresarme und ein Teil des Golfes von Aden. Das Model des Roten Meeres (kurz: RS-Model) mit einer hohen Auflösung des Gitters von 2 km und mit 30 vertikalen Schichten ist angetrieben worden mit den acht semidiurnalen und diurnalen Tide-Konstituenten, die benutzt wurden, um die Tidenhöhe an der offenen Grenze der Model-Domäne zu berechnen. Daneben wurden die Antriebskräfte für den Transport durch Salinität (S) und Temperatur (T) entlang der Abschnitte der offenen Grenzen vorgeschrieben. Die Oberflächen-Grenzschicht in dem Model wird durch realistische atmosphärische Kräfte in Hochfrequenz angetrieben. Das RS-Model wurde mithilfe der Einfachen-Ozean-Daten-Assimilation (SODA, Simple Ocean Data Assimilation) initialisiert.

Eine Sensitivitäts-Analyse der numerischen und physikalischen Parameter wurde durchgeführt... Eine Beurteilung der Model-Voraussagen wurde mithilfe verfügbarer Beobachtungen der Wasserstände, durch Fernerkundung gewonnene Daten der Temperatur an der Meeresoberfläche (AVHRR/Pathfinder) und den verfügbaren früheren Arbeiten durchgeführt. Es wurde festgestellt, dass die Leistungsfähigkeit des Models angemessen dargestellt wird anhand der Tidebedingungen in der Region, der Stratifikations-Charakteristik

, die im Sommer beobachtet wird, zusätzlich zu den umgekehrten Prozessen des saisonalen Austausch-Strömungs-System in der Strasse von Bab el Mandeb.

Im ersten Teil der Thesis werden die Tidecharakteristiken im Roten Meer untersucht. Das RS Model legt nahe, dass das dominierende Muster in der Region primär semidiurnal mit dem Auftreten diurnaler Charakteristiken an Orten ist, an denen sich amphydrome Systeme etablieren. Die wesentlichen semidiurnalen und diurnalen Tidekonstituenten sind M_2 , S_2 , N_2 und K_1 . Die vorangehenden verfügen über drei amphydrome System gegen den Uhrzeigersinn, die sich nördlich der Strasse von Bab el Mandeb ($\sim 13.5^\circ\text{N}$), im zentralen Teil des Roten Meeres (19.5°N) beziehungsweise am Eingang des Golfes von Suez befinden. Letzterer hat lediglich einen amphidromen Punkt, der um 15.5°N zentriert ist. Die hydrodynamischen Simulationen der Tide sagten Tideströme von ~ 0.5 m/s in der Strasse von Bab el Mandeb, ungefähr 0.3 m/s am Golf von Suez vorher und Strömungen im Bereich von 0.1 m/s sind vorherrschend innerhalb der Domäne des Roten Meeres vor.

Der zweite Teil der Thesis behandelt die saisonalen Zirkulationsmuster und thermohaline Strukturen im Roten Meer. Simulationsergebnisse decken einige interessante Eigenschaften der Zirkulation in der Region auf. Die Modelresultate weisen darauf hin, dass das Becken des Roten Meeres verschiedene Aspekte mit anderen halb geschlossenen Randmeeren gemeinsam hat, wie etwa dem Mittelmeer, wo die allgemeine Zirkulation ein Resultat der kombinierten Effekte der windgetriebenen und der thermohalin getriebenen Strömungen ist, sowie komplexer mesoskaliger Stromwirbel-Felder und des Wasseraustausches mit dem offenen Ozean. Die Simulationsergebnisse zeigen, dass die Zirkulationsstruktur des Roten Meeres kompliziert ist.

Die wesentlichen Eigenschaften, die vom RS-Model vorhergesagt werden, beinhalten die Existenz von verschiedenen zyklonalen und antizyklonalen Wirbeln, kleinen Stromwirbeln (Eddies) sowie intensivierten Randströmungen an beiden Landgrenzen. Das Model legt nahe, dass unter kombinierter Einwirkung von Wind-Stress und thermohalinen Antriebskräften das Sommer-Zirkulationsmuster durch eine Serie organisierter, energiereicher antizyklonaler Wirbel. Im Gegensatz hierzu besteht die Zirkulation während der Wintermonate aus alternierenden zyklonalen und antizyklonalen Wirbeln. Das wesentlichste Merkmal während der Winterperiode sind Wirbel-Aktivitäten, die im nördlichen Teil des Roten Meeres angesiedelt sind und die wesentlich beitragen zur Bildung von aus dem Roten Meer ausströmendem Wasser (Red Sea outflow Water, RSOW).

Die wesentlichen Bereiche, Zeiträume und Mechanismen, die an der Bildung von RSOW beteiligt sind, werden näher untersucht. Die Simulation legt nahe, dass der nördliche Teil des Roten Meeres die dominierende Region für die Genese ist, wo die Instabilitätsmechanismen der barometrischen Gradienten den Bildungsprozess von RSOW kontrollieren. Die Konvektionsereignisse umfassen Zeiträume von drei Monaten (Januar bis März), in denen drei Konvektions-Kamine gebildet werden. Die Resultate zeigen, dass der Bildungsprozess keine tief eindringende Konvektion einschliesst und die maximale Tiefe der Konvektion liegt bei ~ 150 m. Eine Reihe von Strömungswirbeln bewirken intensivierten südwärts gerichtete Strömungen entlang der westlichen Grenze (Küste) zusätzlich zu den Strömungen, die das Meeresbecken in westlicher Richtung in der Mitte des Meeresbeckens queren, um das gebildete RSOW in Richtung der Bab el Mandeb Strasse zu bewegen. Ein hochaufgelöster atmosphärischer Antrieb ist als ein bedeutsamer Ansatz für Studien der Zirkulation im Roten Meer identifiziert worden.

Im dritten Teil der Thesis wird die relative Bedeutung von Windantrieb und thermohalinen Kräften für die wesentlichen Zirkulationseigenschaften mit Hilfe von zusätzlichen numerischen Experimenten untersucht. Die numerischen Experimente zeigten, dass die windgetriebene Zirkulation stärker ist und die thermohalin angetriebene Zirkulation dominiert. Die Resultate deuten darauf hin, dass die Antriebskräfte durch Windstress die antizyklonalen Merkmale und den Einstrom von Wasser im südlichen Teil verstärken, während die zyklonale Zirkulation im Wesentlichen durch thermohaline Effekte angetrieben wird.

Keywords: *Rotes Meer, Delft3D Modellierungssystem, Amphidrome Systeme, Wind- und thermohaliner Antrieb, Wind und thermohaline Zirkulation, Bildung von Wasserkörpern, Konvektion im offenen Ozean*

Contents

Acknowledgments	III
Notation	IV-V
Abstract	VI-VII
Zusammenfassung	VIII-X
Contents	XI-XIV
List of Figures	XVI-XX
List of Tables	XXI

Chapter 1. Introduction

1.1	Overview.....	1-2
1.2	Brief Information of previous studies.....	3-4
1.3	Numerical Models and Data.....	4-5
1.4	Motivation and Scientific Goals.....	5-6
1.5	Methodology.....	6
1.6	Outline of the Dissertation.....	7-8

Chapter 2. Literature Review

2.1	Introduction	9-10
2.2	Definition and Importance of Numerical Models.....	10-11
2.3	Advantages and Disadvantages of Numerical modeling.....	11-12
2.4	Dimensions of a Numerical Model.....	12
	2.4.1 One-Dimensional Model.....	12
	2.4.2 Two-Dimensional Model.....	12-13
	2.4.3 Three-Dimensional Model.....	13
2.5	Model Evaluation	14
	2.5.1 Sensitivity Analysis.....	14
	2.5.2 Calibration.....	14
	2.5.3 Validation.....	15
2.6	Three-Dimensional Circulation Model	15
	2.6.1 Theory and basic approximation.....	15-16
	2.6.2 Aspects of 3-D Modeling.....	16

2.6.3	Grids, Horizontal and Vertical Discretization.....	16
2.6.3.1	Horizontal Discretization.....	17
2.6.3.2	Vertical Discretization.....	17
2.6.3.2.1	Z-coordinate model.....	18
2.6.3.2.2	σ -coordinate model.....	18
2.6.3.2.3	ρ -coordinate model.....	18
2.7	Hydrodynamic and Circulation	19
2.7.1	Tides.....	19-21
2.7.2	Wind Stress.....	20-21
2.7.3	Atmospheric Pressure Variation.....	21-22
2.7.4	Surface Circulation.....	22-24
2.7.5	Deep Circulation and Water Mass Formation.....	24-26

Chapter 3. Overview of the Study Area

3.1	Introduction	27
3.2	Geographical Location of the Red Sea.....	27-28
3.3	Geological history and formation of the Red Sea.....	28
3.4	Topography and Bathymetry.....	29-30
3.5	Climate Characteristics.....	31
3.5.1	Prevailing Winds.....	31-32
3.6	Hydrodynamic Processes	33
3.6.1	Tidal Conditions.....	33-34
3.6.2	Circulation Patterns.....	34
3.6.2.1	Wind driven circulation.....	34-35
3.6.2.2	Observational and modeling studies.....	35-38
3.6.2.3	Deep circulation and water mass formation.....	38-39
3.6.3	Water Exchange with surrounding system.....	39-40
3.6.4	Hydrographic properties.....	40-43
3.7	Available Data	44
3.7.1	Water Level Data.....	44-46
3.7.2	Harmonic Analysis.....	47-48
3.7.3	Salinity and Temperature Data.....	49-50

Chapter 4. Model Description (Delft3D modeling system)

4.1	Introduction	51
4.2	General Information of the Modeling system.....	51-52
4.3	Delft3-Flow Model.....	52-53
4.4	Model Configuration.....	53
4.4.1	Grid and Coordinates.....	53-54
4.4.2	Numerical Stability.....	54
4.4.3	Hydrodynamic Equations.....	55
4.4.3.1	Continuity equation.....	55-56

4.4.3.2 Momentum equation.....	56
4.4.3.3 Hydrostatic pressure assumption.....	56
4.4.3.4 Vertical Velocity.....	56-57
4.4.4 Transport Equation.....	57
4.4.4.1 Turbulence Closure Model.....	57-58
4.4.5 Boundary Conditions.....	58
4.4.5.1 Vertical Boundary Conditions.....	58
4.4.5.2 Bottom Roughness.....	58-59
4.4.5.3 Lateral Boundary Conditions.....	59
4.5 Heat Flux Models	60-61

Chapter 5. Development of the Red Sea Model (RS-Model)

5.1	Introduction.....	62
5.2	Flow Model setup.....	63
	5.2.1 Model Domain of the RS-Model.....	63-64
	5.2.2 Constructing the Grid.....	64
	5.2.2.1 Grid Requirements.....	64-65
	5.2.2.2 Model Grid.....	65-66
	5.2.3 Shoreline and Bathymetry of the RS-Model.....	66-67
	5.2.4 Two dimension and Three-dimensional approach.....	67-68
5.3	Definition of the Open Model Boundary.....	68
	5.3.1 Model Forcing.....	68
	5.3.1.1 Tidal Forcing.....	69-71
	5.3.1.2 Atmospheric forcing.....	72
	5.3.1.3 Transport forcing at the open boundary.....	72-73
5.4	Numerical and physical parameters.....	74
5.5	Initial condition.....	75
5.6	Model Sensitivity Analysis.....	75
	5.6.1 Introduction.....	75-76
	5.6.2 Open Boundary Condition.....	76-79
	5.6.3 Numerical Parameters.....	79
	5.6.3.1 Decision on Grid Size in the horizontal plan.....	80-82
	5.6.3.2 Grid resolution in vertical plan.....	82-84
	5.6.3.3 Effect of the time step.....	84-85
	5.6.4 Physical Parameters.....	86
	5.6.4.1 Effect of the bathymetry variations.....	86-87
	5.6.4.2 Effect of the Bottom Roughness.....	87-88
	5.6.4.3 Effects of Horizontal Eddy Viscosity and Diffusivity.....	88-91
	5.6.4.4 Coefficients for ocean heat model.....	91-93
	5.6.4.5 Effect of wind drag.....	93-96
	5.6.4.6 Effects of initial conditions.....	97
5.7	Validation of the RS-Model	98
	5.7.1 Introduction.....	98-99
	5.7.2 Validation in terms of Surface Elevations.....	99-104
	5.7.2.1 Statistical analysis of the residual water level.....	104-108
	5.7.3 Validation in terms of Salinity and Temperature.....	108
	5.7.3.1 Validation for Temperature and Salinity profiles.....	109-110

5.7.3.2 Comparison of RS-Model Sea Surface Temperature (SST) With AVHRR Pathfinder.....	110-113
5.8 Conclusion	113-114

Chapter 6. Simulation of Tides in the Red Sea

6.1 Introduction	115
6.2 RS-Model	116
6.3 Tidal characteristics based on model Results	116
6.3.1 Co-range and Co-tidal charts.....	117
6.3.1.1 Semidiurnal Tidal waves.....	117-119
6.3.1.2 Diurnal tidal wave.....	119-120
6.4 Form Factor	120-121
6.5 Hydrodynamic Features	121-124
6.6 Conclusion	124-125

Chapter 7. Simulation of Circulation in the Red Sea

7.1 Introduction	126-127
7.2 Circulation patterns and thermohaline structure (summer season)	128
7.2.1 Horizontal patterns of the circulation.....	128-129
7.2.2 Horizontal patterns of the thermohaline fields.....	130-131
7.2.3 Vertical thermohaline structure.....	130-132
7.3 Characteristics of the water masses at the strait of Bab el Mandeb	132-134
7.4 Intrusion of the Gulf of Aden Intermediate Water (GAIW)	134-136
7.5 Intermediate circulation	137
7.6 Circulation patterns and thermohaline structure (winter season)	138
7.6.1 Horizontal patterns of the circulation.....	138-140
7.6.2 Horizontal patterns of the thermohaline fields.....	140-141
7.6.3 Vertical thermohaline structure.....	141-142
7.7 Experiments of Wind and Thermohaline Forcing	142-143
7.7.1 Horizontal patterns of the circulation (summer season).....	143-145
7.7.2 Horizontal patterns of the circulation (winter season).....	145-147
7.7.3 Vertical thermohaline structure (summer season).....	147-149
7.7.4 Vertical thermohaline structure (winter season).....	147-151
7.8 Formation of water masses in the Red Sea	151-152
7.8.1 Red Sea Outflow Water Mass (RSOW).....	152-159
7.8.2 Red Sea Deep Water (RSDW).....	159-161

Chapter 8. Conclusion and Recommendation

8.1 Conclusion	162-168
8.2 Recommendations	169-170
List of References.....	171-180

Appendices

Appendix A: individual terms of the total heat flux equation.....183-185

Appendix B: Grid Requirements of the RS-Model.....186-187

Appendix C: Sensitivity analysis on Horizontal Eddy Diffusivity.....188-189

Appendix D: Vertical distribution of Temperature and Salinity along the main axis of the Red Sea.....190-191

List of Figures

Figure 1.1 Geographical location of the study area.....	2
Figure 1.2 Structure of the thesis.....	7
Figure 2.1 Main types of vertical coordinate representation in ocean modelling, Z (left), σ (middle) and ρ (right) coordinate system [adopted from Chassignet <i>et al.</i> , 2002].....	17
Figure 2.2 Ekman Spiral describes how the horizontal wind sets surface waters in motion, As represented by vectors, the speed and direction of water change with increasing depth [adopted from Paul, 2003].....	23
Figure 2.3 Schematic representation of the global thermohaline circulation [adopted from Rahmstorf, 2006].....	25
Figure 2.4 A cross-sectional longitudinal profile of the Atlantic Ocean from 60° N to 60° S showing the location of the mixed layer, pycnocline and deep layer [adopted from Rahmstorf, 2006].....	25
Figure 2.5 A schematic diagram of the three phases of open-ocean convection: (a) precondition, (b) deep convection, (c) lateral exchange and spreading. Surface buoyancy loss and the water mixed by convection is represented by curly and shaded arrows.....	26
Figure 3.1 Map of the area under investigation.....	28
Figure 3.2 Bathymetry map of the Red Sea.....	29
Figure 3.3 Monthly mean wind climatology over the Red Sea.....	32
Figure 3.4 Mean winter (left panel) and summer (right panel) of surface circulation over 9 years of simulation [Sofianos and Johns, 2003].....	37
Figure 3.5 Monthly mean of altimeter-derived sea level anomaly (SLA) distribution over the Red Sea and part of Gulf of Aden, obtained from AVISO datasets.....	38
Figure 3.6 Schematic of the circulation patten in the layers, upper deep layers and deep layers (after Quadfasel, 2001).....	39
Figure 3.7 Sketch of water masses exchange (circulation patterns) in the Bab el Mandeb Strait, (A) winter and (B) summer season, where SW: surface water, GAIW: Gulf of Aden intermediate water and RSOW: Red Sea outflow water [adopted from Smeed 2004].....	40
Figure 3.8 Horizontal distribution of sea surface temperature SST (upper panel) and sea surface salinity SSS (lower panel) over the Red Sea and part of Gulf Aden for January, April, July and October, obtained from World Ocean Atlas-2001.....	42
Figure 3.9 Hydrographic-section along the main axis of the Red Sea, (a) temperature in °C, (b) salinity [based on the cruises, of R/V Mauric Ewing during August 2001], [adopted from Sofianos & Johns 2007].....	43

Figure 3.10 Study area map showing locations of the available measurements, water level (Black dots) and salinity and temperature marked by three cross-sections and six stations distributed along the main axis.....45

Figure 3.11 (A) Tidal variations at two locations in the Gulf of Aden at ADEN and DJIBOUT stations for period of October-2008, and (B) tidal variations at four locations along the eastern side Red Sea at JIZAN, JEDDAH, RABIGH and DUBA stations for period of April-2001.....46

Figure 3.12 the amplitudes of semidiurnal and diurnal constituents as derived from harmonic analysis of the available data at A) ADEN, B) DJIBOUTI, C) JIZAN, D) JEDDAH, E) RABIGH and F) DUBA stations.....47

Figure 3.13 Typical profiles of temperature and salinity at locations along the Red Sea axis,49

Figure 3.14 Northern I, Middle II and Southern III hydrographic sections: As) Temperature and Bs) Salinity55

Figure 4.1 A layout of a vertical co-ordinate systems, σ -grid (left) and Z-grid (right) [Delft3D-Flow, User-Manual, 2011].....53

Figure 4.2 Staggered grid used in Delft3D-flow.....54

Figure 5.1 Border of the Red Sea model (**RS-Model**) domain indicated by Red dashed-line.....64

Figure 5.2 Computational grid of the Red Sea model66

Figure 5.3 Bathymetry of the Red Sea model based on GEBEGO_8.....67

Figure 5.4 Comparison of measured and modelled water level at DUBA and JIZAN Stations based on TPXO7.2.....70

Figure 5.5 Comparison of the measured and modeled water level at DUBA, and JIZAN Stations after adjustment to the open sea boundary conditions.....71

Figure 5.6 Temperature distribution [$^{\circ}$ C] over the Red Sea and part of Gulf of Aden based from SODA and close view of cross section along the open boundary.....73

Figure 5.7 Location map showing the monitoring points considered in the sensitivity analysis.....75

Figure 5.8 Comparisons of water level between the measurements and the predictions at JIZAN Station.....78

Figure 5.9 Comparisons of water level between the measurements and the predictions at JEDDAH Station.....78

Figure 5.10 Comparisons of water level between the measurements and the predictions at RABIGH Station.....78

Figure 5.11 Comparisons of water level between the measurements and the predictions at DUBA Station.....78

Figure 5.12 Effect of the horizontal grid resolution on water level at monitoring points JIZAN, JEDDAH, RABIGH and DUBA for RS-Model82

Figure 5.13 Effect of different time step on water level at monitoring points JIZAN, JEDDAH, RABIGH and DUBA for RS-Model.....85

Figure 5.14 Effect of different bathymetry (water depth) on water level at monitoring points JIZAN, JEDDAH, RABIGH and DUBA for RS-Model.....87

Figure 5.15 Effect of different values of Che`zy coefficient on water level at monitoring points JIZAN, JEDDAH, RABIGH and DUBA for RS-Model.....88

Figure 5.16 Effect of different values of Eddy Viscosity on water level at monitoring points JIZAN, JEDDAH, RABIGH and DUBA for RS-Model.....89

Figure 5.17 Effect of different values of Eddy diffusivity on vertical temperature profile, cross section along the main axis of the Red Sea.....90

Figure 5.18 Effect of different values of Eddy diffusivity on vertical salinity profile, cross section along the main axis of the Red Sea.....91

Figure 5.19 Example of the wind drag coefficient (after Delft3D-Flow User-Manual, 2011).....93

Figure 5.20 Mean wind speed and direction for the period considered in the sensitivity analysis.....94

Figure 5.21 Effect of different values of wind drag coefficient on water level at monitoring points JIZAN, JEDDAH, RABIGH and DUBA for RS-Model.....95

Figure 5.22 Effect of different values of wind drag coefficient on salinity along the main axis of the model domain.....96

Figure 5.23 Effect of different values of wind drag coefficient on salinity over three-sections of the model domain, northern, middle and southern part.....96

Figure 5.24 Comparison of measured and simulated water levels at ADEN Station-01st to31st of October-2008.....100

Figure 5.25 Comparison of measured and simulated water levels at DJIBOUTI Station- 01st to31st of October-2008.....100

Figure 5.26 Comparison of measured and simulated water levels at GIZAN Station-01st to28st of February-2001.....101

Figure 5.27 Comparison of measured and simulated water levels at RABIGH Station-01st to28st of February-2001.....101

Figure 5.28 Comparison of measured and simulated water levels at DUBA Station-01st to28st of February-2001.....101

Figure 5.29 Comparison of measured and simulated water levels at GIZAN Station-01st to30st of April-2001.....102

Figure 5.30 Comparison of measured and simulated water levels at JEDDAH Station-01st to30st of April-2001.....102

Figure 5.31 Comparison of measured and simulated water levels at RABIGH Station-01st to30st of April-2001.....102

Figure 5.32 Comparison of measured and simulated water levels at DUBA Station-01st to30st of April-2001.....103

Figure 5.33 Comparison of measured and simulated water levels at Obhor Creek station, 1st to 31st of July 2011.....103

Figure 5.34 Comparison of measured and simulated water levels at Saroom Station, 1st to 31st of July 2011.....104

Figure 5.35 Vertical profiles of observed and simulated temperature nad salinity at locations A,B,C,D,E and F.....110

Figure 5.36 Comparison of simulated (left) and satellite AVHRR Pathfinder (right) of SST, January-2008.....111

Figure 5.37 Comparison of simulated (left) and satellite AVHRR Pathfinder (right) of SST, July -2008.....	112
Figure 5.38 Comparison of average monthly modelled and remotely sensed (AVHRR / Pathfinder) SST at different locations, (a), extreme northern part, (b) middle part and (c,d) southern part of the Red Sea.....	113
Figure 6.1 Distribution of amplitudes and phases of M_2 tide in the Red Sea using the RS-Model, (left panel) co-tidal lines and (right panel) co-range lines. Amplitudes are given in centimeters and phases in degrees.....	118
Figure 6.2 Distribution of amplitudes and phases of S_2 tide in the Red Sea using the RS-Model, (left panel) co-tidal lines and (right panel) co-range lines. Amplitudes are given in centimeter and phases in degrees.....	118
Figure 6.3 Distribution of amplitudes and phases of N_2 tide in the Red Sea using the RS-Model, (left panel) co-tidal lines and (right panel) co-range lines. Amplitudes are given in centimeters and phases in degrees.....	119
Figure 6.4 Distribution of amplitudes and phases of K_1 tide in the Red Sea using the RS-Model, (left panel) co-tidal lines and (right panel) co-range lines. Amplitudes are given in centimeters and phases in degrees.....	120
Figure 6.5 Form Factor distribution in the Red Sea based on calculated modeled diurnal (O_1 , K_1) and semidiurnal (M_2 , S_2) amplitudes.....	121
Figure 6.6 Snapshot of the model showing the current velocity field (m/s) for the Flood condition (left panel) and for the Ebb condition (right panel) (depicted by colour size) in the Red Sea during spring tide.....	122
Figure 6.7 Snapshot of the model showing the current velocity field (m/s) for the Flood condition (left panel) and for the Ebb condition (right panel) (depicted by colour size) in the Red Sea during neap tide.....	122
Figure 6.8 Distribution of the spring surface elevation (m) in the Red Sea using the RS-Model, (left panel) Flood condition and (right panel) Ebb condition.....	123
Figure 6.9 Snapshot of the model showing the current velocity field (m/s) for the Flood condition (left panel) and for the Ebb condition (right panel) (depicted by colour size and vector direction) in the Red Sea during spring tide.....	124
Figure 7.1 Mean surface current velocity field in the Red Sea based on RS-Model over summer months (June-September) [Full forcing].....	129
Figure 7.2 Horizontal distribution of simulated (a) sea surface temperature SST ($^{\circ}$ C), (b) sea surface salinity SSS (psu) during summer season (June-September).....	131
Figure 7.3 Vertical distribution of simulated (a) temperature ($^{\circ}$ C) and (b) salinity (psu) along the main axis during summer season (June-September) based on RS-Model, [Scenario-1: Full forcing].....	132
Figure 7.4 Vertical distribution of simulated temperature ($^{\circ}$ C) (a) winter, (b) summer, and salinity (c) winter and (d) summer [Zonal cross-section in the southern part of the Red Sea along 14° N].....	133
Figure 7.5 Seasonal means of volume transport for Surface, Intermediate and deep layers at a cross-section located at $\sim 12.5^{\circ}$ N].....	134

Figure 7.6 Horizontal distributions of salinity field (psu) and currents (m/s) at 80 m depth from June to November representing the full cycle of Gulf of Aden intrusion (GAIW) and structure of propagation into the Red sea.....136

Figure 7.7 Vertical cross-section of (a) temperature and (b) salinity at 16°N based on RS-Model during August-2008.....136

Figure 7.8 Mean current velocity field in the Red Sea at depth representing the RSOW based on RS-Model over summer season (June-September).....137

Figure 7.9 Mean surface current velocity field in the Red Sea based on RS-Model over winter months (Jan-March) [Full forcing].....140

Figure 7.10 Horizontal distribution of simulated (a) sea surface temperature SST (°C), (b) sea surface salinity SSS (psu) during winter season (Jan-March).....141

Figure 7.11 Vertical distribution of simulated (a) temperature (°C) and (b) salinity (psu) along the main axis during winter season (June-September) based on RS-Model, [Scenario-1: Full forcing].....142

Figure 7.12 Mean current velocity field in the Red Sea based on scenario-II (No-wind) and scenario-III (No-Fluxes) over summer season (June-September).....145

Figure 7.13 Mean current velocity field in the Red Sea based on scenario-II (No-wind) and scenario-III (No-Fluxes) over winter season (Jan-March).....147

Figure 7.14 Vertical distribution of (a) temperature and (b) salinity during summer season based on scenario-II (No-wind) and scenario-III (No-Fluxes).....149

Figure 7.15 Vertical distribution of (a) temperature and (b) salinity during winter season based on scenario-II (No-wind) and scenario-III (No-Fluxes).....150

Figure 7.16 Monthly means of transport for Surface, Intermediate and deep layers at a cross-section located at ~ 12 °N. Top (Scenario-II), Middle (Scenario-III) and bottom (Scenario-I and sum of Scenario-II and Scenario-III).....151

Figure 7.17 Axial distribution of (a) Evaporation heat flux and Total heat flux, (b) Free convection of Latent and Sensible Heat (average during Jan-March) based on the RS-Model.....154

Figure 7.18 Simulated horizontal current field and density from the period October to March.....156

Figure 7.19 Vertical distribution of simulated density from the period October to May, representing the sequence of formation and re-stratification of the mixed layer phases. [Meridional section along the main axis of the northern Red Sea].....158

Figure 7.20 Mean current velocity field in the Red Sea at depth 160 m, typical depth of the RSOW based on RS-Model.....159

Figure 7.21 Vertical distribution of simulated average salinity [psu] and temperature over winter season at the Gulf of Suez (Left) and the Gulf of Aqaba (Right), As: Longitudinal section along the main axis, Bs and Cs: cross-sections across the mouth of the two Gulfs.....161

List of Tables

Table 2.1 Major tidal constituents [Pugh, 1987].....	21
Table 2.2 Important shallow water tidal constituents.....	21
Table 3.1 Regions of bottom of the Red Sea.....	30
Table 3.2 Periods of measured water levels.....	45
Table 3.3 Tidal type based on <i>F</i> factor.....	48
Table 4.1 A brief description of the modules used in the study.....	52
Table 4.2 Turbulence Closure Models implemented in Delft3D-Flow system.....	58
Table 5.1 Amplitude and phase of the astronomical constituents extracted from TPXO7.2	70
Table 5.2 Amplitude and phase of the adjusted constituents.....	71
Table 5.3 Optimal parameters sitting used for the RS-Model.....	74
Table 5.4 Parameters selected during Boundary Condition study.....	77
Table 5.5 Statistical analysis of discrepancies at JIZAN station.....	79
Table 5.6 Statistical analysis of discrepancies at JEDDAH station.....	79
Table 5.7 Statistical analysis of discrepancies at RABIGH station.....	79
Table 5.8 Statistical analysis of discrepancies at DUBA station.....	79
Table 5.9 type of models considered in the sensitivity analysis.....	80
Table 5.10 Characteristics of the proposed grids used during sensitivity analysis.....	81
Table 5.11 Vertical distribution of the <i>Z</i> -model grid.....	84
Table 5.12 Time steps and courant number used in the sensitivity analysis.....	85
Table 5.13 Sensitivity analysis with different bathymetry depths.....	86
Table 5.14 Eddy Viscosity values used in the sensitivity analysis.....	88
Table 5.15 Eddy Diffusivity values used in the sensitivity analysis.....	89
Table 5.16 Overview of Dalton and Stanton numbers found in the literature.....	93
Table 5.17 Wind drag coefficient values used in the sensitivity analysis.....	94
Table 5.18 Periods used for the RS-Model validation processes.....	99
Table 5.19 Statistical analysis of the model validation at ADEN, DJIBOUTI, JIZAN, JEDDAH, RABIG and DUBA stations based on Root mean square difference and absolute difference mean.....	105
Table 5.20 Tidal amplitude and phase of observed and computed tidal constituents at JIZAN.....	107
Table 5.21 Tidal amplitude and phase of observed and computed tidal constituents at JEDDAH.....	107
Table 5.22 Tidal amplitude and phase of observed and computed tidal constituents at RABIGH.....	108
Table 5.23 Tidal amplitude and phase of observed and computed tidal constituents at DUBA.....	108
Table 5.24 statistical analysis derived from Delft3D-TRIANA.....	108

Chapter 1

Introduction

1.1 Overview

Marginal seas (semi-enclosed basin) have drawn the attention of the oceanographic scientists for many decades. They have been of such interests because in the majority of cases, they play a significant role socially, environmentally and economically. The Red Sea is considered one of these seas, where it presents a unique large marine ecosystem which deserves scientific attention. Beside its extraordinary biotic richness, the Red Sea is an important international shipping path connecting eastern and southern Asia with the Middle East and Europe. Recently, estimates concerning oil-related activities indicate that about 3.4 million barrels of oil is being transported daily through the Red Sea (WOTC, 2012).

The Red Sea basin whose hydrodynamic processes are the subject of this dissertation, is a narrow elongated-shaped sea (semi-enclosed) separating the land masses of Africa and Arabia, oriented from the north-northwest (NNW) to south-southeast (SSE). Geographically, it is located between the latitude 30-10°N and longitude 36-45°E and extends over a distance of about 2000 km covering a total surface area of about 440,000 km² (Figure.1.1). The Red Sea has an average width of approximately 280 km and the minimum width of about 26 km is found at the southern end. The physical boundary of the Red Sea is delineated by the coastline of Egypt, Sudan, Eritrea and part of Djibouti in the western side and the coastline of Jordan, Saudi Arabia and Yemen on the eastern side. In the southern part of the basin, it links with the Gulf of Aden and the Indian Ocean through a narrow, shallow strait (26 km wide, 150 km long) known as Bab el Mandeb while in the north part it consists of the so-called Gulf of Suez and Gulf of Aqaba.

Geologically, the Red Sea is a young widening basin and it might turn into an ocean in the future. It was formed as a result of tectonic plate movement the African, Arabian and Mediterranean shields pulling away from each other, creating a great slash in the land (Sheppard *et al.*, 1992 and PERSEGA, 2006). The Red Sea experiences irregular bottom topography. Most of the coastlines of the Red Sea are bordered by shallow fringing reefs. The edges of these reefs shelve steeply into deep water or they slope gently into lagoons bordered by an offshore barrier reef system (Morley, 1975; PERSEGA, 2006 and Albarakati, 2012).

The Red Sea is shallow at its northern and southern ends and its average depth is 490 m while maximum depth is > 2000 m found in the middle axis at 19° N, 38° E. In the southern part of the basin, there are shallow shelves on both sides of the strait of Bab el Mandeb connecting the Red Sea to the Gulf of Aden, the shallowest Sill known as Hanish Sill (~ 150 m) is located at the northern part of the Strait and the narrowest contraction is located at the Perim Narrows in the southern end of the Strait (Morley, 1975, Murray and Johns, 1997 and PERSGA, 2006). More description of the Red Sea bottom division is given in chapter 3 (section 3.4).

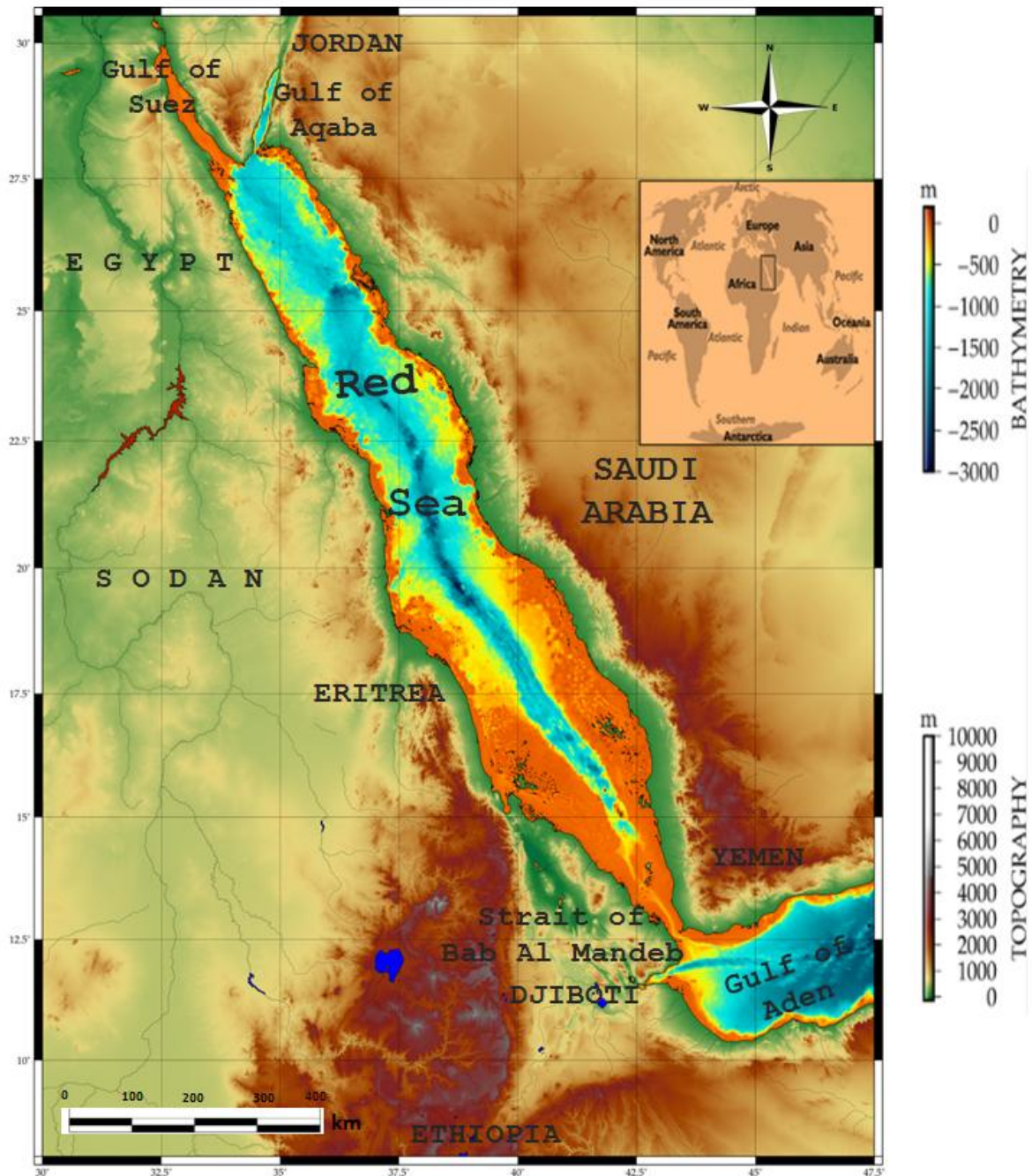


Figure 1.1 Geographical Location of the study area [The Red Sea and part of Gulf of Aden].

1.2 Brief information of previous studies

Despite of its socio-economic and environmental importance, many authors pointed out that the Red Sea is one of the most unexplored areas of the Northern Hemisphere oceans (e.g. Edwards and Head, 1987; Sofianos and Johns, 2003 and Chen *et al.*, 2014). In the past decades, many studies have been carried out in the region however most of these studies have been focused on the vicinity of the southern part of the Red Sea and Bab el Mandeb Strait. These studies aimed at understanding the water exchange between the Red Sea and Gulf of Aden (e.g. Thompson, 1939; Maillard and Soliman, 1986; Murray and Johns, 1997 and Smeed, 2004), circulation patterns (e.g. Clifford *et al.*, 1997; Morcos and Soliman, 1974 and Maillard, 1974) and the heat balance and heat transport between the Red Sea and Gulf of Aden (Patzert, 1974b; Yegorov, 1950 and Sofianos, *et al.*, 2002), temperature and salinity variations (Vercelli, 1927), tides have been described by Defnat (1961).

Inside the Red Sea domain, very little information is found concerning tides and circulation processes in the literature that are mainly based on few published studies and unpublished report. During the last century, a dynamical explanation of actual tides was supplied based on few analytical analyses made to determine the tides in the strait of Bab el Mandeb (Defant, 1961) and the results of these analyses were used to explain tidal dynamics in the whole Red Sea basin. The conclusion drawn suggests that the tidal regime in the Red Sea is essentially co-oscillations with those of the Gulf of Aden, characterized by its low tidal range with semidiurnal characteristics. Nevertheless, it has been pointed out by Edwards and Head (1987) that there is disagreement on a complete explanation of the Red Sea tides. On the other hand, the previous observation-based studies (Sultan *et al.*, 1995 and Saad, 1997) were basically limited to very few observations which are confined to the coastal region. The details of these studies are given in Chapter 3. Studies on tides of the Red Sea using numerical modelling approach do not exist.

On the other hand, the circulation processes inside the Red Sea domain has not received many investigations and therefore, it remains largely unexplored. In marginal seas there is often net buoyancy loss to the atmosphere either due to heat flux or fresh water flux or both. The Red Sea experiences many of the same features like other marginal seas (e.g. the Mediterranean Sea, the Labrador Sea) however; there are unique characteristics compared to other marginal seas. For instance, due to the large meridional extent of the Red Sea, it has been suggested that β -effect could be important than in other marginal sea (Fares, 1997).

The current knowledge on the circulation processes inside the Red Sea domain is very limited due to absence of intensive field and numerical modelling studies. Most of the observational efforts performed inside the Red Sea domain during the winter were carried out in the northern part of the basin (Morcos, 1970; Morcos and Soliman, 1974; Maillard, 1974; Clifford *et al.*, 1997) in addition to very few observations sparse in space (Vercelli, 1927; Vercelli, 1931). The conclusion drawn from these observational studies provide only a simple

story about the circulation regime during the winter season. On the other hand, observational studies concerning the summer season are mainly based on few field data which were collected along the main axis of the basin (Quadfasel and Baudner 1993; Sofianos and Johns 2007). However, such observations can only reflect the status at the time of the research period including the size and the nature of the area involved.

Numerical modelling studies in relation to the Red Sea circulation are very limited and mainly initiated during 1997-2003 (Eshel and Naik 1997; Al Barakati et al. 2002; Sofianos and Johns 2003) and a very recent studies conducted by Yao et al. (2014a, b). The general emerged features of these studies indicate that the Red Sea circulation consists of a complex three-dimensional circulation including features of cyclonic and anticyclonic gyres or eddies and intensified boundary currents which extended over hundreds of kilometres along eastern and western boundaries with different spatial structures. It should be mentioned that there is a controversy among them on for instance the structure and location of the sinking process, the dense water formation processes, the general circulation pattern and its seasonal variability and role played by the wind and buoyancy flux. A description of the previous observational and modelling studies is provided in Chapter 3.

In view of the above mentioned, it is obvious that the current study aims towards a better understanding of hydrodynamics in the Red Sea region since there is a need to carry out more researches to broaden our understanding about the tides and circulation processes in the Red Sea. Therefore, in this study we attempt to produce an additional contribution to the present knowledge of the spatial and temporal variability of the circulation in the Red Sea region.

The question comes up why we should learn more about these processes. The answer to this question would be simply; such processes may play significant role in sediment transport, nutrient distribution as well as in pollutant dispersion. Most of the Red Sea coasts are bordered by extensive coral reefs and the intensified boundary currents may transport nutrients and organism along the reef. Furthermore, carrying out ecological and other relevant environmental studies in the region should be built on enough knowledge about the hydrodynamic processes. Therefore, this study will provide and produce significant information for future studies.

1.3 Numerical Models and Field Data

There is no doubt that observations and field measurements are necessary components and an early step should be considered on the one hand to gain idea about the dominant processes in the area of interest, and on the other hand to be used for calibration and validation purposes the numerical models. Furumai (2010) for instance pointed out that the model development cannot proceed without scientific information and knowledge on the processes exists in a particular area. However, the data should be collected over a continuous and long period of time in order to reflect and provide accurate insights into the nature of the parameters that impact on the system (Schwartz, 2005). From another angle, it should be taken into account

the high costs of field data collection including other requirements involved in the processes such as research vessels and instruments.

With the measuring several parameters that include synoptic coverage and advancement in numerical modelling, larger data sets for further researches in the area of interest can be obtained. However, numerical models are not without problems since algebraic approximations to the differential equations are used, which can produce spurious solutions (Swapna, 2005). In general, at the present time numerical models have proven to be a very practical tool and are widely used.

In the last decades, numerical modelling capabilities have improved considerably as a result of increasing computer technology, improved methods in computational fluid dynamics and improved knowledge in ocean circulation. Thus, nowadays numerical models are highly used to simulate and determine the combined processes that cannot be achieved using a way or another. Nowadays, computer models allow users to simulate in one, two, and three dimensions. In addition, they enable users to model water bodies that are either steady state or dynamic systems.

Several authors have been thrown light on the necessity of the use of computer-based models in order to gain insight into the complex interactions between processes such as winds, currents and waves, tide, etc (e.g. Black, 1995). This means that the modellers have the possibility to setup different conditions in the same domain area and study their influences and interactions together. It should be considered that the performance of the numerical models is largely dependent upon the available field information that play significant role for a proper calibration and validation of the models (Adkins and Pooch, 1977; Reeve, D. *et al.*, 2004). More information about numerical modelling including the aspects and concept of the mathematical representations is presented in chapter 2. In the present study, the *Delft3D* modelling system developed by *Delft Hydraulic* has been implemented. The details of this model and its applications are presented comprehensively in chapter 4.

1.4 Motivation and Scientific Goals

The unique features of the Red Sea represented by the environmental and economic importance make it very interesting basin water to study. From the brief introduction of the previous works, it was found that for example the tidal observations used by the previous researchers were confined to the coastal region. The hydrographic data sets used by the previous researchers were also restricted to a small region under specific timing. Another example is that the relative importance about the main mechanism that controls the circulation in the Red sea is highly debated. In this content, numerical models became the only way to understand the influences of various parameters involved in the problem. One of the biggest advantages lies in the fact that they can produce the required results for everywhere defined in the model and for any time.

The overall aim of this study is to improve our understanding about the hydrodynamic processes in the Red Sea basin where there is lack of information. In order to achieve the main aim, a number of specific objectives were considered:

- i. To study the tidal characteristics in the Red Sea region.
- ii. To describe the seasonal cycle of circulation and hydrographic properties.
- iii. To investigate the relative importance of the wind forcing and thermohaline fluxes on the modelled key features of the circulation.
- iv. To identify the physical mechanisms that controls the circulation.
- v. To identify the main causes of generating features like eddies and gyres.
- vi. To identify the major source of the seasonal cycle in the exchange flow system exists through the Bab el Mandeb at the entrance to the Red Sea.
- vii. To investigate how, where and when the saline, dense Red Sea Outflow Water are formed.
- viii. To provide recommendations for future work.

1.5 Methodology

In order to fulfil the aim and objectives, the following methodology was adopted:

- i. Studying the physical system of the Red Sea by means of a detailed literature study including the available measurements and other data source such as satellite technique.
- ii. Establishing a 2-D dimensional hydrodynamic model incorporating the whole Red Sea region and part of the Gulf of Aden.
- iii. Extending the 2-D model into 3-D hydrodynamic model.
- iv. Calibrating and validating the hydrodynamic model with available measurements as well as remote sensing data.
- v. Obtaining the necessary data for the purposes of model forcing, calibration and validation processes.

1.6 Outline of the dissertation

This thesis has been organized in a total of eight chapters and briefly presented below as follows:

Figure 1.2 shows the structure of this thesis.

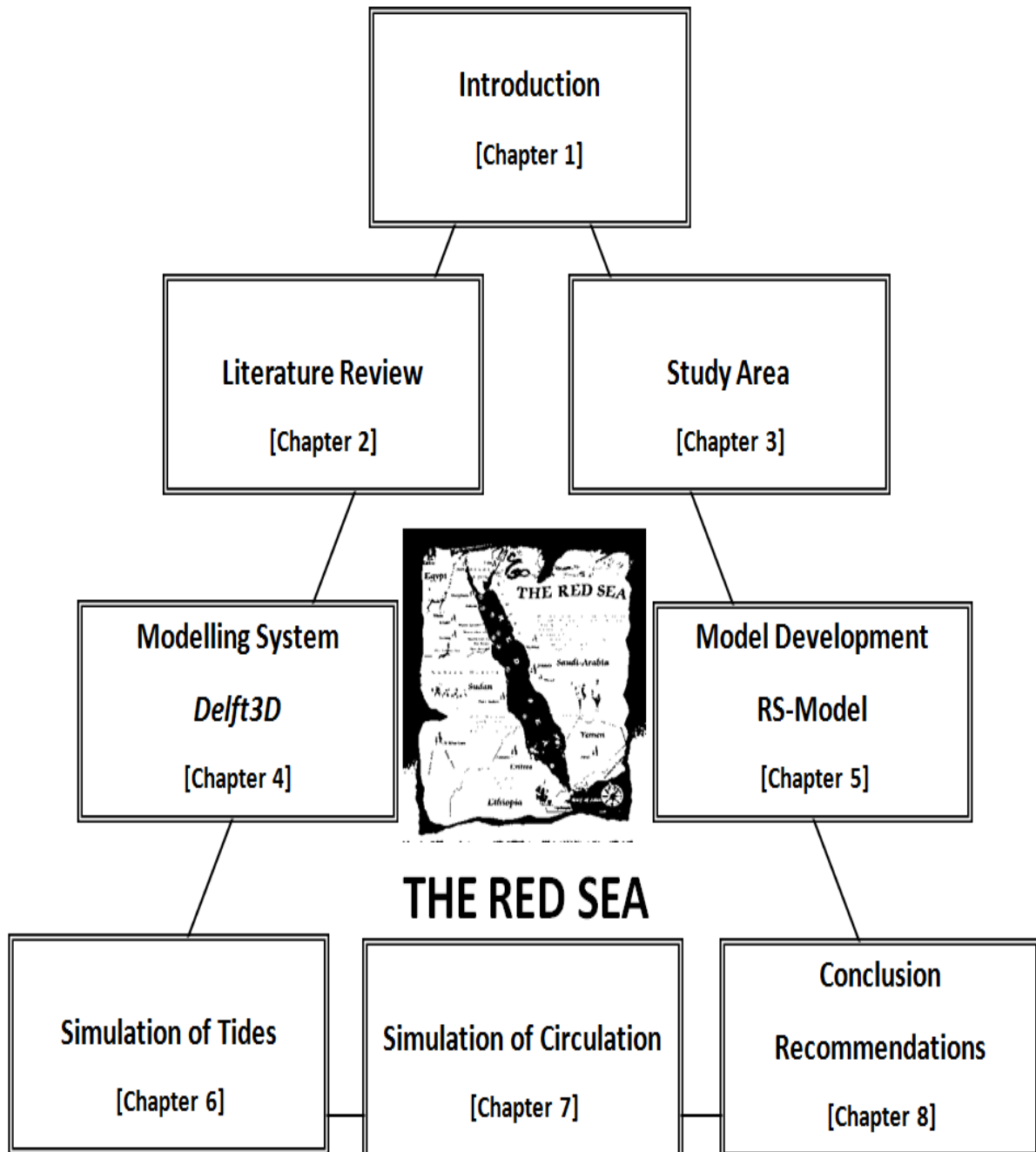


Figure 1.2 Structure of the thesis.

Chapter 1 Introduction

Here, the introduction, main scope, objectives and outline of this dissertation is presented.

Chapter 2 Literature review

Here, the state of the art knowledge on numerical modelling as well as description of the physical factors that derive the ocean circulation is presented.

Chapter 3 Study area, The Red Sea

Here, the general characteristics of the study area in terms of its physical settings, the state of its topography, climate characteristics, hydrodynamic conditions and sea water properties based on the available literature and other data sources are described. Subsequently, the available data obtained during the course of this investigation, their sources and analysis is presented.

Chapter 4 Delft3D modelling system

A brief description of the numerical modelling system used in the present study (*Delft3D* modelling system) commencement with general information of the system is given; then the basic theoretical information on the governing equations of the numerical model and their discretization and implementation is presented.

Chapter 5 Regional Red Sea model development

A description of the model setup is presented here. This includes the definition of the model domain, grid generation, bathymetry and boundary conditions. Afterwards, an extensive sensitivity test with respect to numerical and physical parameters is presented. In addition to that, the general aspects of calibration and validation processes are presented. This includes the comparison between the model simulations and measurements graphically as well as statistically.

Chapter 6 Simulation of Tides

Here, the characteristics of tides in the Red Sea based on the model simulation are presented.

Chapter 7 Simulation of Circulation and thermohaline structure

Here, the seasonal features of circulation and thermohaline structure based on the model simulation are given and discussed. Afterwards, additional numerical experiments aiming at investigating the relative importance of the main mechanisms controlling the circulation are presented. In addition, the period, possible sites and processes involved in the Red Sea outflow water formation are identified.

Chapter 8 Conclusions and recommendations

Here, the main conclusions of this study in addition to recommendations for further studies are provided.

Chapter 2

Literature Review

2.1 Introduction

The motions in the oceans are turbulent and cover a wide range of temporal and spatial scales (Swapna, 2005). The main processes that derive oceanic circulation are the internal density structure of the water mass, radiative and turbulent heat fluxes and the forcing imposed at the sea surfaces mainly the wind and buoyancy fluxes. Among the methods to study such phenomenon are the field measurements and numerical models. Field measurements however, alone cannot provide enough information on the variability of circulation on larger space and time scale. In spite of the fact that field observation and measurements are considered essential elements in this regard, there are some issues concerning the field data collection that must be considered. One of these issues is that field measurements usually are carried out in a small and localized area for limited periods. Therefore, this kind of field data and their analysis can only reflect a picture on the behaviour of the water system under the conditions exist during the period of measurements. It is well known that most of the processes occur over long time and have large spatial extents. Thus the costs involved in the data collection are high.

The overall structure of the oceans and patterns for circulation have been obtained by in-situ measurements, however, studies based only on observations cannot provide quantitative information about the nature of circulation and their variability under different atmospheric conditions. With the recent developments in satellite techniques in measuring several parameters that include synoptic coverage in addition to advancement in numerical modelling, significant amount of data sets for further research in the area of interest can be obtained. However, remote sensing technique has some limitations. This includes measuring some processes only near or at the surface, low spatial resolution, lack of data near the coastlines and missing data due to clouds and dust in the atmosphere. On the other hand, numerical models are not without problems since algebraic approximations to the differential equations are used, which can produce spurious solutions (Swapna, 2005).

As defined in chapter [1] the main aim of this study to improve our understanding about hydrodynamics in the Red Sea using a numerical modelling approach. Therefore, a survey of literature about numerical modelling on the one hand and the main processes that play major role in the ocean circulation on the other hand was found essential.

This chapter gives a brief general introduction about the numerical modelling including its definition and importance in sections (2.2). This is followed by pointing out the main advantages and disadvantages of numerical models in section (2.3). Subsequently, types and dimensions of a numerical model are given in section (2.4). This is followed by introducing the steps of numerical model evaluation including sensitivity analysis, calibration and validation processes in section (2.5). Afterward, section (2.6) gives information about the 3-D circulation models including theory and basic approximation and aspects of 3-D modelling. This is followed by throwing the light on the main processes controlling the oceanic circulation in section (2.7).

2.2 Definition and Importance of Numerical Models

During the past 50 years, the developments of numerical models have shown considerable progress associated with the developing computer technology. In the present time, with the support of increasing capacity in the computational resources, the applications of numerical models have proven to be a very practical tool and are widely used in the analysis of several processes interacting in the same domain area. It is very important to mention that the performance of the numerical models is highly dependent upon the field information that play significant role in calibration and validation processes of the models (Adkins and Pooch, 1977; Reeve, *et al.*, 2004).

Some researchers indicated that the definition of modelling may vary based on the application but in general the basic idea remains the same. In general, numerical modelling can be defined as a mathematical representation of the actual physical world (Adkins and Pooch, 1977; Reeve, *et al.*, 2004; Sisson, 2010). In this frame, a hydrodynamic model is used to reproduce the flow conditions as realistically as possible by means of a set of algebraic equations in addition to suitable model inputs. However, it is necessary to consider the essential steps, the processes to be simulated and the modelling sequence.

Several authors have been thrown light on the necessity of the use of computer-based models in order to gain insight into the complex interactions between processes such as winds, currents and waves, tide, etc (e.g. Schwart, 2005; Swapna, 2005; Black, 1995). This means that the modellers have the possibility to setup different conditions in the same domain area and study their influences and interactions together. Accordingly, numerical models have been used to simulate some physical phenomenon that cannot be carried out adequately in any other ways in addition to provide detailed data on both temporal and spatial scale.

Ji (2008) have categorized numerical models in terms of model representations of space and time as following:

- Steady state or time dependent (dynamic),
- Zero, one, two, or three dimensional.

The temporal characteristics involves whether the model is steady state or time dependent, depending upon the treatment of the time derivative in the governing equations. However, understanding the field and data collection is considered the first and most important step to derive reasonable results from the numerical models (Ji, 2008).

2.3 Advantages and Disadvantages of Numerical Modelling

All methods and consequently numerical models have their own advantages and disadvantages. Adkins and Pooch (1977) pointed out that one of the major advantages of numerical models is that simulation experiments can be run many times to test different scenarios with varying input parameters and check the behaviour of the system under a variety of conditions. Another advantage is that time compression in which operation of the system over extended periods of time can be simulated in minutes particularly with fast computers. In addition to that, sensitivity analysis by changing the input variables can be carried out. Besides that, they are quicker and cheaper comparing to other methods and also provide detailed results.

On the other hand, there are some main problems associated with numerical models. One of the problems in numerical simulation is that capturing the main features of the flow requires understanding of the underlying physics in detail. Nevertheless, a complete description of the flow would yield a complex system of equations; therefore they require and consume more time to be solved. Generally, it is not possible to have a complete description since there are some terms not well understood and have to be approximated or modelled empirically such as turbulent shear stresses and bed stresses (Adkins and Pooch 1977).

The numerical models use algebraic approximations to the differential equations which do not always consider the underlying physics. Therefore, these approximations can produce large errors in the solution (Swapna, 2005). In addition to that, numerical models provide only information at grid points of the model. This means that they do not provide information about the flow between the points. The ocean is turbulent, and to resolve such processes, it needs grid points spaced millimetres with time steps of millisecond. Practical ocean models contain grid points spaced tens to hundreds of kilometres in the horizontal and tens to hundreds of meters in the vertical. In this case, turbulence cannot be computed directly and therefore, the influence of turbulence must be parameterized (Swapna, 2005).

It has been pointed out by Denner (1989) that one of the troublesome aspects in numerical modelling is the open boundaries of the model. This includes the boundary conditions prescribed at the open boundaries which must be appropriate with physical processes being simulated within the interior of the model domain. Another issue in the numerical simulation method associated with the gridding of the computational domain. Usually these kinds of

problems appear particularly with complicated geometries with highly irregular coastlines, in addition to the presence of islands and complex harbour and breakwater configurations (Abbot *et al.*, 1973). However, curvilinear coordinates in such cases assist in solving this kind of problem with producing a boundary fitted grid (Tevfik, 2006).

2.4 Dimensions of a Numerical Model

Classification of numerical models depends on the number of spatial dimensions over which variables are permitted to change. They are classified into three types namely, one, two and three dimensions. Therefore, there are clear differences in the approach and capabilities among these types. In a one-dimensional flow model (1-D), flow parameters like currents are averaged over two dimensions (width and depth) and vary only in one direction (longitudinal direction). In two-dimensional models (2-D) “depth-averaged models”, variables are averaged over one spatial dimension, over the water depth or width. It should be mentioned that averaging always causes loss of information. Three dimensional models (3-D) do not average the flow parameters and solve equations accounting for variation of the variables in all three dimensions (longitudinal, vertical and transverse axes). More information about the three types of spatial dimensions is discussed in the following sections.

2.4.1 One-Dimensional model

In general, one-dimensional models can be set up quickly and require fewer amounts of field data for calibration, in addition to the least amount of computer time and capacity. According to Martin and McCutcheon (1999) one-dimensional models solve the unsteady, cross-sectionally averaged equation for the hydrodynamic without solving the details over the cross-section. This means that this approach does not provide details of vertical and horizontal velocity distribution, salinity stratification or circulation within large water basins. In this approach, model parameters have the same value over the entire width of the cross section. Therefore, one-dimensional models are not appropriate option for simulating two- or three-dimensional phenomena.

2.4.2 Two-Dimension Model

Two-dimension of depth integrated models are based on the depth-integrated equations of motion and continuity (McAnally *et al.*, 1986; Tevfik, 2006). The water surface elevation, depth-averaged velocity are computed at each of many points across the cross-section. However, the flow characteristics are assumed to be uniform through the water column at each computational point, so stratification is not described.

According to Moffatt and Nichol (2000), two-dimensional models can be categorized into two-dimensional horizontally averaged (2-DH) and two dimensional vertically averaged (2-DV) models. The former scheme is used where depth-averaged velocity or other parameters relevant to hydraulic and transport can adequately describe the variation of the parameters across a channel. In this case, the flow field does not show large variations in vertical direction and the fluid density is stable (e.g. tidal flow in well-mixed estuaries). The later

scheme is used where width-averaged hydraulic and transport parameters can adequately describe the condition in the vertical direction. In this case, the flow in one horizontal direction is uniform but it shows large variations in vertical direction (e.g. wind-driven circulation perpendicular to the coast).

It has been pointed out by Moffatt and Nichol (2000) that 2-DH models have the capability to handle several features such as Coriolis Effect, transverse components of flow, realistic friction and non-linearity by means of the distribution of flow through arbitrary cross-section. On the other hand, 2-DH cannot describe secondary circulation, whether transverse and vertically sheared like at bends, or driven by lateral differences in salinity due to differential ebb or flood currents. Furthermore, 2-DH models cannot represent water circulation. 2-DH models are more time consuming to set up compared to 1-D model and require more computer time to run in addition to more field data for calibration and validation processes (Moffatt and Nichol, 2000).

2.4.3 Three-dimension model

Three-dimension models are similar to two-dimension models except that the vertical dimension is modelled through a number of layers. The thickness of layers may be of uniform type, or may represent the water depth in a number of layers of unequally spaced. Therefore, three-dimension models can handle the vertical structure of the water column and provide more details about the hydrodynamic system.

It is well known that the flow phenomena in nature have three dimensions. Therefore, to simulate the hydrodynamic and transport processes more realistically, three dimensional (3-D) model schemes are necessary. Turbulence is basically three-dimensional phenomenon (Moffatt and Nichol 2000), and three-dimensional models are very useful for the simulation of turbulent heat and mass transport. These models are based on the Reynolds-averaged form from the Navier-Stokes equations, using additional equations of various degree of complexity for the turbulence closure.

Three-dimensional modelling is a very powerful tool; the flow is integrated and computed for each time step taking into account both horizontal and vertical components. However, the data required for setup, calibration and validation processes are extensive and expensive due to the necessity of a comprehensive field program to capture the complexity of flow in three directions. In addition to that, the computational time consumes longer computer simulation times as compared to two schemes (Moffatt and Nichol, 2000).

Many researchers (e.g. Moffatt and Nichol, 2000; Tevfik, 2006) pointed out that the major problem faced by 3-D modelling is the determination of suitable, realistic initial and boundary conditions. This often involves a very extensive and expensive field measurement program. On the other hand, they also pointed out that the suitability of the use of 3-D models is related to the number of the grids applied in the vertical direction. If the vertical distributions are not defined accurately, the desirable results cannot be obtained from the 3-D

model. This means that in some cases refined grids are required in order to obtain efficient and accurate results.

2.5 Model Evaluation

Model evaluation composes of analysing the model errors and comparing simulated outputs with field measurements. The main aim of evaluation is to get an estimate about the usefulness of a model and judging the predictive ability of the model. If the simulation results are in a good agreement with the measurements then the model can be considered reliable.

2.5.1 Sensitivity Analysis

Sensitivity analysis is one of the essential steps in the model set up processes. The major aim of sensitivity analysis is to obtain an estimate on the general performance of the model and determine the influences of input variation on the model results (Furbringer and Roulet, 1999; Palacio *et al.*, 2005). Sensitivity analysis requires changing the model's input by a small amount and checking their significance on the model's results. It has been pointed out by Law and Kelton (1982) that if the output varies significantly due to a small change in an input parameter, that input parameter may require reconsideration. It is suggested that multiple runs are necessary to assess the sensitivity of the model to different parameters values. A comprehensive sensitivity analysis can give the modellers idea about the robustness of the model in addition to provide insights into whether the obtained simulation results conform to reality. Based on the sensitivity analysis, the numerical parameters (grid resolution and time step) are fixed while the physical parameters (e.g. boundary conditions, bottom roughness and wind drag coefficients) that influences the simulation results are identified.

2.5.2 Calibration

Calibration process appears as a second phase in model development which highly depends on data availability and researchers opinion. The main aim of calibration is to adjust the physical parameters in the numerical model to reproduce the conditions exist in the studying area. This means that calibration processes involve adjustments to the physical parameters in the model which were identified during the sensitivity analysis in order to match the field measurements as realistic as possible. In case of hydrodynamic modelling, the calibration is frequently made by qualitative comparison of time series of predicted and measured data for the same location and period of time (Metha, 1995; Hsu, *et al.*, 1999).

It is worth mentioning that measurements may contain inaccuracies and errors. In addition to that, it should be taken into consideration that adjusting certain model parameters to match observations at one location and time, may decrease the quality of the model results with respect to the measurements in other locations in the model domain area. Therefore, the modeller in such cases should arrive at balance during calibration phase for a certain parameter and seek on the "good enough" condition (Palacio *et al.*, 2005). However, the modeller cannot over-calibrate the model because the calibration is made with one parameter at a specific time while in reality all parameters are acting simultaneously.

2.5.3 Validation

The validation processes is considered the last phase in the model development before the application. The aim of this process is to assess the credibility of the simulation models. This step involves that, the calibrated models are used to predict another different measured period. Therefore, the degree to which the models can predict this period is a measure of its predictive ability (Metha, 1995; Hsu, *et al.*, 1999).

However, a comprehensive validation of such models against field data cannot be carried out because of the lack of field data with sufficient spatial coverage. According to Palacio *et al.*, (2005), validation of numerical model for field condition requires a data set of sufficient length to cover variations in the tidal cycle and varying wave and wind conditions. In addition to that, he pointed out the importance of availability of dense spatial instrumental coverage within the modelling area in order to obtain an accurate representation of the spatial flow pattern.

2.6 Three-dimensional circulation models

Three dimensional models to simulate oceanic circulation witnessed high development in 1980_s taking the advantages from the increase in computing capacity and in the breakthroughs in turbulence modelling (Moore *et al.*, 2004). In 1990_s, hydrodynamic models were consolidated and a number of models with great visibility started to appear. In the second half of the 1990_s, with the technology advances in the hardware and software, integrated models and coupled modules started to emerge. Currently, research efforts on modelling is taking place towards operational modelling systems integrating different disciplines and assimilating as much field data as possible with special emphasis to remote sensing (Moore *et al.*, 2004). The improvements in the development of 3-dimensional numerical models in the field of hydrodynamic and oceanography have assisted in simulating, understanding and predicting several phenomena. The following sections briefly throw the light on the range of numerical methods available to represent and identify some key phenomena in ocean modelling.

2.6.1 Theory and basic approximation

The movement of ocean currents and other fluid flow phenomena is governed by the Navier-Stokes (momentum), continuity and energy equations (more details about the general form of the basic equations can be found in the literature e.g. Metha, 1995; Bryan, 1969). In most cases, the variable to be solved are the velocity components u, v, w , the pressure P , the volumic mass of the fluid ρ , the temperature T and salinity S of the fluid. These variables are functions of space and time coordinate. According to Metha (1995), the basic hypotheses applied in ocean modelling are as follows:

- Fluids in ocean modelling are treated as incompressible.
- The Coriolis force and the gravity force are taken into account while the centrifugal forces can be neglected.
- The density variation can be neglected in all terms of the equations except in the gravity force due to their significant effects. (Boussinesq approximation)
- The internal energy is only temperature dependent because the fluids are considered incompressible.
- The energy equation is simplified into one temperature equation and one salinity equation.

2.6.2 Aspects of 3-D Modelling

Three dimensional numerical models are based on the same set of governing equations but their performance differs widely. It has been pointed out by Swapna (2005) that, when the same equations are discretized for solution on a digital computer, the behaviour of the resulting discretized forms of governing equation can differ because of the horizontal and vertical discretization schemes used, time stepping methods adopted and the way of handling important terms like advection and diffusion. Each modelling case requires specific model, and the decision to select a suitable model should be made based on modelling needs. Modellers should therefore, choose a suitable model to resolve the phenomena of concerned taking into consideration accuracy and efficiency. In order to decide which horizontal and vertical discretization schemes are appropriate for the Red Sea domain, a detailed description of these schemes is given in the following sections.

2.6.3 Grids, Horizontal and Vertical Discretization

To solve the hydrodynamic equations of motion (fluid movement, pressure and transport of constituents) numerically, approximations are introduced. These approximations are algebraic equations that are solved at separate points or cells (Tevfik, 2006). This means that the domain of the area of interest is represented as a grid. There are two types of grids usually adopted for such purpose i.e. structured and unstructured Grids. The former type is used if the computational domain is selected to be rectangular in shape and the interior points are distributed along the orderly defined gridlines. The latter is used when the grid points cannot be associated with orderly defined gridlines. The same as all methods, and consequently grid types have some advantages and disadvantages. Tevfik (2006) indicated that there is no unique approach to decide which method is better, but the geometry plays a role in this regard and gives one type more advantages than the other. However, a grid selection depends mainly upon the problem of interest.

2.6.3.1 Horizontal discretization

To solve the three-dimensional hydrodynamic equations, two commonly methods known as finite difference and finite element methods are used. In case of rectangular domains, it is suggested that finite difference equations are most efficiently solved with equal grid spacing. But in reality it is impossible to have rectangular domains. Therefore, the non-rectangular physical domain in this case should be transformed into rectangular computational domain where grid points are equally spaced (Tevfik, 2006). In finite difference approach, usually the variables are staggered in space by using staggering techniques such as Arakawa C-grid (see chapter 4).

On the other hand, if the domain is very irregular such as bays and river branches, unstructured grids are appropriate to represent the irregularities. The triangular elements are flexible in shape to fit any type of boundary. Finite element methods are generally used with unstructured grids (Tevfik, 2006). However, finite element methods are complicated and require larger CPU memory space and also time. Therefore, the finite difference method is frequently preferred over the finite element method. According to Moffatt and Nichol (2000), finite difference calculations are more computationally efficient for a given net size than finite element calculations.

2.6.3.2 Vertical Discretization

The choice of the vertical coordinate system is one of the most important aspects in the ocean model design. This is because the bottom topography and its gradients are very important to the circulation and to the horizontal and vertical transport of properties such as temperature and dissolved substances (Swapna, 2005; Chassignet *et al.*, 2002). In numerical ocean models, there are three different vertical discretization systems known as; “z-coordinate model” (e.g. Modular Ocean Model, Bryan, 1969), “Isopycnal coordinate model” (e.g. Miami Isopycnal Coordinate Ocean Model, Bleck and Smith, 1990) and “ σ -coordinate model” (Phillips, 1957). Figure 2.1 gives a picture about the main types of vertical discretization currently being used in ocean modelling. It can be seen clearly differences among the three vertical coordinates (e.g. the mixed layer depth).

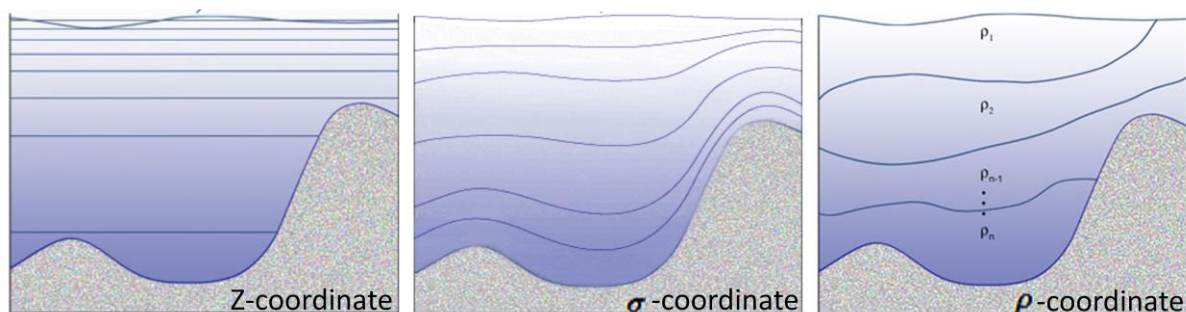


Figure 2.1 Main types of vertical coordinate representation in ocean modelling, Z (left), σ (middle) and ρ (right) coordinate system [Chassignet *et al.*, 2002]

2.6.3.2.1 Z-coordinate model

Z-coordinate systems are the simplest numerical discretization and have been used for many decades. In the z-coordinate system, the model domain is divided using equal spacing layers over the vertical. The Z-grid has horizontal co-ordinate lines that are almost parallel with density interfaces (isopycnals) in regions with steep bottom slopes (Swapna, 2005; Chassignet *et al.*, 2002). The bottom and free surface is usually not a co-ordinate line and is represented as a staircase. The number of grid cells in the vertical varies from grid point to grid point and it depends on the local depth. The advantage of this type of system is the ability to represent the horizontal pressure gradient terms accurately. These models are suitable to areas that are well-mixed because they can provide the very fine resolution needed to represent three-dimensional turbulent processes (Chassignet *et al.*, 2002). However, Z-coordinates have a disadvantage in regions of sloping topography where the levels intersect the bathymetry (unrealistic vertical velocities near the bottom can result). To overcome this problem, the number of vertical layers needs to be increased to improve the representation of bottom topography and thus, flow in the near bottom area. However, the computational time in this case would be high (Chassignet *et al.*, 2002).

2.6.3.2.2 σ -coordinate model

In the σ -coordinate system, the vertical coordinate follows the bathymetry, keeping the same number of vertical grid points everywhere in the domain, regardless of the local water depth. Due to the nature of this type of model, the layer thickness is non-uniform changing with time and space (Tevfik, 2006; Swapna 2005; Chassignet *et al.*, 2002). This type is usually important and appropriate for wind-driven flows, heat exchange with the atmosphere and the near bed area (sediment transport). The disadvantage of sigma-coordinate system is that it has difficulties to represent the horizontal pressure gradient accurately where stratified flow can occur in combination with steep topography (Swapna, 2005; Haney, 1991; Chassignet *et al.*, 2002). Because the “ σ ” level is boundary fitted, it will not have enough resolution around the pycnocline which is strictly horizontal in the physical space. Pressure gradient error can give rise to unrealistic flows. To overcome such problems, increasing the horizontal resolution and smoothing bathymetry is recommended (Haney, 1991; Chassignet *et al.*, 2002).

2.6.3.2.3 ρ -coordinate model

The ρ -coordinate system uses the potential density referenced to given pressure as the vertical coordinates (Bleck and Smith, 1990; Chassignet *et al.*, 2002). In the ρ -coordinate models, the water column is divided into distinct homogeneous layers and the thicknesses of these layers vary from place to place and from one time step to the next. The advantage of isopycnal models is the ability to represent the horizontal pressure gradients and keeping the conservation of the mass between the equipotentials. However, this type of model has limited application in coastal areas and in the surface and bottom boundary layers because the cross-isopycnal mixing is not available in this coordinate system. Therefore, the representations of the surface mixed layer and the bottom boundary are considered large weaknesses.

2.7 Hydrodynamics and Circulation

Circulation of a marine environment in general is highly complex. It can be derived from both barotropic and baroclinic forces. The former forces are those where density is considered constant and pressure is a function of the vertical depth only $\rho(z)$ whereas the latter are those where density of the fluid is not assumed constant and functions of x , y , and z .

A Barotropic flow includes tides, wind induced currents and atmospheric pressure, which are usually uniform throughout the water column (Apel, 1987; Paul, 2003). Because tides are considered to be long waves (wavelength greater than wave height), tidal velocities do not change with respect to vertical distance below the sea water surface with exception at the ocean bottom where frictional forces are effective.

Baroclinic flows on the other hand are derived from pressure gradients and variations in the vertical. They are characterised by lower frequencies and take longer to spread and propagate in comparison to barotropic flows (Apel, 1987; Paul, 2003). Examples of baroclinic flows are flows caused by salinity and temperature gradients caused by heating, evaporation and freshwater inflow or a combination of them. It should be pointed out that there are some additional factors that have constantly active role with different degrees such as Coriolis effects, freshwater and storm surge. More information about the circulation driven forces is discussed in the following sections.

2.7.1 Tides

Tides are defined as the periodic motion of the water surface resulting from the gravitational attraction of the moon and the sun in combination with the centrifugal force. The lunar effect is larger than the solar influence due to the distances between the moon and the earth is significantly less in comparison to the sun. When the earth, moon and sun form one line, the full or new moon, the solar and lunar tides produce large tidal amplitudes. This is known as spring tide phenomenon (the tidal range at a maximum). Another phenomenon occurs when solar and lunar tides are 90° out of phase, their influences are reducing each other resulting less tidal amplitude. This phenomenon is known as neap tide (the tidal range at a minimum).

Tides propagate as long waves on the rotating earth. The combined constraint of ocean basin geometry in addition to the influence of the Coriolis force leads to the development of amphidromic system which make the tidal wave rotates around the amphidromic point in counter-clockwise direction in the northern Hemisphere and in clockwise direction in the Southern Hemisphere. The tidal range at amphidromic point is zero and increases outward away from it. The locations of these points in an ocean basin depend mainly upon factors like the geometry of the basin including the coastal configuration and bathymetry (Pugh, 1987 and Paul, 2003).

Tide can be represented by number of harmonic constituents. Table 2.1 lists the major tidal constituents, their period and angular speeds. The general form of describing each of the tidal constituents is expressed as:

$$H_n \cos(\omega_n t - g_n) \quad (2-1)$$

Where: H_n is the amplitude, ω_n is the angular speed (related to period T_n as $\omega_n = 2\pi/T_n$), g_n is the phase lag of the observed constituents relative to the theoretical Equilibrium Tide obtained by adjusting ‘ G_n ’ to a particular time meridian. ‘ G_n ’ is the phase lag of the constituent on the Equilibrium Tide at Greenwich, in Greenwich Mean Time. The relation between the two phase lag is expressed as:

$$G_n = g_n + T_z \omega_n \quad (2-2)$$

Where: T_z is the time zone defined as the shift in time at any place with respect to the Greenwich Mean Time.

Tides in narrow water bodies such as marginal seas and estuaries act quite differently due to the shape of these areas. Bathymetry and configuration of sea bed play also role in the propagation of tide. When tides propagate into shallow water, the non-linear mechanism causes transfer of tidal energy to other frequencies (Pugh, 1987; Paul, 2003). These frequencies are represented as shallow-water tidal constituents known as overtides and compound tides (Table 2.2). The frequency of overtides (e.g. M_4 and M_6) is an exact multiplies of the frequency of the constituents that subject to transformation in shallow water. On the other hand, a compound tide is produced from the shallow water-interaction of two major tidal constituents (e.g. MS_4 is produced by the interaction of M_2 and S_2).

To represent the propagation of tides in the ocean and marginal seas, so-called co-range and co-tidal charts are used. The former is used mainly for visualizing the amplitude of the tide while the latter chart is used to illustrate the progression of tides. Co-range line indicates locations that have equal tidal range and the co-tidal line connects locations where the phase of tide is the same.

2.7.2 Wind Stress

When wind blows over the ocean, it will supply momentum and kinetic energy to the upper layer of water. Therefore, this energy drives surface water movements as a result of its frictional drag on the surface (Apel, 1987; Paul, 2003). This dragging generates a shear stress along the water-air interface. According to Paul (2003), stress acting on the sea surface by the wind is measured as the horizontal force per unit area. To estimate the shear stress (τ) caused by the wind, empirical equations are available in the literature. The following relationship represents how wind is related to surface shear force:

$$\tau = \rho C U^2 \quad (2-3)$$

Where: τ represents wind stress vector, ρ represents the density of air, C represents the atmospheric drag and U represents the wind velocity vector measured at a certain height.

Table 2.1 Major tidal constituents [Pugh, 1987]

Types	Tidal species	symbol	Speed [°/hour]	Period [hour]
Semi-diurnal	Principal Lunar	M_2	28.9841	12.4206
	Principal Solar	S_2	30.000	12.0000
	Larger elliptical lunar	N_2	28.4397	12.6584
	Smaller elliptical lunar	L_2	29.5285	12.1916
	Declinational lunar	K_2	30.0821	11.9673
Diurnal	Luni-solar	K_1	15.0411	23.9344
	Principal lunar	O_1	13.9430	25.8194
	Principal solar	P_1	14.9589	24.0659
	Larger elliptical lunar	Q_1	13.3987	26.8684
	Elliptical lunar	J_1	15.5854	23.0984
	Smaller elliptical lunar	M_1	14.4920	24.8412
Long period	Lunar semi-monthly	M_f	1.0980	327.85
	Lunar monthly	M_m	0.5444	661.31
	Solar Annual	S_a	0.0411	8765.76
	Solar semi-annual	S_{sa}	0.0821	4383.05

Table 2.2 Important shallow water tidal constituents

Tidal species	symbol	Speed [°/hour]
Long period	M_{sf}	1.016
Semi-diurnal	$2SM_2$	13.016
	$2MS_2$	27.968
Fourth diurnal	M_4	57.968
	MS_4	58.984
	S_4	60.000
Sixth diurnal	M_6	86.952
	$2MS_6$	87.968

2.7.3 Atmospheric Pressure Variations

Changes of atmospheric pressure are associated according to the seasons. Changes in the pressure exerted by weather systems produce influences on the water levels in the ocean. The measurement of these atmospheric pressure variations is known as barometric pressure. A

decrease in barometric pressure of 1 hPa results in an increase of sea level by 1cm. This relationship is known as inverse barometric effect and is evaluated using the following formula:

$$\Delta\eta = -0.993\Delta P_{\text{atm}} \quad (2-4)$$

Where: $\Delta\eta$ represents the change in water level [cm] and ΔP_{atm} represents the changes in barometric pressure [hPa].

The inverse barometric phenomenon is difficult to measure since there are other factors influence the mean water level such as continental shelf waves and wind (Paul, 2003 and Apel, 1987). However, it is important to identify the barometric pressure as a variable in affecting the water levels.

2.7.4 Surface circulation

Surface ocean currents respond mainly to the wind field. The wind-driven circulation occurs mainly in the upper few hundred meters and therefore is considered as a horizontal circulation. However, vertical motions can be induced when the geometry of surface circulation results in convergences (down-welling) or divergences (upwelling) (Paul, 2003; Rahmstorf, 2006). The depth to which the surface circulation can reached depends mainly upon the water column stratification. For instance, in the equatorial region the currents expand to 30-500 m whereas in the circumpolar region (where stratification is weak) the surface circulation can extend to the sea floor (Paul, 2003).

When the wind blows across the sea surface, it drags the surface along and puts this layer in motion. The direction of water motion is not always the same as the wind direction in case of other factors. Due to the earth rotation this shallow layer is deflected to the right (left) of the wind direction in the Northern (Southern) Hemisphere. For instance, in the Northern Hemisphere the surface currents deflect to the right at (45°) and pushes the beneath layer slightly to the right direction (slightly weaker current) and next layer pushes next layer slightly to right producing a spiral of the current vectors with decreasing speed associated with increasing depth (Figure 2.2a). This phenomenon or feature is known as the Ekman spiral.

Under the influence of a strong, persistent wind, the Ekman spiral may extend to a depth of between 100 and 200 m, below which wind-induced effects are negligible (Paul, 2003; Rahmstorf, 2006). Ekman calculated the net transport over the wind-driven spiral (called Ekman transport) to be 90° to the right of the wind in the Northern Hemisphere and to the left in the Southern Hemisphere (Figure 2.2b). This calculation represents the average of all the directions and speeds of the current spiral.

It is important to mention that Ekman transport plays important role in other types of surface water currents. That is, when the wind blows parallel to a shore (this depends on the hemisphere), the resultant Ekman transport moves the near-surface water offshore. As a

result, water rises from below to compensate for the seaward surface flow. This vertical process is known as upwelling. The sinking of surface water (known as downwelling) on the other hand is caused along a shoreline by winds blow parallel to the coast; Ekman transport drives water against the land and causes surface water to sink. However, these vertical processes are not limited to the edges of continents but they also can occur in the open ocean where winds cause surface waters to diverge from a region (causing upwelling) or to converge toward some region (down-welling) (Paul, 2003; Rahmstorf, 2006).

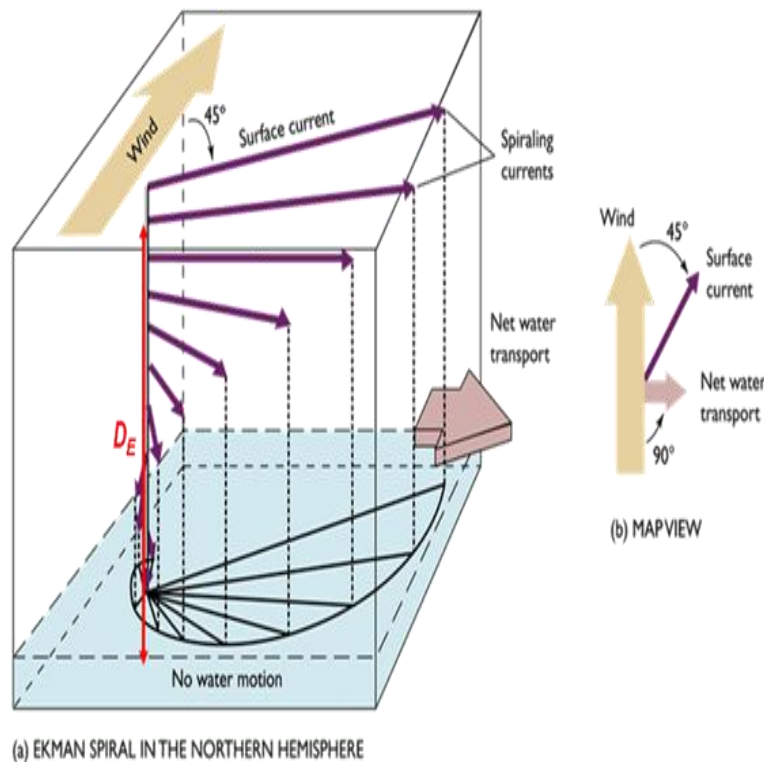


Figure 2.2 Ekman Spiral describes how the horizontal wind sets surface waters in motion. As represented by vectors, the speed and direction of water motion change with increasing depth. [Adopted from Paul, 2003]

In the oceans, over time scales longer than several days and at spatial scales longer than several kilometres, the equilibrium of forces in the horizontal is between the pressure gradient force and the Coriolis force (Paul, 2003). The steady currents resulting from a balance between the two forces is known as geostrophic currents. When the flow is geostrophic, other forces (except the pressure gradient and Coriolis forces) become negligible. Under geostrophic equilibrium, the pressure gradient derives the water parcel to move from high to low pressure, but Coriolis force moves the parcel to the right in the Northern Hemisphere and to the left in the Southern Hemisphere. On the other hand, in a steady geostrophy state, the water parcel moves exactly perpendicular to the pressure gradient force. The vertical force balance that associates with geostrophy is hydrostatic balance (Paul, 2003). The mathematical formula for the geostrophy is as following:

$$-fv = -\frac{1}{\rho_0} \frac{\partial P}{\partial x} \quad (2-5)$$

$$fu = -\frac{1}{\rho_0} \frac{\partial P}{\partial y} \quad (2-6)$$

The hydrostatic balance is

$$0 = -\frac{\partial P}{\partial z} - \rho g \quad (2-7)$$

Where: f represents the Coriolis force, u, v represent the components of the horizontal velocity, ρ and ρ_0 represent the density and a constant reference value respectively, x, y, z represent Cartesian coordinates with z oriented upward and P represents the pressure.

2.7.5 Deep Circulation and Water Mass Formation

As mentioned above the geostrophic currents of the ocean are largely limited to the upper layer of the water column as a result of direct affect of wind power. Deep water is not influenced directly by the wind however, is in motion at all depths. These subsurface currents are referred to as thermohaline circulation (THC) which resulting from density differences between water masses. It has been pointed out by Paul (2003) that studying the thermohaline circulation is difficult and expensive since it occurs in the subsurface of Open Ocean. In addition to that, these subsurface currents tend to flow very slowly making their speeds technically challenging to measure directly. Nevertheless, physical oceanographers have successfully identified the general pattern of subsurface water motion.

Temperature (*thermo*) and salinity (*haline*) are the most important characteristics of seawater which determine and control the density of the water (the major factor governing the vertical movement of ocean waters). The so-called “thermohaline circulation” is the part of the ocean circulation driven mainly by fluxes of heat and freshwater at the surface and by density differences in the internal ocean (Rahmstorf, 2006 and Paul, 2003). In contrast to the wind driven-currents, the thermohaline circulation is not limited to the surface water but can be regarded as overturning of the world ocean from top to bottom. As the ocean is not a linear system, it is difficult to separate the thermohaline driven circulation from the wind driven circulation (Gill, 1982). For example, buoyancy forcing depends upon wind speed.

Studies of the circulation and identification of water masses started in the second half of the 19th century. For example, Nansen (1906) was the first to observe the Greenland Seas Deep Water and later observed dense overflows in the Denmark Strait and at the Iceland-Faroe Ridgw. Helland-Hansen and Nansen (1909) carried out comprehensive and detailed survey to study the statues of circulation and hydrograph in the Nordic Seas (Blindheim and Østerhus, 2005). In 1916, they introduced the *TS*-diagram which has become valuable oceanographic tool in classifying different water masses. A schematic representation of the global thermohaline circulation is shown in Figure (2.3).

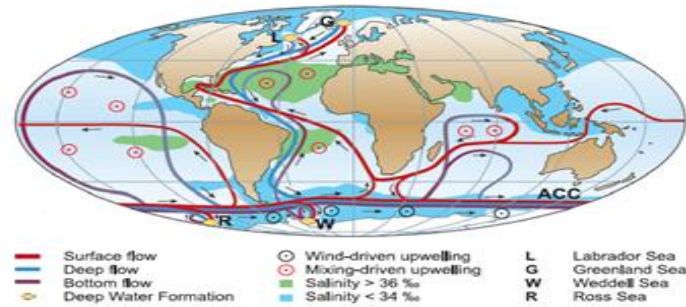


Figure 2.3 Schematic representation of the global thermohaline circulation, surface currents are shown in red, deep waters in light blue and bottom waters in dark blue. The main deep water formation sites are shown in orange [adopted from Rahmstorf, 2006].

As already mentioned the density of the water is the major factor governing the vertical movement of ocean waters. Therefore, in terms of vertical structure, the ocean is divided into three horizontal depth zones according to density (exception at high latitudes). These are the mixed layer, pycnocline and deep layer (Figure 2.4). Surface currents are subject to changes as a result of continuous variations in the wind, precipitation, and heating or cooling. Movements of surface waters due to wind produce a well-mixed layer of almost uniform density. Therefore, the surface layer of the ocean is called the mixed layer. The pycnocline layer is situated between the mixed layer and the deep layer where density increases with depth as a result of changes in temperature and salinity. When temperature is responsible for the increase in density with depth, the pycnocline is known as thermocline while if an increase in salinity is responsible for the increase in density with depth, the pycnocline known as a halocline. The layer below the pycnocline is the deep layer that accounts for most of the ocean’s mass. In this layer, the density gradually increases and waters move slowly. However, only at a few locations near the bottom the water moves fast enough to be considered currents (Paul, 2003).

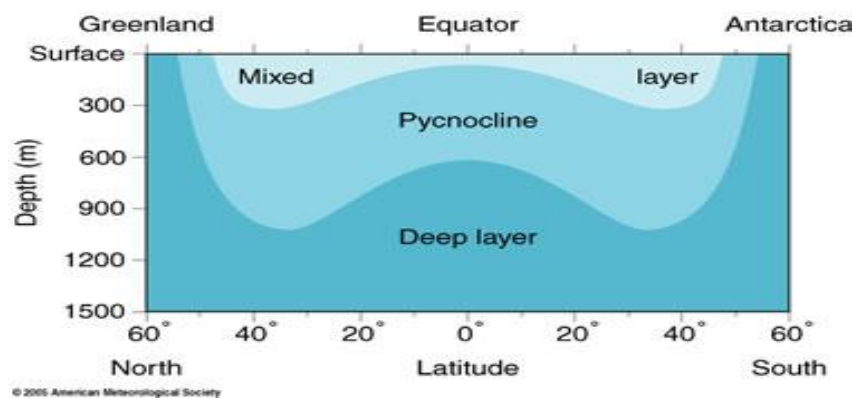


Figure 2.4 A cross-sectional longitudinal profile of the Atlantic Ocean from 60° N to 60° S showing the location of the mixed layer, pycnocline and deep layer adopted from [Rahmstorf, 2006]

Open-ocean deep or intermediate convection is one of the most important mechanisms involved in the water mass formation in the ocean. Open-ocean deep convection occurs usually in winter in few regions of the world ocean. Deep water formation by convection process has been observed in the western Mediterranean (Leaman and Schott, 1991), eastern Mediterranean (Lascaratos, 1993), Labrador Sea (Clarke and Gascard, 1983), Greenland Sea (Schott et al., 1993); Weddell Sea (Gordon, 1978; Muench, 1988), Gulf of Lion (Grignion *et al.*, 2010) and commonly is believed to be driving the thermohaline circulation. Three phases of convection have been described earlier by MEDOC-Group, (1970): the preconditioning phase, the violent mixing phase and the sinking plus spreading phase (Figure 2.5).

Three conditions are required for open-ocean convection to take place: i) the water column is largely homogenized or weakly stratified, ii) the cyclonic gyre with doming isopycnals carries the densest deep water towards surface and iii) strong sea surface buoyancy loss to the atmosphere due to cooling and evaporation (MEDOC-Group, 1970; Swallow and Caston, 1973). Once, these conditions are fulfilled, strong vertical mixing take place in the preconditioned area. In the violent mixing phase, convection is observed in the centre of the convective area, leading to strong mixing and deepening of the mixed layer. Relevant studies showed that sinking occurs in plumes of horizontal scale of (1 km) where the dense water sinks at vertical speeds of about 10 cm/s (Leaman and Schott, 1991; Grignion *et al.*, 2010). In the last phase “the sinking and spreading” the mixed water sinks and spreads away from the formation site horizontally.

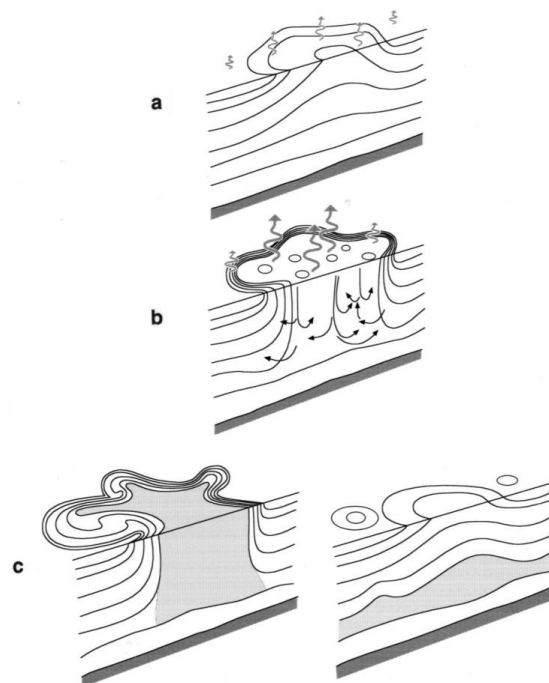


Figure 2.5 Schematic diagram of the three phases of open-ocean convection: (a) precondition, (b) deep convection, (c) lateral exchange and spreading. Surface buoyancy loss and the water mixed by convection is represented by curly and shaded arrows.

Chapter 3

Overview of the Study Area

3.1. Introduction

As defined earlier in chapter [1] the underlying thesis focuses on the simulation of tides, the circulation patterns and thermohaline processes in the Red Sea. The study area is an inlet of the Indian Ocean lying between Africa and Arabia. As the first step in developing the hydrodynamic numerical model for the Red Sea as to obtain overview about the study area and to identify the most relevant processes in the site in question by means of literature review. This overview will be supported using data based from satellite technique or field measurements to verify and study the information found in the literature and to provide more insight into the physical system. Based on this information, the key and major processes that have to be resolved by the model are identified.

This chapter presents general view of the characteristics of the area of investigation. This includes the geographical location, geology and topography background of the Red Sea (section 3.2 to 3.4). This is followed by a description of the climate characteristics in section (3.5). Subsequently, the hydrodynamic processes of the Red Sea including tidal conditions, circulation patterns, exchange processes with surrounding system and hydro-graphic properties are given in section (3.6). The available field measurements that have been used for calibration and validation purposes, their sources and analysis are given in section (3.7).

3.2 Geographical Location of the Red Sea

The Red Sea is a narrow elongated-shaped sea (semi-enclosed) separating the land masses of Africa and Arabia, oriented north-northwest (NNW) and south-southeast (SSE). Geographically, it is located between the latitude 30-12° N and longitude 36-45° E and extends over a distance of about 2000 km covering a total surface area of about 440,000 km² (Figure 3.1). The physical boundary of the Red sea is defined by the western and eastern coastlines. The coastline of Egypt, Sudan, Eritrea and part of Djibouti define the western boundary of the Red Sea, while the coastline of Jordan, Saudi Arabia and Yemen define the eastern coastline. In the south, the Red Sea meets the Gulf of Aden and the Indian Ocean through a narrow strait (26 km wide and 200m deep) known as Bab el Mandeb. In the north,

at about 28°N the Red Sea consists of two gulfs known as Gulf of Aqaba and Gulf of Suez. The Red Sea's width is about 180 km in the north and increases towards the middle region to 350 km and starts to narrow southwards reaching about 28 km at Bab el Mandeb strait.

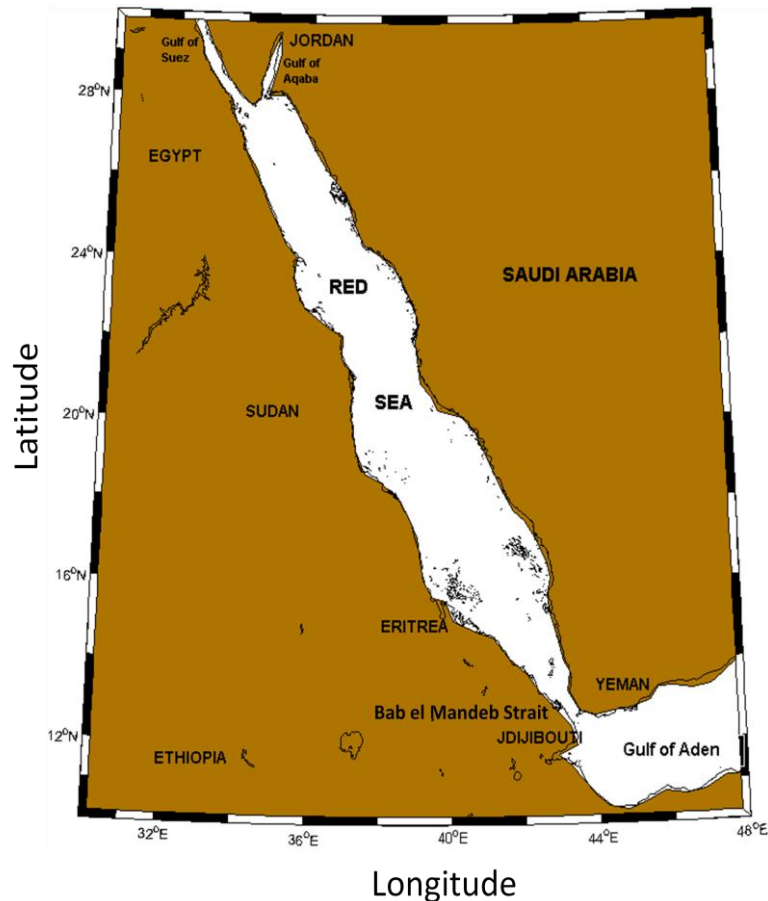


Figure 3.1 Map of the study area (Red Sea) including the Gulfs of Suez and Aqaba in the northern part of the Red Sea and part of the Gulf of Aden.

3.3 Geological history and formation of the Red Sea

A brief description concerning the Red Sea formation is presented here. For a detail description reference is made to Sheppard *et al.*, (1992). The region was formed as a result of tectonic plate movement of the African, Arabian and Mediterranean shields pulling away from each other, creating a great slash in the land. Rifting has not been continuous but paused in the first half of the tertiary, during which important episodes of volcanic activity led to the extrusion of volcanic islands.

3.4 Topography and Bathymetry

Figure 3.2 shows the bathymetric map of the study area. The Red Sea experiences irregular bottom topography. It is shallow at its northern and southern ends and the average depth is 524m while maximum depth is > 2000 m found in the axial trough at 19° N, 42° E. In addition to that, there are shallow shelves in southern part of the Red Sea on both sides of the strait of Bab el Mandeb connecting the Red Sea to the Gulf of Aden. Most of the coastlines of the Red Sea are bordered by shallow fringing reefs. The edges of these reefs shelve steeply into deep water or they slope gently into lagoons bordered by an offshore barrier reef system (Morley, 1975; PERSGA, 2006). The bottom of the Red Sea is divided into six regions mainly the coral reef zone, coastal shelves, the main trough, the axial trough, the hot brines region and the Strait of Bab el Mandeb (Drak and Girdler 1964; Knolt *et al.*, 1966; Morcos, 1970). Table 3.1 presents a brief description of this division.

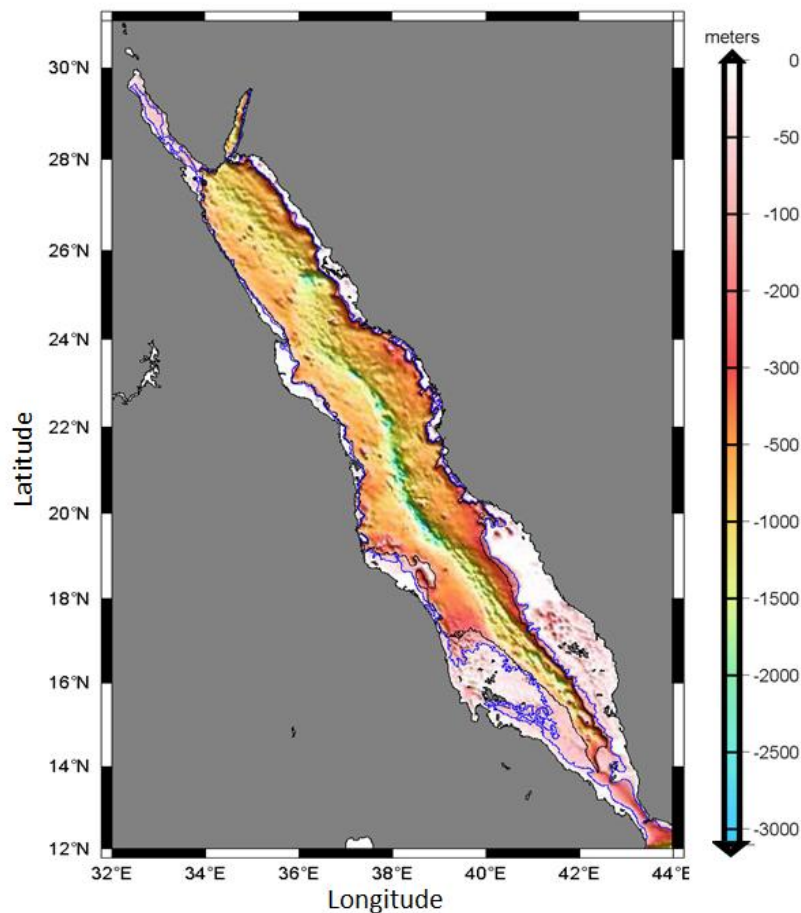


Figure 3.2 Bathymetry map of the Red Sea [Institute of Hydrological and Oceanic Sciences, Taiwan].

Table 3.1 Regions of bottom of the Red Sea.

Region	Description
Coral reef zone	Growing vigorously of depth less than 50m. Development occurs along Saudi Coast about 400 km long and several km wide.
Coastal Shelves	Extending from the shore to a depth of 300 m to 600m. The coastal shelf is wider on the Asiatic side than on the African side and increases in width south of 19°N
The main trough	Extending from a depth of 600m to 1100m. Deepening more than 1000m depth extends to the southern tip of the Sinai Peninsula. South of 15° N, depth is generally less than 500m, indicating the absence of the main trough. Isolated deep pockets of water occur in the main trough between 26° N and 23°N
Axial trough	Between 23° N and 17° N, the 1000 m isobaths encloses a continues deep. Between 22° N and 19° N, a continuous isobaths encloses more than 1500 m. In places, the axial trough in more than 2000m deep and more than 20 km wide.
The hot brines region	Located in the central part of the axial trough between 21° 10' N and 21° 30' N at depth greater than 2000m, characterized by temperatures greater than 60oC, salinity greater than 300‰.
Strait of Bab el Mandeb	Extending between Bab Al-Mandeb and Siyan. Divided by Miyurn Island into two channels, [I] 4km wide and 25 deep in the eastern side [II] 20 km wide and 300m deep south west of Miyurn Island. In the southern side of the Strait, the bottom slopes down to the Gulf of Aden.

3.5 Climate Characteristics

The Red Sea region is characterized by a typical desert and semi-desert climate with high temperatures in summer (June-September) ranging between 30-35°C and in winter (October-May) between 24-28°C. As a result, the Red Sea has higher rate of evaporation (E) among most oceans and seas which exceeds the precipitation (P) rate in the region. The average evaporation rate for the Red Sea as a whole has been estimated by Sofianos *et al.*, (2002) to be 2.1my⁻¹. However, they reviewed the previous estimates of the evaporation rates in the Red Sea and concluded that the estimates range from 2.3 m/year to 1.5 m/year. The rainfall over the Red Sea is low and the annual rainfall is subject to great variations from year to year (Morcos, 1970). In addition to that, there is no rivers inflow in the Red Sea. In general, the average annual rainfall is estimated to be less than 250 mm.

3.5.1 Prevailing Winds

The wind patterns over the Red Sea have been described by several authors (e.g. Patzert, 1974a; Quadfasel and Baudner, 1993; Sofianos and John 2003). In general, the wind field over the Red Sea blows mainly along the axis of the basin due to high mountains and plateaus on both sides of the basin. In the northern part of the basin (north of 20°N) the winds blow from north-northwest (NNW) throughout the year. The climate of the southern part of the Red Sea (south of 20° N) including Bab el Mandeb and the Gulf of Aden are subject to two monsoonal events (Northeast and Southwest). During the NE monsoon (October to May), winds blow into the Gulf of Aden from an easterly direction and into the Red Sea from the SSE. In contrast, during the SW monsoon (June to September) winds are from the NNW over the southern Red Sea and from SW over the Gulf of Aden, causing strong upwelling along southern Arabia (Quadfasel and Baudner, 1993). On the whole, the winds over the Red Sea region are stronger during the winter months compared to summer months. The surface winds can reach speeds of more than 10 m/s.

To confirm the monsoon cycle described above, wind data from satellite derived QuikSCAT are used (“QuikSCAT data are produced by Remote Sensing Systems and sponsored by the NASA Ocean Vector Winds Science Team, data are available at <http://podaac.jpl.nasa.gov/quikscat/>). These data cover the period from January-2000 to December-2007. The data were averaged to construct the patterns of monthly mean winds under different months. The patterns of monthly mean winds under different months over the Red Sea region are shown in Figure 3.3. As can be seen from the plots, the general wind patterns over the Red Sea is directed along the main axis of the basin and the monsoon wind directions are clearly visible. According to the figure, wind conditions of the Red Sea can be divided into three main regions as following:

- Northern Red Sea (Northward of Latitude 20° N): In this region, the prevailing winds are mainly NNW all the year round.
- Southern Red Sea (Southward of Latitude 20° N): This region including Bab el Mandeb and the Gulf of Aden are subject to two annually changing monsoonal events. From May to September winds blow from the same direction as in the northern Red Sea. In October, winds gradually change to SSE and retain this direction until April.
- Intermediate Region (Latitudes between 18° and 20° N): This region develops in the winter months due to the weak NNW winds (2.5-4.5 ms⁻¹) of the northern part and the strong SSE winds (6.8-9.5 ms⁻¹) of the Southern part of the Red Sea. It is characterized by relatively low-pressure resulting in calm conditions. By the beginning of summer it moves gradually to the south, giving way to a transition as the prevailing wind changes from SSE to NNW.

The description of wind patterns over the Red Sea in the previous studies suggests a uniform definition; nevertheless, Sofianos and John (2003) mentioned that, details of the wind field estimates differ between different data sets particularly in the northern part of the Red Sea. However, in their study data from Comprehensive Ocean Atmosphere Data Set (COADS) were used, which showed similar patterns (see Figure 2 in their paper), indicating that the basic seasonal cycle in the region is a very robust feature.

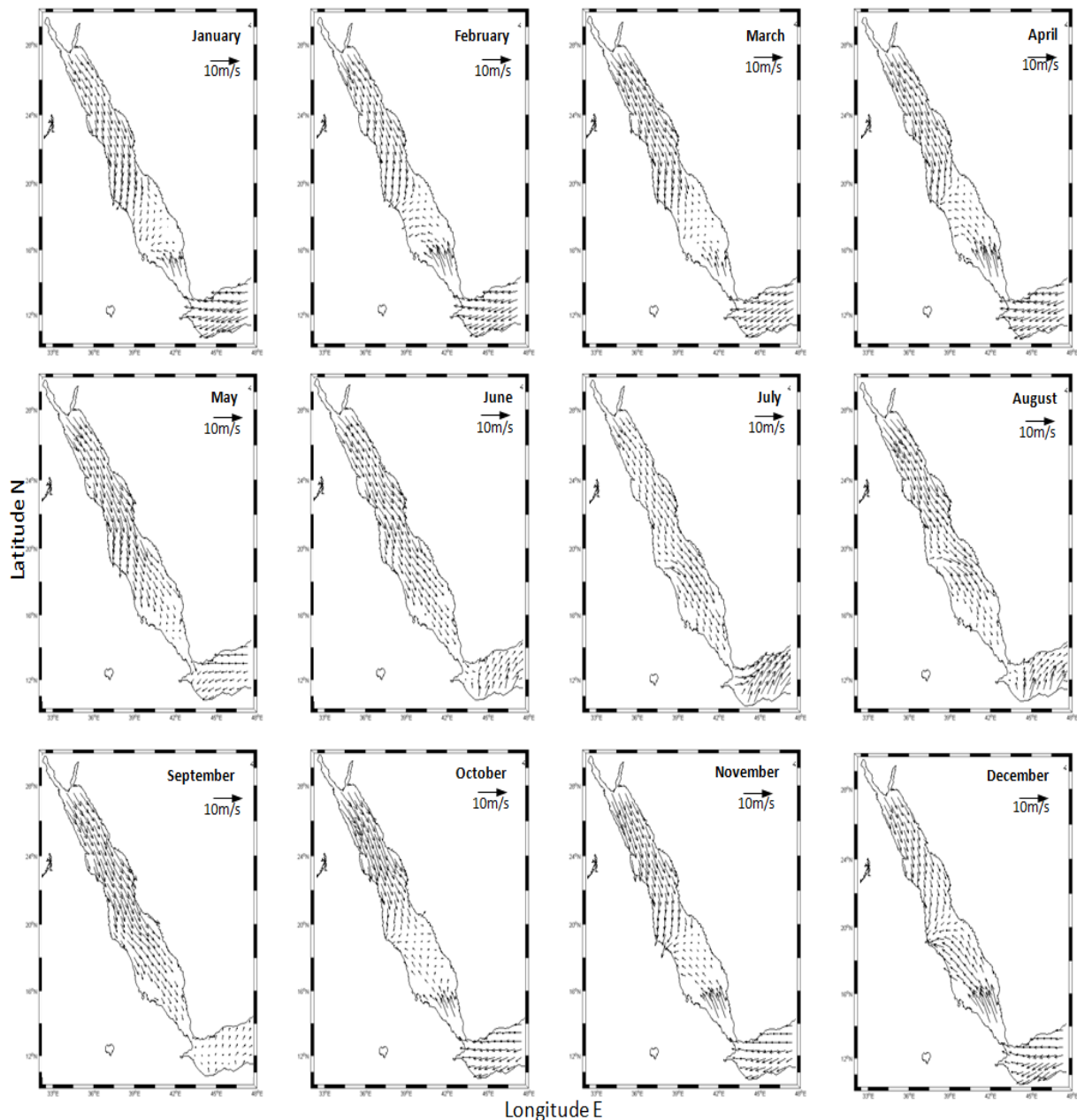


Figure 3.3 Monthly mean wind climatology over the Red Sea and part of Gulf of Aden, Obtained from QuikSCAT, averaged over 2000-2007.

3.6 Hydrodynamic Processes

3.6.1 Tidal conditions

From the available literature, it was found that very few attempts have been carried out to study the tides in the red Sea. Due to the few published work, most of the general information presented in this section about the tidal conditions in the red Sea were obtained from a unpublished report which was prepared by Intergovernmental Organization known as Regional Organization for the Conservation of the Environment of the Red Sea and Gulf of Aden (PERSGA).

The tide in the Red Sea has been described earlier by Defant (1961). He supplied a dynamical explanation of actual tides based on few analytical analyses made to determine the tides in the strait of Bab el Mandeb. The results of these analyses were used to explain tidal dynamics in the whole Red Sea basin. The conclusion drawn suggests that the tides are essentially co-oscillations with those of the Gulf of Aden and the astronomical forces producing small modifications in the phase of the semidiurnal tide. However, Edwards and Head (1987) pointed out that a complete explanation of the Red Sea tides is not yet agreed. According to PERSGA (2006) the tide of the Indian Ocean and Gulf of Aden does not propagate into the Red Sea due to the narrow connection between them. As a result, the tides of the Red Sea are relatively small.

The tidal conditions of the Red Sea are characterized by its low tidal range with semidiurnal characteristics. There is a difference of six hours between the time of high water in the north and south. This means that when it is high water at the southern end of the Red Sea signals low water at the northern part and vice versa. The tidal range changes from north to south with greatest values at the two ends. In the north at the entrance of Suez and Aqaba Gulfs the spring range is about 0.6 m while in the southern part of the Red Sea (at Massawa and Kamaran Island) is around 0.9 m. However, the range decreases towards the central part of the Red Sea near Jeddah and Port Sudan where amphidromic system (counter-clockwise) exists. In the central part of the Red Sea there is no appreciable semidiurnal tide. There are also another two nodal zones across the Red Sea with negligible tidal ranges occurring to the north of Bab el Mandeb and at the entrance of Gulf of Suez. It has been pointed out by PERSGA, (2006) that in places where the semi-diurnal tides are very weak, diurnal character may appear. This happens at the nodal zones, where some diurnal type of tide may appear, but only for short periods and in very restricted positions.

In the literature, very few published studies on tidal observations are found. Sultan *et al.*, (1995) used time series of hourly sea level records for one year to classify the type of tidal regime at two stations located in the central part of the Red Sea (Jeddah and Port Sudan). Their analysis showed that the tide at Jeddah can be classified as mixed type dominated by semidiurnal tide. On the other hand, they found that the semidiurnal components (M_2 , S_2) at Port Sudan are smaller in comparison with those at Jeddah and the amplitudes of the

fortnightly and monthly components are large. Based on the form ratio (F) value, the tide at Port Sudan was found to be of diurnal type. This was attributed to the proximity of Port Sudan to the amphidromic point. Saad (1997) performed harmonic analysis of hourly sea level records for the period (1992-1994) in the southern part of the Red Sea at JIZAN (Lat $16^{\circ} 53'49''$ N, Long $42^{\circ} 35'05''$ E). His analysis showed that the tide at JIZAN is dominated by the large amplitudes of the major semi-diurnal constituents M_2 , S_2 , and N_2 . Diurnal components on the other hand (O_1 , K_1) showed the smallest amplitudes among the others. Using the form ratio (F) to determine the character of the tide, a ratio less than 0.25 is found, indicating the type of semidiurnal tide.

3.6.2 Circulation patterns

From the available literature, similar to the tides, it was found that very few attempts have been made to study the circulation inside the Red Sea domain. During the past century most of the studies carried out in the Red Sea were focused on the southern part of the Red Sea mainly at the strait of Bab el Mandeb, aiming at understanding the water exchange between the Red Sea and Gulf of Aden or the spreading of Red Sea outflow into the Gulf of Aden as well as the Arabian Sea (see section 3.6.3). Inside the Red Sea domain, observational studies are very limited and sparse in space which leads to difficulties in constructing a picture of the three-dimensional circulation in the Red Sea.

There is a general agreement that the large-scale circulation in the Red Sea is derived and controlled by two main mechanisms namely the wind and the thermohaline forcing. However, there has been disagreement over the relative importance of the thermohaline and wind forcing and their role in the circulation and stratification of the Red Sea. Several authors such as Maury (1855); Phillips (1966); Eshel *et al.*, (1994) and Tragou and Garrett (1997) believe that circulation in the upper layer could be attributed to thermohaline forcing. This was explained by the incoming fresh warm water from the Gulf of Aden into the Red Sea which moves northwards and become cools due to the high evaporation in the northern region. As a result, formation processes of very saline and denser water take place; therefore, it sinks and flows out of the Red Sea over the shallow sill of Bab el Mandeb. On the other hand, Thompson, (1939), Siedler (1969) and Patzert, (1974a) argued that the wind plays primary role while the thermohaline forcing plays a secondary role in determining the circulation patterns.

3.6.2.1 Wind driven circulation

As described earlier in section 3.5.1 the monthly-mean surface winds over the Red Sea flow mainly parallel to the axis of the basin due to the high mountain on both sides. In the northern part of the basin (north of 20° N) the winds blow from NNW throughout the year while in the southern part (south of 20° N) the winds reverses its direction seasonally from NNW in winter to SSE in summer (Figure 3.3). Thus, the surface circulation in the Red Sea is influenced by the monsoon winds (Thompson, 1939; Patzert, 1974a; Edwards & Head 1987 and PERSGA, 2006). In the following, the main features of circulation driven by wind in the Red Sea are described.

During the northeast Indian monsoon (October-May), the winds in southern region (south of 20° N) increase in strength in winter time and drive the surface current from the Gulf of Aden towards the Red Sea with a mean surface flow of 15-20 cm s^{-1} . The current flows northwards against the weak prevailing NNW wind in the northern region (Thompson, 1939 and Patzert, 1974a).

During the SW monsoon (June-September), the prevailing wind (NNW) drives the surface currents south towards the strait of Bab el Mandeb and the mean surface currents flow to the southeast towards the Gulf of Aden. During summer, the strong NNW wind increases the speed of the south southeast current in the north of the Red Sea (north of 26° N). However, during July and August the wind over the southern region are weak and there is strong surface current flowing south in the central part of the Red Sea at about 18° and 20° N. The strongest outflowing surface current is found to be over 20 cm s^{-1} in early July in the vicinity of Bab el Mandeb (Patzert, 1974a).

3.6.2.2 Observational and Modelling Studies

Observational studies performed inside the Red Sea domain are very limited, thus, very few circulation features can be identified. Vercelli (1927) carried out measuring campaign during winter season in the southern part of the Red Sea and observed significant northward currents close to the coasts, especially the African coast (western side of the Red Sea). In winter 1929, he also carried out another cruise in the central part of Red Sea near Port Sudan and observed a southward counter-current at depths greater than 250 m in the open sea but less than 150 m near the coast (Vercelli, 1931).

In the northern part of the basin (north of 23° latitude), two winter cruises (*1935 on the R/V MABAHISS and 1963 on the R/V CDT ROBERT GIRAUD*) consisting of several hydrographic sections were carried out (Morcos, 1970; Morcos and Soliman, 1974 and Maillard, 1974). The analyses of these measurements in general suggested that there is a cyclonic gyre at the extreme north which penetrates up to 300 m depth and an anti-cyclonic gyre about 2° to the south. During 1993–1994, a series of five drifter tracks were released in the northern part of the Red Sea also confirm the presence of cyclonic eddy patterns north of 26° N (Clifford *et al.*, 1997). In addition to that, Quadfasel and Baunder (1993) analyzed temperature observations and the results also support the existence of these features with colder water at the centre of the cyclonic flow and much warmer in the centre of the anti-cyclonic flow. It has been pointed out by Clifford *et al.*, (1997) that the formation of eddies in the Red Sea depends upon the wind direction. They suggest that there are more eddies when the wind has a cross-basin component. Recently, in 2010 King Abdullah University of Science and Technology (KAUST) released surface drifters in the central and northern part of the Red Sea between 20° and 28° N. The trajectories of these surface drifters also suggest the presence of a well-defined anti-cyclonic eddy (200-km diameter) between 22° and 24° N. The eddy appears in March and becomes stronger in April with velocities of about 1 m/s.

In terms of modelling studies, very few attempts have been carried out to describe the circulation in the Red Sea (Eshel and Haik, 1997; Sofianos and Johns, 2003; Yao *et al.*, 2014a, 2014b). However, these studies showed inconsistent results. The models employed in these studies were different; an Ocean General Circulation Model (OGCM) was used in the study of Eshel and Haik (1997), the Miami Isopycnic Coordinate Ocean Model (MICIM) in the study of Sofianos and Johns (2003) and the MITgcm model in the study of Yao *et al.*, (2014a, 2014b). The earlier modelling studies have been forced by monthly means (climatological forcing) conditions and used similar low horizontal resolution (10 km) while the very recent study of Yao *et al.*, (2014a, 2014b) was forced by high-frequency atmospheric forcing and used higher horizontal resolution. These modelling studies suggested that the Red Sea circulation has a complex three-dimensional structure. It should be mentioned that in the study of Eshel and Haik (1997), eddy features observed in the field (in the northern part of the Red Sea) were not resolved by the model. In contrast, the general picture drawn from the study of Sofianos and Johns (2003) suggests that the surface circulation of the Red Sea is complicated consisting of series of eddy-like features as well as intensified flow towards the coasts. However, all these studies showed different spatial structures of the Red Sea circulation. On the other hand, the study of Eshel and Haik (1997) and Yao *et al.* (2014b) showed disagreement on the location of the sinking processes in the Red Sea. The study of Sofianos and Johns (2003) suggested that the hypersaline intermediate water is formed in a cyclonic gyre in the northern Red Sea.

Sofianos and Johns (2003) calculated the mean of surface circulation over nine years of simulation and found that there is a strong surface and westerly inflow during winter in the strait of Bab el Mandeb (Figure 3.4a). These currents generated a mesoscale anti-cyclonic gyre located between 15° and 16°N; with velocity exceeding 50 cm/s. In the vicinity of 16° N the currents were interrupted by the north-northwest wind along the western boundary during summer as shown in Figure (3.4b). In addition, an easterly boundary current was observed following the northward, however it is weaker compared to the southern currents. During summer, the westerly boundary current in the southern part of the Red Sea disappears. The main feature for the summer season is irregular patterns of currents and the circulation is weaker than winter. In addition to that, a strong feature of cyclonic gyre in the northern part between 24° and 26° N with velocities of about 50 cm/s was observed.

The influences of wind stress and the thermohaline forcing in the study of Sofianos and Johns (2003) were analyzed by separating the two forces by means of numerical experiments. The results of this analysis suggest that the thermohaline effect is the dominant forcing mechanism in the Red Sea. Nevertheless, it should be noted that these results are based from model simulations forced by climatological conditions of the Red Sea. Taking into consideration the effect of the variability of the atmospheric forcing at frequencies higher than the seasonal is very important in understanding such process. Therefore, in the current study, realistic high-frequency forcing of atmospheric forcing was considered to investigate the relevance of the atmosphere forcing on the circulation in the Red Sea.

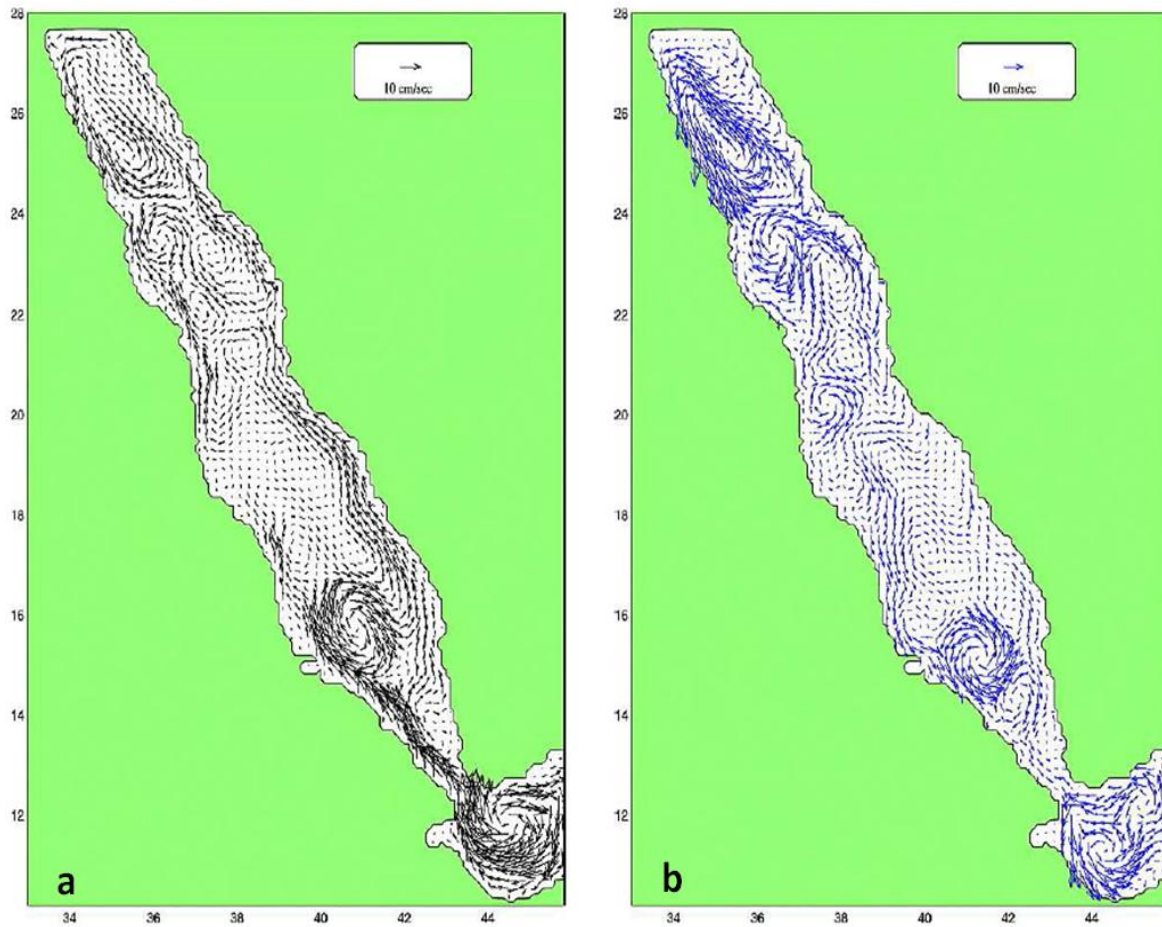


Figure 3.4 Mean winter (left panel) and summer (right panel) of surface circulation over 9 years of simulation [Sofianos and Johns, 2003].

In order to increase the general picture about the surface features and confirm the existence of rotating ocean currents in the Red Sea, the satellite altimeter derived sea level anomaly (SLA) data were considered. The SLA data were obtained from AVISO (Archiving, Validation and Interpretation of Satellite Oceanography Data) and averaged over a 10 years period. Figure 3.5 shows the monthly mean distribution of SLA over the Red Sea which clearly reflects the existence of cyclonic and anticyclonic gyres and small eddies in the region. As can be seen, there are spatial variations concerning the location of the eddy or gyres features over the months.

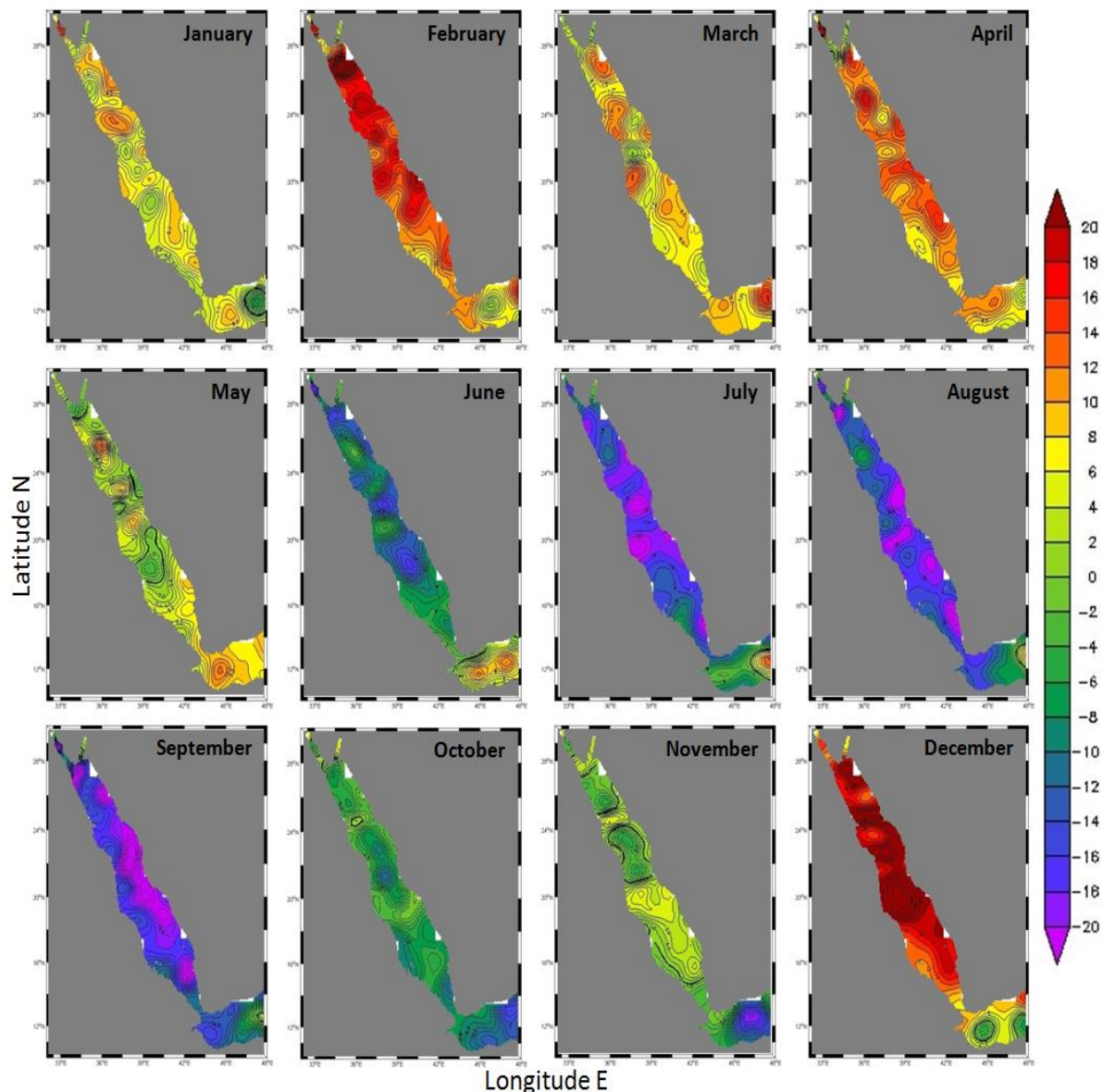


Figure 3.5 Monthly mean of altimeter-derived sea level anomaly (SLA) distribution over the Red Sea and part of Gulf of Aden, obtained from AVISO data sets [average over 10 years].

3.6.2.3 Deep circulation and water mass formation

There are no direct deep current measurements in the Red Sea. The major source of the present information about subsurface and deep circulation is based on tracer observations. In general, three different sources for the formation of deep water in the Red Sea have been suggested by Maillard (1974); Wyrski (1974) and Cember (1988). The first source is the Gulf of Suez which is characterised by higher salinity (42 psu) than salinity of the deep basin (40.5 psu). The second source is the outflow of dense water from the Gulf of Aqaba over the shallow sill (300 m depth) of the Strait of Tiran. The third source is the open-ocean deep convection at the northern end of the Red Sea.

Morcos (1970), Manins (1973) and Cember (1988) suggested that the formation of deep water in the Red Sea occurs in the north basin. Figure 3.6 shows a simple schematic of the suggested formation processes. The figure shows that the surface water in the southern part of Gulf of Suez and Aqaba sinks to the bottom (due to increase in density when evaporation and cooling at maximum) and moves southwards. In the southern part of the Red Sea near the sill, part of the bottom upwells back to the upper layer and then the water returns northwards at depths of about 300-500 m. As the intermediate water moves northwards, it mixes with the pycnocline water. Maillard (1974) argued that the deep water of the Red Sea is an equal mixture of the high dense outflow from the mouth of the Gulf of Suez and the water in the upper layers (0-150 m) formed during the winter. This argument was based on temperature and salinity measurements in the winter season.

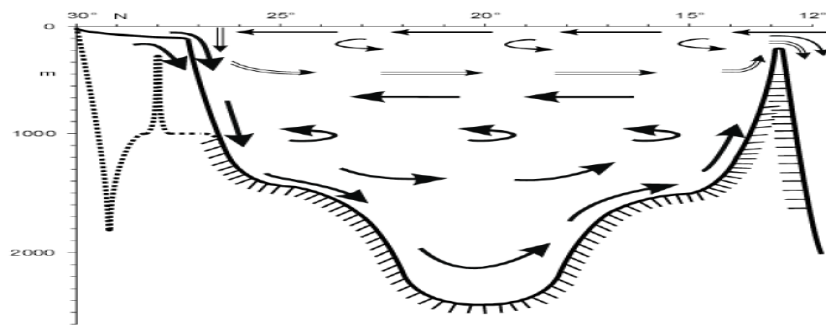


Figure 3.6 Schematic of the circulation pattern in the upper layers (single arrows), upper deep layers (double arrows, driven by open ocean convection) and deep layers (bold arrows, driven by plume convection) in the Red Sea (Quadfasel, 2001). Dotted topography represents the Gulf of Aqaba.

3.6.3 Water Exchange with surrounding system

As mentioned earlier that the Red Sea is connected in the south to the Gulf of Aden and the Indian Ocean via a narrow Strait (26 km) so-called Bab el Mandeb. During the past century most of the studies carried out in the Red Sea were focused on the southern part of the Red Sea mainly at the strait of Bab el Mandeb. The main aim of these studies was to improve the understanding about the water exchange between the Red Sea and Gulf of Aden or the spreading of Red Sea outflow into the Gulf of Aden as well as the Arabian Sea. Many studies pointed out that there is seasonal variation in the exchange flow associated with monsoon winds (e.g. Thompson, 1939; Morcos, 1970; Maillard and Soliman, 1984; Murray and Johns, 1997 and Smeed, 2004). These studies indicate that there is a 2-layer exchange flow system in the winter (October-May) and a 3-layer exchange flow system in the summer season (June-September). Figure 3.7 shows the sketch explaining the exchange flow patterns between the Red Sea and Gulf of Aden. In the 2-layer system (Figure 3.7-left panel) the Red Sea outflow water (RSOW) flows out with a cool temperature of 23° C and higher salinity of 40.5 psu (as a result of higher density) beneath the incoming surface water (SW) layer from the Gulf of Aden with a warm temperature of 25° C and salinity of 36.5 psu which is driven by SSE winds. The volume flux of inflow water and outflow through the strait of Bab el Mandeb has been estimated by Souvermezoglou (1989) to be 0.38 Sv (1 Sv = 10⁶ m³/s) and 0.352 Sv respectively with evaporation rate of 0.025 Sv.

Contrary to the winter situation, the exchange flow system in the summer season is replaced by a 3-layer structure (Figure 3.7-right panel). These are the surface flow from the Red Sea (SW) towards the Gulf of Aden with a shallow depth of about 20 m characterized by a warm temperature ($\sim 29^{\circ}\text{C}$) and a high salinity (~ 37.5 psu), the incoming Gulf of Aden Intermediate water (GAIW) between the depth of 30-80 m ($\sim 18^{\circ}\text{C}$, low salinity ~ 36 psu) and the deep Red Sea outflow water (RSOW) characterized by $\sim 21^{\circ}\text{C}$ and a high salinity of 40.0 psu. It is believed that the observed 3-layer system during the summer is due to the upwelling in the Gulf of Aden which induced by SW monsoon winds (Patzert, 1974a; Cromwell and Smeed 1998 and Smeed, 2004). The volume transport with 0.035 Sv evaporation rate was found to be 0.1 Sv and 0.06 Sv for the Red Sea surface and deep outflow layer respectively while for the intermediate inflow layer was found to be 0.19 Sv (Souvermezoglou, 1989).

Murray and Johns (1997) carried out analysis of moored ADCP and hydrographic observations lasting 18 month's period of the exchange flow at the strait of Bab el Mandeb. Their analyses suggest that the average transport of RSOW in winter (November-March) is 0.6 Sv with speed of 0.8-1 m/s. In contrast, the RSOW transport in summer (July-September) is reduced to 0.05 Sv with a speed of 0.2-0.3 m/s. The speed of the upper layer was found to be 0.4-0.6 m/s in winter and maximum exchange was observed in the mid of February.

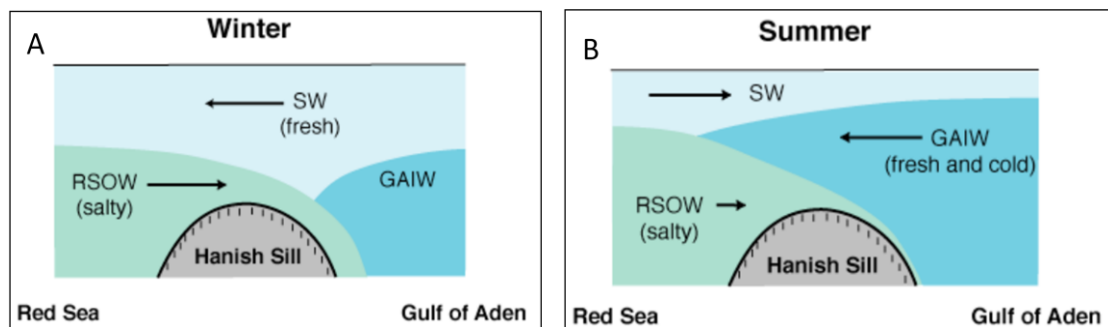


Figure 3.7 Sketch of water masses exchange (circulation patterns) in the Bab el-Mandeb strait, (A) winter and (B) summer season, where SW: surface water, GAIW: Gulf of Aden intermediate water and RSOW: Red Sea outflow water [adopted from Smeed 2004].

3.6.4 Hydrographic Properties (Salinity & Temperature)

The Red Sea is characterized by very high temperature and salinity. The surface salinity and temperature distributions in the Red Sea experiences seasonal variations (Eshel *et al.*, 1994; Maillard and Soliman, 1984; Patzert, 1974a; Quadfasel and Baudner, 1993 and PERSGA, 2006). In general, there is a linear relationship between the surface water temperature (SST) and the air temperature. Both increase southwards to about 14°N and after that they decrease towards the Strait of Bab el-Mandeb. The highest sea surface temperature (SST) reaching a maximum of ($\sim 33^{\circ}\text{C}$) at about 14°N occurs in late summer. In early winter, the temperature decreases and becomes 26°C in this region and migrates toward the north until it reaches at 20°N . The seasonal changes are attributed to the monsoons events.

From an oceanographic point of view, the Red Sea is a data sparse region. Therefore, to describe the distribution of sea surface temperature and salinity in the Red Sea, data from World Ocean Atlas Data-2001 (WOA01) at spatial resolution of $0.25^\circ \times 0.25^\circ$ were used. Figure (3.8-upper panel) shows the horizontal distribution of monthly mean sea surface temperature (SST) over the Red Sea region and part of Gulf of Aden. The mean SST clearly reflects the distribution of the seasonal variations of sea surface temperature. As can be seen from the figure the seasonal variation of the SST varies meridionally to about 8°C in the northern part of the Red Sea and 5°C in the southern Red Sea (Bab el Mandeb Strait). Moreover, SST on the eastern coast in the winter is higher than on the west coast as a result of cyclonic circulation. In the summer season however the situation is opposite.

During the summer season, the wind blows from NNW along the main axis of the Red Sea generating a clockwise circulation at right angles to the direction of the winds. This is due to the piling up of surface warm water along the west coast and the upwelling of deeper water moving in an easterly direction. On the other hand, the opposite occurs in the winter months when the wind blows from SSW direction (Thompson, 1939; Morcos, 1970). It has been reported by Morcos (1970), that the eastern coast of the Red Sea is characterized by higher water temperatures at all depths as compared to the western coast with exception to the wind convergence zone ($18\text{-}19^\circ\text{N}$) where the situation is reversed.

In terms of salinity, the Red Sea is the most saline water body of the entire world's ocean. This is due to the high rate of evaporation, negligible precipitation and absence of river discharge. The result of the very high evaporation leads to a gradual increase in salinity. The sea surface salinity (SSS) in the region increases from 36.5 psu in the southern part of the Red Sea (near Bab el-Mandeb Strait) to 41 psu in the north at the entrance of the Gulf of Aqaba and Gulf of Suez (Edwards and Head, 1987; Cember, 1988; Sofianos, *et al.*, 2002 and PERSGA, 2006). Generally, the salinity in the Red Sea is higher in summer than winter. Figure (3.8-lower panel) shows the horizontal distribution of monthly mean sea surface salinity (SSS) over the Red Sea region. The climatology clearly illustrates the distribution of the seasonal variations of sea surface salinity. It has been reported by Morcos (1970) that the seasonal variation in the northern and southern parts of the Red Sea is about 1 psu and 0.5 psu respectively.

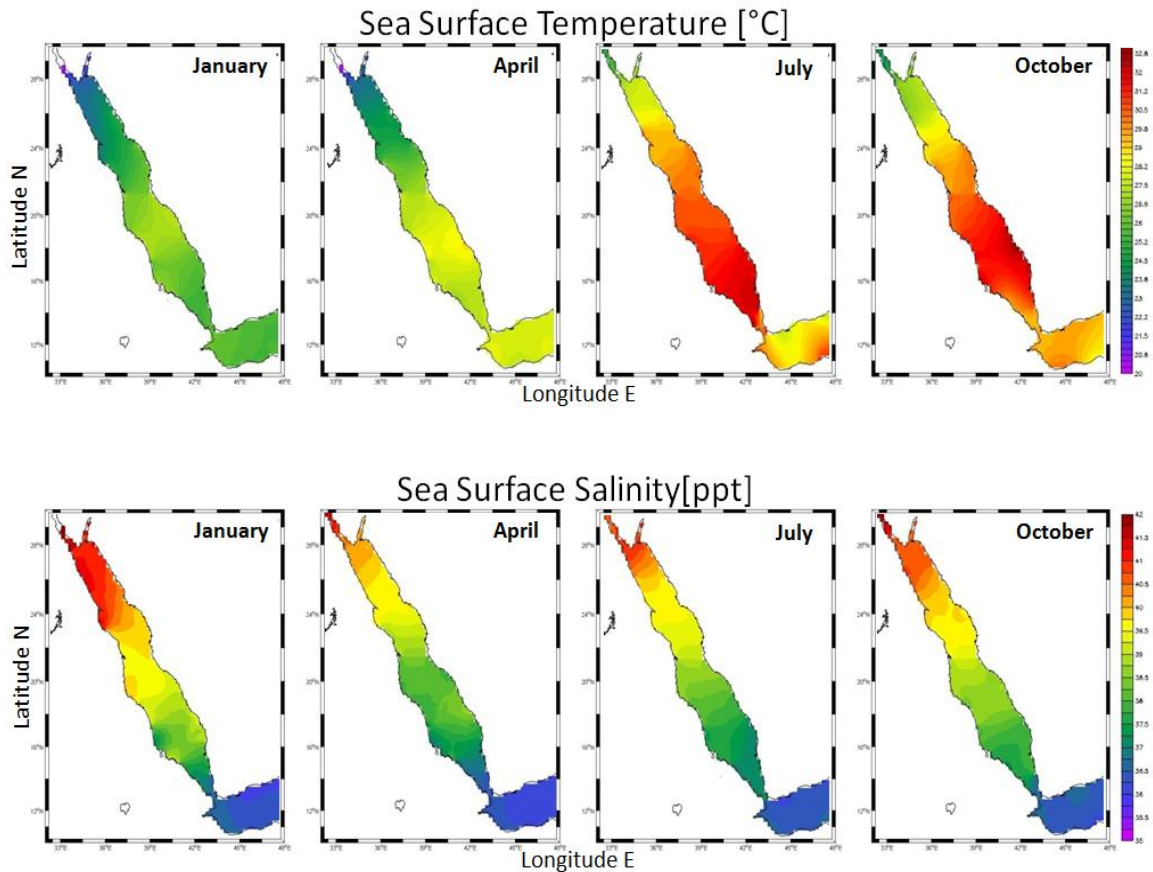


Figure 3.8 Horizontal distribution of Sea Surface Temperature [SST] (upper panel) and Sea Surface Salinity [SSS] (lower panel) over the Red Sea and part of Gulf of Aden for the months January, April, July and October, obtained from (World Ocean Atlas-2001).

To describe the vertical distribution of the hydrographic properties (temperature and salinity), measurements taken during the summer periods along the main axis of the Red Sea are available. These data were analyzed from the cruise, of R/V Mauric Ewing during August 2001 (Sofianos and Johns, 2007). The vertical distribution of the salinity, temperature obtained from the summer cruise is shown in Figure 3.9. Quadfasel (2001) reported that the upper layers in the Red Sea experience significant variations due to atmospheric forcing variations between the two monsoons. The Figure shows that a layer of cool and fresh water from the Gulf of Aden flows below the shallow warm and saline mixed layer leading to unstable stratification. On the other hand, the vertical temperature stratification is stable throughout the basin in the winter season with the inflow of a warm and fresh water layer at the surface and outflow of a cool and saline water layer at the bottom.

Below the thermocline layer, as can be seen, there is a gradual decrease of the temperature to a minimum of 21.6°C at a depth of 300 m. However, the temperature variation in the bottom layer of 1000-2000 m is less than 0.5°C as a result of isolation from the Gulf of Aden by the sill at a depth of 160 m in the southern region (Sofianos and Johns, 2007). In contrast, in the Gulf of Aden, the temperature decreases steadily from 10°C to 3°C at the same level due to the free connection with the Indian Ocean (Morcos, 1970). In terms of salinity, there is an

increase with depth and the depth gradient is larger in the southern Red Sea due to the influence of low salinity water from the Gulf of Aden.

Beneath 300 m, the Red Sea basin is characterized by water of remarkably homogenous temperature, salinity and potential density of about 21.5-21.6°C, 40.5-40.6 psu and 28.6 kg m⁻³ respectively (Sofianos and Johns, 2007). However, Woelk and Quadfasel (1996) observed a remarkable change in the northern part of the Red Sea (north of 26° N) between 1982 and 1983. The properties of the new deep water (cooler and fresher) suggested to be originated from the Gulf of Suez from vertical convection and mixing with fresher surface water masses.

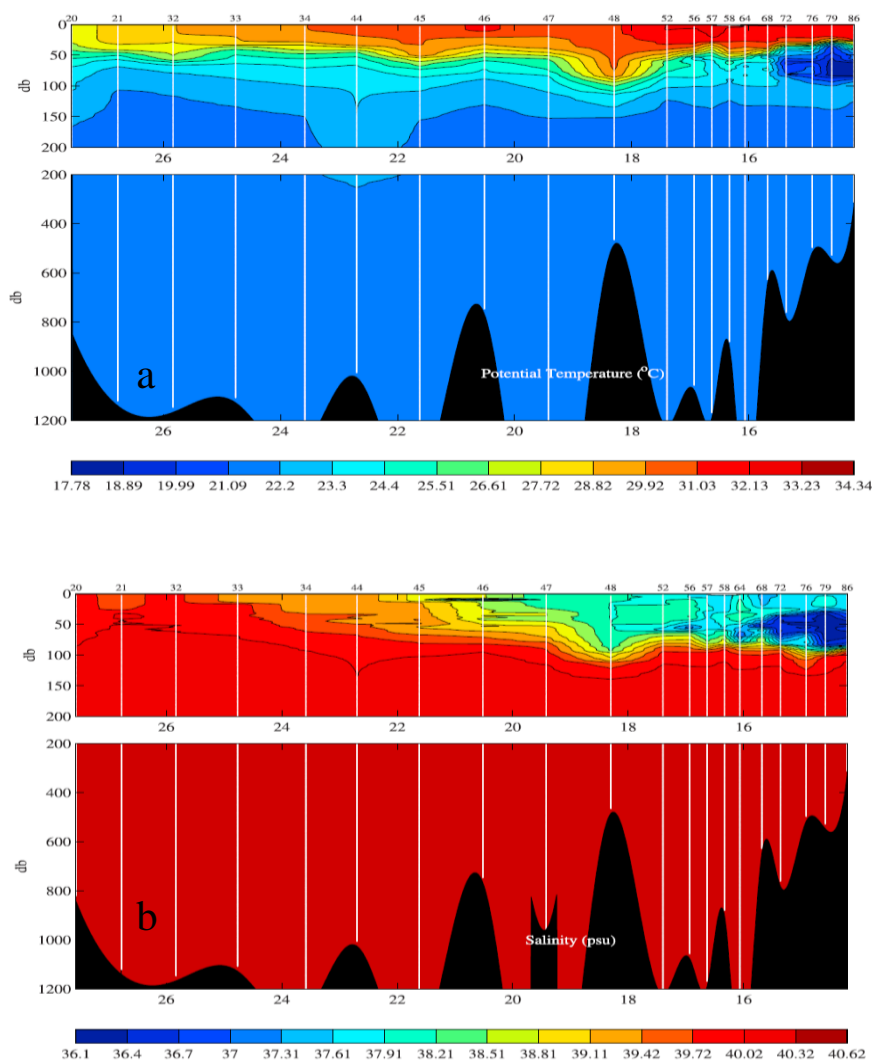


Figure 3.9 Hydrographic-section along the main axis of the Red Sea, temperature in °C [upper panel], (b) salinity psu [lower panel] based on the cruises, of R/V Mauric Ewing during August 2001. [Sofinos and Johns, 2007].

3.7 Available Data

Field data are essential elements in the processes of numerical models set up, calibration and validation. Hardisty, (2007) pointed out that the amount of data requirements for hydrodynamic modelling can be quite huge depending upon the model used and the accuracy requirements. In this study, two types of data were used. They are characterized as input data for setting up and running the model and the data used for the model calibration and validation. The necessary data used in the model setup were undergone through several processes to be ready for the required format by Dleft3D modelling system. These include coastline, bathymetry, astronomical tides, temperature and salinity, winds and surface fluxes (see chapter 5). On the other hand, the available measured data for model calibration and validation processes include time series of water level, instantaneous temperature and salinity measurements. Details about these data, their sources and analysis are presented in the following sections. It should be mentioned that satellite data of sea surface temperature (SST) were also used for validation processes of the hydrodynamic model (see chapter 6).

3.7.1 Water Level

Measurements of water levels are very important in both calibration and validation processes of numerical hydrodynamic models. In addition to that, a tidal analysis can be performed in order to determine the astronomical constituents that govern the tide in the area of interest. During this research the available data used are tidal elevations from five tide gauges stations along the eastern coast of the Red Sea (indexed as JIZAN, JEDDAH, YANBU, RABIGH and DUBA) operated by Saudi ARAMCO Oil Company. In addition to that, in 2011, an intensive cooperation between Faculty of Marine science at King Abdulaziz University in Jeddah (Saudi Arabia) and Research and Technology Centre-CORELAB at Kiel University (Germany) was carried out aiming at development and application of a Coastal Monitoring System (CMS) covering the coastal areas of Jeddah. As a result, three ultrasonic acoustic tide gauges were installed along the coast of Jeddah at Obhor Creek (northern side of Jeddah), Gahaz (Jeddah) and Saroom (southern side of Jeddah). On the other side of the basin, only one tidal station of water level located on the western coast of the Red Sea (Port of Sudan) was made available during this study. Since the model domain extends to the Gulf of Aden at 48° N (see chapter 5), time series of water level records from two additional stations located in the Gulf of Aden (at Aden and Djibouti) obtained from the Sea Level Centre at University of Hawaii (UHSLC) were also made available (See Figure 3.10 for their location). All these time series of water levels are at hourly intervals.

These data were used on the one hand to perform tidal analysis and determine the major semidiurnal and diurnal constituents and on the other hand is to be used for calibration and validation of the Red Sea hydrodynamic model. As was stated earlier in Chapter 1, that one of the main objectives of this study is to simulate tides and generate the co-range and co-chart of the major tidal constituents. Thus, once the major tidal constituents (semidiurnal and

diurnal) are determined, separate simulations of the dominant tidal constituents will be carried out in order to generate the co-range and co-chart (see chapter 6).

Moreover, based on the amplitudes and phases derived by means of a tidal analysis, relative comparisons will be carried out between observation and model results (see chapter 5).

Figure 3.10 shows map of the study area including positions of the tide gauges stations which are marked by black dots. The remaining coloured dots along the main axis of the Red Sea (A to F) and cross-sections are mainly related to salinity and temperature measurements which will be discussed in the next section. The selected periods for calibration and validation processes of the Red Sea model are listed in Table 3.2. Note that two different periods (Period I and Period II) are used for the calibration and validation purpose.

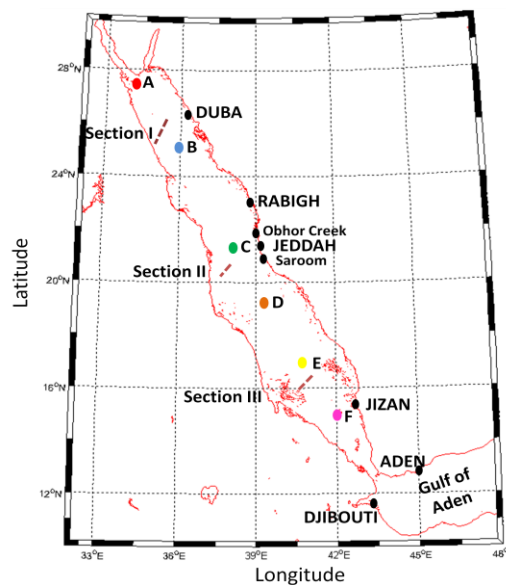


Figure 3.10 Study area map showing locations of the available measurements, water level (Black-dots), and salinity and temperature marked by three cross-sections and six stations distributed along the main axis (A-F).

Table 3.2 Periods of available measured water levels

Station ID	Period I	Period II
ADEN	01/10/2008 to 31/10/2008	----
DJIBOUTI	01/10/2008 to 31/10/2008	----
JIZAN	01/02/2001 to 28/02/2001	01/04/2001 to 30/04/2001
JEDDAH	01/02/2001 to 28/02/2001	01/04/2001 to 30/04/2001
RABIG	01/02/2001 to 28/02/2001	01/04/2001 to 30/04/2001
DIBA	01/02/2001 to 28/02/2001	01/04/2001 to 30/04/2001
OBHOR	01/07/2011 to 31/07/2011	----
SAROOM	01/07/2011 to 31/07/2011	----

As can be seen all water level stations are confined to the coastal regions and their spatial distribution is not ideal. However, they reflect considerable insight to how the tidal parameters vary in the region. An example of the characteristic observations of the water level fluctuations at ADEN and DJIBOUTI stations as well as JIZAN, JEDDAH, RABIGH and DUBA stations is shown in Figure (3.11-A and 3.11-B). The time series obviously display a change in the tidal range and regime. It is clear that the tides of the Red Sea are relatively small and the magnitude varies according to the location. On the other hand, the magnitude of the tidal signal at ADEN and DJIBOUTI behaves differently indicating different tidal regime characterized by a mixed type with diurnal and semidiurnal fluctuations. However, in the northern and southern part of the Red Sea characterized by the JIZAN and DUBA stations, the semidiurnal fluctuations dominate the record. In addition to that, the time series illustrate a reduction in the tidal range between the northern and southern part of the Red Sea towards the central part at Jeddah where amphidromic system (counter-clockwise) exists as was reported previously by several authors (see section 3.6.1).

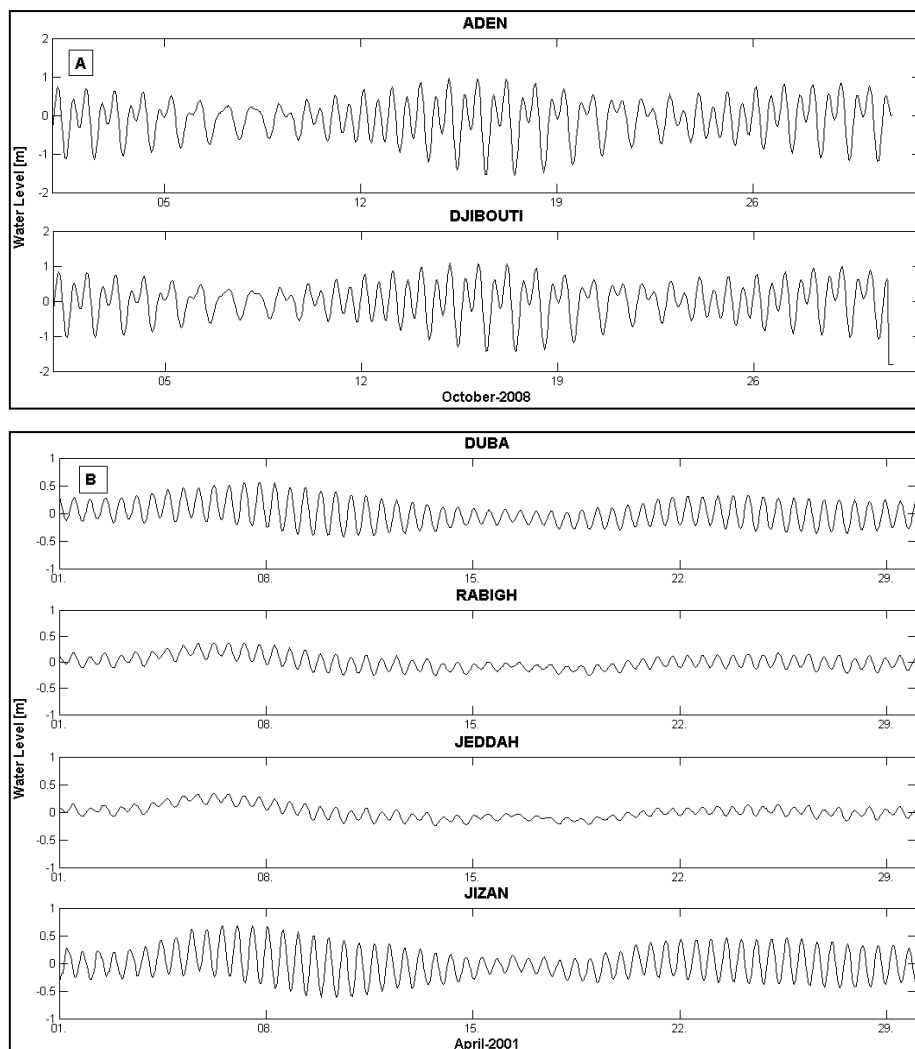


Figure 3.11 (A) tidal variations at two locations in the Gulf of Aden at ADEN and DJIBOUTI stations for period of October-2008, and (B) tidal variations at four locations along the eastern side Red Sea at JIZAN, JEDDAH, RABIGH and DUBA stations for period of April-2001.

3.7.2 Harmonic Analysis

The hourly tide gauge data at ADEN, DJIBOUTI, JIZAN, JEDDAH, RABIGH and DUBA were used to compute the amplitudes and phases of the eight primary semidiurnal and diurnal tidal constituents (Q_1 , O_1 , P_1 , K_1 , N_2 , M_2 , S_2 and K_2). Tidal harmonic analyses were performed using the World Tides program ver.2009 (Boon, 2004). This program is a GUI-based program for tidal analysis and prediction using up to 35 tidal harmonic constituents under Matlab package based on the least squares method. (For details about this program, the reader can refer to Boon, (2004)).

The amplitudes of the eight primary semidiurnal and diurnal tidal constituents derived from the tidal analysis of observed water levels are shown in Figure 3.12. At ADEN (A) and DJIBOUTI (B), it was found that M_2 and S_2 tide are among the semidiurnal constituents relatively significant while the diurnal components K_1 and O_1 are also significant respectively. Inside the Red Sea domain, it is clear that M_2 amplitude is higher at JIZAN (C) and DUBA (F) stations while at RABIGH (D) and JEDDAH (E) it is quite small. These analyses showed the clear dominance of the semidiurnal constituents namely the M_2 inside the Red Sea domain. The figure shows that the major semidiurnal constituents are M_2 , S_2 and N_2 respectively, while the major diurnal tide is K_1 . The contribution of the semidiurnal constituents M_2 , S_2 and N_2 for the total astronomical tide represents about 90%. This indicates that the total astronomical tide is well represented by the major tidal constituents. On the other hand, the contribution of other constituents on the total astronomical tide suggests that the constituents with smaller amplitude than the K_1 may be neglected.

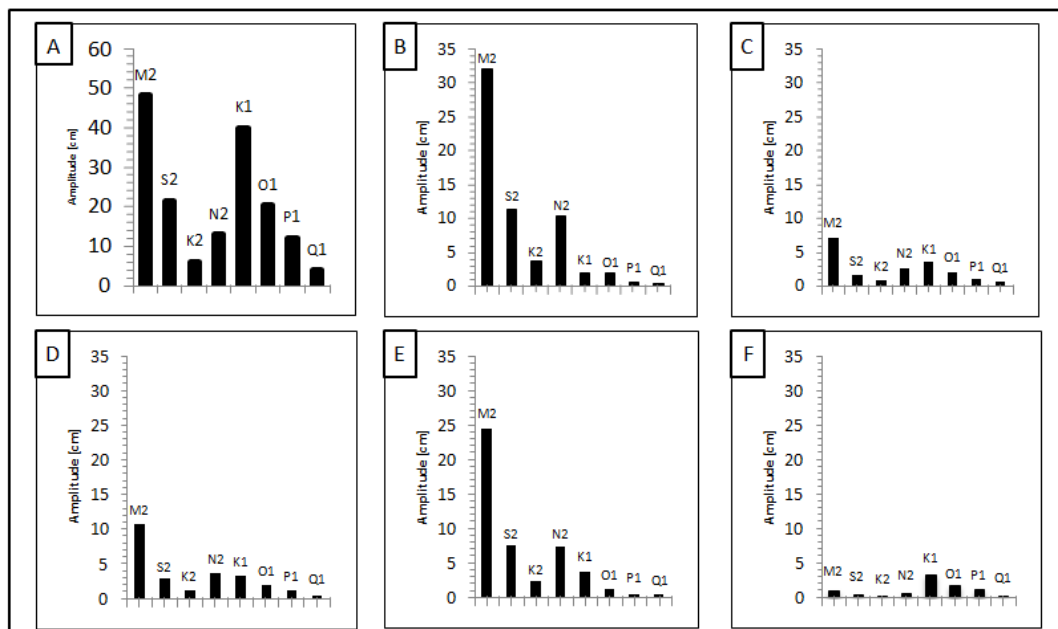


Figure 3.12 the amplitudes of semidiurnal and diurnal constituents as derived from harmonic analysis of the available data at A) ADEN, B) DJIBOUTI, C) JIZAN, D) JEDDAH, E) RABIGH and F) DUBA stations.

The general type of the tidal regime can be determined on the basis of the factor F which is used to classify the characteristics of the local tide in terms of diurnal and semidiurnal amplitudes of the constituents. The equation of F factor is written as (Pugh, 1987):

$$F = \frac{K_1 + O_1}{M_2 + S_2} \quad (3-1)$$

where: K_1 represents luni-solar diurnal constituent, O_1 represents lunar diurnal constituent, M_2 represents principal lunar semidiurnal constituent and S_2 represents principal solar semidiurnal constituent.

Based on the value of F , the following classification can be considered:

- $F < 0.25$, the tide is fully semi-diurnal (two HW and LW per day of about the same height).
- $0.25 < F < 1.5$, the tide is mixed, mainly semi-diurnal (two HW and LW per day which are different in height and time).
- $1.5 < F < 3$, the tide is mixed, mainly diurnal (most of the time one HW per day and for a short time two HW with a strong inequality in height and time)
- $F > 3$, the tide is fully diurnal (one HW per day and one LW per day)

Table 3.3 lists the computed values of F factor. The calculation of the ratio F gives a value of 0.86 and 0.84 at ADEN and DJIBOUTI respectively indicating that the tides of mixed type with the semidiurnal tide dominate. In the case of JIZAN and DUBA the values are smaller than 0.25. In consequences the tide is classified as semidiurnal. However, at JEDDAH and RABIGH stations the ratio ranges between of 0.25 and 1.5 indicating that the tides are of mixed type mainly semidiurnal.

Table 3.3 Tidal type based on F factor

ID station	Factor F	Type of tides
ADEN	0.86	Mixed, mainly semi-diurnal
DJIBOUTI	0.84	Mixed, mainly semi-diurnal
JIZAN	0.08	Fully semi-diurnal
JEDDAH	0.65	Mixed, mainly semi-diurnal
RABIGH	0.37	Mixed, mainly semi-diurnal
DUBA	0.08	Fully semi-diurnal

3.7.3 Salinity & Temperature Data

As clearly mentioned this study concerns with the simulation of thermohaline structure in the Red Sea. Therefore, measurements of temperature and salinity are necessary. It was mentioned earlier in section (3.6.4), that most of the available hydrographical data in the Red Sea domain are based from hydrographic stations and/or data sets from ships that follow the central axis of the basin. During the course of this study, few measurements of salinity and temperature represent the summer season were made available. These data is very useful in terms of calibration processes of the hydrodynamic model. Positions of the salinity and temperature measurements are shown in Figure (3.10) (marked by coloured dots along the main axis of the Red Sea as well as three cross sections taken in the north, middle and south of the basin). The interpolated data are presented in Figure 3.13 and 3.14 respectively. Typical vertical profiles of temperature and salinity along the main axis of the Red Sea are shown in Figure 3.13. It is clear from the plot that the mixed layer occurs from the surface until depths of almost 50 m while the thermocline layer extends from 50 m to 200 m. The distribution of the temperature and salinity in the deep layers is remarkably homogenous.

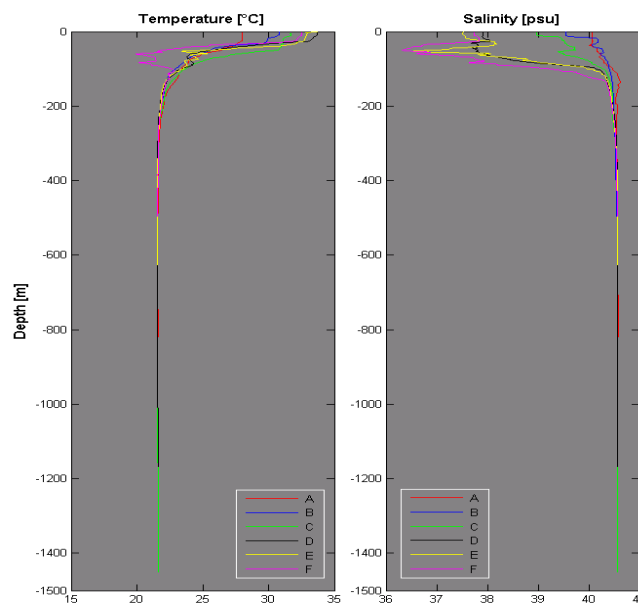


Figure 3.13 Typical profiles of temperature and salinity at locations along the Red Sea axis

Figure 3.14 shows the Vertical distributions of the hydrographic properties (salinity and temperature) at three sections marked in the location map (Figure 3.10). The plots illustrate that the sea surface salinity (SSS) increases from the south (section III) at about 38 psu towards the northern part of the Red Sea (section I) reaching about 40.2 psu. On the other hand, the sea surface temperature (SST) increases southwards from about 29 °C to 33 °C. The observations show a surface mixed layer which is about 50 to 70m thick, salty and warm due to heating and evaporation.

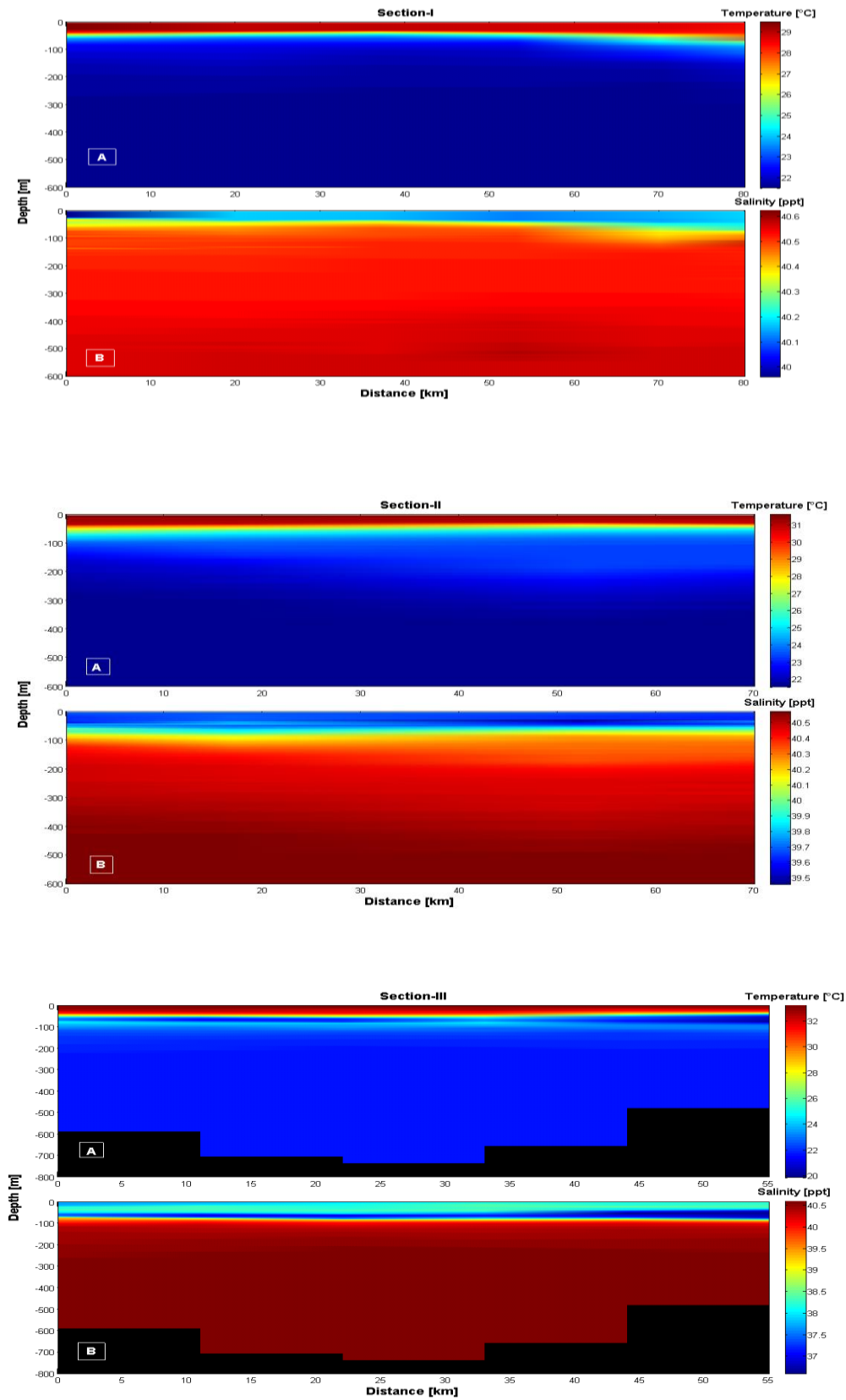


Figure 3.14 Northern I, Middle II and Southern III hydrographic sections As) Temperature and Bs) Salinity.

Chapter 4

Model Description

4.1 Introduction

The present study concerns with the simulation of tides, the circulation and thermohaline structure in the Red Sea. In order to model these phenomena, the Delft3D modelling system developed by WL *Delft* Hydraulics in the Netherlands is used. Based on the model discretization and forcing, the identified processes in chapter 3 should be reproduced by the model.

In this chapter, brief general information concerning the Delft3D modelling system is introduced in section (4.2). As this study focuses only on hydrodynamics, a brief description of the Flow-module is presented in section (4.3). It is followed by the model formation including the numerical methods, overview of hydrodynamic and transport equations; information on turbulence closure models and boundary conditions in section is provided (4.4). Section (4.5) presents a brief description concerning the heat flux model used in the present investigation. It should be noted that most of the information about the modelling system were taken from the Delft3D-Flow user-manual (2011).

4.2 General Information of the Modelling System

The numerical modelling system implemented in this study is Delft3D modelling system developed by WL *Delft* Hydraulics in the Netherlands. The system is an integrated modelling scheme (Delft3D package) where it comprises basic modules that simulate the time and space variations of six phenomena, namely hydrodynamics (Delft3D-Flow), Sediment transport (Delft3D-SED), Morphology (Delft3D-MOR), Waves (Delft3D-Wave), Water Quality (Delft3D-WAQ) and Ecology (Delft3D-ECO). The system is applicable to shallow seas, coastal areas, estuaries, lagoons, rivers and lakes and has the ability to carry out the interactions between these processes. Delft3D system has been widely applied in a number of studies for instance South-Eastern German Bight (Palacio *et al.*, 2005), Egmond the Netherlands (ELias *et al.*, 1998) and San Diego Bay and Coastal region (Dongeren, 2009). It has been used successfully to simulate tidal, wind driven flow conditions in Lunenburg Bay

and used to study the hydrodynamics and morphology of a seasonally forced tidal inlet system (Nghiem *et al.*, 2008).

In the present study, only the Delft3D-Flow module was used. Some additional programs included in the package such as RGFGRID, QUICKIN, QUICKPLOT modules and TRAINA tool were utilized. For using Delft3D-FLOW the first two auxiliary software tools are important for preparing input files. For post-processing purposes the last two packages were used. Table 4.1 presents a brief description of the additional programs. For more information about these programs and their use, the reader refers to the User-Manual-2011.

Table 4.1 A brief description of the tools used in the study

Module	Description
RGFGRID	Program to construct, modify and visualise a grid in Cartesian or Spherical co-ordinates for the Delft3D-Flow module. The program includes tools that can optimise the criterions of the grid (orthogonality and smoothness).
QUICKIN	Program to construct, interpolate, modify and visualise bathymetries for the Delft3D-Flow module.
QUICKPLOT	Program to visualise and animate the results produced by Delft3D modules. The program is based on MATLAB.
TRAINA	Tool to perform tidal analysis of Delft3D output. The program is capable of analysing time series of water levels generated by Delft3D-Flow module and also compare the results with known values for tidal constituents statistically.

4.3 Delft3D-Flow Module

Delft3D-Flow is a multi-dimensional (2DH, depth-averaged) or (three-dimensional, 3D) hydrodynamic model aiming to solve unsteady flows and transport phenomena that result from tidal and meteorological forcing including the effects of density differences (due to a non-uniform temperature and salinity distribution) on a rectilinear or curvilinear boundary fitted grid. The flow model aims to simulate flow phenomena of which the horizontal length and time scales are considerably larger than the vertical scales. The flow is forced by water levels or tides at the open boundaries, wind stresses at the free surface, pressure gradients due to free surface gradients (barotropic) or density gradients (baroclinic). The discharge and withdrawal of water can also be included in the equations.

Delft3D-flow is structured to execute hydrodynamic computations and computation of the transport of salinity, transport and heat transfer simultaneously. It should be pointed out that the accuracy of the model outputs for flow characteristics depends largely upon the physical and numerical parameters settings used in the model. The former parameters are those which reflect the nature of the area and that can be measured directly in the field or calculated indirectly via other field parameters. The latter parameters like grid resolution, time step, the

marginal depth and smoothing time are employed as a matter of modelling. Delft3D-Flow should however resolve the physical processes described earlier in chapter 3. Therefore, the requirements that should be met by Delft3D-Flow can be summarized as following:

- It has to take into account the space and time varying wind and atmospheric pressure system.
- It should be able to resolve temperature and salinity transport.
- It should be able to resolve the net heat flux cycle.
- It should be able to resolve transport forcing (lateral) and circulation forcing at the open boundaries.
- It should be able to resolve large-scale effects related to bathymetry constraints.
- It should be able to resolve vertical temperature variability and stratification over the water column.

4.4 Model Configuration

The system of equations in Delft3D modelling system includes the momentum equation, the continuity equation, the transport equation and turbulence closure model. To solve the hydrodynamic equations, a Cartesian rectangular, orthogonal curvilinear or spherical grid is available in the modelling system. Brief reviews of these equations are introduced in following sections.

4.4.1 Grid and Coordinates

The numerical methods of Delft3D-Flow system is based on finite differences in solving the partial difference equations. To discretise the 3D shallow water equations in space, the model area is represented by rectangular, curvilinear or spherical grids. In 3-D simulations, Delft3D-Flow provides two different vertical grid systems. A multi-layer is known as sigma co-ordinate system (σ -grid) introduced by Phillips (1957) for atmospheric models and the Cartesian Z co-ordinate system (Z-grid). Figure 4.1 displays the two vertical systems employed in Delft3D. In the sigma grid system, the vertical coordinate follows the bathymetry, keeping the same number of vertical grid points everywhere in the domain. The relative layer thickness usually is non-uniformly distributed to allow for increased vertical resolution in the area of interest. In the z-coordinate system, this type of model divides the domain using equal spacing between each layer (the vertical coordinate is depth). The number of grid cells in the vertical varies for each horizontal grid point.

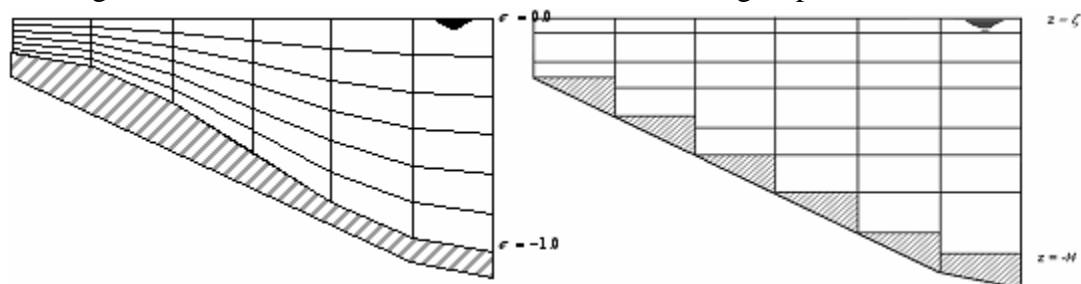


Figure 4.1 Layout of the vertical co-ordinate systems, σ -grid (left) and Z-grid (right) [Delft3D-Flow, User-Manual, 2011].

All the variables which describe the flow are defined in the so-called staggered grid (Arakawa C-grid). Figure 4.2 displays the pattern of the staggered grid of Delft3D-Flow system. In a staggered grid, each grid cell consists of a water level point, concentration of constituents, a point for the depth, a point for the velocity in the x-direction and y-direction. As can be seen in the figure, the water level points (pressure points) and the concentration of constituents are defined in the centre of a cell, whereas the velocity components are located perpendicular to the grid cell faces and the depth points are situated on the corner of the grid cell.

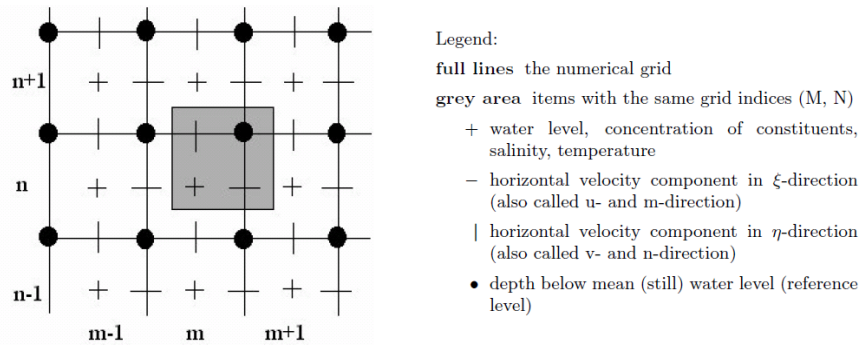


Figure 4.2 Staggered grid used in Delft3D-Flow [Delft3D-Flow, User-manual-2011]

4.4.2 Numerical Stability

In Delft3D-Flow system, the applied numerical scheme is an alternating direction implicit (ADI). There are a number of limitations on the allowable model step size due to stability and accuracy requirements for time integration of the shallow water equations. Computational stability in Delft3D is a function of the Courant number (indicator for numerical stability and accuracy). The Courant number provides the relation between the propagation speed and time step. In the case of places with large differences in bottom geometry or coastline, it is suggested that the Courant number should not exceed the value of 10. However, the total computational time depends upon the magnitude of the time step. Thus, in order to reduce the total computational time, one should select the largest time step possible, but taking into consideration the accuracy and stability. The Courant number formulation is expressed as:

$$C_r = 2\Delta t \sqrt{gh \left(\frac{1}{\Delta x^2} + \frac{1}{\Delta y^2} \right)} < 10 \quad (4-1)$$

where: C_r is the Courant number (Courant-Friedrich-Levy number); Δt is the time step (s), g is the gravity acceleration [m/s^2], h denotes the total water depth [m], Δx and Δy represent the grid spacing in x and y direction [m].

Some other numerical approximation parameters included in the flow module are summarized as following:

- I. Threshold depth: indicates the limit height above the bottom where the grid cell will be considered dry. This prevents the water depth to become negative in just one time step.
- II. Marginal depth: is the depth value after which the local gradients will be calculated by one-side differences.
- III. Smoothing time: is the time period to have a smooth transition between initial and boundary conditions. The model adjusts the initial and the boundary conditions prescribed. As the initial values are closer to the actual values, the warming-up period (adjustment of the initial conditions) will be shorter.

4.4.3 Hydrodynamic Equations

The hydrodynamic model computes the non-steady shallow water equations derived from the three dimensional Navier Stokes for incompressible free surface flow, under the Boussinesq assumption, in two (depth-averaged) or three dimensions. The system of equations consists of the horizontal equations of motion, the continuity equation, the transport equation and a turbulence closure model. The vertical momentum equation is simplified assuming hydrostatic pressure as the vertical acceleration are assumed to be small compared to gravitational acceleration thus are not taken into account. In 3-D simulations, the vertical velocities are computed from the continuity equations. The set of partial differential equations including the initial and boundary conditions are solved on a finite difference grid (orthogonal curvilinear co-ordinates or in spherical co-ordinates). In the following, the hydrodynamic equations employed in Delft3D system are presented. It should be mentioned that the hydrodynamic equations described here are similar for both the σ - and Z-co-ordinates systems.

4.4.3.1 Continuity equation

The depth-averaged continuity equation in Delft3D (in 2D and 3D) is defined as:

$$\frac{\partial \zeta}{\partial t} + \frac{1}{\sqrt{G_{\xi\xi}\sqrt{G_{\eta\eta}}}} \frac{\partial [(d+\zeta)u\sqrt{G_{\eta\eta}}]}{\partial \xi} + \frac{1}{\sqrt{G_{\xi\xi}\sqrt{G_{\eta\eta}}}} + \frac{\partial [(d+\zeta)v\sqrt{G_{\xi\xi}}]}{\partial \eta} = Q \quad (4-2)$$

where: d is water depth below some horizontal plane of reference [m]. t is time; ζ is free surface elevation above some horizontal plane of reference [m]. ξ and η are horizontal coordinates [m]. $\sqrt{G_{\xi\xi}}$ is coefficient used to transform curvilinear to rectangular coordinates [m]. u and v represent flow velocity in $\xi - \eta -$ direction [m/s] and Q represents discharge source or sink per unit area. Furthermore, Q represents the contributions per unit area due to the discharge or withdrawal of water, precipitation and evaporation; therefore it could be expressed as:

$$Q = (d + \zeta) \int_1^0 (q_{in} - q_{out}) d\sigma + P - E \quad (4-3)$$

where: q_{in} represents the local source of water per unit of volume [1/s] and q_{out} is the local sink of water per unit of volume [1/s]. P is the non-local source term of precipitation and E is the non-local sinks term of evaporation. σ represents the vertical direction of the co-ordinate system which is given as:

$$\sigma = \frac{z-\zeta}{d+\zeta} \quad (4-4)$$

4.4.3.2 Momentum equations

The momentum equation in Delft3D is expressed as:

$$\frac{\partial U}{\partial t} + U \frac{\partial U}{\partial x} + V \frac{\partial U}{\partial y} + \frac{\omega}{h} \frac{\partial U}{\partial \sigma} - fV = -\frac{1}{\rho_0} P_x + F_x + M_x + \frac{1}{h^2} \frac{\partial}{\partial \sigma} \left(v_V \frac{\partial U}{\partial \sigma} \right) \quad (4-5)$$

$$\frac{\partial V}{\partial t} + U \frac{\partial V}{\partial x} + V \frac{\partial V}{\partial y} + \frac{\omega}{h} \frac{\partial V}{\partial \sigma} - fU = -\frac{1}{\rho_0} P_y + F_y + M_y + \frac{1}{h^2} \frac{\partial}{\partial \sigma} \left(v_V \frac{\partial V}{\partial \sigma} \right) \quad (4-6)$$

where u, v and ω (x, y, σ, t) are the velocity components in the horizontal x, y and vertical σ -directions, respectively [m/s]. f is the Coriolis parameter. P_x and P_y describe horizontal pressure terms [$\text{kg}/\text{m}^2/\text{s}^2$]; F_x and F_y describe horizontal viscosity terms; v_V is the vertical eddy viscosity coefficient which is determined by a turbulence closure model [m^2/s] (see section 4.4.3.1); ρ_0 is the reference density of water [kg/m^3] and M_x, M_y are the external momentum due to source and sinks in x - y -direction [m/s^2].

4.4.3.3 Hydrostatic pressure assumption

Under the ‘‘shallow water assumption’’ the vertical momentum equation is reduced to the hydrostatic pressure equation. The vertical acceleration is assumed to be small (due to buoyancy effects) in comparison with gravitational acceleration and therefore is not taken into account. The resulting formula therefore is expressed as following:

$$\frac{\partial P}{\partial \sigma} = -\rho gh \quad (4-7)$$

where: g is the gravitational constant [m/s^2] and ρ is density of water [kg/m^3].

4.4.3.4 Vertical velocity

The vertical velocity ω is computed from the continuity equation:

$$\frac{\partial \omega}{\partial \sigma} = -\frac{\partial \zeta}{\partial t} - \frac{\partial [hU]}{\partial x} - \frac{\partial [hV]}{\partial y} \quad (4-8)$$

In the 3-D simulation, the vertical velocity is computed considering horizontal velocities, water depth, water levels and vertical velocities as follows:

$$W = \omega + U \left(\sigma \frac{\partial h}{\partial x} + \frac{\partial \zeta}{\partial x} \right) + V \left(\sigma \frac{\partial h}{\partial y} + \frac{\partial \zeta}{\partial y} \right) + \left(\sigma \frac{\partial h}{\partial t} + \frac{\partial \zeta}{\partial t} \right) \quad (4-9)$$

4.4.4 Transport Equations

In Delft3D-Flow, the transport of matter and heat is solved by an advection-diffusion equation in the three co-ordinate directions. The equation is expressed as:

$$\begin{aligned} \frac{\partial (d + \zeta)c}{\partial t} + \frac{\partial [(d + \zeta)uC]}{\partial x} + \frac{\partial [(d + \zeta)vC]}{\partial y} + \frac{\partial (\omega C)}{\partial \sigma} \\ = \left[\frac{\partial}{\partial x} \left(D_h (d + \zeta) \frac{\partial C}{\partial x} \right) + \frac{\partial}{\partial y} \left(D_h (d + \zeta) \frac{\partial C}{\partial y} \right) \right] + \frac{1}{d + \zeta} \frac{\partial}{\partial \sigma} \left[D_v \frac{\partial C}{\partial \sigma} \right] \\ - \lambda_d (d + \zeta)C + (d + \zeta)(q_{in}C - q_{out}C) + Q_{tot} \end{aligned} \quad (4-10)$$

where: C represents concentration of dissolved substances, salinity or heat; D_h , D_v are the horizontal and vertical diffusivity, respectively, λ_d represents first order decay processes and Q_{tot} represents the exchange of heat through the free surface.

4.4.4.1 Turbulence Closure Model

Delft3D-Flow solves the shallow water equations for an incompressible fluid on a computational grid. Turbulence is responsible for most of the vertical exchange. Usually the grid in both horizontal and/or vertical directions is too coarse and the time step large to resolve the turbulent scales of motion. In Delft3D system, the turbulent processes are carried out using a sub-grid method. In this process, details of the turbulent are neglected and only the effect of turbulence on the mean flow behaviour are accounted for. The contribution of 3D turbulent eddies to the vertical exchange of horizontal momentum and mass is modelled through a vertical eddy viscosity and eddy diffusivity coefficient (eddy viscosity concepts). In general, the horizontal eddy viscosity coefficients V_H and eddy diffusivity coefficient D_H are much larger than the vertical coefficients V_V and D_V . In Delft3D-Flow system, there are four closure models implemented to determine the vertical viscosity coefficient V_V and the eddy diffusivity coefficient D_V . Table 4.2 presents a summary of the four models including their concepts. The coefficient can be specified as a constant or computed by means of an algebraic, k - L or K - ϵ turbulence model where K is the turbulent kinetic energy; L is the mixing length and ϵ is the dissipation rate of turbulent kinetic energy. In the present investigation, the turbulence closure model K - ϵ was selected. For detailed information about these closure models, the reader is referred to the User-Manual (2011).

Table 4.2 Turbulence Closure Models implemented in Delft3D-Flow system

Model	Description
Constant coefficient	This model is the simplest closure model based on a constant value. The constant eddy viscosity leads to parabolic vertical velocity profiles, which is correct for laminar flow.
AEM Algebraic eddy viscosity model	This model does not involve transport equations for the turbulent quantities. This so-called zero order closure scheme is a combination of two algebraic formulation. This model uses analytical formula to determine K and L .
K - L	This model involves one transport equation for k and is called a first order turbulence closure scheme. The mixing length L is prescribed analytically and the same formulation is used for the AEM model.
K - ϵ	This model is a second order turbulence closure model. In this model both the turbulence energy k and dissipation rate of turbulent kinetic energy ϵ are calculated by a transport equation. From k and ϵ the mixing length L and viscosity V_V are determined. The mixing length now is a property of the flow, and in the case of stratification no damping functions are needed.

4.4.5 Boundary Conditions

Boundary conditions are very important components in numerical modelling. Therefore, in order to obtain satisfactory results from the numerical model, well-defined boundary conditions are necessary. In this regard, hydrodynamic and transport conditions must be specified as correct as possible at the open boundaries. To solve the systems of equations, the following boundary conditions need to be specified.

4.4.5.1 Vertical Boundary Conditions

In the σ -coordinate structure, the bed and the free surface correspond with σ -planes. Therefore, the vertical velocities at these boundaries can be simply:

$$\omega(-1) = 0 \text{ and } \omega(0) = 0 \quad (4-11)$$

Where: ω represents velocity in the σ direction.

4.4.5.2 Bottom Roughness

The bottom roughness in Delft3D-Flow program can be defined in several ways. In the case of depth-averaged flow (2D) the shear stress on the bed in the x- and y-direction induced by a turbulent flow is given by a quadratic friction law:

$$\tau_{bx} = \rho_w g \left(\frac{|u|u}{C^2} \right) \quad (4-12)$$

$$\tau_{by} = \rho_w g \left(\frac{|v|v}{C^2} \right) \quad (4-13)$$

The 2D-Chézy coefficient C may be determined with the following formulations:

- 1- Chézy formulation: $C = \text{Chézy coefficient [m}^{1/2}/\text{s]}$
- 2- Manning formulation: $C = \frac{\sqrt[6]{h}}{n}$
 $h = \text{total water depth [m]},$
 $n = \text{Manning coefficients. [m}^{1/3}/\text{s]}$
- 3- White Colebrook's formulation: $C = 18 \log_{10} \left(\frac{12h}{k_s} \right)$
 $h = \text{total water depth [m]},$
 $k_s = \text{Nikuradse roughness length [m]}.$

In the case of a 3D computation, the bed stress formulation is quite similar. In these computations the bed shear stress is related to the current in the first layer, using u_b (velocity at bed boundary layer) instead of U and C_{2D} instead of C_{3D} .

4.4.5.3 Lateral Boundary Conditions

There are two types of lateral boundaries basically closed boundaries which are the land-water lines and open boundaries which are artificial. The former are natural boundaries and the fluxes along them set to zero (known as free-slip condition), preventing interaction with the outside world. The latter is always “water-water” boundaries. The use of open boundaries in numerical flow model aims at limiting the computational area that is modelled and hence the computational time. However, open boundaries must be defined far enough from the area of interest to avoid their influences on the area under investigation. To run the hydrodynamic model, external forcing to start computations is required. There are four types of open boundaries available in Delft3D system mainly water level, velocity, discharge or linearised Riemann invariant (weakly reflective boundaries). However, the selection of the type of boundary conditions depends upon the phenomena to be studied and also the availability of field data. Boundary conditions however, can be obtained from measurements or by extracting the needed boundary conditions from a larger model in the case of absence measurements.

4.5 Heat Flux Models

The exchange of heat at the surface is determined by a number of physical processes. In Delft3D-Flow the heat exchange at the free surface is modelled by taking into account the separate effects of solar (short wave) and atmospheric (long wave) radiation, and heat loss due to back radiation, evaporation and convections. Solar radiation and incident atmospheric radiation are the sources of energy input to the system whereas back radiation, evaporation and convection are the processes where the system loses energy. The total heat flux through the free surface can be formulated as following:

$$Q_{tot} = Q_{sn} + Q_{an} - Q_{br} - Q_{ev} - Q_{co} \quad (4-14)$$

where: Q_{tot} is the net heat flux; Q_{sn} is the net incident solar radiation (short wave); Q_{an} is the net incident atmospheric radiation (long wave); Q_{br} is the back radiation (long wave); Q_{ev} represents the evaporative heat flux (latent heat) and Q_{co} denotes the convective heat flux (sensible heat) [W/m^2]

The change in surface layer temperature due to the net heat flux presented in equation (4-14) is formulated as:

$$\frac{\partial T_s}{\partial t} = \frac{Q_{tot}}{\rho_w c_p \Delta z_s} \quad (4-15)$$

where: Q_{tot} is the net heat flux through the free surface [W/m^2]; ρ_w is the specific density of water [kg/m^3]; c_p is the specific heat capacity of sea water [$m^2/(s^2 \text{ } ^\circ C)$] and Δz_s represents the thickness of the top layer [m]. In Delft3D-Flow, the heat exchange at the bed is assumed to be zero. This may lead to over-prediction of the water temperature in shallow areas. On the other hand, the effect of precipitation on the water temperature is not taken into account.

Equation (4-15) is added to the transport equation to include advection and diffusive terms and therefore the formula becomes:

$$\frac{\partial T_s}{\partial t} = advection + diffusion + \frac{Q_{tot}}{\rho_w c_p \Delta z_s} \quad (4-16)$$

In Delft3D-Flow system five different heat models are implemented for various model requirements and based on data availability. In this study the ocean heat flux model is used for the Red Sea model. General information about this model is given in the following section.

Ocean Heat Flux Model

The individual terms presented in equation (4-14), as formulated in the ocean heat model are described in details in the Appendix-A. Only brief description about the ocean heat flux model and its required coefficients are presented here.

In the ocean heat flux model, the net short wave solar radiation is calculated for a clear sky based on the declination between the Sun and the Earth's surface. This declination depends upon the geographical position on the earth and the local time. The total long wave atmospheric and back radiation and the heat losses due to evaporation and convection are computed by the model based on prescribed meteorological fields. Evaporation and convection depend on the air temperature, the water temperature near the free surface, relative humidity and wind speed (Delft3D-Flow, User-manual-2011).

Using the ocean heat flux model requires several coefficients that play a role in controlling the magnitude of heat flux terms. These are, the Stanton number (c_h) which is a transfer coefficient which controls the magnitude of the convective heat flux. The Dalton number (c_e) which is a transfer coefficient controlling the magnitude of the evaporative heat flux. The Ozmidov length scale (L_{inf}) which specifies the magnitude of turbulent mixing by internal waves (See appendix-A).

There are some advantages provided by the ocean heat model compared with other models implemented in the Delft3D-Flow system. In this heat model, the short wave flux is prescribed using time and latitude-dependent relations and an average solar flux. Therefore, the formulation gives a higher temporal and spatial short wave flux resolution than those prescribed by atmospheric datasets prescribing clear day-night variation (Delft3D-Flow, User-manual-2011). As a result of latitude dependency, the model is applicable for large water bodies and suitable for regions like the Red Sea which is almost over 20 degree in latitudinal direction. Another advantage is that, space varying meteorological surface forcing can be prescribed. Therefore, the total net flux calculated by the model is both time and space dependent which is a desirable property considering the model domain (see chapter 5). De Goede *et al.*, (2000) pointed out that this heat model is the best model of available temperature models in Delft3D-Flow due to practicality, robustness and simplicity.

Chapter 5

Development of the Red Sea Model (RS-Model)

5.1 Introduction

The main aim of this study is the simulation of tides, circulation and thermohaline structure in the Red Sea region. To achieve this goal, a numerical hydrodynamic model based on Delft3D modelling system is setup. Brief overview of the modelling system and its general characteristics was given in chapter 4. This model should be able to resolve the processes identified in chapter [3] using forcing data described in this chapter.

In this chapter a numerical model covering the entire Red Sea region and extending to the eastern part of the Gulf of Aden at longitude 48°E have been setup, calibrated and validated. Initially a detail description about the relevant processes is provided. This includes the hydrodynamic model setup including definition of the model domain in section (5.2), the processes of generating the grid and its properties in section (5.2.2), the bathymetry data and their interpolation methods in section (5.2.3) and the definition of the open boundary condition in section (5.3). This is followed by introducing the main numerical and physical parameters settings applied in the model in section (5.3.1).

Sensitivity analysis of the numerical and physical parameters and heat model coefficients is given in section (5.6). Based on the results of the sensitivity analysis, decisions on model forcing and parameterizations are made for final model runs. Consequently, the Red Sea model has been validated using sea surface elevation data from a number of tide gauge stations located along the eastern coastline of the Red Sea as well as two additional stations located in the Gulf of Aden, in-situ measurements of temperature and salinity and climatology of sea surface temperature SST based on satellite technique obtained from AVHRR / Pathfinder (Casey et al., 1010) (section 5.7). Accordingly, a conclusion of the model performance is drawn in section (5.8).

5.2 Flow Model Setup

A description of the Delft3D-Flow module is given in chapter 4. To setup a model, several processes including the definition of the model domain, construction of grid, open boundary definition and the model bathymetry, numerical and physical parameters are required. On the other hand, some decisions have to be made related to the choice of 2-D (depth-averaged) or 3-D (three-dimensional approach) model and the definition of the boundary conditions which include the forcing of the hydrodynamic in the model. In the following sections, all these issues are discussed and addressed.

5.2.1 Model Domain of the RS-Model

The first and most important step in the setup of a hydrodynamic model is the definition of the model domain. On the one hand, the modeller should take into consideration the area of interest in terms of evaluation and analyses the model results, the surrounding systems that have influences on the hydrodynamics, the location of the model boundaries (open/closed), the boundary conditions to be imposed. Besides, the computational requirements and also the processes to be simulated in the selected area should be accounted for.

Based on the aforementioned considerations and taking into consideration the processes to be resolved by the model, the model domain of the Red Sea has been defined. The Red Sea is elongated-shaped sea extending from the north to the south between 30° N to 10° N over a distance of about 2000 km (oriented NNW to SSE). In the southern part, it links with the Gulf of Aden and Indian Ocean through a narrow strait (26 km wide and 200m deep) known as Bab el Mandeb. Therefore, to ensure a proper representation of the hydrodynamics in the region, the model domain of the RS-Model as shown in Figure 5.1 (limited by the Red dashed-line) was selected to include the entire Red Sea region, the Gulf of Aqaba, the Gulf of Suez and extends towards Gulf of Aden at longitude 48° E.

The Gulf of Aden was included due to the fact that the strait of Bab el Mandeb is the only open boundary of the water basin where advective freshwater and heat fluxes can occur to balance the air-sea fluxes over the basin. As the water exchange in the region play significant role in the flow process it must be included. Besides tidal wave propagation from the Gulf of Aden is the major forcing of tidal motion in the Red Sea as pointed out by Defant (1961). Moreover, Patzert (1974) pointed out that important water masses and dynamics involved in the seasonal circulation may be located in the area outside the Red Sea basin. Most importantly, as mentioned previously in chapter [3], most of the previous studies focused in the southern part of the Red Sea including Bab el Mandeb and Gulf of Aden; therefore, covering this part in the domain assists in validation of the model results. Based on the model results, the model domain was found to be adequate for resolving the processes involved in the study area.

Once the model domain was selected, a grid was constructed to describe the bathymetry of the Red Sea. A detailed description of the grid generation and its properties is given in the following section (5.2.2).

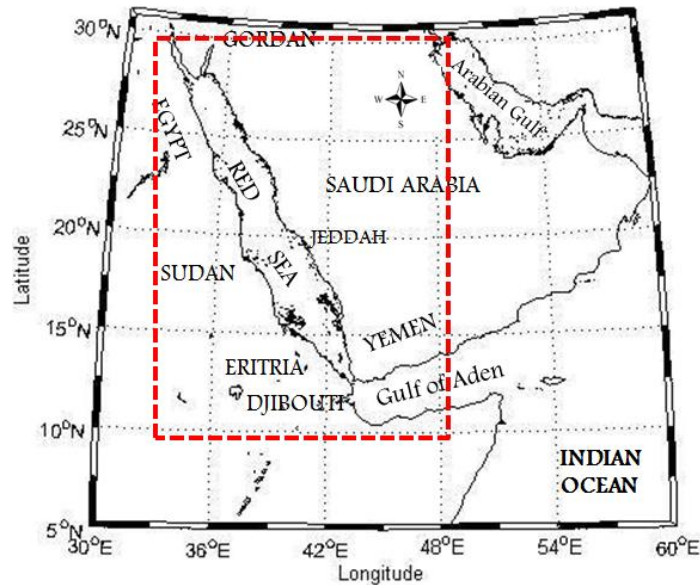


Figure 5.1 Border of the Red Sea model (**RS-Model**) domain indicated by red dashed-line.

5.2.2 Constructing the Grid

Numerical models require construction of a mesh for the selected domain in order to solve the equations governing the physical processes. Once the model domain has been defined, the grid configuration and resolution is defined. The design processes of the grid and the resolution together should involve systematically the optimal representation of the modelled processes and underlying bathymetry, the fulfilling of grid requirements taking into consideration the computational costs (computational time and computer requirements).

5.2.2.1 Grid Requirements

As already mentioned the equations are solved on finite difference grids. An optimal numerical accuracy requires some criterions to be taken into consideration within the preparation processes of the grid. The main requirements to be considered during building the grid are the so-called orthogonality and smoothness criterions. The former means that at each grid cell, the two lines drawn from the adjoining; opposite grid cell centres should intersect as perpendicular as possible (the angles between the horizontal and vertical grid lines should be close to 90 degrees). The latter means that the grid spacing must vary smoothly (M and N direction) over the computational region. These two factors are of great importance due to their significant role in the accuracy of the numerical solution of the flow equations.

The order of the orthogonality of a grid is determined by the cosine of the angle between the crossing grid lines in horizontal direction. According to Delft3D manual (2011), values in the range of 0.02 (angle: 88.85 - 91.15 degrees) in the area of interest to 0.04 (87.7-92.3 degrees) in remote areas are suggested. For the RS-Model, the values of the orthogonality in the entire grid are zero (see Appendix B-II).

The factor of grid smoothness is defined as the ratio between adjacent grid cell lengths in horizontal direction. This factor should be considered in order to minimize errors in the difference approximations. The recommended values of smoothness in the area of interest are 1.2 (see Delft3D Manual). The distribution of smoothness of the grid along the coordinates M and N direction for the RS-Model are fulfilled (see Appendix B-III).

5.2.2.2 Model Grid

The previous section has thrown light on the grid requirements that should be taken into consideration through the processes of building up the grid. Based on the model domain defined and the described grid requirements, the model grid of the Red Sea was generated. Tefvik (2006) suggests that in case of rectangular domains, finite difference equations are most efficiently solved with equal grid spacing. Therefore, some modifications on the grid should be carried out to arrive at adequate level of representation of the modelled area. The decision was made to schematize the grid on a rectangular mesh with a uniform grid spacing horizontally. To generate the computational grid, the Delft3D-RGFGRID generator program was used for this purpose. In early step, the configuration of the grid was selected to give a rough shape of the initial grid and also to make sure the final grid scheme will follow the expected flow direction avoiding numerical diffusion in the calculations. The final layout of the grid is based generally on depth data and land boundary outlines.

The resolution of the model grid is very important factor in terms of ability to resolve the spatial variability of the flow characteristics. Therefore, the model should have sufficient spatial resolution to represent the desired processes. Moffatt and Nichol (2000) pointed out that in some cases the grid has to be finer than the optimum grid size in order to capture particular features of importance. For the Red Sea model (RS-Model), the final grid resolution was chosen to be 2 km based on the sensitivity tests (see section 5.6 for sensitivity analysis). The model grid covers the entire Red Sea and extends to the eastern part of Gulf of Aden at longitude 48°E.

Figure 5.2 shows the resulting computational grid of the RS-Model. The model has only one open boundary situated in the eastern part of Gulf of Aden at longitude 48° E and divided into 25 segments. The open boundary has been selected far enough from the area of interest to avoid its effects on the hydrodynamics and model results. The coordinates system of the grid is spherical and therefore the variation of the Coriolis force is determined in the latitude direction. Considering the Courant number criterion ($C_r = <10$), the selected time step is set at 1 min (see section 4.4.2 for more details about the Courant number).

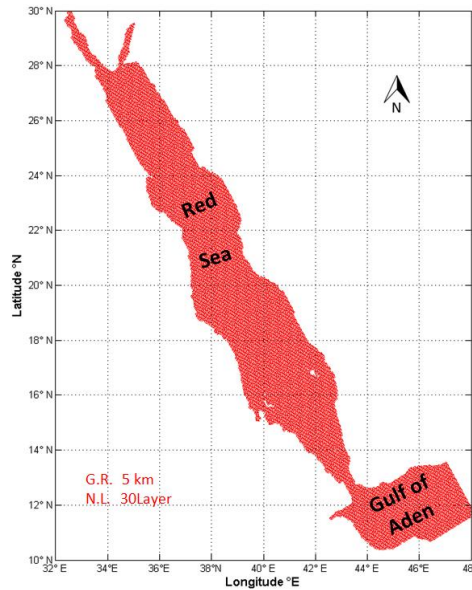


Figure 5.2 Computational grid of the Red Sea model, **RS-Model**

5.2.3 Shoreline and Bathymetry of the RS-Model

In order to setup a hydrodynamic model, bathymetric information on the area under investigation is necessary. It should be mentioned that the performance of a numerical model depends highly upon accurate representation of sea bottom levels. Currently there are several bathymetric datasets available with different coverage, resolutions and accuracies. Among them there is the GEBCO_08 (General Bathymetric Chart of the Oceans) bathymetric grid. GEBCO_08 is a 30 arc-second bathymetry grid produced largely by combining quality controlled ship depth sounding with predicted depths between the sounding points guided by satellite-derived gravity data.

The bathymetric data of the RS-Model were sourced from the global bathymetry dataset for the world ocean “GEBCO_08” database at a 30 arc-second horizontal resolution (The GEBCO_08 Grid, version 20090202, <http://www.gebco.net>). Data for the Red Sea model domain were extracted and converted into the appropriate file format required.

To schematize the bathymetry of the RS-Model, the QUICKIN-Module of the Delft3D modelling system package was used. QUICKIN-Module is used for constructing, preparing and interpolating the bathymetry data onto the model grid. The program provides three methods to interpolate the samples into the grid. These are the so-called “Grid cell averaging”, “triangulation interpolation” and “internal diffusion”. For more explanations with respect to interpolation methods, reference is made to Delft3D-QUICKIN user manual, 2011.

The selection of the method is very much related to the density of the sample. For High resolution data, “Grid cell averaging” method is used. “Triangulation interpolation” method is best suited for less number of samples, and “internal diffusion” method is used to fill the

areas that do not contain samples. For the RS-Model, the interpolation of the bathymetric data onto the computational grid was made initially by applying “Grid Cell averaging” method. This is followed by “Internal diffusion” approach. Figure 5.3 shows the resulting bathymetry map for the RS-Model.

The Red Sea as described earlier in chapter [3] experiences irregular bottom topography. Different gradients in the bathymetry are found along the coastlines where depths range from 20 to 150 m and then slope into deep waters. It can be seen from the figure that most of the deepest areas in the Red Sea are found in the central axis where water depth can reach more than 2000 m. In the northern part of the Red Sea the deepest areas reach around 1200 m while in the south the maximum depth is about 200m. This is particularly the case at Bab el Mandeb strait where the shallow shelves connect with the Gulf of Aden.

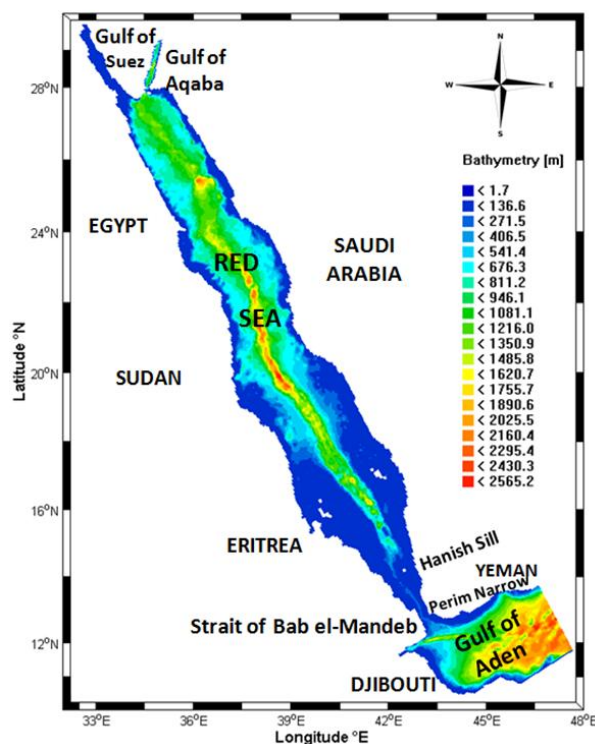


Figure 5.3 Bathymetry for the Red Sea model (RS-Model) based from GEBECO_8. The depths are in meter.

5.2.4 Two dimension (depth-averaged) and three-dimensional model approximation

The decision on the choice to use two and/or three-dimensional model approximating essentially on the main physical characteristics of the water system in the area of interest which basically based on the field measurements. Therefore, the importance of three-dimensional approach becomes essential for processes that cannot be adequately represented by the depth-integrated model.

As stated previously the Red Sea links with the Gulf of Aden via Bab el Mandeb strait. The model domain was defined to include the entire Red Sea and part of the Gulf of Aden (Figure

5.1) for the reasons discussed above (section 5.2.1). Therefore, the selected model domain should provide information about the flow velocity and temperature and salinity for both the horizontal plane and the water column. On the basis of literature, it was found that the circulation in the region of Bab el Mandeb is characterized by two-layer exchange flow during winter season. In contrast, this pattern is replaced during the summer season by three layers flow (see chapter 3). In addition to that, the available field measurements of salinity and temperature that were collected along the main axis of the Red Sea during summer-2001 have shown stratified water column. Taking these considerations, 2D models (depth-averaged) are unable to describe the vertical distribution of current or density variations throughout the water column. Therefore, in simulating the circulation and thermohaline processes in the Red Sea, a two dimensional model cannot be used in this regard. Accordingly, a three-dimensional approach has been selected to simulate the processes in question.

5.3 Definition of the Open Model Boundary

The definition of the open sea boundary is of major importance because it reflects the relation between the hydrodynamics in the model domain and surrounding areas. Open boundaries are always artificial “water-water” boundary. Selecting the type of boundary forcing depends mainly on the model requirements on the one hand and on the available data set on the other hand.

The open boundary of the RS-Model is selected far away from the area of interest in the Gulf of Aden at longitude 48°E to avoid its influences on the hydrodynamics and model results (see figure 5.2 for position). This boundary has been divided into a number of segments to ensure appropriate representation of the varying conditions along them. At the beginning and end of each segment conditions are prescribed and linearly interpolated.

5.3.1 Model Forcing

In order to simulate tides, circulation and thermohaline structure in the Red Sea adequate, model forcing should be applied. However, the applied data should have adequate spatial and temporal resolution to represent the desirable results. These data include the momentum transfer and pressure at free surface, momentum and transport forcing at the open boundaries and the heat exchange at the free surface. In the following, description about the model forcing data used is given.

As mentioned previously the Red Sea is a deep sea with depths changing from a hundred meters along its west and east coast to few thousand meters along the centre. Therefore, to compute the hydrodynamics the model must include the tide generating forces on the water body in addition to the ocean tide wave that enters through the strait of Bab el Mandeb.

5.3.1.1 Tidal Forcing

Since the first part of the current study concerns the simulation of tides, in a first step a two dimensional (depth-averaged) model driven by tide alone has been considered. Therefore, this step on the one hand assists in reducing the computational time and on the other hand leads to faster calibration procedure. This is followed by efficient validation of the model with locally available surface elevation records. The tidal model can then be modified to incorporate meteorological forcing, transport forcing to simulate the circulation and thermohaline structure.

Tidal forcing plays an important role in the dynamics of the ocean; therefore, it should be included as accurately as possible. The best approach for identifying the tidal forcing of flow models is the use of water levels of gauge stations located along or near the open sea boundaries. In the absence of measured data, large-scale models can be forced by astronomical constituents extracted from a global Ocean tide model. In the present study, water levels data near the open boundaries are not available for specifying boundary conditions in the model domain; thus the decision was made to extract the required boundary conditions from the global ocean tide models. It should be mentioned that the global tidal models can provide reliable predictions of tide in the oceans. However, in the shallow areas and near the coast of some regions the accuracy of these models usually is limited.

There are several global tide models that produce tidal constants with different resolutions and accuracies. Among them is the TPXO7.2 (on $\frac{1}{4} \times \frac{1}{4}$ degree resolution global grid) developed at Oregon State University by assimilating satellite altimetry data of the TOPEX/Poseidon project (T/P). This model is one of the most accurate global tidal solutions (Egbert and Erofeeva, 2002). The model produces the eight primary semidiurnal and diurnal tidal components and other components. As a starting point, the TPXO7.2 model was used to compute the astronomical constituents for each boundary cell of the open sea boundary. The model results were evaluated by comparing the results with available observations. Details about this scenario and its outcomes are discussed in the following section. The model settings used in the simulations are listed in Table 5.9.

Boundary Forcing based on TPXO7.2 global tidal model

In the first scenario the global tidal model TPXO7.2 has been used to compute the astronomical constituents at the open boundary cells. The tidal constants of the model include the eight primary semidiurnal and diurnal components (M_2 , S_2 , N_2 , K_2 , K_1 , O_1 , P_1 , and Q_1), and other components (Mf , Mm , M_4 , MS_4 and MN_4). Table 5.1 presents the amplitudes and phases of the astronomical constituents obtained from TPXO7.2 for only three selected segments. The assessment of this scenario was carried out by comparing the simulation results with the available measured water levels. The location of JIZAN and DUBA gauge stations were selected to compare the predicted tidal signal with the observed water level time series. A comparison between predicted and observed water levels from 19th until 25th of

April-2001 at the two locations is shown in figure 5.4. In general, it was found that the model produces similar trend of variations of computed and observed water level, however, discrepancies related to phase lag conditions are observed.

In addition to that, the model slightly underestimates the high and low water. Therefore, adjustments to the tidal constituents prescribed on the open boundary are necessary to reach a reasonable level of agreement with observations. To adjust and calibrate the open boundary conditions, the simulated water levels have been harmonically analysed and compared with harmonic constants of measurements. For this purpose, the Delft3D-TRIANA module was used. In this program, errors of amplitude and phase of the harmonic constants between the simulated and observed are computed (see section 5.6.2 for more details about the calibration process).

Table 5.1 Amplitude and phase of the astronomical constituents extracted from TPXO7.2

Tidal Constituents	Section I		Section II		Section III	
	Amplitude [m]	Phase [Deg]	Amplitude [m]	Phase [Deg]	Amplitude [m]	Phase [Deg]
M_2	0.358	136.1	0.359	136.3	0.359	136.4
S_2	0.165	157.4	0.166	157.6	0.166	157.7
N_2	0.092	133.7	0.092	133.8	0.093	133.9
K_2	0.036	157.7	0.036	157.8	0.036	157.9
K_1	0.372	347.2	0.372	347.3	0.372	347.4
O_1	0.192	351.4	0.192	351.5	0.192	351.6
P_1	0.115	348.3	0.115	348.4	0.115	348.5
Q_1	0.041	352.2	0.041	352.3	0.041	352.4
Mf	0.013	11.12	0.013	11.10	0.013	11.07
Mm	0.006	4.81	0.006	4.80	0.007	4.74
M_4	0.001	286.3	0.001	283.8	0.001	281.3
MS_4	0.0	-21.1	0.0	-21.3	0.0	-22.3
MN_4	0.0	-112.4	0.0	-106.4	0.0	-107.2

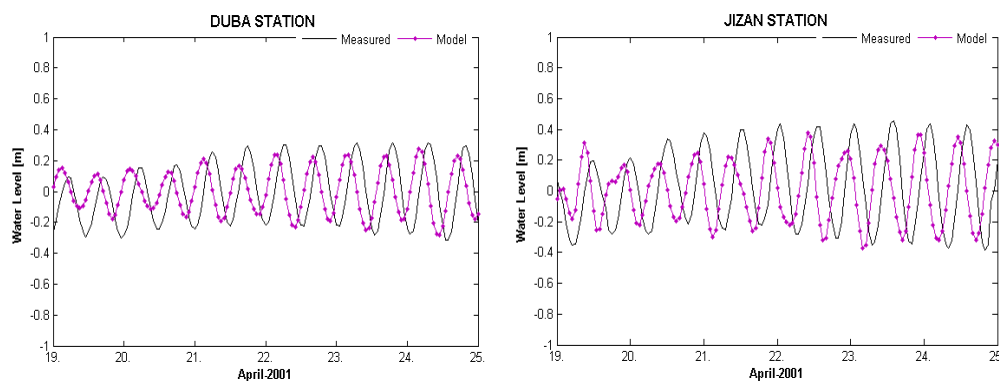


Figure 5.4 Comparison of measured and modelled water level at DUBA and JIZAN Stations based on TPXO7.2.

Based on the amplitude ratio and phase differences computed by Delft3D-TRIANA, the amplitudes and phases of the eight primary semidiurnal and diurnal constituents (M_2 , S_2 , N_2 , K_2 , K_1 , O_1 , P_1 , and Q_1) have been adjusted. Note that the tidal components M_f , M_m , M_4 , MS_4 and MN_4 were not considered due to their small contribution to the tidal behaviour. Table 5.2 presents the adjusted amplitudes and phases of the primary semidiurnal and diurnal constituents. The assessment of this scenario was carried out by comparing the simulations results with the measured water level time series at the same locations considered previously (JIZAN and DUBA). Figure 5.5 shows a comparison between predicted and observed water levels from 19th until 30th of April-2001. As can be seen in the figure, good improvements have been achieved. After tuning the tidal constituents at the open boundary, the model produces the high and low water with good accuracy. With respect to occurrence time, there is almost no phase lag between the model predictions and measurements. At high and low tide the simulated water level was always in phase with the observed tide.

Table 5.2 Amplitude and phase of the adjusted astronomical constituents

Tidal Constituents	Section I		Section II		Section III	
	Amplitude [m]	Phase [Deg]	Amplitude [m]	Phase [Deg]	Amplitude [m]	Phase [Deg]
M_2	0.55	252	0.55	252	0.55	252
S_2	0.251	257	0.251	257	0.251	257
N_2	0.176	285	0.176	285	0.176	285
K_2	0.086	275	0.086	275	0.086	275
K_1	0.38	32	0.38	32	0.38	32
O_1	0.17	120	0.17	120	0.17	120
P_1	0.048	83	0.048	83	0.048	83
Q_1	0.039	125	0.039	125	0.039	125

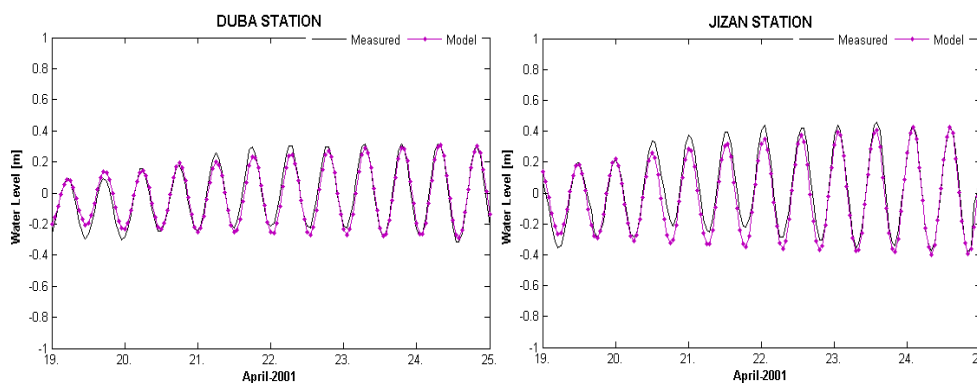


Figure 5.5 Comparison of the measured and modelled water level at DUBA, and JIZAN Stations after adjustment to the open sea boundary conditions.

5.3.1.2 Atmospheric forcing

Wind and Pressure forcing

As stated in chapter [3] the characteristics of the monsoon wind regime in the Red Sea region are very important in defining the circulation and thermohaline processes. To resolve the large-scale monsoon driven circulation, wind and pressure forcing have to be prescribed as space and time varying through the model domain. In addition to that, this data is required to determine the net heat flux at the free surface.

The wind speed and direction, pressure data were obtained from the German Metrological Service (the climate centre of Deutscher Wetterdienst, DWD) and interpolated to the model grid. This data has a spatial resolution of 1.5 degree at 6 hrs interval. These resolutions are adequate to resolve the large-scale monsoon system and also to resolve the large-scale seasonal heat flux cycle. The data considered in this study covers the period of eight years from January 2000 to December 2008.

Heat flux forcing

As mentioned in chapter [3] the seasonal temperature cycle in the Red Sea region is controlled by the net heat fluxes. The seasonal cycle of the heat flux is modelled by the shortwave flux, cloud coverage and monsoon wind. Delft3D-Flow system includes five different heat flux models to calculate the surface heat flux (see section 4.5). In this study, the ocean heat model was used. This model is considered to be the best (De Goede *et al.*, 2000) because it provides the possibility to apply the required space and time dependent heat flux forcing. The ocean heat model requires space and time varying cloud coverage, wind, air temperature and relative humidity as input fields. Similarly, the data covers the period of eight years from January 2000 to December 2008. The data are obtained from the German Metrological Service (the climate centre of Deutscher Wetterdienst, DWD) and interpolated to the model grid. The data has a spatial resolution of 1.5 degree at 6 hrs interval. These resolutions are also adequate to resolve the large-scale seasonal heat flux cycle.

5.3.1.3 Transport forcing at the open boundary

As described in chapter [3] exchange between the Red Sea water and surrounding system occurs via Bab el Mandeb Strait. There is seasonal variation in the exchange flow associated with monsoon winds. During the NE monsoon, water from the Red Sea flows out (RSOW) with a cool temperature and high salinity beneath the incoming surface water (SW) from the Gulf of Aden of a warm temperature and lower salinity. In contrast, during the SW monsoon, surface flow from the Red Sea towards the Gulf of Aden characterized by a warm temperature and high salinity takes place. Moreover, intermediate water (GAIW) between depths of about 40-80 m (18° C and 36 psu) from the Gulf into the Red Sea and deep outflow characterized by 21° C and high salinity (40 psu) into the Gulf was observed. Therefore, at the open boundary, temperature and salinity transport forcing has to be prescribed to account for influxes/outfluxes processes.

Measurements of temperature and salinity near to the open boundary are not available. The salinity and temperature data on the open boundary of the Red Sea model were obtained from SODA data (Simple Oceanic Data Assimilation). SODA data is produced by an Ocean General Circulation Model (OGCM), with horizontal resolution of $0.5^\circ \times 0.5^\circ$, and 40 vertical levels with 10-m spacing near the surface (Carton and Giese, 2008). This data is available every five days and considered to provide the best three dimensional TS distribution.

SODA data is prescribed at fixed depth levels, the spacing of which increases with depth. The data is linearly interpolated to the model grid in both horizontal and vertical directions. Therefore, it is prescribed as vertical profiles in Delft3D-Flow. This implies that at the open boundary, temperature and salinity are prescribed with time and vertically varying data. Thus, the values of temperature and salinity are calculated by linear interpolation between the boundary end points. Figure 5.6 shows an example of the temperature distributions over the Red Sea and close view of cross section along the open boundary.

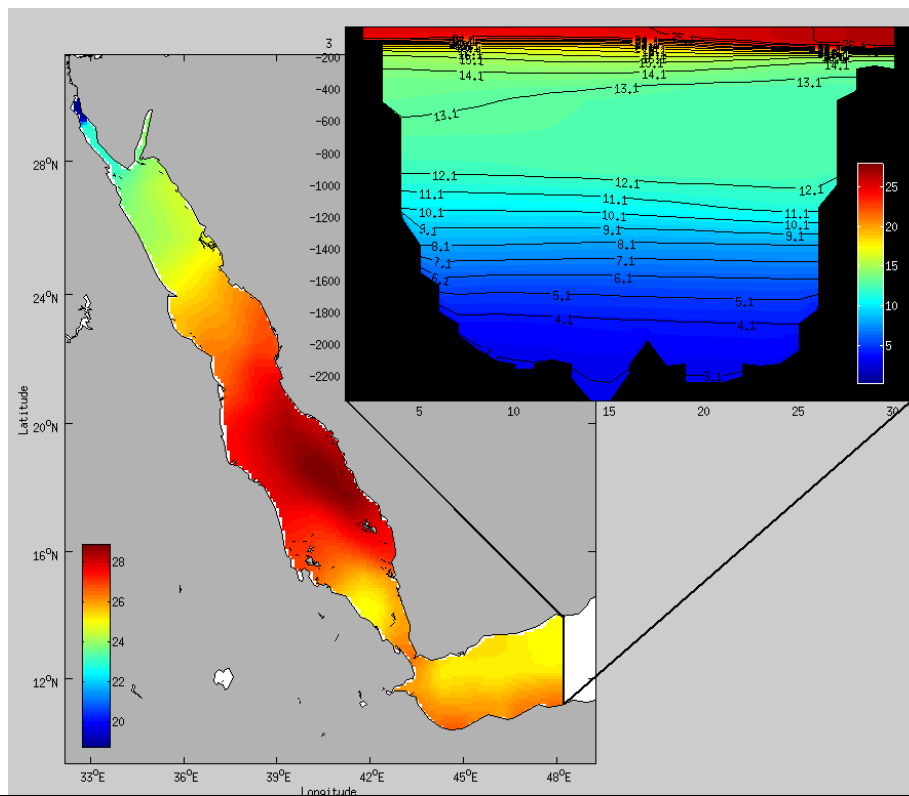


Figure 5.6 Temperature distribution [$^{\circ}\text{C}$] over the Red Sea and part of Gulf of Aden based from SODA and close view of cross section along the open boundary.

5.4 Numerical and physical parameters

In the present study, the main considerations of the model are tides, circulation and thermohaline processes. Setting up a hydrodynamic model involves determination of the numerical and physical parameters. These parameters are usually subject to sensitivity tests aiming at understanding their influences on the model results. Accordingly, the major parameters that have influences on the model results are identified. Therefore, the optimal values of the parameters are chosen to improve the model results based on observations. However, there are some constant values which have definite values in all simulation cases such as the gravitational acceleration and water density.

With respect to numerical parameters in the model, all the parameters except time step have been kept at their default values. Since the model stability and accuracy depends highly on time step (section 4.4.2), selection of optimal time step for the hydrodynamic model should be based on the sensitivity tests. On the other hand, relevant physical parameters like bottom roughness, wind drag coefficient and eddy viscosity parameters have been subjected to the sensitivity analysis. Salinity and temperature values have been considered space and time varying. The variation of the Coriolis force is taken into account in the latitude direction by setting the spherical coordinate system. The optimal values of the numerical and physical parameters employed in the hydrodynamic model are summarized in Table 5.3. Sensitivity analyses of the numerical and physical parameters are given in the next section. Moreover, heat flux model parameters and coefficients are discussed and addressed in section (5.6.4.5).

Table 5.3 Optimal parameters sitting used in the RS-Model

	Parameters	Value	Unit
	Gravitational acceleration	9.81	m/s ²
	Water Density	1028	kg/m ³
	Air Density	1	kg/m ³
	Temperature	variable	°C
Physical	Salinity	variable	pus
	Bottom roughness Che`zy (uniform)	65	m ^{1/2} /s
	Horizontal eddy viscosity	1	m ² /s
	Horizontal eddy diffusivity	10	m ² /s
	Vertical eddy viscosity	0.00001	m ² /s
	Vertical eddy diffusivity	0.00001	m ² /s
	Time Step	2	min
	Numerical	Threshold depth	0.1
Marginal depth		-999	m
Smoothing time		60	min

5.5 Initial condition

The solution of the shallow water equations is determined by a set of initial and boundary conditions (Delft3D-User Manual 2011). Initial values at every grid cell and for all predictive variables involved in the simulation are required. In this study, two main types of initial conditions are required i.e. dynamic (water level and velocity) and conservative constituents (salinity and temperature).

For the tidal model (2D-model), the initial condition for water level throughout the model domain was set equal to zero in all runs. The same applies to the velocity field, it is set to zero. In this respect, usually the equilibrium state in terms of water levels is reached after a few tidal cycles. Therefore, the first three days of simulation period have been ignored in the analyses.

For the three-dimensional model (3D-model), an initial condition file has been introduced to define the values of salinity and temperature along the model domain for each of the vertical layers. The temperature and salinity distributions used as initial conditions were obtained from SODA datasets at horizontal resolution of 0.5×0.5 degrees. Initial tests were carried out aiming at getting a rough idea about the time needed for reaching a balance in terms of salinity and temperature with a cold start condition. More details about initial conditions are presented in section (5.6.4.6). An example of the temperature distributions interpolated onto the model domain is shown in figure 5.6.

5.6 Model Sensitivity Analysis

5.6.1 Introduction

Since the physical and numerical parameters defined in the model set-up determine the characteristics of the flow simulation, their influences on the model outputs should be investigated through sensitivity analysis. As mentioned earlier in chapter 2 section 2.5.1 the major aim of sensitivity tests is to get an estimate on the general performance of the numerical model and determine the parameters to be tuned. This implies that the sensitivity analysis involve changing the model' inputs and checking the effects on the model results. The conclusion drawn from these analyses would be used later in the so-called calibration processes.

Initially, the sensitivity analyses for the most important parameters of the flow model are carried out. In the first step, sensitivity analysis was carried out to study the influences of grid resolution on the model results. Subsequently, effects of different time step on the model results are considered. Once these essential parameters are fixed, the analyses of the physical parameters were carried out. To select the horizontal grid resolution, optimal time step and also to investigate the open sea boundary conditions, a two-dimensional depth-integrated model was used. On the other hand, to analyse factors that require results in the vertical such as wind forcing and density distribution, a three dimensional model approximation was considered.

The analyses were carried out at four monitoring points indexed (JIZAN, JEDDAH, RABIGH and DUBA) in the model domain as shown in Figure 5.7. These locations were selected on the basis of available water level measurements. In addition to that, these locations are located far from the open boundary; therefore, the effectiveness of the open boundary conditions is taken into consideration. The time frame selected for the sensitivity tests was set for five days from 25th of April 2001 00:00hrs to 30th of April 2001 00:00hrs. This time covers several tidal cycles during spring tide. Detailed description about the sensitivity analysis of the model is presented in the following sections.

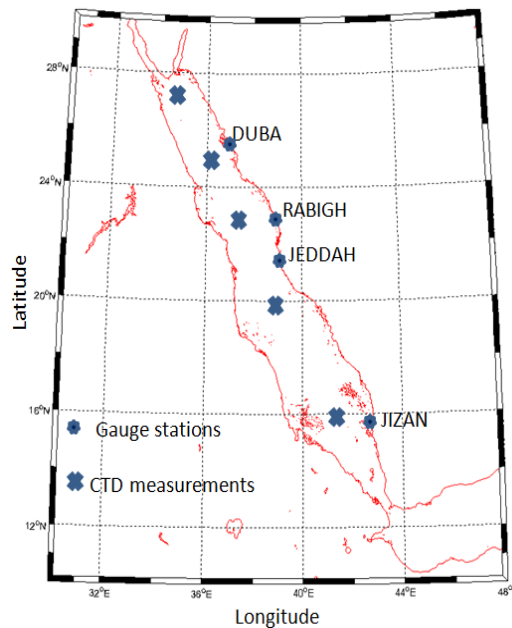


Figure 5.7 Location map showing the monitoring points considered in the sensitivity analysis.

5.6.2 Open Boundary Condition

In the present study, the TPXO7.2 global ocean tide model was used as starting point for determining the open sea boundary conditions. This model is described above in section (5.3.1.1). The RS-Model has only one open boundary divided into twenty five segments to form the open boundary of the model domain (see Figure 5.2). The primary semidiurnal and diurnal tidal constituents (M_2 , S_2 , N_2 , K_2 , K_1 , O_1 , P_1 , and Q_1), and other components (M_f , M_m , M_4 , MS_4 and MN_4) extracted from the TPXO7.2 global ocean tide model were prescribed at open boundary cells and linearly interpolated. An early test was carried out to determine the suitability of the open boundary conditions. In this regard, the adequacy of the prescribed open boundary conditions is tested against the water level measurements at JIZAN, JEDDAH, RABIGH and DUBA stations. The total period of simulations considered in the analysis is 15 days covering neap-spring tidal cycle from 15th to 30th of April 2001. However, taking into consideration initialization influences, the first four days are ignored and therefore not taken into account in the analysis. In the analysis, graphical comparisons as well as statistical evaluation between measured and simulated water levels were carried out. Table

5.4 lists the model settings used throughout the investigation of the open boundary conditions.

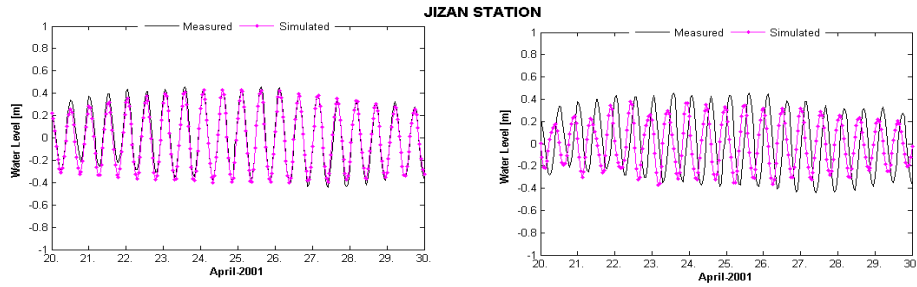
Table 5.4 parameters selected during Boundary Condition study

Parameters	Selected values
Grid Size	Reference Grid
Time Step	1 min
Eddy Viscosity	1 m ² /s
Bottom Roughness	65 m ^{1/2} /s
Initial Condition	Uniform water level equal to zero
	Uniform velocity equal to zero

The resulting water level time series are shown in Figure 5.8 through 5.11 (right-panel), respectively. Based on the simulation results, astronomical constituents obtained from the global tidal model TPXO7.2 produce discrepancies when compare with the measurements. It was found that the model prediction tends to underestimate high water amplitudes at JIZAN and DUBA stations and overestimate the low water amplitudes at RABIGH station. In addition to that, the simulated water level lagged 2 to 3 hours. At JEDDAH station, low water amplitudes are reproduced slightly better but high water levels are underestimated by the model. With respect to occurrence time, there is also phase lag between the model results and measurements. Based on these findings, adjustments of the open boundary conditions were carried out to reach a reasonable level of agreement between the simulation results and measurements.

To adjust the open boundary conditions, the water levels results from the model simulation have been analysed harmonically and compared with tidal constants from observations. For this purpose, the Delft3D-TRIANA program has been used. This tool performs offline tidal analysis of time series generated by Delft3D-Flow and computes the errors between the computed tidal constants and reference set of tidal constants arise from observed water levels. The statistical information provided is the amplitude ratio and phase difference. For details reference is made to the Delft3D-TRIANA-Manual, 2011.

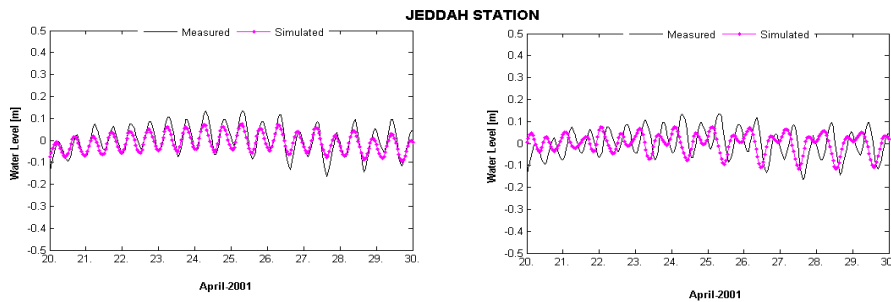
Using the mean amplitude ratio and phase differences, the adjustments to each individual tidal constituent were carried out. It can be seen from the Figures (5.8-5.11, left-panel); that significant improvements in terms of amplitude and phase have been achieved. The model estimates the high and low water level accurately at JIZAN and DUBA monitoring points. At RABIGH station, it can be seen that the model overestimates the low water and slightly the high water. At JEDDAH station, the model reproduces the low water accurately. However, the high water is underestimated by the model. On the other hand, the model predictions based on the adjusted conditions do not produce any phase lag during high or low water level.



I. Adjusted

II. TPXO7.2

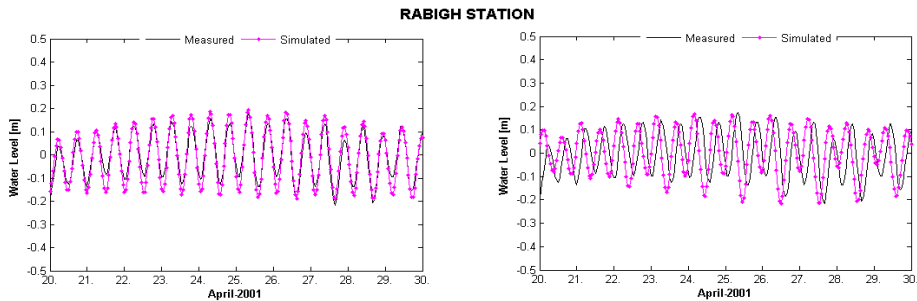
Figure 5.8 Comparisons of water level between the measurements and the predictions at JIZAN Station.



I. Adjusted

II. TPXO7.2

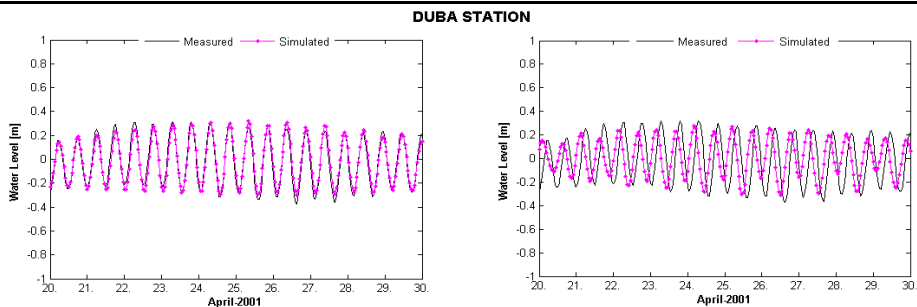
Figure 5.9 Comparisons of water level between the measurements and the predictions at JEDDAH Station.



I. Adjusted

II. TPXO7.2

Figure 5.10 Comparisons of water level between the measurements and the predictions at RABIGH Station.



I. Adjusted

II. TPXO7.2

Figure 5.11 Comparisons of water level between the measurements and the predictions at DUBA Station.

To assess the discrepancies between the measurements and the model results of each simulation, statistical calculation of the discrepancies is carried out. Statistical parameters in terms of the mean error (ME), mean absolute error (MAE) and root mean square error (RMSE) have been determined. Table 5.5 through 5.8 lists the statistical evaluation for the observation points JIZAN, JEDDAH, RABIGH and DUBA. RMS error for the model predictions based on adjusted astronomical constituents at all stations considered in the analysis was found to vary from 0.03 to 0.06 meter, while the MAE values were 0.03 meter at JEDDAH, RABIGH stations and 0.04meter at JIZAN and DUBA. On the other hand, RMS error for the model results based on TPXO7.2 varies from 0.08 to 0.3 meter, and MAE ranges from 0.07 to 0.3 meter. Therefore, very good improvements have been obtained from the adjusted astronomical constituents at the open boundary in comparison to the TPXO7.2 predictions.

Table 5.5 Statistical analysis of discrepancies at JIZAN station

Parameters		Adjusted	TPXO7.2
ME	[m]	-0.0241	-0.0153
MAE	[m]	0.0439	0.3080
RMSE	[m]	0.0570	0.3466

Table 5.6 Statistical analysis of discrepancies at JEDDAH station

Parameters		Adjusted	TPXO7.2
ME	[m]	-0.0105	0.0012
MAE	[m]	0.0301	0.0700
RMSE	[m]	0.0371	0.0823

Table 5.7 Statistical analysis of discrepancies at RABIGH station

Parameters		Adjusted	TPXO7.2
ME	[m]	-0.0024	-0.0103
MAE	[m]	0.0387	0.1192
RMSE	[m]	0.0342	0.0882

Table 5.8 Statistical analysis of discrepancies at DUBA station

Parameters		Adjusted	TPXO7.2
ME	[m]	0.0075	0.0212
MAE	[m]	0.0459	0.2121
RMSE	[m]	0.0434	0.2403

5.6.3 Numerical Parameters

Table 5.9 lists summary of the model types used in the sensitivity analysis. The evaluation of the influences on the model results was carried out at four monitoring points (JIZAN, JEDDAH, RABIGH and DUBA) located along the eastern coast of the Red Sea. The analyses of the numerical parameters include the grid resolution and time step.

Table 5.9 types of models considered in the sensitivity analysis

Parameters	Type of analysis	Approximation
BC	Open sea boundary condition	Two-dimensional
Numerical	Grid Resolution	
	Time Step	
Physical	Horizontal Eddy Viscosity	
	Bottom Roughness	
	Wind	
	Horizontal Eddy diffusivity	
	Vertical Eddy Viscosity	
	Vertical Eddy diffusivity	
	Density Gradients	

5.6.3.1 Decision on Grid Size in the horizontal plan

In a numerical model, considerations and attention should be taken in terms of computational time on the one hand and sufficient grid resolution on the other hand to represent the desired results. To determine the optimal grid resolution, sensitivity tests have been carried out with three different grid resolutions. The final grid resolution is selected on the basis of the sensitivity analysis.

Initially, a reference grid of 5 km resolution has been constructed and by using refinement/de-refinement processes the coarse and finer grids are obtained. Table 5.10 provide an overview of the proposed grid characteristics including maximum Courant number and time step. Column 2 in the table lists the total number of each case considered in the analysis. The time step and corresponding maximum Courant number is shown in column 4 and 5 respectively. The spacing of the coarse mesh is 10 km. The medium grid (Reference) has a resolution of 5 km while the finer grid resolution is 2 km. Note that the flow simulations using finer configuration consumes almost as much as twice the computing time when compared to the reference grid.

In general, the same bathymetric data and the same interpolation methods have been applied onto each grid. In the case of time step, the Courant number was set as similar as possible for the three grids. Therefore the time step was selected based on the Courant number of the finer grid and kept constant for all computational grids. That means that, the time step was assessed according to the finer grid resolution in the computational area specified by the Courant number. Bottom roughness (Chezy coefficient) and eddy viscosity parameters were set as default values as given by the Delft3D-Flow system. All the sea water properties were

prescribed as presented in Table 5.3. Simulations were carried out using the same parameters setting for each grid.

Table 5.10 Characteristics of the proposed grids used during sensitivity analysis

Grid	Number of Grid Cells	Grid Resolution [km]	Time Step [min]	Maximum Courant Number
Coarse	93.000	10	2	6.5
Reference	184.075	5	1.5	6
Finer	368.114	2	1	6

In order to select the optimal grid resolution, comparisons between the computed water levels at the selected locations for the three different grid spacing are plotted. Figure 5.12 presents the comparison of the simulated water levels from the three models. The figure reveals that computed water levels of the reference and finer grid reflect tiny discrepancies at the monitoring points JIZAN and DUBA while at JEDDAH and RABIGH the models produce similar results. In the case of coarse grid, it was found that it under-predicts the tidal amplitude in addition to the occurrence time (phase lag of about one hour) as can be seen at JIZAN and DUBA stations. The same applies to JEDDAH and RABIGH stations. The coarse grid produces large discrepancies as compared to the reference and finer grids.

Regardless of the tiny differences between the reference and fine grids at JIZAN and DUBA monitoring points, the consuming time that the finer grid takes is almost twice of the reference mesh. In the comparison between the measurements and the model predictions it was found that the reference grid produces good matching with measured water level. Hence, it can be concluded that the resolution of the reference grid configuration is appropriate to carry out the current study. Moreover, the interpolation of the sample points in creating the bathymetry depends on the grid size; it was also found that the resolution of the reference grid is sufficient for the representation of the coastline and the bathymetrical gradients. Therefore, the reference grid was adopted in this study and it will be used later used in all simulations.

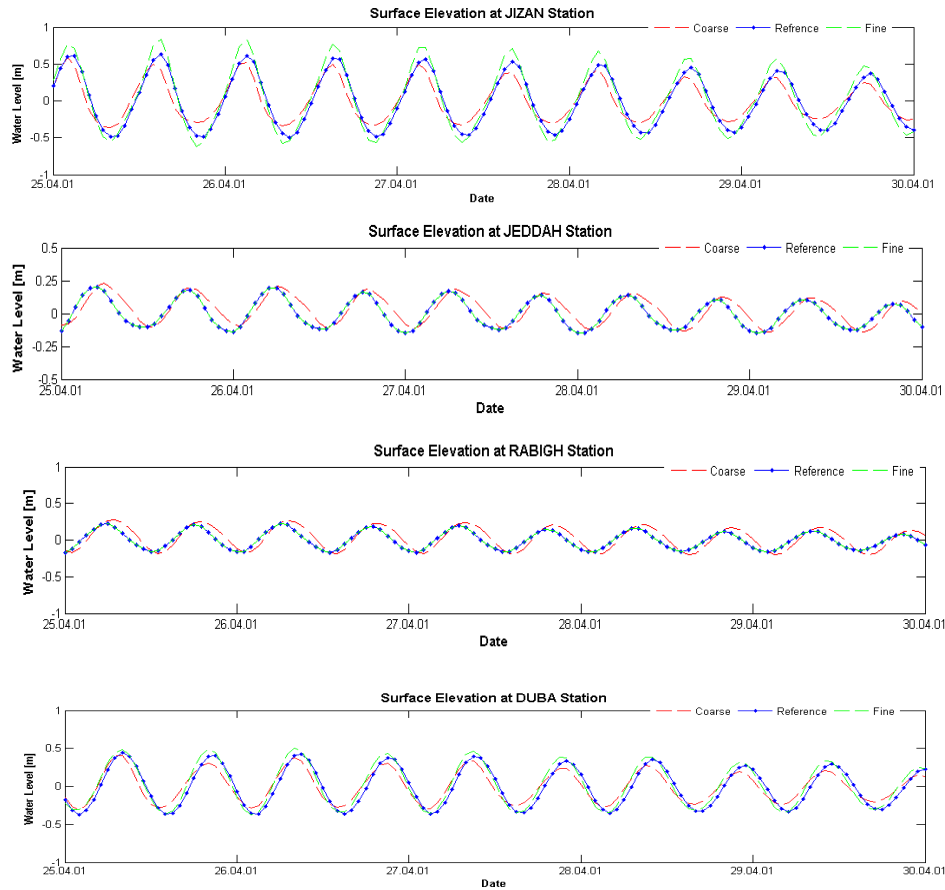


Figure 5.12 Effect of the horizontal grid resolution on water level at monitoring points JIZAN, JEDDAH, RABIGH and DUBA for **RS-Model**.

5.6.3.2 Grid resolution in vertical plan

In order to simulate the circulation and thermohaline processes, the 2-D RS-Model was extended into the 3-D mode. The suitability of using three-dimensional models is on the one hand related to the number of the grids applied in the vertical direction and on the other hand to the vertical coordinate systems. If the vertical distributions are not defined accurately, the desirable results cannot be derived in a good manner. Nevertheless, special attention should be considered concerning the computational time which depends on the number of grids in the vertical discretization. It is known that applying more number of layers definitely consumes more time computation. Therefore, an optimum number of layers should be achieved taking into account the computational time on the one hand and the accuracy of the results on the other hand.

As a first step, it is important to select the optimal vertical coordinate system that meets all the requirements of the current study. As stated previously the Delft3D-Flow system solves unsteady flows on boundary fitted grid (sigma-coordinate system). This coordinate system has significant errors where stratified flow occurs particularly in combination with steep bathymetry (see chapter 2). This is very important in the case of the Red Sea which experiences stratified flow as well as steepness in bathymetry. The Red Sea is characterized

by different sea bed gradients along the coastlines which slope into deep waters in central axial where water depths can reach over 2000 m (see section 5.2.3). Besides, a complex exchange flow exists between the Red Sea and Gulf of Aden via Bab el Mandeb strait. This is characterized by two layers flow system in winter and three layers flow system in summer. Because the “ σ ” level is boundary fitted (the vertical coordinate follows the bathymetry, keeping the same number of vertical grid points everywhere in the domain), it does not have enough resolution around the pycnocline which is strictly horizontal in the physical space. As a result, errors in the pressure gradient can give rise to unrealistic flows. Therefore, the sigma-coordinate system cannot be used in this study. In 2003, a second vertical grid coordinate system based on Cartesian coordinates (known as Z-grid) was introduced in Delft3D-Flow for 3-D simulations of stratified water systems. The Z-coordinate system has horizontal lines which are almost parallel with density interface in regions like the Red Sea. The number of grid cells in the vertical varies from grid point to grid point and it depends on the local depth (see section 2.6.3.2.1 for more details about Z-coordinate). Thus, the second vertical grid coordinate system based on Cartesian coordinates was used to meet all the requirements of this study.

In the second step, a decision was made concerning the number and thickness of layers taking into consideration the computational time as well as the required results. On the basis of measurements, it was found that a thermocline in the main axis of the Red Sea region is always above 200 meters depth (see section 3.6.4). In addition to that, the potential temperature and salinity distribution varies significantly between the two monsoon seasons. Beneath the depth of 200 m, the Red Sea basin is characterized by water of remarkably homogenous temperature, salinity and potential density. The analysis of the available measurements showed that the mean thermocline depth is located between 50 and 100 meters (section 3.7.3). A maximum thermocline depth is found between the depth 100 and 150 meters. Since the mixed layer is located above the thermocline depth, special attention should be considered to distinguish between the layers. Consequently, the model vertical resolution in the upper layers should be sufficient to represent variability in the study area.

Taking into account the aforementioned descriptions about the complex dynamics in the upper part of the water column, the water column is resolved by 30 vertical layers with 15 of these concentrated in the upper 200 m. The vertical distribution is defined per grid point as percentage of the total depth of 2700 m. The vertical discretization is defined with layer depths increasing from 5 m at the surface to 250 m at the bottom, thus keeping the higher resolution at the surface in order to capture the dynamic of the upper ocean. The resulting vertical distributions based on the depths are presented in Table 5.16. Based on the model results, it was found that the distributions of the vertical resolution are sufficient to adequately represent the processes in question (see chapter 7).

Table 5.11 vertical distribution of the Z-model grid

Layers	Depth [m]	Z-Level
1	5	0.1924
2	10	0.3848
3	10	0.3848
4	10	0.3848
5	11	0.4231
6	12	0.4616
7	12	0.4616
8	13	0.5000
9	14	0.5385
10	15	0.5770
11	17	0.6539
12	19	0.7310
13	23	0.8847
14	27	1.0385
15	31	1.1924
16	39	1.5000
17	50	1.9231
18	63	2.4231
19	85	3.2693
20	113	4.3462
21	150	5.7693
22	189	7.2693
23	221	8.5000
24	239	9.1924
25	250	9.3996
26	250	9.3996
27	250	9.3996
28	250	9.3996
29	250	9.3996
30	250	9.3996

5.6.3.3 Effect of the time step

Time step is an important parameter because it plays significant role in the accuracy and stability conditions of the model. It is well known that smaller time steps lead to higher accuracy of the computations. However, as the time step decreases, the computational time increases. Thus, an optimal time step should be achieved with the highest possible value avoiding any numerical instability.

As mentioned previously in chapter [4] the model time step is limited by the Courant number formulation which gives rough idea about the possible range of time step. In the sensitivity analysis of the model due to grid resolution (section 5.6.3.1), the simulations were performed by setting the time step to 1 minute associated with Courant numbers of 6. In the following analysis, three scenarios were carried out to determine the influence of different time step on the model predictions. The values of time steps have been chosen based on the maximum

Courant number given by each of these three cases as listed in Table 5.12. All other parameters were left as given by Delft3D-Flow system.

Table 5.12 Time steps and courant number used in the sensitivity analysis

Cases	Time Step	Max. Courant Number
Case I	0.5 min	3.5
Case II	1 min	6
Case IV	2 min	13

The influence of different time steps on water levels at the monitoring points JIZAN, JEDDAH, RABIGH and DUBA is shown in Figure 5.13. Based on the simulation results, the changes of time steps from 0.5 to 2 minute reveal that the water level predictions are not influenced. Since the three cases produce similar results, the computed results from the original simulation (Case I) can be considered as stable and representative. Note that the flow simulation using 2 minute time step reduce the computing time compared with the one minute. However, this time step corresponds with Courant number of 13. Therefore, for accuracy and numerical stability a time step of 1 minute is adopted in this study.

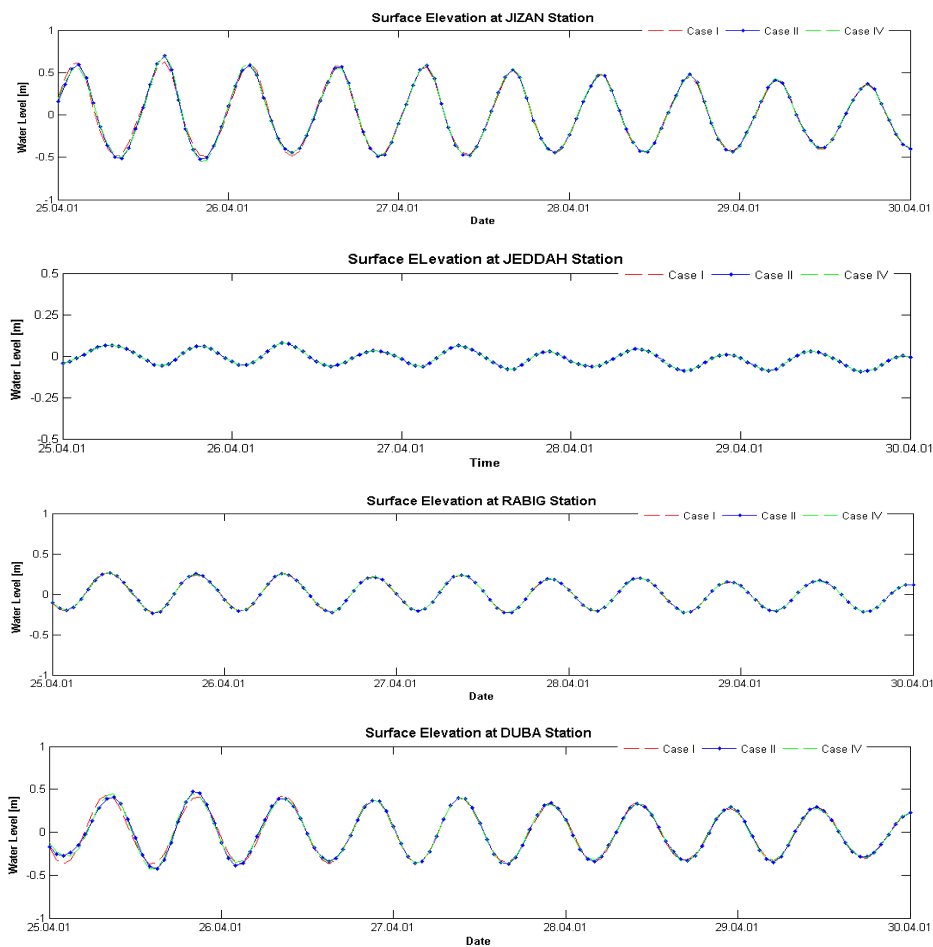


Figure 5.13 Effect of different time steps on water level at monitoring points JIZAN, JEDDAH, RABIGH and DUBA for RS-Model.

5.6.4 Physical Parameters

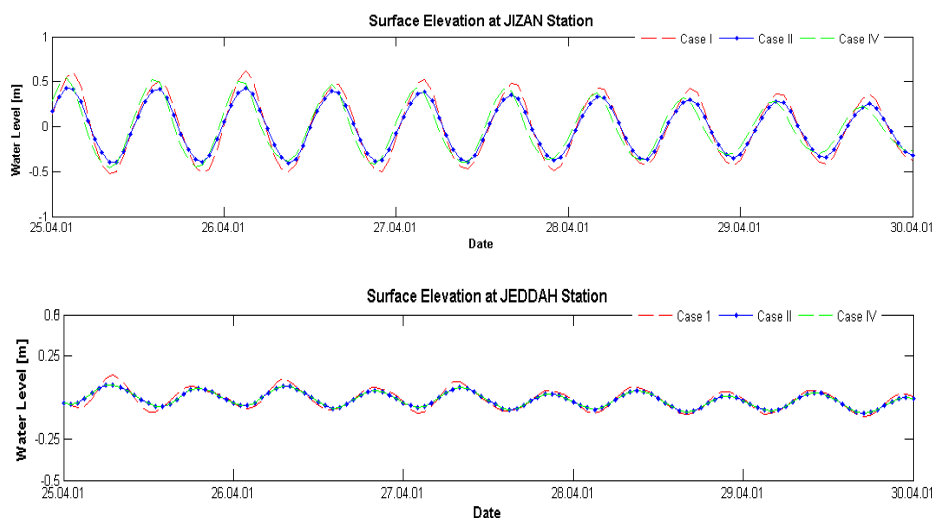
In the previous sections sensitivity analysis of the numerical parameters has been carried out. As a result, numerical parameters values have been fixed and no longer subject to the investigation. In the following sections the sensitivity analyses of the most important physical parameters in the flow model are carried out. The physical parameters include bottom roughness, eddy viscosity, bathymetry changes and wind.

5.6.4.1 Effect of the bathymetry variations

As stated previously in section 5.2.3, in the present study, the bathymetry map prepared for simulating all the cases was based on the digital open source GEBCO_8 database at a 30 arc-second horizontal resolution. Therefore, it is important to investigate the relative influence of different bathymetrical depths on the model results. This was done by considering three cases as illustrated in Table 5.13.

cases	description
Case I	Increase 5% of depth from original bathymetry
Case II	Original bathymetry
Case III	Decrease 5% of depth from original bathymetry

Figure 5.14 presents the model predictions of water levels due to changes in bathymetry at the stations of JIZAN, JEDDAH, RABIGH and DUBA. Based on the simulation results, increases and decreases in the bathymetry by about 5% from the original values have insignificant influence at the monitoring points JEDDAH and RABIGH. On the other hand, minor variations on the water levels resulted at the locations of JIZAN and DUBA. The results obtained show that increasing in the bathymetry of about 5% cause an average change of few cm.



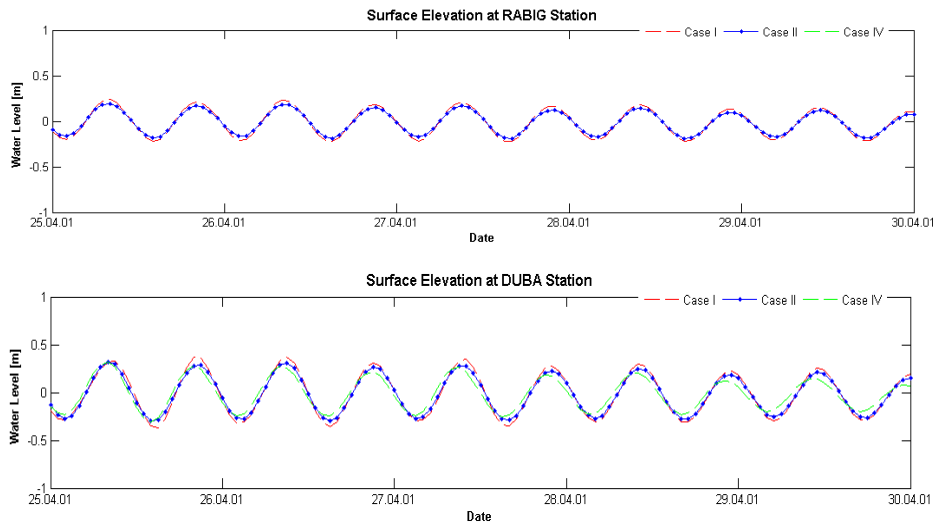


Figure 5.14 Effect of different bathymetry (water depth) on water level at monitoring points JIZAN, JEDDAH, RABIGH and DUBA for **RS-Model**

Relevant Model Coefficients

There are a number of coefficients that should be specified because of their relative role either in controlling the magnitude of model forcing or the representation of model processes. These include bottom roughness, horizontal and vertical diffusivity and viscosity parameters, heat model coefficients and wind drag coefficient (C_d). However, optimal determination of these coefficients is based on the sensitivity analysis. In the following, all these coefficients are discussed and addressed.

5.6.4.2 Effect of the Bottom Roughness

Bed resistance is one of the most effective parameters in the hydrodynamic models. Roughness coefficient represents the resistance of the bed to the flow. In the current study, the bottom roughness value was considered as uniform over the whole domain. To determine the influences of bottom roughness on the simulation results, three cases are analysed. This analysis was carried out by running three scenarios including three different values of Chezy's coefficient equal to $45\text{m}^{1/2}/\text{s}$, $65\text{m}^{1/2}/\text{s}$, and $85\text{m}^{1/2}/\text{s}$ respectively. The simulations were carried out using the same parameters setting listed in Table 5.4.

Figure 5.15 shows the influence of bottom roughness on water levels at the monitoring points JIZAN, JEDDAH, RABIGH and DUBA. Based on the simulation results, the usage of lower or higher Chezy coefficients reveals that the water level predictions are not influenced significantly. Therefore, in this study a Chezy roughness coefficient equal to $65\text{m}^{1/2}/\text{s}$ is adopted for the RS-Model.

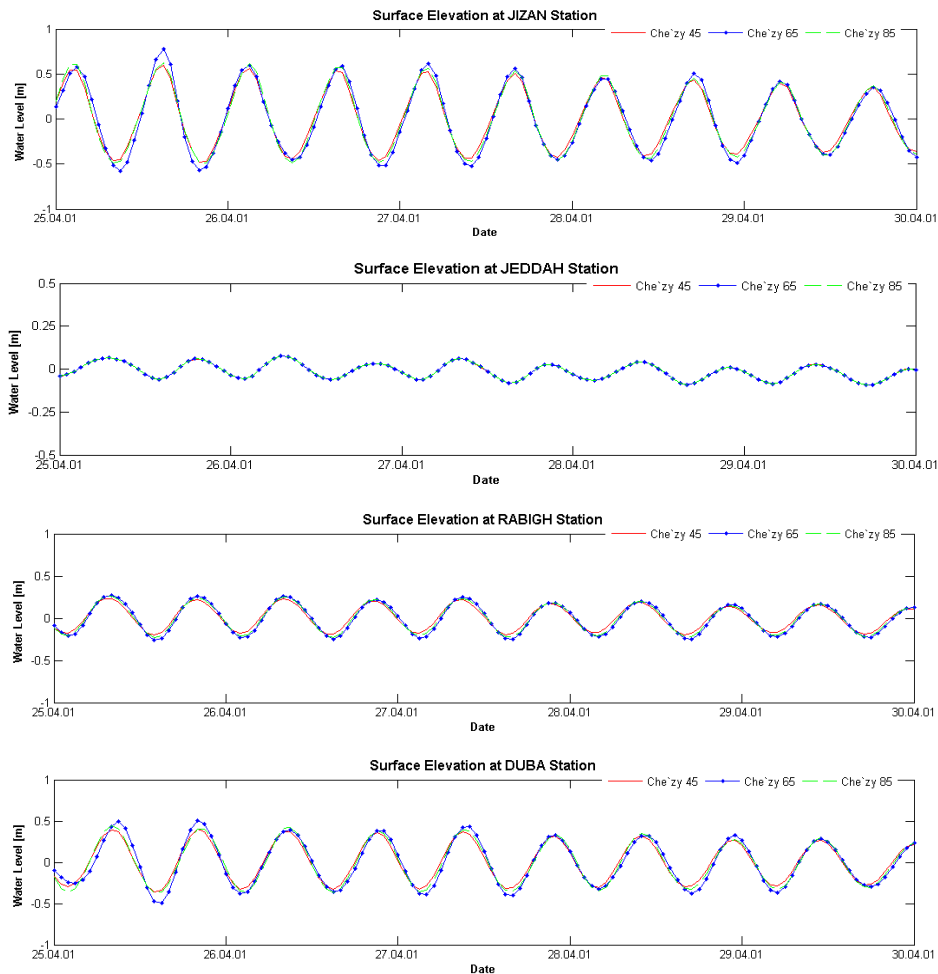


Figure 5.15 Effect of different values of Che`zy coefficient on water level at monitoring points JIZAN, JEDDAH, RABIGH and DUBA for **RS-Model**.

5.6.4.3 Effects of Horizontal Eddy Viscosity and Diffusivity

The horizontal viscosity / diffusivity parameters specify the magnitude of turbulent mixing on a sub-grid scale based on a turbulent closure model. In this study the $k-\epsilon$ turbulent closure model is used. The Reynolds stresses within the momentum equation are determined by the eddy viscosity concept. The contribution of 3D turbulent eddies to the vertical exchange of horizontal momentum and mass is modelled through a vertical eddy viscosity and eddy diffusivity coefficient. In the turbulent closure model ($k-\epsilon$), the turbulent kinetic energy k and the dissipation rate of turbulent kinetic energy ϵ are determined by transport equations. In general, the horizontal eddy viscosity coefficients V_H and eddy diffusivity coefficient D_H are much larger than the vertical coefficients V_V and D_V .

In this section, the influence of the Horizontal Eddy Viscosity (HEV) parameter is investigated by comparing three cases with the default value given by Delft3D-Flow system ($1 \text{ m}^2/\text{s}$). The HEV was considered as a constant value in time and space uniformly throughout the whole domain. Table 5.14 lists the eddy viscosity values used in the investigation. The comparison is made in terms of water levels at the stations JIZAN,

JEDDAH, RABIGH and DUBA. In all simulations, the other parameters were adopted as prescribed in Table 5.4.

Table 5.14 Eddy Viscosity values used in the sensitivity analysis.

Cases	Eddy Viscosity parameter
Case I	0.1 m ² /s
Case II	1 m ² /s
Case III	20 m ² /s
Case IV	60 m ² /s

The influence of horizontal eddy viscosity on the simulated water levels at monitoring points of JIZAN, JEDDAH, RABIGH and DUBA is shown in Figure 5.16. Based on the simulation results, the eddy viscosity coefficient has a negligible effect on the outcomes of the simulations in terms of water levels. Therefore, eddy viscosity value of 1 m²/s is adopted for the RS-Model.

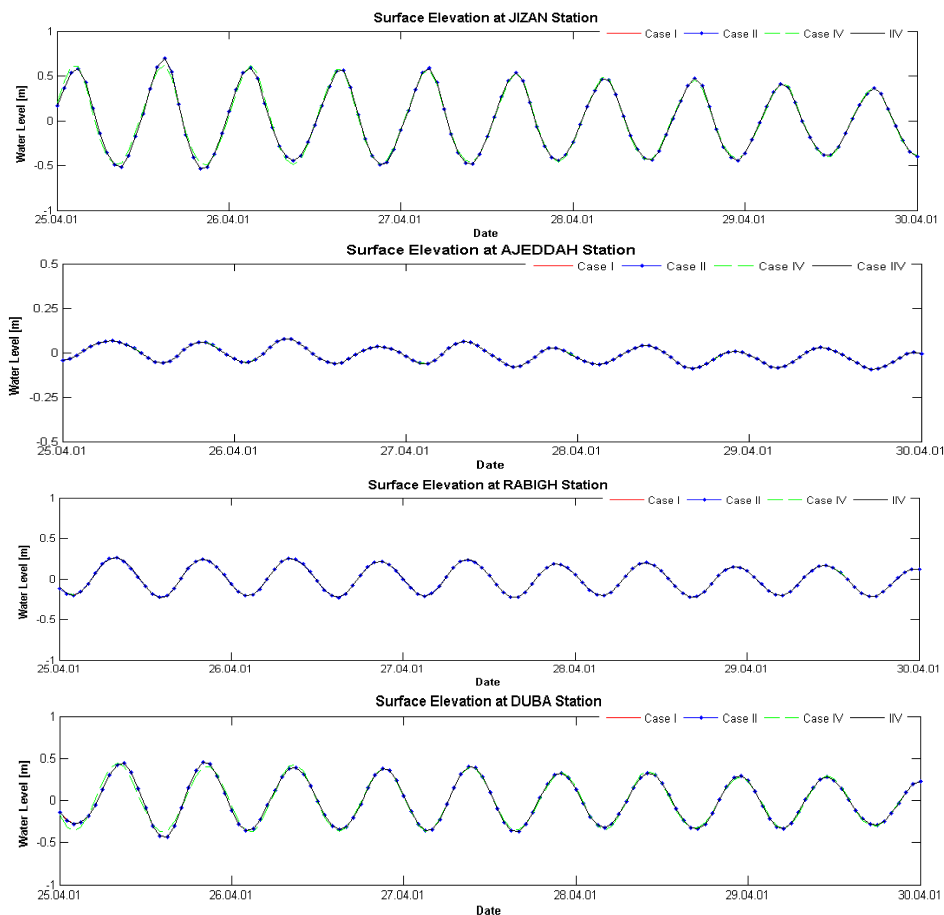


Figure 5.16 Effect of different values of Eddy Viscosity on water level at monitoring points JIZAN, JEDDAH, RABIGH and DUBA for RS-Model

The evaluation of the model sensitivity due to horizontal diffusivity was analysed on the basis of temperature and salinity. The influence of the eddy diffusivity parameter are analysed by comparing three different values with the default value given by system (10 m²/s). Table 5.15 lists the eddy diffusivity values considered in the analysis. In all simulations, the other parameters were adopted as prescribed earlier in Table 5.4.

Table 5.15 Eddy Diffusivity values used in the sensitivity analysis

Cases	Eddy Diffusivity parameter
Case I	1 m ² /s
Case II	10 m ² /s
Case III	100 m ² /s
Case IV	200 m ² /s

The influence of horizontal eddy diffusivity on temperature and salinity is shown in Figure 5.17 and 5.18 respectively. Based on the simulations results, increasing the horizontal diffusivity reflect some effects on the model results. The effect of diffusivity can be seen clearly in case III and IV particularly at latitude 20° to 16° N. This can be explained due to the fact that an increase in horizontal diffusivity lead to increased effects of turbulent mixing on sub-grid scale. On the other hand, the exchange system between the Red Sea and the Gulf of Aden via Bab el Mandeb Strait associated with the monsoon plays an important role (see chapter 3). In appendix 3, maps of sea surface temperature and salinity showing the spatially patterns are provided. These figures clearly indicate that increasing the value of horizontal diffusivity reduces the exchange features. Therefore, decreasing the horizontal diffusivity may improve the model quality in representing the exchange processes. Therefore, an eddy diffusivity value of 10 m²/s is adopted for the RS-Model.

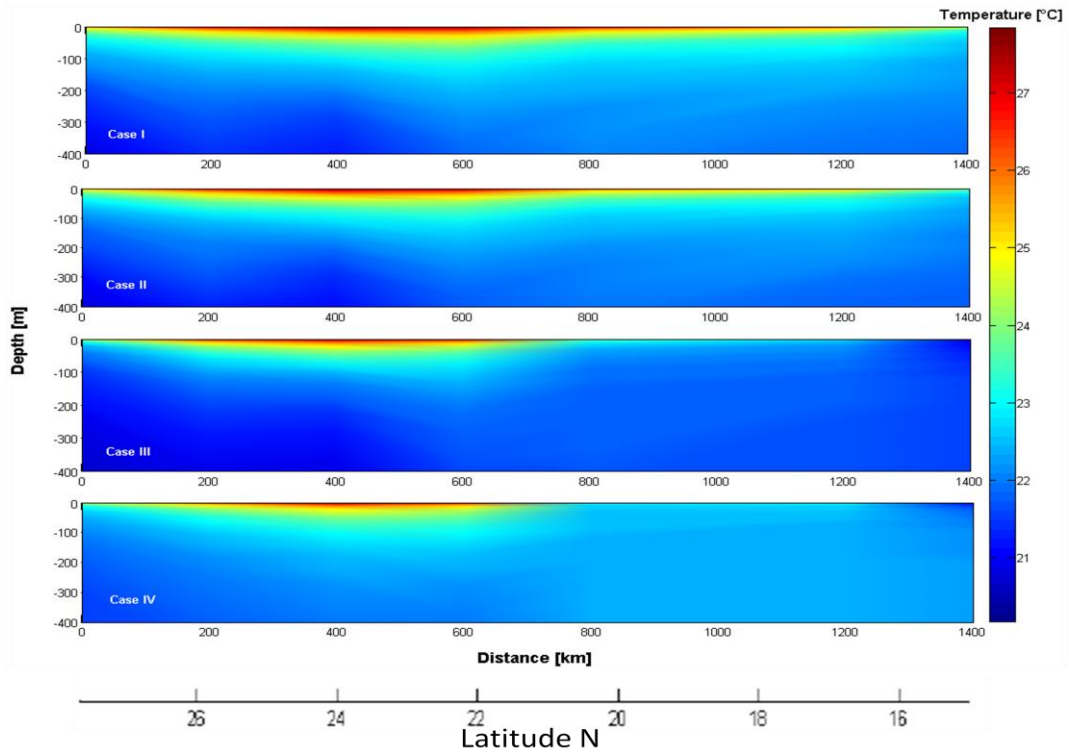


Figure 5.17 Effect of different values of Eddy diffusivity on vertical temperature profile, cross section along the main axis of the Red Sea.

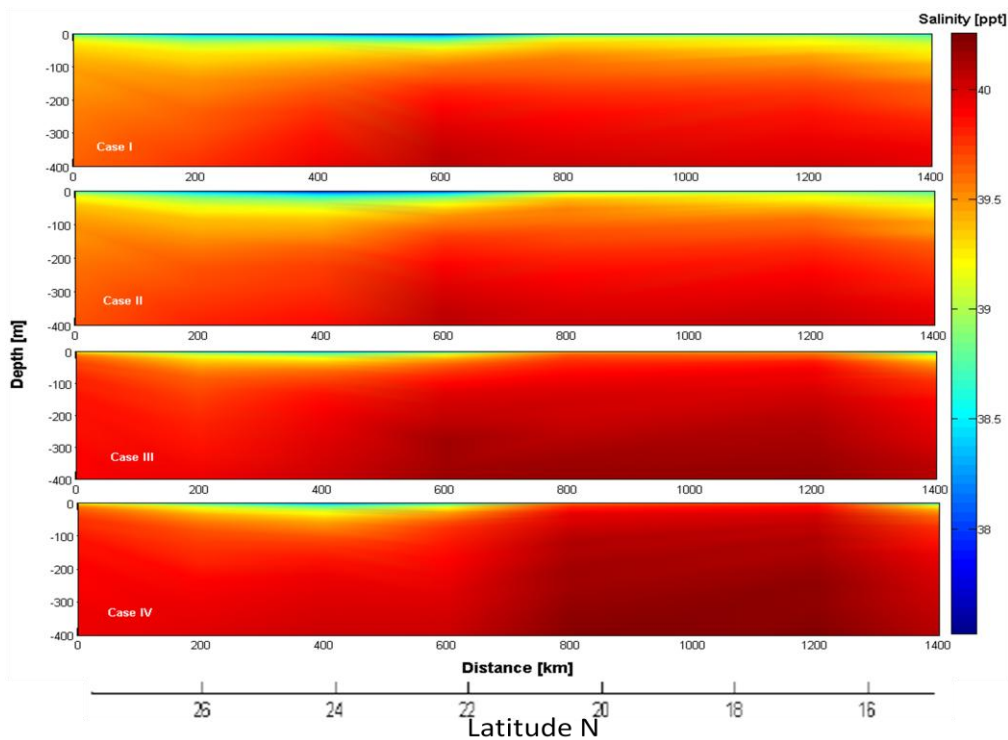


Figure 5.18 Effect of different values of Eddy diffusivity on vertical salinity profile, cross section along the main axis of the Red Sea

5.6.4.4 Coefficients for ocean heat model

As mentioned earlier in chapter [4], in this study the ‘‘Ocean Heat Model’’ was used. This mode requires a number of coefficients which play an important role in controlling the heat flux forcing in the numerical model. These coefficients are: the Stanton number (c_h), the Dalton number (c_e) and the Ozmidov length scale (L_{inf}). The Stanton coefficient is specified to control the magnitude of the convective heat flux while the Dalton coefficient responsible for the evaporative heat fluxes. The Ozmidov length scale parameter on the other hand determines the magnitude of turbulent mixing by internal wave.

To select the optimal values of the mean coefficient, a literature review was carried out. This step was aimed at identifying the most commonly specified magnitudes. Consequently several simulations were carried out based on different values of Dalton (c_e) and Stanton (c_h) numbers described in the literature. In this regard, (c_e) and (c_h) are calibrated by determining the optimum fit between sea surface temperature (SST) changes of the model and SST observations. Table 5.16 presents an overview of different coefficients found in the literature. It should be mentioned that these values are determined based on climatological, annual mean atmospheric variables.

In the literature, several numbers of Dalton and Stanton coefficients are applied. This is due to the fact that these coefficients are determined based on comparisons of empirical measurements with reference data and thus have only limited physical meaning (Gill, 1982). According to Saad and Ahmad (1995), the evaporative and sensible heat fluxes depends on the choice of heat exchange coefficients (c_e) and (c_h). Hastenrath and Lamb (1979) used a constant coefficient of $1.4 * 10^{-3}$ for (c_e) and (c_h) to calculate the heat fluxes in the Red Sea. They concluded that using this value lead to underestimation of evaporation flux when considering the monthly mean of meteorological variables.

Budyko (1963), used a value of $2.1 * 10^{-3}$ in constructing the ‘‘Atlas of the heat balance of the earth’’ for calculating evaporation from the world oceans. This value was used by Bunker *et al.* (1982) in calculating the heat balance in the Mediterranean and Red Seas. Ahmad and Sultan (1987) have also used this value for calculating heat fluxes of the Red Sea from monthly mean meteorological data. Their conclusion indicated that this value produces a reasonable estimate when considering the annual average. Robinson (1966) suggests the value of $2.0 \pm 0.3 * 10^{-3}$ for oceanic heat balance. On the other hand, Anderson and Smith (1981) recommended a value of $1.3 * 10^{-3}$ for c_e at wind speed up to 10 m/s. However, this value increases with increasing wind speed.

Ahmad and Sultan (1989) calculated the evaporative and sensible heat fluxes in the central part of the Red Sea by applying a lower value equal to $1.7 * 10^{-3}$ suggested by Robinson (1966). Surface heat fluxes and advective heat transport through Bab el Mandeb was studied by Ahmad & Sulatn (1995). In their study the exchange coefficient of $2.0 * 10^{-3}$ was used to calculate the evaporative flux while in calculating the sensible heat the values suggested by Gill (1982) are $c_h = 0.83 * 10^{-3}$ (for stable condition) and $c_h = 1.1 * 10^{-3}$ (for unstable

condition) were adopted. The conclusion drawn from this analysis indicated that the latent heat exchange coefficient (c_e) shows high sensitivity in estimating the evaporative flux and a value of $2.0 * 10^{-3}$ represents reasonable results.

The formulation of the heat flux equation used in the ocean heat model in Delft3D package is based on those described by Gill (1982). A mean wind speed of 6 m/s is observed over the Red Sea. Nevertheless, during the monsoon highs, higher wind speeds exceed 10 m/s. According to Anderson and Smith (1981), the Stanton number should in this case be increased to account for turbulent conditions associated with higher wind speeds. Therefore, Dalton and Stanton coefficients described by Gill (1982) are assumed representative. A Dalton number of $1.5 * 10^{-3}$ and a Stanton number of $0.9 * 10^{-3}$ will be used as starting point. In addition to that, the value considered by Bunker *et al.* (1982), Ahmad and Sultan (1987) in calculating heat fluxes of the Red Sea can be examined since it produces reasonable estimates.

Based on this review, the representative magnitude of the convective heat flux and the evaporative heat flux were determined. The default values in Delft3D system are $1.3 * 10^{-3}$ for both Dalton and Stanton coefficients. With these coefficients a number of simulations were carried out using the same model settings described previously. Sensitivity analysis suggested that changing the coefficients lead to minor influences mainly in the range of about 0.5 to 1 °C. Therefore, the values equal to $1.3 * 10^{-3}$ are applied.

Table 5.16 Overview of Dalton and Stanton numbers found in the literature.

Reference	Dalton (c_e)	Stanton (c_h)
[Gill, 1982]	$1.5 * 10^{-3}$	$0.83 * 10^{-3}$ (stable condition) $1.1 * 10^{-3}$ (unstable condition)
[Millar et al., 1999]	$1.5 * 10^{-3}$	$0.79 * 10^{-3}$
[Anderson & Smith, 1981]	$1.32 * 10^{-3}$	$1.1 * 10^{-3}$
[Bunker et al., 1982]	$2.1 * 10^{-3}$	$2.1 * 10^{-3}$
[Hastenrath & Lamb, 1979]	$1.4 * 10^{-3}$	$1.4 * 10^{-3}$
[Budyko, 1963]	$2.1 * 10^{-3}$	$2.1 * 10^{-3}$
[Robinson, 1966]	$2.0 \pm 0.3 * 10^{-3}$	$2.0 \pm 0.3 * 10^{-3}$
[Ahmad & Sultan, 1987]	$2.1 * 10^{-3}$	$2.1 * 10^{-3}$
[Ahmad & Sulatn, 1989]	$1.7 * 10^{-3}$	$1.7 * 10^{-3}$
[Saad & Ahmad, 1995]	$2.0 * 10^{-3}$	$0.83 * 10^{-3}$

5.6.4.5 Effect of wind drag

In the modelling system, two options are available to prescribe wind conditions i.e. global or local. The former corresponds to uniform wind in space and varying in time while the latter (local winds) vary both in space and time in combination with space and time varying atmospheric pressure. In this study, space and time varying winds and atmospheric pressure are used. The wind drag coefficient (C_d) determines the magnitude of the surface wind stress. The wind shear stress at the free surface is defined as:

$$|\vec{\tau}| = \rho_a C_d U_{10}^2$$

where: τ represents the wind shear stress at the free surface [N/m^2], ρ_a represents the air density [kg/m^3], C_d represents the wind drag coefficient, U_{10} represents the wind speed at 10 m above the free surface [m/s]. The wind shear stress increases linearly with air density ρ_a and wind drag coefficient C_d and quadratically with increasing wind speed U_{10} at 10 m height. Delft3d-Flow allows specifying a three wind drag coefficients values and three wind speed values. The three wind drag coefficients determine three breakpoints in the piece-wise linear function of wind drag and wind speed as illustrated in Figure 5.19. The default breakpoints are $C_{dA}=0.00063$ at $U_{10A} = 0$ m and $C_{dB} = 0.00723$ at $U_{10B} = 100$ m/s and $C_{dC} = 0.00723$ at $U_{10C} = 100$ m/s. The first two coefficients determine the wind drag value from zero wind speed up to the wind speed specified at the first breakpoint. For the third breakpoint, the two coefficients specify the constant wind drag coefficient from the specified wind speed and higher.

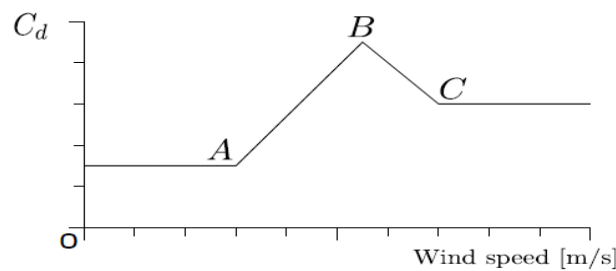


Figure 5.19 Example of the wind drag coefficient (Delft3D-user-Manual, 2011)

A variety of empirical relations are suggested in the literature to specify the magnitude of C_d . However, in majority of cases, relations dependent on wind speed U_{10} at 10 m height and on coefficients based on extreme wind conditions (such as storm surges) are used. Therefore, these coefficients reflect a strong regional dependency since they are determined from empirical relations. In the Open University (1989), a value of $C_d = 2 \times 10^{-3}$ is suggested to be a realistic and provides reasonable results. However, the modelling system a value of $C_d = 2.5 \times 10^{-3}$ is considered to be more realistic. In order to assess and determine the influence of the wind drag coefficient on the model results three different cases have been analyzed besides a simulation without applying wind. Table 5.17 lists the three settings considered in the analysis. The first and second settings (the realistic spectrum) represent the values suggested by the Open University (1989) and the default value of the modelling system respectively. The third case represents a higher C_d value which therefore reflects more clearly the nature of the effects. The total simulation period considered in the analysis is 30 days (01/04/2001 0:00hrs to 30/04/2001 0:00hrs). The influences of wind forcing in terms of water levels have been carried out at the monitoring points JIZAN, JEDDAH, RABIGH and DUBA respectively. In the three simulations, space and time varying winds are applied.

Table 5.17 Wind drag coefficient values used in the sensitivity analysis

Cases	Case I	Case II	Case III
C_{dA} 0 m/s	0.00063	0.00063	0.00063
C_{dB} 100 m/s	0.002	0.0073	0.0125

Figure 5.20 shows the mean wind magnitude and direction for the period considered in the analysis. The prevailing wind direction in the northern and central part of the Red Sea is NNW while in the southern part it is SSE. The mean wind speed during this month was found to be about 5.5 ms^{-1} and the maximum wind speed is equal to 10 ms^{-1} .

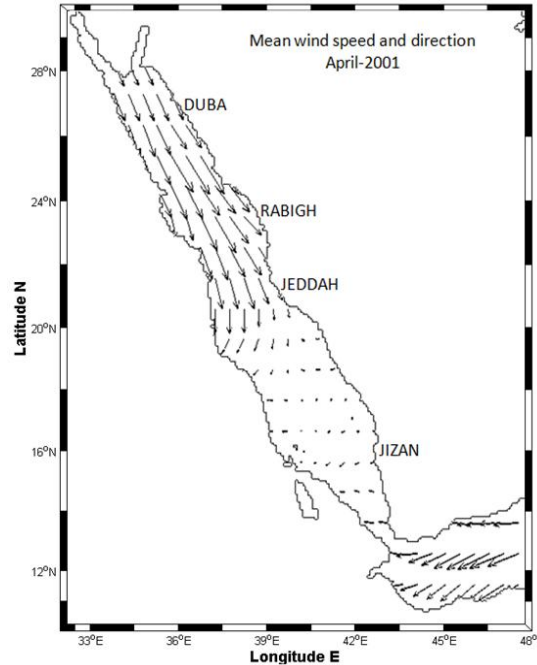


Figure 5.20 mean wind speed and direction for the period considered in the analysis

The influence of different wind drag coefficients on water levels including the simulated water level without wind at the four stations is shown in Figure 5.21. It can be seen from the figure that the water level set up induced by the wind differs depending on wind speed. The water levels of the simulation without wind indicate that the main movements of the hydrodynamics are forced by the horizontal open sea boundary conditions. However, the effect of the wind is obvious. The higher variations of the applied wind shear stresses during higher wind velocities are obvious. It was observed that the water level set up induced by the wind applying case III corresponding to higher velocities is in order of about 45 cm in April 6-7 2001 at JIZAN location. Similarly, the water level set up in DUBA reaches about 40 cm. In the middle part of the model domain near the stations JEDDAH and RABIGH location maximum water level set up is observed during the same period which is in order of 65 cm. The winds in the central part of the Red Sea are reported to be strong in the whole year. The water level differences for lower C_d values (case I and II) are small in JIZAN than JEDDAH or RABIGH as a result of higher wind speed. As a result, the differences between JIZAN and JEDDAH increase for increasing wind drag. The variability of the water level is higher for high C_d values in JEDDAH and lower for high C_d at JIZAN. On the other hand, the effect of the wind drag coefficient is tiny associated with lower wind velocities as observed at the monitoring points from 9-15 of April-2001.

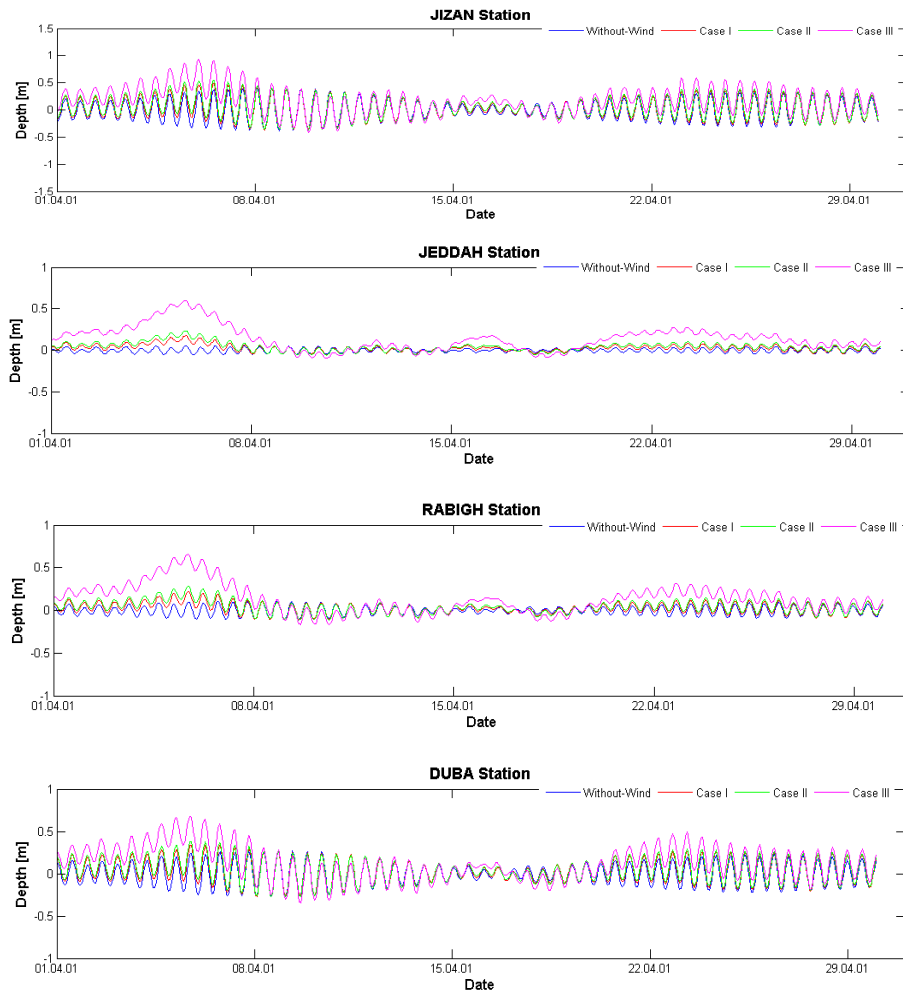


Figure 5.21 Effect of different values of wind drag coefficient on water level at monitoring points JIZAN, JEDDAH, RABIGH and DUBA for **RS-Model**

The influences of different wind drag coefficients have also been analyzed in terms of salinity distributions. Figure 5.22 and 5.23 shows vertical salinity distributions along the main axis of the model domain and three cross-sections representing the northern, middle and southern parts of the model domain respectively at 06 of April 15:00hr. The influence of case III is pronounced when compared with case I. The higher wind shear stresses (case III) enhance turbulences and thus the vertical exchange and mixing of the constituents. However, the water level differences due to density currents are expected to be small compared to the above discussed influences. The wind influences density driven currents temporarily depending on the wind drag coefficient.

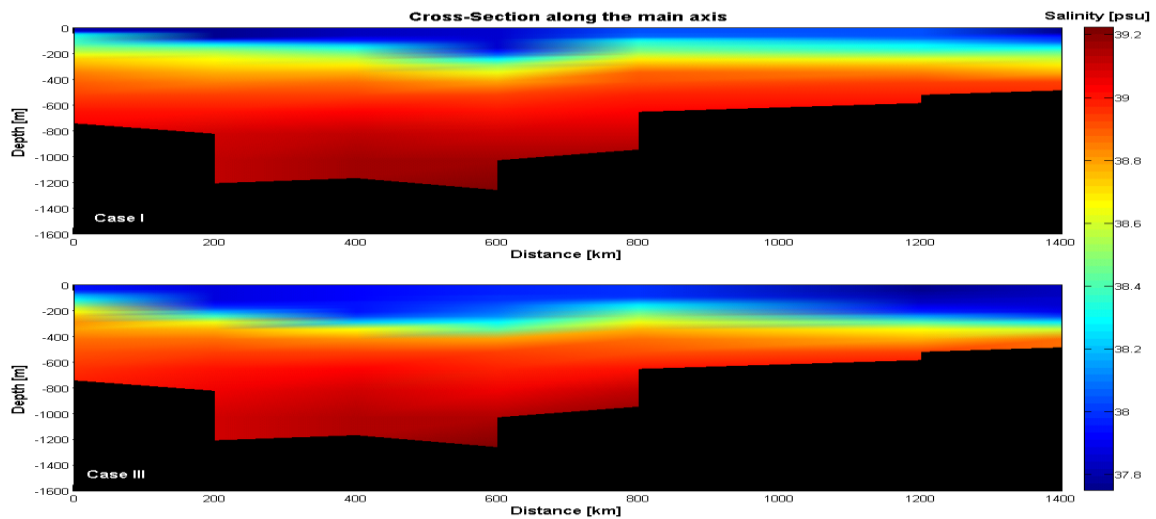


Figure 5.22 Effect of different values of wind drag coefficient on salinity distribution along the main axis of the model domain, RS-Model

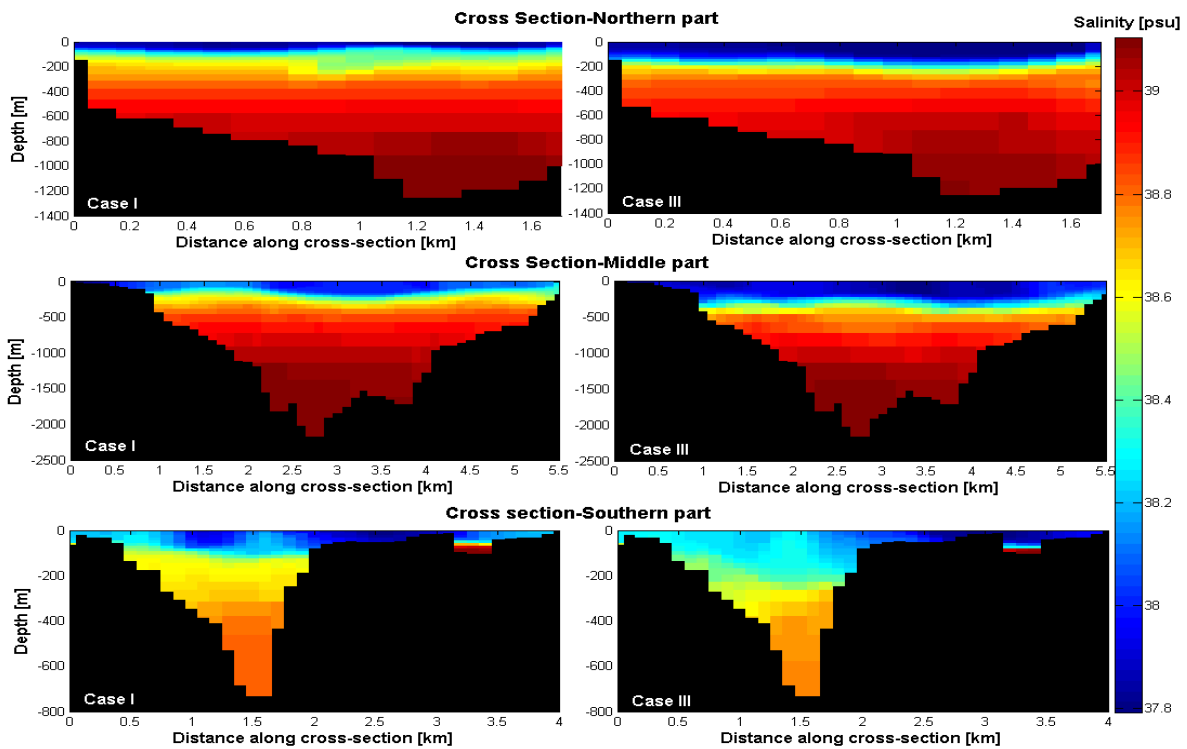


Figure 5.23 Effect of wind drag coefficient on salinity distribution over three cross-sections of the model domain, Northern, Middle and Southern part.

5.6.4.6 Effects of initial conditions

In the hydrodynamic modelling, one of the major challenges of the model set up is to achieve proper initial conditions particularly for temperature and salinity. The optimal way to start the simulation is to use initial conditions which are in dynamic equilibrium with all boundary conditions. Such conditions can be obtained from previous simulations which will support in reducing the warm up period of the model. Because when the model is started with other values, this leads to increasing the time to reach a dynamic equilibrium. During the warm up period, the model results consist of uncertainty. Therefore, it should be determined how much time is required to reach stable conditions with a cold start conditions and accordingly ignoring the erroneous data from that period. The time-scale to reach equilibrium state usually depends on the vertical diffusion of salinity and temperature (Bernsen et al., 2008).

In this study, two main types of initial conditions are required. The first is dynamic (water level and velocity) and the second is conservative constituents (salinity and temperature). For the conservative constituents, the initial conditions of salinity and temperature have been reproduced from SODA data (Simple Ocean Data Assimilation) at horizontal resolution of $0.5^\circ \times 0.5^\circ$, and 40 vertical levels. The temperature and salinity have been interpolated on the model grid with internal diffusion to assign a value of these parameters on every grid cell. Transport boundary conditions at the open boundary have been prescribed at fixed depth levels, the spacing of which increases with depth. This data is linearly interpolated to the model grid in both horizontal and vertical directions. Therefore, it is prescribed as vertical profiles. This implies that at the open boundary, temperature and salinity are prescribed with time and vertically varying data.

On the basis of simple scaling arguments, a 8-years period of simulation was considered for the model to spin-up. Assuming that the spin up period T_s is the time that momentum takes to travel from the surface to the thermocline through turbulent diffusion, then $T_s \approx h^2/k_z$, where h^2 the distance and k_z the vertical eddy diffusion coefficient (Bernsen et al., 2008). Accordingly, in the case of the Red Sea typical values of h and k_z are ~ 150 m and 10^{-4} m²/s, T_s is about 8 years. As starting point, the model was run for a period of one year and the last time step was saved in a restart file. Therefore, the last time step of the previous simulation was used for the rest of the simulations. Although this cannot be considered sufficient warming up period, starting with already existing results of previous model run leads qualitatively to less initialization effects with less warming up period. Using the restart file, the model was run for a period of eight years from 1st January 2000 until December 2008. Therefore, the results presented in this study include only the last year (2008) of the entire simulation since the results derived from the last year of a selected 8-year simulation showed reasonable agreement with observational evidence.

5.7 Validation of the RS-Model

5.7.1 Introduction

In this study, a hydrodynamic model has been setup covering the entire Red Sea, the Gulf of Aqaba, and Gulf of Suez. The model includes also part of Gulf of Aden with open boundary set at 48° E. As part of quality control, validation of the model is usually the final process of the development before the application. This process involves the verification of model results with measured data and also explains the model performance. As stated in chapter [2] the objective is to confirm the reliability and the quality of the model settings by considering other periods different than that used in the sensitivity analysis or in the calibration processes. However, the possibility to validate the model depends upon the quality of the available data. The availability and accessibility of field measurements is always a major issue in this regard especially in the case of the RS where there is lack of hydrographic observations. However, the model performance was evaluated using few available surface elevations at different locations along the eastern boundary and only one station positioned at the western side (port of SUDAN) of the Red Sea and salinity and temperature measurements which are available only for the summer season. Remotely sensed Sea Surface Temperature (SST) in addition to the available published documents was also considered. As mentioned previously in Chapter 2, during the validation processes the model parameters adopted in the calibration stage should not be modified. Therefore, the same parameters settings listed in Table 5.3 are considered.

In terms of water levels, the model performance was assessed by using hourly data of observed water levels recorded from tide gauge stations. The stations are located far enough from the open boundaries of the model domain and therefore, this will assist in testing the efficiency of the open boundary conditions. The evaluation of the model performance includes both graphical and statistical analyses. Two approaches were considered to evaluate the differences between model simulations and observations. In the first approach, the discrepancies are evaluated by computing the absolute difference mean (**ADM**) and root mean square differences (**RMSD**) between observed and simulated time series of water levels. In the second approach, the discrepancies in amplitude and phase of each astronomical component have been evaluated on the basis of the standard deviation of tidal analysis, the upper and lower extreme of the residuals and the so-called summed vector difference. The location of the observation points considered in the validation process are presented in Figure 5.7 while the period selected for this purpose is listed in Table 5.18. Note that the measured data used to validate the model covers different periods.

On the other hand, the model performance was assessed using *in situ* salinity and temperature measurements distributed along the main axis of the Red Sea. Remotely sensed sea surface temperature data from the AVHRR / Pathfinder was used due to its synoptic coverage which provides more complete picture about the temperature behaviour on seasonal scales. The AVHRR / Pathfinder data represents monthly mean temperature and has high spatial resolution of 4.9 km.

Table 5.18 Periods used for the RS-Model validation process

Station ID	Period I	Period II
ADEN	01/10/2008 to 31/10/2008	----
DJIBOUTI	01/10/2008 to 31/10/2008	----
JIZAN	01/02/2001 to 28/02/2001	01/04/2001 to 30/04/2001
SAROOM	01/07/2011to 31/07/2011	----
JEDDAH	01/02/2001 to 28/02/2001	01/04/2001 to 30/04/2001
OBHOR	01/07/2011 to 31/07/2011	----
RABIGH	01/02/2001 to 28/02/2001	01/04/2001 to 30/04/2001
DUBA	01/02/2001 to 28/02/2001	01/04/2001 to 30/04/2001

5.7.2 Validation in terms of Surface Elevations

This section presents the validation processes of the RS-Model by comparing the model results with the available measured water levels. Eight observation points are selected in the domain for the validation of tidal elevations on the basis of the available measurements. These points are named ADEN, DJIBOUTI, JIZAN, SAROOM, JEDDAH, OBHOR, RABIGH and DUBA. As specified in the second and third column in Table 5.18, two periods of measurements at some stations were selected to validate the model for surface elevations. At ADEN and DJIBOUTI stations, water levels of the period of 1st/10/2008 0:00hrs to 31st/10/2008 0:00hrs are available. At JIZAN, JEDDAH, RABIGH and DUBA water levels covering two periods of the year 2001 were selected, from 1st/02/2001 0:00hrs to the 28st/02/2001 0:00hrs and 1st/04/2001 0:00hrs to the 30st/04/2001 0:00hrs. From the new installed devices of tide gauges in the vicinity of JEDDAH coastal waters, water levels at SAROOM and OBHOR stations for the period from 1st/07/20110:00hrs to 31st/07/20110:00hrs were chosen. The length of all the time series water levels represents an entire neap-spring tidal cycle.

Period I: 1st to 31st of October-2008

Figure 5.24-A and 5.25-A show the measured water level time series plotted with the modelled results for the ADEN and DJIBOUTI stations. The absolute difference (residual) between the measured and modelled water levels is presented in the bottom of the same figures (5.24 and 5.25-B-Green colure). Note that the residual water level includes both the discrepancies in amplitude and in phase between the tidal signals. Consequently, it is considered to be primarily a basic measure for the performance of the model. In general, the Figures reflect a good agreement between the modelled and measured water levels at both stations. However, the model underestimates the high and low water amplitudes during spring and neap tide. On the other hand, phase conditions (occurrence time) of high and low water are in good agreement with observed data. Statistical analysis of the discrepancies in terms of absolute difference mean (**ADM**) and root mean square differences (**RMSD**) is given in section 5.7.2.1.

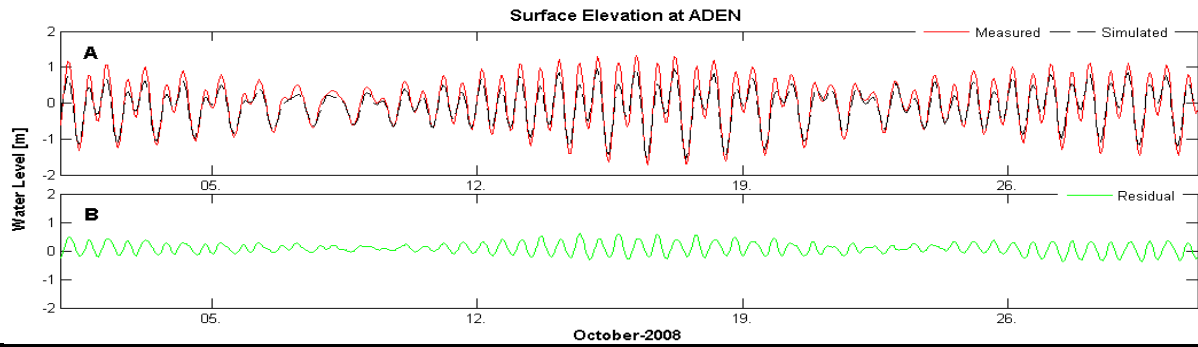


Figure 5.24 (A) Comparison of measured and simulated water levels at ADEN Station, 01st to 31st of October-2008; (B) is the residual.

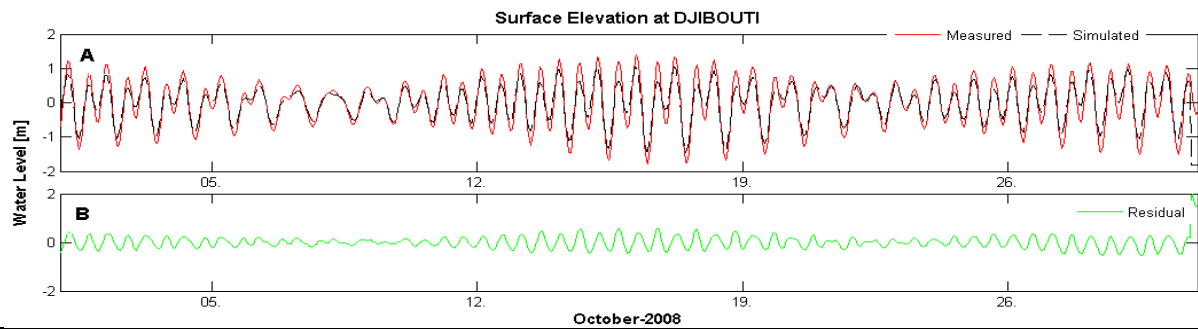


Figure 5.25 (A) Comparison of measured and simulated water levels at DJIBOUTI Station, 01st to 31st of October-2001; (B) is the residual.

Period I: 1st to 28st of February-2001

In this period, surface elevation records from the tidal gauges at JIZAN, RABIGH and DUBA have been compared with the model simulations. Figures 5.26-A through 5.28-A show the measured water level time series plotted against the modelled results for the three mentioned observation points. The absolute difference (residual) between the measured and modelled water levels is presented in the bottom of the same figures (5.26, 5.27 and 5.28-Bs-Green colour). In general, a good agreement between the modelled and measured results is observed. From the figures, it is obvious that the model slightly underestimates the low water amplitudes during spring tide while the high water amplitudes in a good agreement with the measurements at JIZAN and DUBA monitoring points. On the other hand, the model predictions at RABIGH stations are showing larger discrepancies. This is most probably due to wind effects as this simulation was carried out without wind conditions.

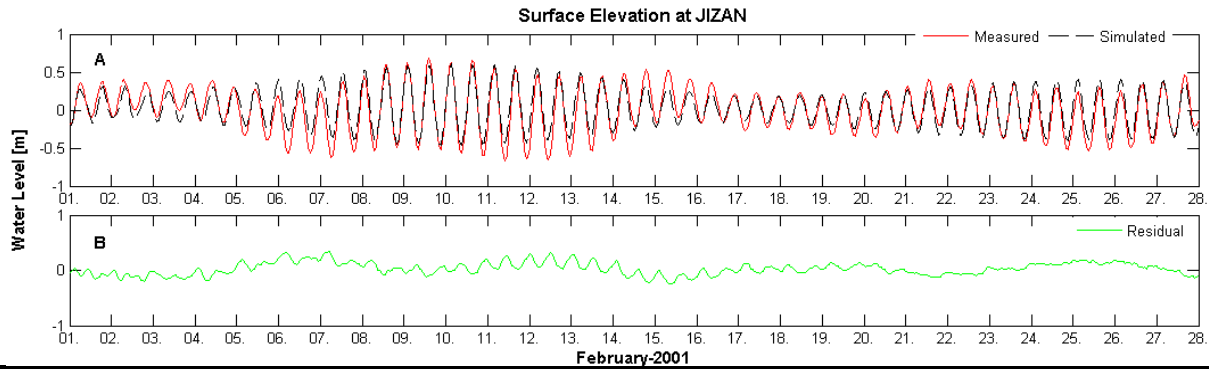


Figure 5.26 (A) Comparison of measured and simulated water levels at JIZAN Station, 01st to 28st of February-2001; (B) is the residual.

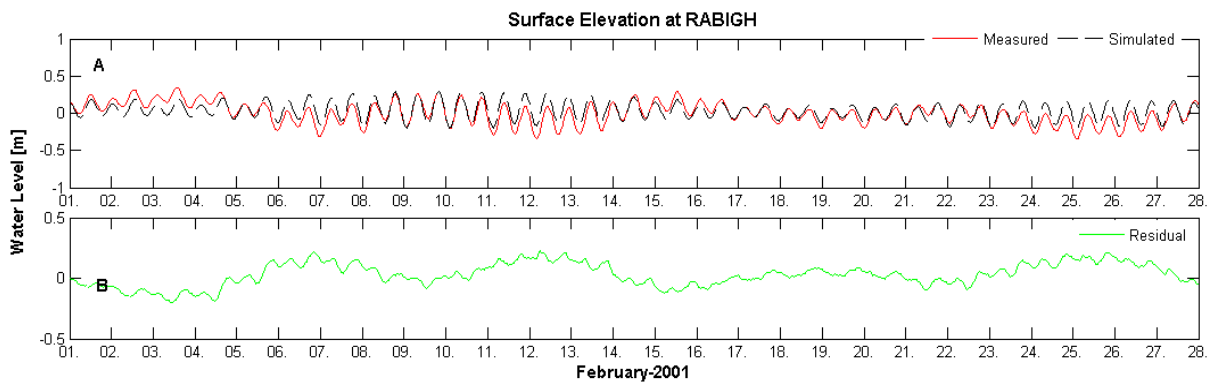


Figure 5.27 (A) Comparison of measured and simulated water levels at RABIGH Station, 01st to 28st of February-2001; (B) is the residual.

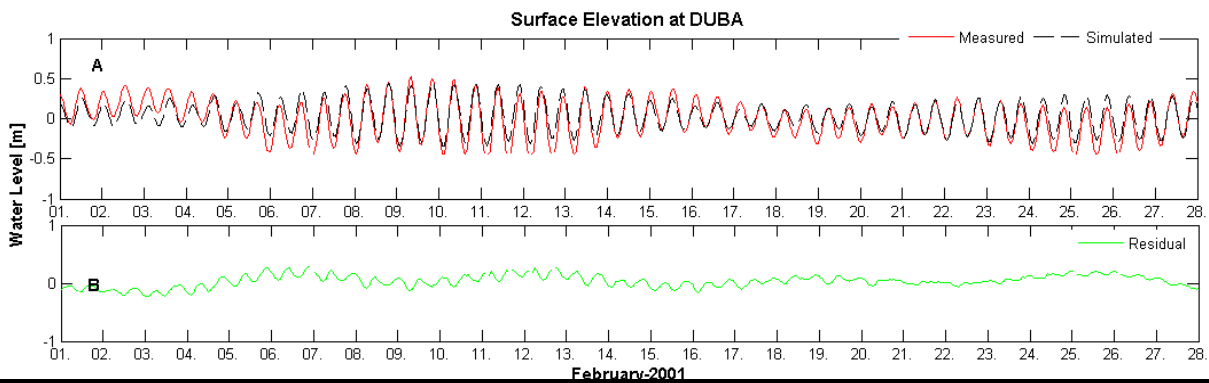


Figure 5.28 (A) Comparison of measured and simulated water levels at DUBA Station, 01st to 28st of February-2001; (B) is the residual.

Period I: 01st to 30st of April 2001

In this period, the simulated water level is compared with the measurements obtained from JIZAN, JEDDAH, RABIGH and DUBA tidal stations. Figure 5.29-A through 5.32-A present comparisons between predicted and measured surface elevations. It can be seen that the simulated results basically in good agreement with the observations. An acceptable estimation of spatial distribution of water levels was observed. The discrepancies (residual) in amplitude and in phase between the tidal signals are shown in the lower Figures (5.29

through 5.32-Bs- Green colure). Model predictions at JIZAN and DUBA monitoring points, during spring-neap tide conditions are in a good agreement with the measurements. Both high and low water levels are reproduced with good accuracy by the model, however, with slight underestimation of high water amplitudes at DUBA during neap tide. Predicted tidal phases were also in good agreement with measured data. On the other hand, at JEDDAH and RABIG stations larger discrepancies are observed between the periods of 3 to 8-2001.

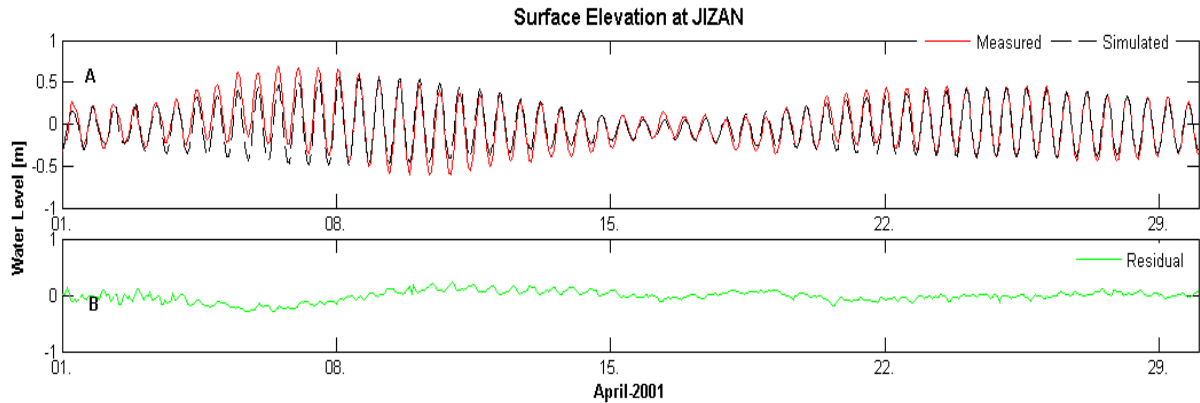


Figure 5.29 (A) Comparison of measured and simulated water levels at JIZAN Station, 01st to 30st of April-2001 (B) is the residual.

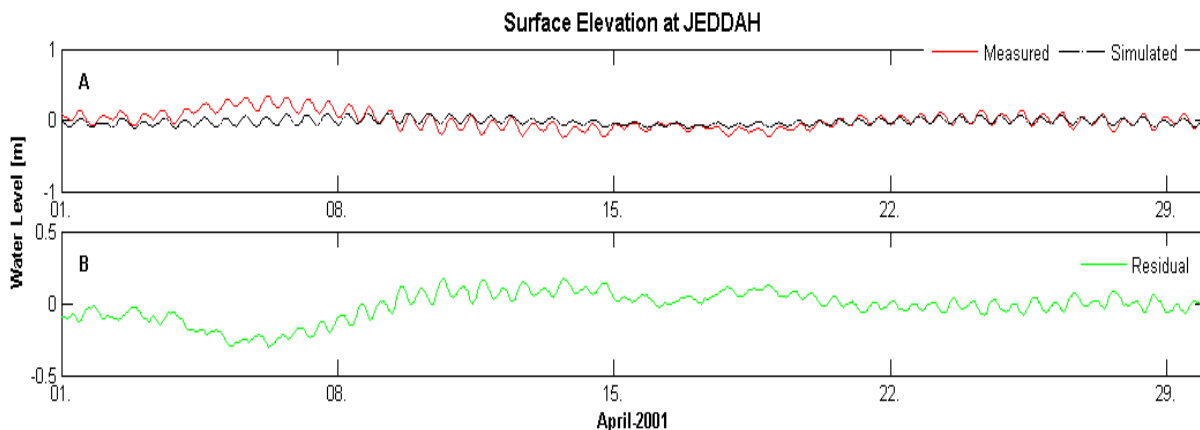


Figure 5.30 (A) Comparison of measured and simulated water levels at JEDDAH Station, 01st to 30st of April-2001 (B) is the residual.

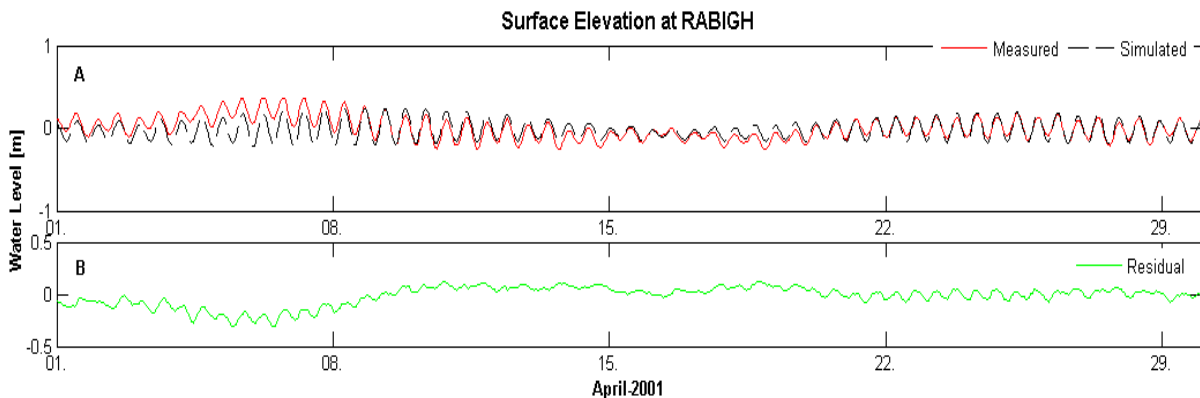


Figure 5.31 (A) Comparison of measured and simulated water levels at RABIG Station, 01st to 30st of April-2001, (B) is the residual.

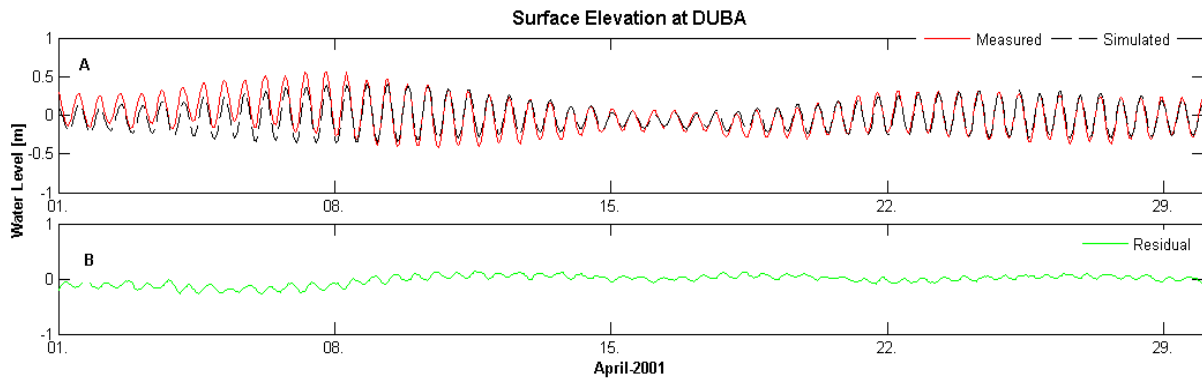


Figure 5.32 (A) Comparison of measured and simulated water levels at DUBA Station, 01st to 30st of April-2001, (B) is the residual.

Period II: 1st to 31st of July 2011

In this period, surface elevation records from the tidal gauges at Obhor Creek and Saroom stations are compared with the model simulations. Figures 5.33-A and 5.34-A show the measured water level time series plotted with the modelled results. The absolute difference (residual) between measured and modelled water levels is presented in the same figures (5.36 and 5.37-Bs Green colour). Graphically, a good agreement between the modelled and measured results is observed. From the figures, it is obvious that the model slightly underestimates the low water amplitudes while the high water amplitudes is in good agreement with the measurements at OBHOR and SAROOM monitoring points. Although the visual comparisons showed that the hydrodynamic model of the Red Sea (RS-Model) is able to reproduce the water levels in the Red Sea reasonably well, the need for more specific measures and assessments of the model is indispensable. Therefore, to quantify the differences between the tidal signals obtained from simulations and the measurements for all the periods considered in the validation, a statistical analysis was performed. Statistical analysis of the discrepancies in terms of absolute difference mean (ADM) and root mean square differences (RMSD) is given in next section.

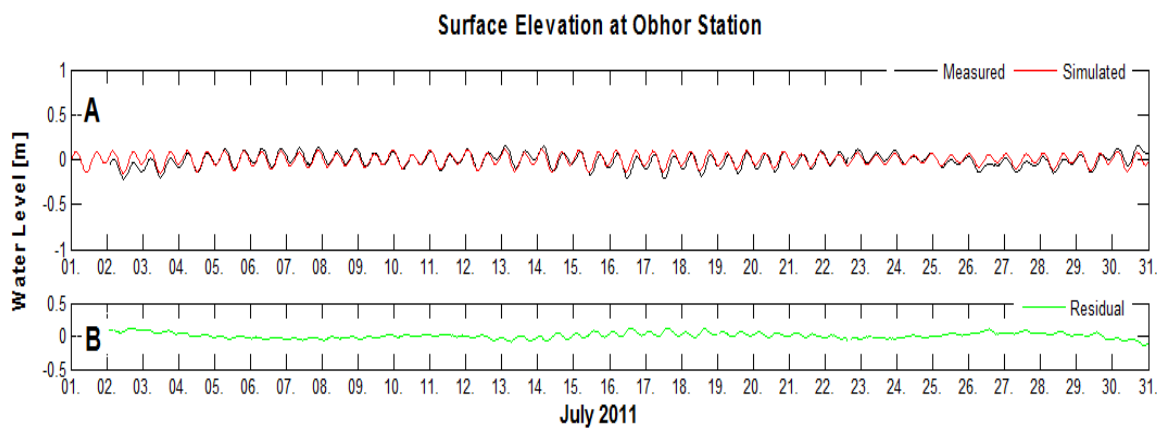


Figure 5.33 (A) Comparison of measured and simulated water levels at Obhor Creek station, 1st to 31st of July 2011, (B) is the residual.

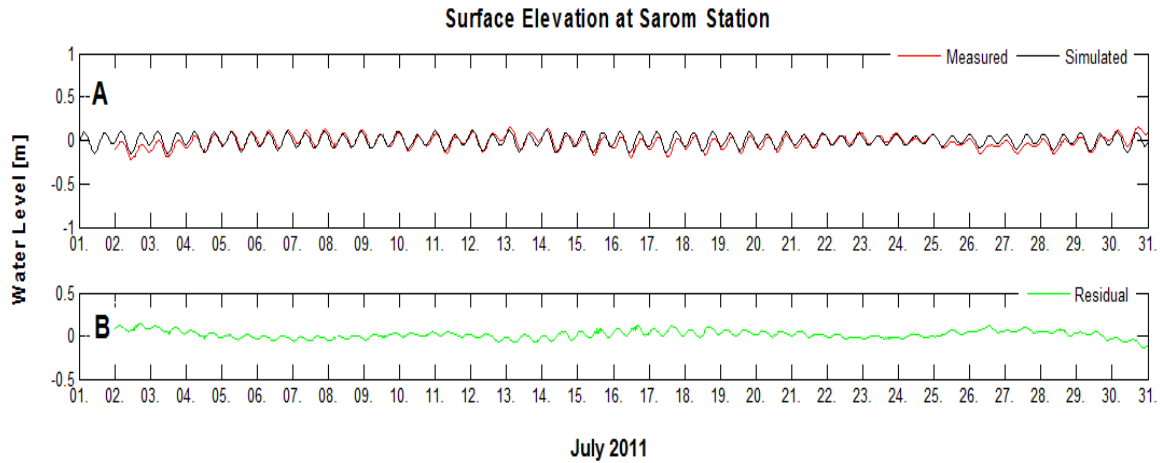


Figure 5.34 (A) Comparison of measured and simulated water levels at Sarom Station, 1st to 31st of July 2011 (B) is the residual.

5.7.2.1 Statistical analysis of the residual water level

In the previous section, the result of qualitative comparisons between model results and observed surface elevations are presented. Graphically, it was found that the model results are in a good agreement with the measurements. However, to complete the picture and provide more details about the overall accuracy of the model performance, a statistical analysis of the discrepancy between measured and modelled water levels (residual water level) is carried out.

In several studies, a number of researchers suggest that the goodness of hydrodynamic models can be determined by calculating the absolute difference mean (**ADM**) and root mean square differences (**RMSD**) between observed and simulated (see for example Hsu *et al.*, 1999).

The absolute differences mean (**ADM**) is defined as the mean of the absolute values of all differences between simulated and observed values. **ADM** is expressed as the following:

$$ADM = \frac{1}{n} \sum_{1}^{n} Abs (Simulated - Observed)$$

The Root Mean Square Difference (**RMSD**) between observed and modelled values is computed by summing the square of the difference between the two, then taking the square root of the total and dividing it by the number of records (n). **RMSD** is written as:

$$RMSD = \sqrt{\frac{1}{n} \sum_{1}^{n} (Simulated - Observed)^2}$$

Where: n is the number of records.

Both **ADM** and **RMSD** parameters were computed to provide a measure of discrepancy between measured and simulated values. Table 5.19 presents a summary of the statistical evaluation of the residual water levels. Statistical parameters have been determined for the visual interpretation of Figure 5.24-5.25 and 5.29 to 5.34 respectively.

As can be seen from the table, RMS error for all stations located in the Red Sea region vary from 0.08 to 0.1 meter, while the ADM value resulted equal to 0.07 meter at JIZAN, RABIGH and DUBA stations and 0.08 meter at OBHOR and SAROOM stations. The mean discrepancies in water levels resulted in the range of 0.1 meter. On the other hand, RMSE for ADEN and DJIBOUTI stations shows larger discrepancies in the range of 0.2 meter. In general, the tidal model of the Red Sea is performing well.

Table 5.19 Statistical analysis of the model validation based on Root mean square difference and absolute difference mean.

Station ID	Root Mean Square Difference (RMSD) in meter	Absolute Difference Mean (ADM) in meter
ADEN	0.20	0.17
DJIBOUTI	0.26	0.19
JIZAN	0.08	0.07
JEDDAH	0.10	0.07
RABIG	0.09	0.07
DUBA	0.08	0.07
OBHOR Creek	0.10	0.08
SAROOM	0.10	0.08
Mean	0.11	0.1

5.7.2.2 Analysis in Terms of Harmonics

In this section, tidal analysis of the simulated water levels is presented. The model results have been compared with the astronomical constituents obtained from the tidal analysis of the measurements. In this regard, the model was run for one year and the results were used to perform the tidal analysis. Tidal analyses have been performed to provide only the main diurnals (Q_1 , O_1 , P_1 , and K_1) and semidiurnal constituents (N_2 , M_2 , S_2 , and K_2). The water level predictions have been analysed by Delft3D-TRIANA program to derive tidal constants and compare with the tidal constants obtained from the tidal analysis carried out at the same locations JIZAN, JEDDAH, RABIGH and DUBA. An overview of the results obtained at the stations JIZAN, JEDDAH, RABIGH and DUBA is presented in Table 5.20, 5.21, 5.22 and 5.23 respectively. Notation in the table: H_c : Computed amplitude, H_o : observed amplitude, G_c : computed phase, G_o : observed phase, $H_c - H_o$: amplitude difference, $G_c - G_o$: Phase difference, H_c / H_o : Amplitude ratio.

From the Tables, it can be seen that the computed and observed amplitudes and phases in general are in good agreement. For instance, for M_2 the amplitude error ($H_c - H_o$) is in order of 3 and 5 cm at JIZAN and DUBA station, respectively. However, the major discrepancies were observed in relation to phase lag. The larger difference computed for the phase of the tidal constituents was observed for M_2 and K_2 tide, while N_2 and S_2 tide on average compared to M_2 and K_2 tide showing minor discrepancies. The discrepancies could be attributed to the model bathymetry. The performance of a numerical model depends highly upon accurate representation of the sea bottom levels. The bathymetry of the model was basically based on a deep water data which does not include detailed bathymetry for shallow shelf water. Therefore, such discrepancies are expected.

The standard deviation of tidal analysis, the upper and lower extreme of the residuals and the so-called summed vector difference are also considered. The summed vector difference is given as:

$$\sum_{Obs} \sqrt{[H_c \cos(G_c) - H_o \cos(G_o)]^2 + [H_c \sin(G_c) - H_o \sin(G_o)]^2}$$

In which \sum_{Obs} refers to a summation over the stations with observed amplitude and phase

It was found that the maximum standard deviation of the tidal analysis is in the range of 0.09. An overview of the results obtained at the stations JIZAN, JEDDAH, RABIGH and DUBA is presented in Table 5.24. The so-called summed vector difference, which is a measure for the total error for all components, is about 0.1, 0.075, 0.17 and 0.076 m respectively at DUBA, RABIGH, JIZAN and JEDDAH. In conclusion, it can be stated that there is a satisfactory agreement for both diurnal and semidiurnal and the results have shown that the model reproduces the tidal wave propagation in the Red Sea with a good accuracy.

Table 5.20 Tidal amplitudes and phases of observed and computed tidal constituents at JIZAN

Constituents	H_o	H_c	G_o	G_c	$H_c - H_o$	$G_c - G_o$	H_c / H_o
M_2	0.324	0.360	196.0	224.1	0.036	28.112	1.110
S_2	0.104	0.127	70.0	79.12	0.023	9.126	1.225
N_2	0.103	0.121	101.6	101.3	0.018	-0.300	1.175
K_2	0.037	0.041	219.0	255.4	0.004	36.441	1.120
K_1	0.014	0.006	160.7	100.7	-0.008	-60.25	0.460
O_1	0.016	0.004	183.0	258.3	-0.012	-14.511	0.725
P_1	0.006	0.001	235.4	180.1	-0.005	-55.25	0.085
Q_1	0.004	0.001	304.6	294.1	-0.003	-10.48	0.310

H_o : amplitude of observed tide, G_o : phase of observed tide, H_c : amplitude of modelled tide, G_c : phase of modelled tide, $H_c - H_o$: amplitude difference, $G_c - G_o$: Phase difference, H_c / H_o : Amplitude ratio.

Table 5.21 Tidal amplitudes and phases of observed and computed tidal constituents at JEDDAH

Constituents	H_o	H_c	G_o	G_c	$H_c - H_o$	$G_c - G_o$	H_c / H_o
M_2	0.068	0.051	358.8	23.85	-0.017	25.05	0.756
S_2	0.016	0.013	242.5	221.1	-0.003	-21.35	0.825
N_2	0.025	0.020	256.7	249.7	-0.005	-6.940	0.794
K_2	0.009	0.004	126.9	118.6	0.005	8.278	0.454
K_1	0.036	0.035	192.3	196.6	-0.001	4.310	0.959
O_1	0.020	0.016	20.5	27.23	-0.004	6.730	0.823
P_1	0.013	0.005	213.7	247.3	-0.008	33.57	0.351
Q_1	0.004	0.004	304.0	317.0	0.000	13.00	0.919

H_o : amplitude of observed tide, G_o : phase of observed tide, H_c : amplitude of modelled tide, G_c : phase of modelled tide, $H_c - H_o$: amplitude difference, $G_c - G_o$: Phase difference, H_c / H_o : Amplitude ratio.

Table 5.22 Tidal amplitudes and phases of observed and computed tidal constituents at RABIGH

Constituents	H_o	H_c	G_o	G_c	$H_c - H_o$	$G_c - G_o$	H_c / H_o
M_2	0.107	0.086	5.1	20.49	-0.021	15.398	0.802
S_2	0.028	0.025	246.9	231.5	-0.003	-15.34	0.898
N_2	0.036	0.032	265.7	255.4	-0.004	-10.332	0.876
K_2	0.012	0.008	29.60	47.42	-0.004	17.822	0.657
K_1	0.032	0.037	194.4	196.7	0.005	2.318	1.170
O_1	0.019	0.018	28.8	27.25	-0.001	-1.548	0.926
P_1	0.011	0.005	224.5	247.4	-0.006	22.869	0.449
Q_1	0.004	0.004	301.9	317.0	0.000	15.147	0.978

H_o : amplitude of observed tide, G_o : phase of observed tide, H_c : amplitude of modelled tide, G_c : phase of modelled tide, $H_c - H_o$: amplitude difference, $G_c - G_o$: Phase difference, H_c / H_o : Amplitude ratio.

Table 5.23 Tidal amplitudes and phases of observed and computed tidal constituents at DUBA

Constituents	H_o	H_c	G_o	G_c	$H_c - H_o$	$G_c - G_o$	H_c / H_o
M_2	0.245	0.217	4.3	31.18	-0.028	26.88	0.883
S_2	0.075	0.072	229.0	244.1	-0.03	15.13	0.960
N_2	0.074	0.075	267.7	266.0	0.001	-1.672	1.010
K_2	0.023	0.023	20.6	60.40	0.000	39.801	0.995
K_1	0.038	0.048	155.3	199.7	0.010	44.43	1.269
O_1	0.012	0.022	32.3	29.81	0.010	-2.489	1.811
P_1	0.002	0.006	78.8	250.3	0.004	171.53	2.935
Q_1	0.003	0.005	338.8	319.6	0.002	-19.215	1.589

H_o : amplitude of observed tide, G_o : phase of observed tide, H_c : amplitude of modelled tide, G_c : phase of modelled tide, $H_c - H_o$: amplitude difference, $G_c - G_o$: Phase difference, H_c / H_o : Amplitude ratio.

Table 5.24 statistical analysis derived from Delft3D-TRIANA

Parameters	Station ID			
	JIZAN	JEDDAH	RABIGH	DUBA
Standard deviation of tidal Analysis	0.027	0.022	0.024	0.024
Lower extreme for residuals	-0.082	-0.054	-0.062	-0.061
Upper extreme for residuals	0.080	0.054	0.068	0.069
Summed vector differences	0.170	0.076	0.075	0.102

5.7.3 Validation in terms of Salinity and Temperature

In this section, the RS-Model is validated in terms of temperature and salinity predictions. On the one hand, the performance of the model was assessed using CTD measurements. The type of data is instantaneous salinity and temperature vertical profiles recorded using CTD device. On the other hand, monthly mean sea surface temperature (SST) produced by the RS-Model was compared to time series of remotely sensed SST fields. The latter comparison is useful since it reflects the performance of the model in temporal scale where there are no available in situ measurements for different seasons.

For the remotely sensed data, these data obtained from the Advanced Very High Resolution Radiometer (AVHRR / Pathfinder datasets) satellite data. The datasets combines data from a number of NOAA AVHRR satellites. Their selection in this study was based on its high temporal (24 hrs) and spatial resolution (4.9 km), in addition to substantial coverage period (1985-present) (Barton, 1998).

It should be mentioned that this data represents the temperature of the upper 1 meter of water and the surface layer thickness specified in the RS-Model is 5 metre. Therefore, discrepancies between the RS-Model and AVHRR / Pathfinder SST expected to occur.

5.7.3.1 Validation for Temperature and Salinity profiles

In this section, validation of RS-Model predictions and field measurements in terms of temperature and salinity is carried out. In order to validate temperature and salinity predicted by the hydrodynamic model, comparisons between measurements and model predictions were made at various sites along the main axis of the Red Sea. Using the forcing terms mentioned previously in Chapter5 (heat flux and atmospheric wind and pressure forcing, water level and lateral transport forcing at the open boundary), the RS-Model is able to reproduce the vertical structure of temperature and salinity profiles satisfactorily.

Figure (5.35) shows the comparisons of vertical profiles between observed and simulated temperature and salinity at 6 oceanographic stations positioned along the main axis of the Red Sea. In General, the temperature and salinity profiles produced by the RS-Model exhibit similar profiles constructed from the CTD data with acceptable accuracy. The thermal stratification is reproduced almost correctly by the model. In contrast, the salinity concentrations are slightly low compared to the temperature gradient. It was observed that the RS-Model tends to underestimate salinity values at sites A and B at the surface while there is a good agreement at site C, D, E and F respectively. Although qualitatively the model reflects underestimation of salinity, the discrepancies of salinity values at the surface and also below 100 m depth are in the range of or even below 0.5 ppt.

On the other hand, some discrepancies in the position of the haline layer can be observed, even though the general trend of the profiles is similar. Temperature and salinity at any location in the ocean are complicated functions of depth and time, involving periodic and unsystematic components. The competition between the processes involved in mixing and stratification is complex and difficult to reproduce in numerical model accurately (Bermudez at al. 2013). For instance, each profile in Figure (5.35) represents a different instant of time within the selected period and therefore, corresponds to a different tidal level. However, there is satisfactory agreement between the model results and observations. Therefore, it can be concluded that the RS-Model resolves the vertical structure of salinity and temperature adequately.

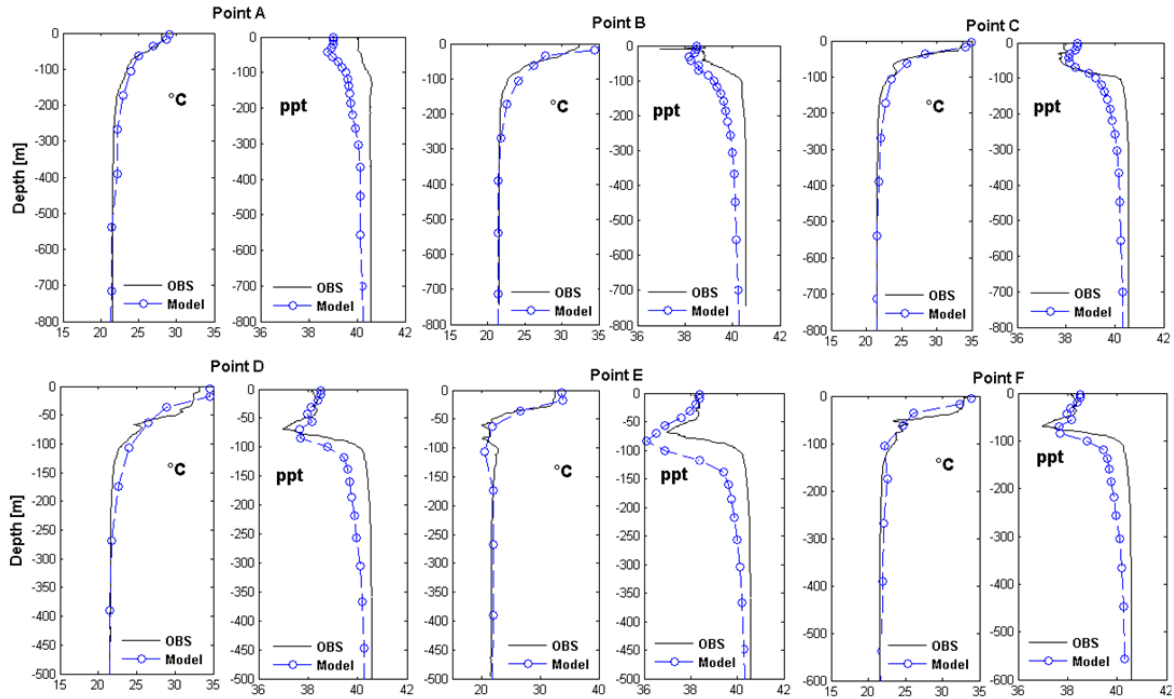


Figure 5.35 Vertical profiles of observed and simulated temperature & salinity at locations A, B, C, D, E and F (see Figure 5.23 for positions)

5.7.3.2 Comparison of RS-Model Sea Surface Temperature (SST) with AVHRR Pathfinder

In this section, remotely sensed SST fields obtained from the Advanced Very High Resolution Radiometer (AVHRR / Pathfinder datasets) satellite data are used to assess the model surface temperature variability on temporal and spatial scale. Monthly mean sea surface temperature (SST) data are compared with the results of the RS-Model simulations. Figure 5.36 and 5.37 show comparisons between the data of AVHRR/Pathfinder and simulated SST for the months January and July respectively. In Chapter 3, these months are identified to correspond with the NE and SW monsoon events. In general, the simulation results are consistent with the satellite data (AVHRR/Pathfinder SST). The satellite data confirm the remarkable differences in predicted SST between seasons. The RS-Model simulates the remotely sensed SST field over the winter fairly well (Figure 5.36), reflecting the main spatial features.

It is obvious that there is a zone in the middle part of the Red Sea (16° N- 21° N) characterized by high sea surface temperature during winter time. This is due to the weak wind velocity in this region where the wind condition is convergent for most of the year. A remarkable feature during winter season is the downwelling events occurring along the eastern boundary between Latitude 16° N and 20° N which is evident in the AVHRR/Pathfinder SST. It can be seen that the coldest SST takes place in the northern part of the Red Sea; however, in the AVHRR/Pathfinder the cold surface region extends further South than the RS-Model (Figure 5.36). There are two interpretations for these results. On the

one hand, it could be that the RS-Model overestimates the magnitude or extend of the southward flowing. On the other hand, it could be that the RS-Model overestimates the eddy diffusivity and/or eddy viscosity which play a role in making the boundary currents narrower and concentrate temperature near the boundaries as observed in the sensitivity analysis (see Appendix 3). During summer period, the entire Red Sea basin becomes very warm as shown in the Figure (5.37). The major pattern produced by the RS-Model in this period is that the SST is higher on the western boundary than the eastern one. The simulated SST is also consistent with the satellite SST to some degree however; the features present on the western boundary north of 24°N are not seen in the AVHRR/Pathfinder SST. This pattern of warmer water is associated with boundary currents that transports warm water as also was observed by previous modelling study of Sofianos and Johns (2003). The pattern in the southern part and the strait for both seasons is associated with the exchange processes with the Gulf of Aden. Based on these comparisons, it can be concluded that the RS-Model resolves the large-scale surface temperature cycle to a reasonable degree.

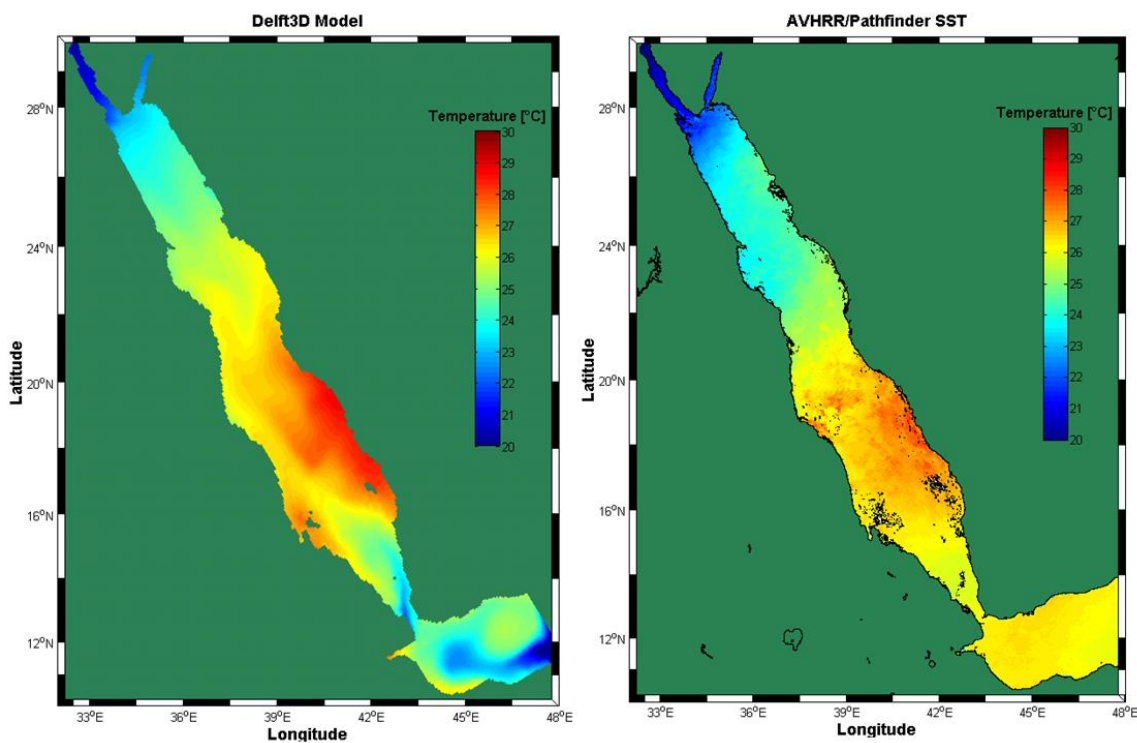


Figure (5.36) Comparison of simulated (left) and satellite AVHRR Pathfinder (right) of SST, January.

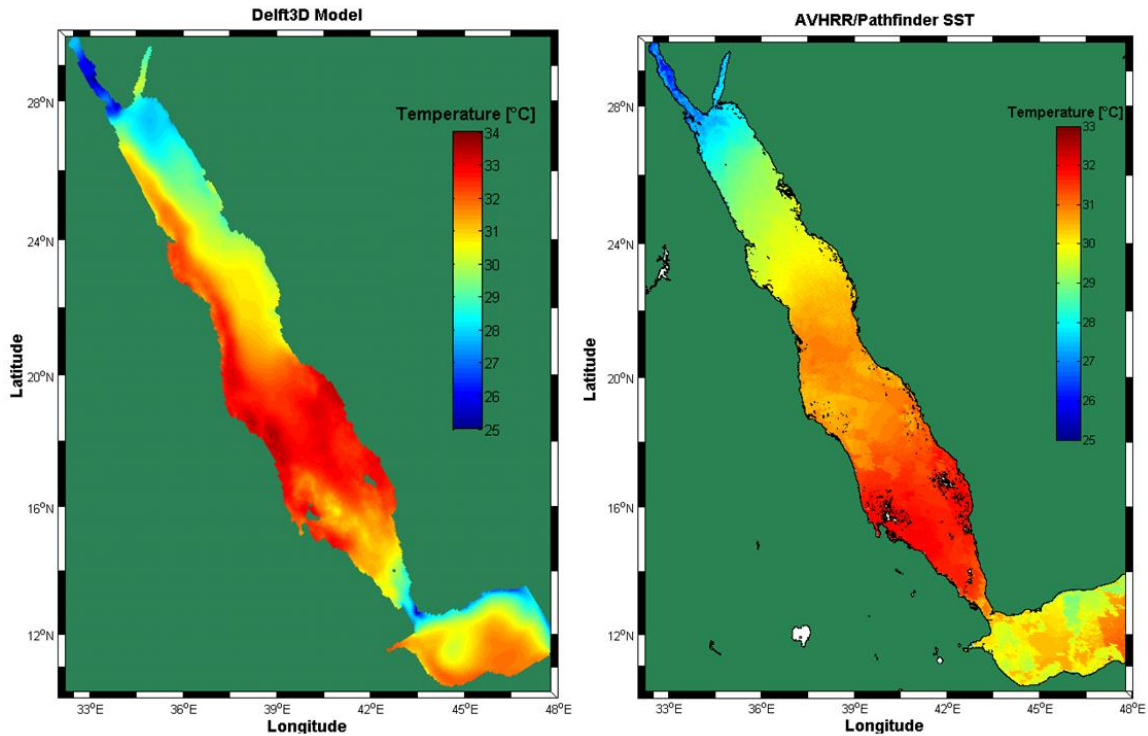


Figure (5.37) Comparison of simulated (left) and satellite AVHRR Pathfinder (right) of SST, July.

To assess the model surface temperature variability on temporal and spatial scale, remotely sensed SST (AVHRR / Pathfinder datasets) are used. A comparison of monthly mean SST produced by the RS-Model simulations and SST of AVHRR / Pathfinder is shown in Fig. 5.38 (a-d). It should be noted that remotely sensed SST represents the upper 1 meter of water whereas the surface layer thickness in the RS-Model is 5 m. Thus some discrepancies are expected. Nevertheless, a good agreement was observed between the SST predictions and remotely sensed SST. The RS-Model simulations showed an increase in temperature from minimum values in winter to maximum values in summer. A similar trend of variations is evident in the remotely sensed SST datasets. Therefore, the RS-Model results are in harmony with the remotely sensed SST field over the winter season, reflecting the main spatial features.

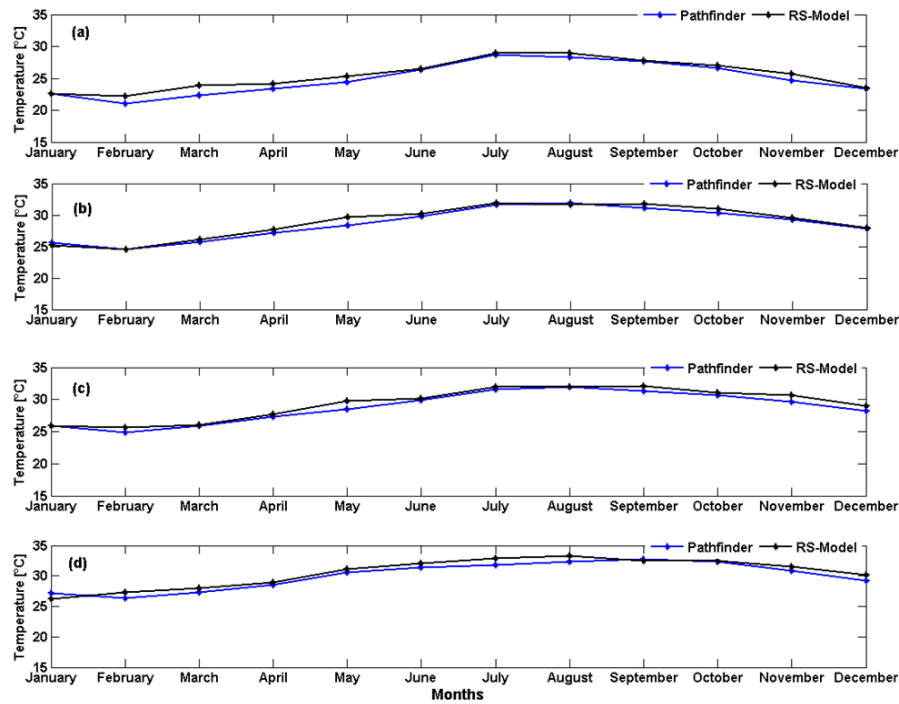


Figure (5.38) Comparison of average monthly modelled and remotely sensed (AVHRR / Pathfinder) SST at different locations, (a), extreme northern part, (b) middle part and (c,d) southern part of the Red Sea.

5.8 Conclusion

In this chapter, the setup, sensitivity analysis and validation processes of the 3-dimensional RS-Model are presented. The computational domain of the RS-Model covers the entire Red Sea (Lon 32° to 48° E & Lat 10° to 30° N), the Gulf of Suez and the Gulf of Aqaba and includes part of the Gulf of Aden. The model domain was schematized on a rectilinear mesh oriented NNW and SSE following the main axis of the Red Sea, with a horizontal uniform grid spacing of approximately $\Delta x = \Delta y = 5$ km. The vertical grid discretization was implemented using z -coordinate system. The advantage of using z -coordinate system over σ – coordinate system is that the Z –grid has horizontal lines that are almost parallel with density interfaces (isopycnals) especially in regions with steep bottom slopes which is important in the case of the Red Sea to avoid horizontal pressure gradients errors associated with σ – coordinate.

The water column is resolved by 30 vertical layers with 15 of these layers concentrated in the upper 200 m. Thus adequately higher resolution was kept at the surface in order to capture the dynamic of the upper ocean. The bathymetric data of the RS-Model were sourced from the global bathymetry dataset for the world ocean “GEBCO_08 Grid” at a 30 arc-second horizontal resolution (~ 1 km). Due to insignificant artificial contact between the Red Sea and the Mediterranean via Suez Canal, the model has only one open boundary was set at the Gulf of Aden at longitude (48° E) and divided into 25 segments (Figure 5.2).

The eastern ocean open boundary (at 48° E) of the RS-Model is forced by the main eight semidiurnal and diurnal (M_2 , S_2 , N_2 , K_2 , K_1 , O_1 , P_1 , and Q_1) tidal constituents.

In terms of transport forcing, the eastern open boundary is controlled by temperature (T) and salinity (S) and velocities components (u , v) obtained from Simple Ocean Data Assimilation (SODA) at every five days intervals. The 3-D RS-Model was initialized with SODA data and the grid cells with missing data were filled by internal diffusion interpolation. The surface boundary of the RS-Model is forced by realistic high-frequency atmospheric forcing (i.e. winds and surface heat fluxes) derived from DWD at spatial resolution of $1.5^\circ \times 1.5^\circ$ with 6 hourly intervals. The optimal settings of the numerical model were determined based on sensitivity analyses.

The 3-D RS-Model was validated against available surface elevations data throughout the model domain. In this regard, discrepancies between the model results and available observations have been determined qualitatively and statistically. Statistical parameters include the absolute mean error (AME) and the root mean square error (RMSE). It was observed that the model predictions and observations of water levels are in very good agreement. The model is reproducing large scale tidal surface elevations within the Red Sea region and clearly provides a reasonable prediction of both the phases and amplitudes of the spring and neap tide.

On the other hand, the performance of the RS-Model in terms of temperature and salinity vertical profiles was assessed by using CTD observations and also by using remotely sensed data. It was observed that there is fair agreement with the observations. Comparison of SST produced by the RS-Model with remotely sensed SST fields (AVHRR Pathfinder SST) also showed acceptable agreement.

Further evaluation was conducted to test the ability of the hydrodynamic RS-Model in reproducing the seasonal variability. It was found that the model is able to reproduce the documented main hydrodynamic features at Bab el Mandeb strait quite well. These features are the reversal processes of the surface flow (SW), subsurface intrusion of Gulf of Aden Intermediate Water (GAIW) and the seasonal variability of the RSOW outflow. Moreover, the cyclonic and anticyclonic gyres observed by several investigators (Morcos, 1970; Morcos and Soliman, 1974; Maillard, 1974) at the extreme north and the anticyclonic eddy feature observed very recently in the central part of the Red Sea by (Bower *et al.*, 2013) were also resolved by the RS-Model. The RS-Model is also able to predict the large eddy (anticyclones) exist in the Gulf of Aden reported by William *et al.* (1999) (for more details about these features, see chapter 7). These major features predicted by the model reflect the predictive capability of the model. Therefore, the RS-Model can be used to study the tide, circulation and thermohaline processes in the Red sea region.

Chapter 6

Simulation of Tides in the Red Sea

6.1 Introduction

As already stated in Chapter 3 there is very little published information regarding tidal characteristics in the Red Sea region. The earlier works on tides were basically limited to observations which are confined to the coastal region. Moreover, during the last century, the tides in the Red Sea have been described based on a few analytical analyses carried out in order to determine the tides in the strait of Bab el Mandeb. The results of these analyses were used to provide a dynamical explanation of the tides in the entire Red Sea basin. On the other hand, studies on tides based on numerical modelling approach do not exist. Considering the advantages of using a numerical modelling approach, the development of a numerical model and its application maybe a good method to carry out such study and provide a comprehensive picture about the tidal characteristics in the Red Sea. Consequently, it is of interest to carry out a study of tides in the Red Sea using a modelling approach. Two dimensional models, namely the depth-averaged or shallow water models, can be successfully applied for simulating tidal flow and flows of water bodies.

As a first step towards simulating the tides in the Red Sea, development of a model driven by tides is considered. This is followed by efficient validation of the model with available surface elevation records in the region. In the previous chapter, the tidal model was setup, calibrated and validated. In the validation of the hydrodynamic model it was shown that the model results are in good agreement with available observations. Accordingly, the model was utilized to study the tidal characteristics in the study area.

This chapter focuses on tidal characteristics in the Red Sea region by using the 2-D RS-Model and analysing its results. Section (6.2) gives a brief view about RS-Model including the domain coverage, boundary conditions and physical settings. This is followed by describing the tidal characteristics in the Red Sea based on the model results including the procedures considered to generate the co-range and co-tidal charts in section (6.3). In section (6.4), the relative importance of the semidiurnal and diurnal tidal constituents is determined based on the form factor. After that, the hydrodynamic features are presented in section (6.5). Section (6.6) throws light on the conclusion of this chapter.

6.2 RS-Model

The RS-Model domain covers the entire Red Sea, the Gulf of Zues, the Gulf of Aqaba and extends to the eastern part of the Gulf of Aden at longitude 48° E (Figure 5.1). The bathymetric data of the RS-Model were sourced from the global bathymetry dataset for the world ocean ‘‘GEBCO_08 Grid’’ at a 30 arc-second horizontal resolution (~ 1 km). The bathymetric contours for the RS-Model are shown in Figure 5.3.

Due to insignificant artificial contact between the Red Sea and the Mediterranean via Suez Canal, the model has only one open boundary which was set at the Gulf of Aden at longitude 48° E. Tidal amplitudes and phases of the eight primary semidiurnal and diurnal tidal constituents (Q_1 , O_1 , P_1 , K_1 , N_2 , M_2 , S_2 and K_2) have been prescribed at boundary cells and linearly interpolated. A time step of 60 seconds was set in all simulations to insure the stability and accuracy of the model. Initial conditions of water levels were set equal to zero in all simulations. As a result, the equilibrium state in terms of water levels is reached after certain time; therefore, the first four days of the simulation were discarded. The physical parameters adopted for the RS-Model are listed in Table 5.3.

6.3 Tidal characteristics based on model Results

This section presents the tidal characteristics in the Red Sea based on the tidal constituents generated from the harmonic analysis of the model results. Two numerical simulations were carried out to describe the tidal characteristics in the Red Sea. In section 3.7.2, available surface elevation data were used to perform tidal analysis. The analyses have shown that the major semidiurnal and diurnal constituents that have relatively higher amplitudes are M_2 , N_2 , S_2 and K_1 respectively (Figure 3.13). In the first scenario, simulations of major tidal constituents (M_2 , S_2 , N_2 , and K_1) were made for the purpose of generating Co-tidal charts and also the form factor. Thus, separate simulations were carried out of each individual constituent to generate Co-tidal and Co-range charts for the Red Sea region. To carry out the simulations, the amplitude and phase of M_2 tide was prescribed and linearly interpolated to each grid point along the open boundary of the model. The simulated M_2 tidal elevation was stored at hourly intervals at all grid points in the model domain. The computed amplitudes and phase from simulated M_2 tide at each grid point were used to generate the Co-range and Co-tidal charts respectively. The same procedures were applied for simulations of other constituents (N_2 , S_2 and K_1).

In the second scenario, the model was forced on the ocean open boundary with the amplitudes and phases of the primary semidiurnal and diurnal constituents (Q_1 , O_1 , P_1 , K_1 , N_2 , M_2 , S_2 and K_2). The purpose of this simulation was to reproduce the behaviour of the hydrodynamic features in the Red Sea at moments of extreme conditions, ebb and flood phases during spring and neap tidal cycles.

6.3.1 Co-range and Co-tidal charts

In this section, the tidal characteristics in the Red Sea based on the tidal constituents generated from the harmonic analysis of the model results are given. To represent the propagation of tides in the Red Sea, the so-called co-range and co-tidal charts are used. Co-tidal and co-amplitude charts of the semidiurnal constituents M_2 , N_2 , and S_2 are shown in Figures 6.1, 6.2 and 6.3, respectively. In general, the dominant feature of the M_2 , N_2 , and S_2 tide is the existence of anticlockwise amphidromic systems in the central part of the Red Sea close to 20° N, at the northern end of the strait of Bab el Mandeb at 13.5° N and at the Gulf of Suez. The co-tidal and co-range chart of the diurnal constituent K_1 are displayed in Figure 6.4. The chart shows only a single anticlockwise amphidromic system in the southern part of the Red Sea centred around 15.5° N. These results are consistent with the analytical results described by Defant (1961).

6.3.1.1 Semidiurnal Tidal waves

Figure 6.1 shows the co-amplitude and co-phase distributions for the M_2 tide. The former is given in centimetres and the latter is expressed in degrees. In general, the amplitude of M_2 , N_2 , and S_2 waves show similar behaviour in the Red Sea basin. It is obvious from the figure that M_2 amplitude is relatively high in the Gulf of Aden (50 to 60 cm) however, as the tidal wave flow into the strait of Bab el Mandeb; the wave speed rapidly decreases along the strait direction due to the narrow connection. Further north, the decrease continues towards a minimum value as shown in the co-amplitude chart of figure (6.1-right panel). Then M_2 tidal amplitude reaches about 5 cm or less in the strait of Bab el Mandeb and tends to increase north-westward. Defant (1961) assumed that this minimum is associated with the amphidromic system generated due to M_2 tidal wave. At the northern end of the strait, M_2 tidal amplitude increases to 20 cm and then expands at both sides eastern and western coasts (15° N) in the southern part of the Red Sea reaching about 35 cm. The M_2 amplitude then tends to decrease from the southern part of the Red Sea towards the north-northwest region while reaching the central part where amphidromic system exists. Further, it begins to propagate and increase again towards the northern part of the Red Sea.

For S_2 tide, again the amplitude of S_2 tide is relatively high in the Gulf of Aden. The amplitude of S_2 tide is low (less than half) compared to the M_2 tide and its variation in the Red Sea is similar to that of M_2 tide as shown in Figure (6.2-right panel). This is due to the influence of bathymetry (the strait morphology) in combination with the amphidromic system and results in a decline in the tidal amplitude. The S_2 tide then propagates northward from the northern end of Bab el Mandeb strait to the inner area of the south of the Red Sea and tends to decrease (16° N) up to the amphidromic system. Similar to M_2 tide, the S_2 amplitude then propagates and increases gradually towards north-northwest. N_2 tide is similar to S_2 tide as illustrated in Figure 6.3. The amplitude of N_2 tidal wave decreases from the southern part of the Red sea toward the central part (amphidromic system) and tends to increase toward north-north west.

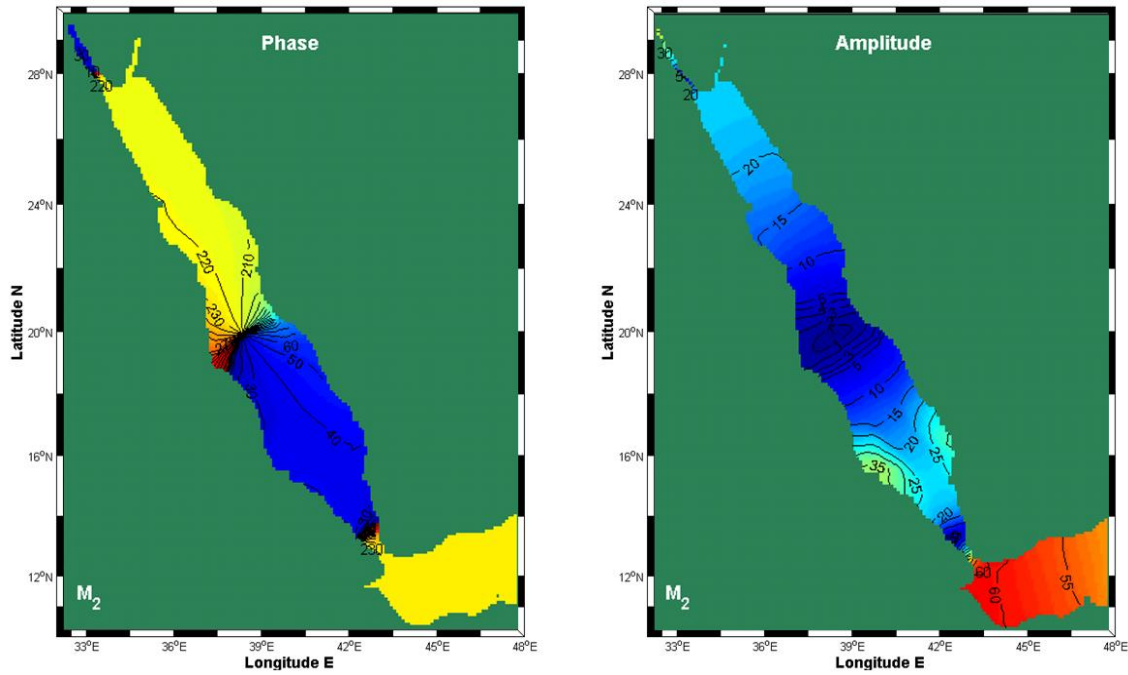


Figure 6.1 Distribution of amplitudes and phases of M_2 tide in the Red Sea using the RS-Model, (left panel) co-tidal lines and (right panel) co-range lines. Amplitudes are given in centimetres and phases in degrees.

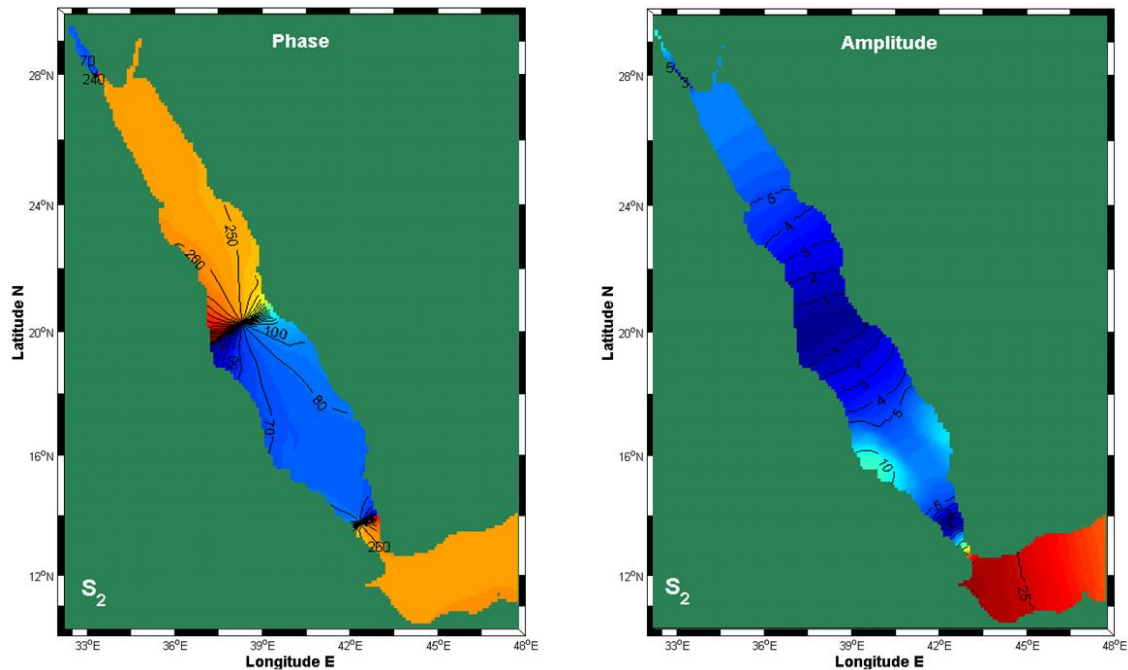


Figure 6.2 Distribution of amplitudes and phases of S_2 tide in the Red Sea using the RS-Model, (left panel) co-tidal lines and (right panel) co-range lines. Amplitudes are given in centimetre and phases in degrees.

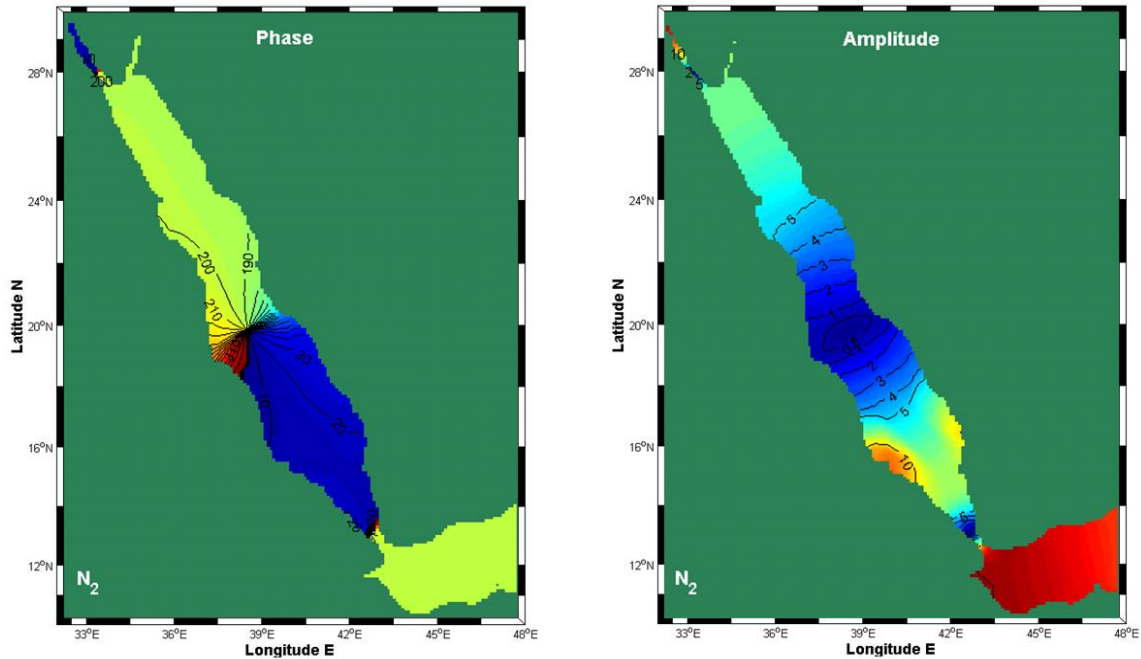


Figure 6.3 Distribution of amplitudes and phases of N_2 tide in the Red Sea using the RS-Model, (left panel) co-tidal lines and (right panel) co-range lines. Amplitudes are given in centimetres and phases in degrees.

6.3.1.2 Diurnal tidal wave

The co-range and co-tidal charts of K_1 are depicted in Figure 6.4. The dominant feature of the phase distribution is the existence of a single anticlockwise amphidromic system located in the southern part of the Red Sea centred around 15.5° N. The distribution of the co-amplitude reflects higher amplitudes at the Gulf of Aden. However, in the strait of Bab el Mandeb, the amplitude of K_1 as shown in the Figure (right panel) is reduced to 10 cm and tends to decrease gradually towards the north along the strait. Contrary to those of semidiurnal constituents M_2 , S_2 and N_2 , K_1 tidal amplitude decrease gradually toward the inner area of the southern part of the Red Sea where amphidromic system is formed. The co-range chart of K_1 tide shows a slight increase in amplitude above 17° N towards the middle part of the Red Sea but the amplitude is very small. Tidal wave of O_1 (not shown) also includes similar features of K_1 tide.

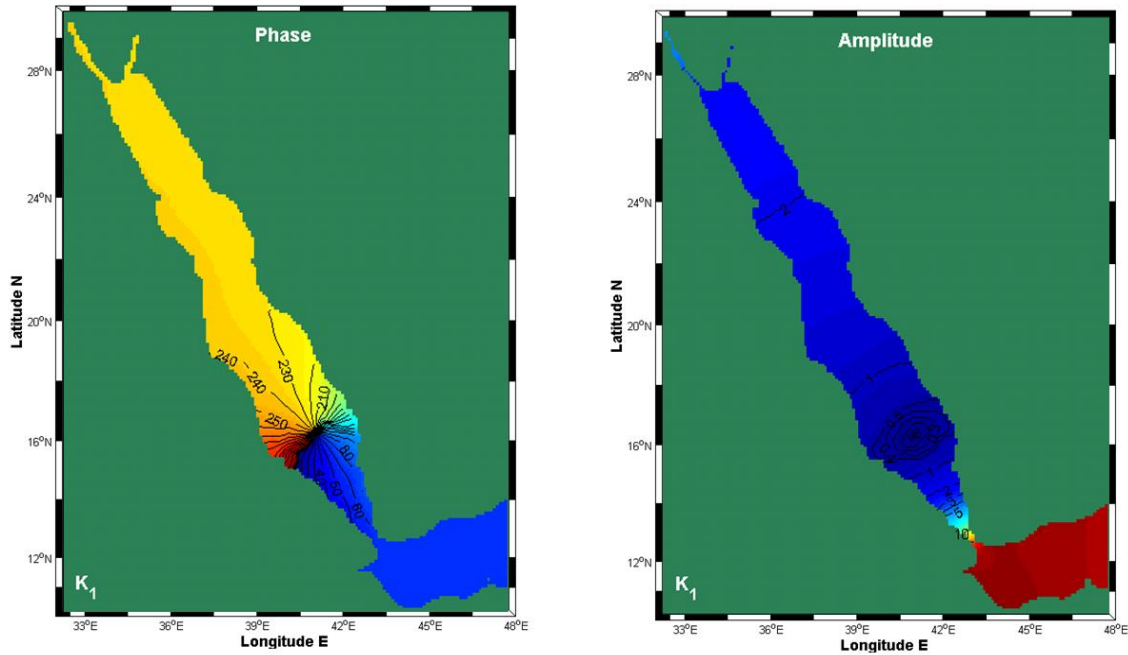


Figure 6.4 Distribution of amplitudes and phases of K_1 tide in the Red Sea using the RS-Model, (left panel) co-tidal lines and (right panel) co-range lines. Amplitudes are given in centimetres and phases in degrees.

6.4 Form Factor

According to Pugh (2004), the relative importance of the semidiurnal and diurnal tidal constituents can be determined based on a form factor. Therefore, it was considered the form factor for the entire Red Sea based on the computed amplitudes using the following expression (Pugh, 1987, 2004):

$$F = \frac{O_1 + K_1}{M_2 + S_2}$$

where O_1 , K_1 , M_2 and S_2 are the amplitudes of the correspondent constituents. Figure 6.5 shows the form factor distribution in the Red Sea basin. As the form factor in all grid points of the computational domain is less than 0.25 (except the central part of the Red Sea and northern part of the strait), it can be confirmed that the type of the tide in the Red Sea is essentially semidiurnal. Assessment of this figure has reflected that the relation between diurnal and semidiurnal constituents is to be seen in the central part of the Red Sea and is not constant in the entire Red Sea. Therefore, the diurnal tidal pattern is stronger in the central part of the Red Sea indicating mixed type mainly dominant with semidiurnal on the eastern coast compared with diurnal tide in the western coast. The results conducted by Sultan *et al.*, (1995) for the area of Port Sudan and Jeddah are in agreement with this work where diurnal character was observed to be larger close to the SUDAN coast. The figure also shows that diurnal character appears at the northern end of Bab el Mandeb strait around 13°N.

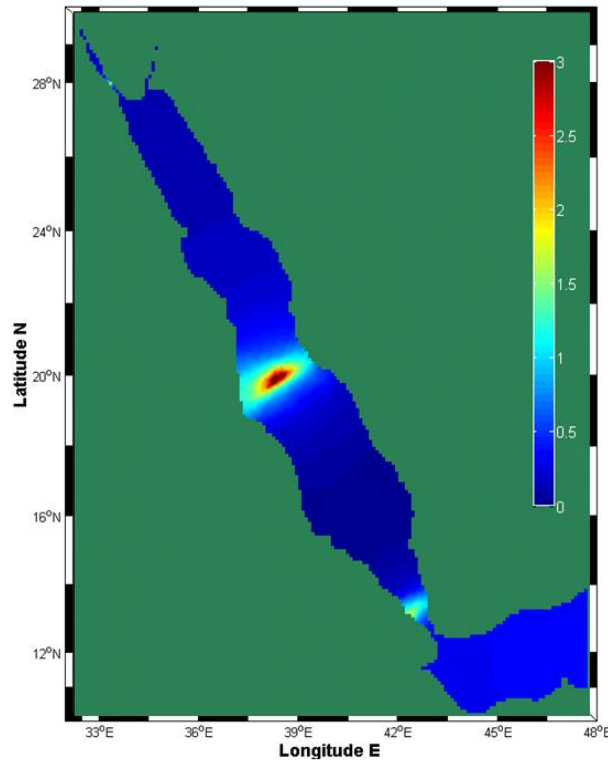


Figure 6.5 Form Factor distribution in the Red Sea based on calculated modelled diurnal (O_1 , K_1) and semidiurnal (M_2 , S_2) amplitudes.

6.5 Hydrodynamic Features

This section presents the patterns of the tidal currents in the Red Sea based on the numerical model. Analysis of tidal currents that is generated by a combination of the primary constituents (Q_1 , O_1 , P_1 , K_1 , N_2 , M_2 , S_2 and K_2) under flood condition and ebb condition during the spring and neap tide were made. The simulated tide-induced current flooding and ebbing patterns in spring and neap tide are displayed in Figure 6.6 and 6.7 respectively. The highest velocities, in the range of 0.5 m/s were observed in Bab el Mandeb strait during flood tide spring condition. However, the tidal currents are varying depending on the geometry in combination with ocean currents of flood and ebb tides.

The snapshot of the current velocity field at the flood condition during spring tide is shown in Figure (6.6-left panel). At this particular time, the maximum current magnitudes reaches up to about 0.5 and 0.3 m/s are observed at Bab el Mandeb strait and Gulf of Suez respectively. Analysis of ADCP data carried out in the strait of Bab el Mandeb by Murray and Johns (1997) showed that the speed in the upper layer ranges between 0.4-0.6 m/s while for the lower layer it is about 0.8 m/s. Inside the Red Sea basin, the model results showed that current magnitude is in the range of 0.1 m/s prevalent. In the inner part of the southern portion of the Red Sea (16° N), current speeds become stronger at the vicinity of shallow shelves on both sides. On the other hand, during neap tide (Figure 6.7) maximum currents magnitude in order of 0.25 m/s are observed in the strait of Bab el Mandeb during flood condition. During ebb condition, it was observed that velocities between 0.05 and 0.1 prevail inside the Red Sea domain.

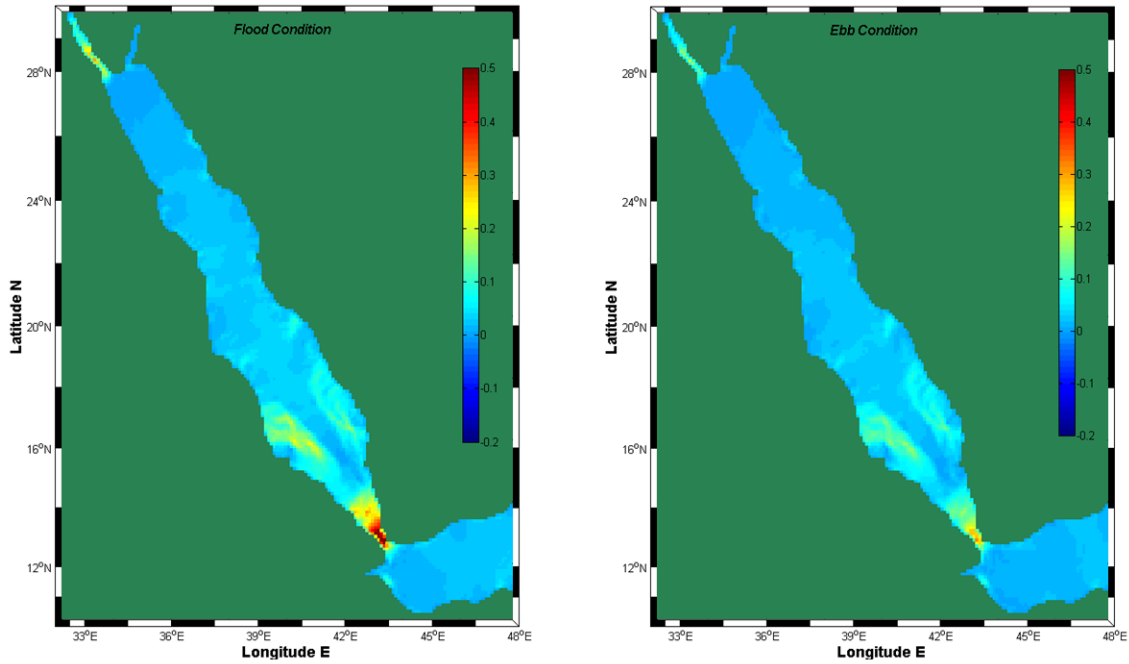


Figure 6.6 Snapshot of the model showing the current velocity field (m/s) for the Flood condition (left panel) and for the Ebb condition (right panel) (depicted by colour size) in the Red Sea during spring tide.

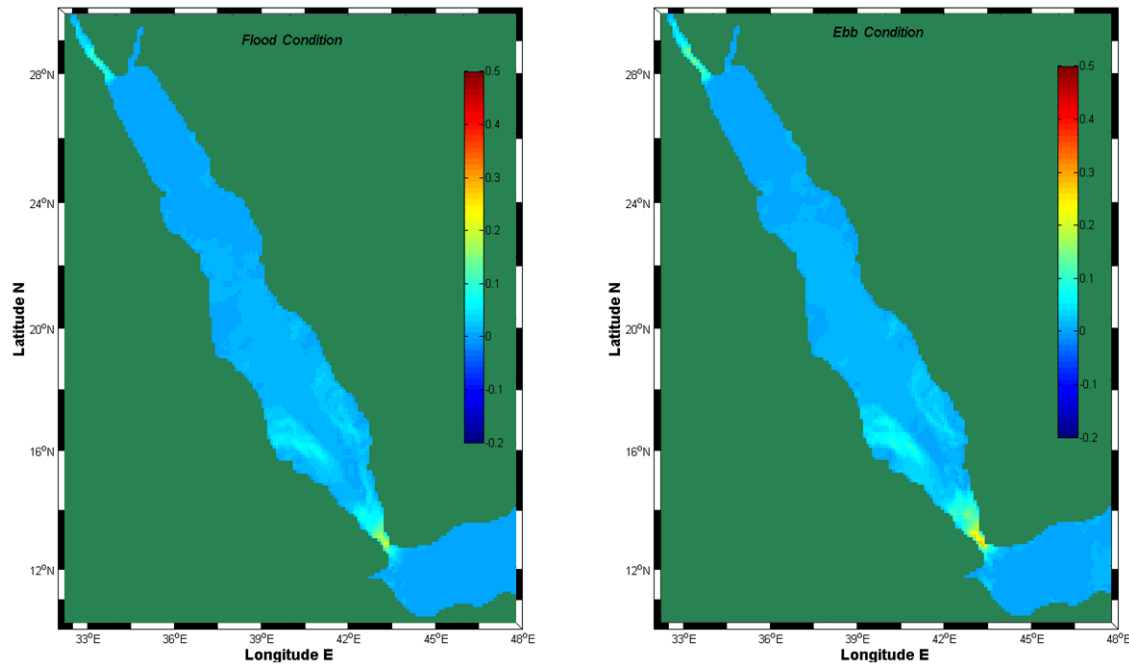


Figure 6.7 Snapshot of the model showing the current velocity field (m/s) for the Flood condition (left panel) and for the Ebb condition (right panel) (depicted by colour size) in the Red Sea during neap tide.

Figure 6.8 and 6.9 display distributions of the simulated surface elevations and currents during spring tides in the Red Sea, produced by a combination of the primary constituents (Q_1 , O_1 , P_1 , K_1 , N_2 , M_2 , S_2 and K_2). It can be seen that the spring tides in the Red Sea are characterized by high water in the southern part of the basin while the northern part by low water and vice versa during ebb condition. Maximum elevations are observed in the southern part particularly over the shallow shelves. They are about 0.5 m and 0.6 m close to eastern coast and western coast, respectively. The figure also reflects an increase in surface gradients along the Gulf of Suez. The model results showed that the tidal currents in the Red Sea are very weak with an average speed less than 0.1 m/s (Figure 6.9). The highest currents occur at the area where the strait is narrowing its land-water boundary and along the Gulf of Suez. The model results indicate that the direction of the currents in the Red Sea includes some variability. The currents during flood condition are directed northward. However, the direction of the currents in the strait and Gulf of Suez is opposite. During ebb condition, the currents from the north propagate towards the southern part. However, in the strait and Gulf of Suez the direction is opposite.

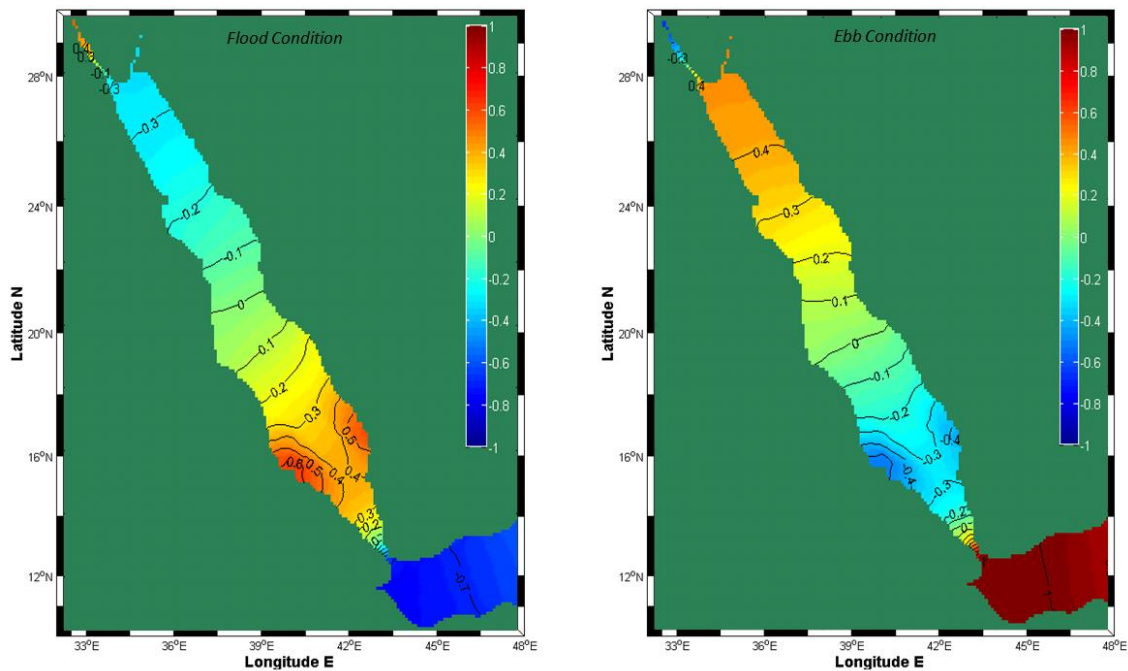


Figure 6.8 Distribution of the spring surface elevation (m) in the Red Sea using the RS-Model, (left panel) Flood condition and (right panel) Ebb condition.

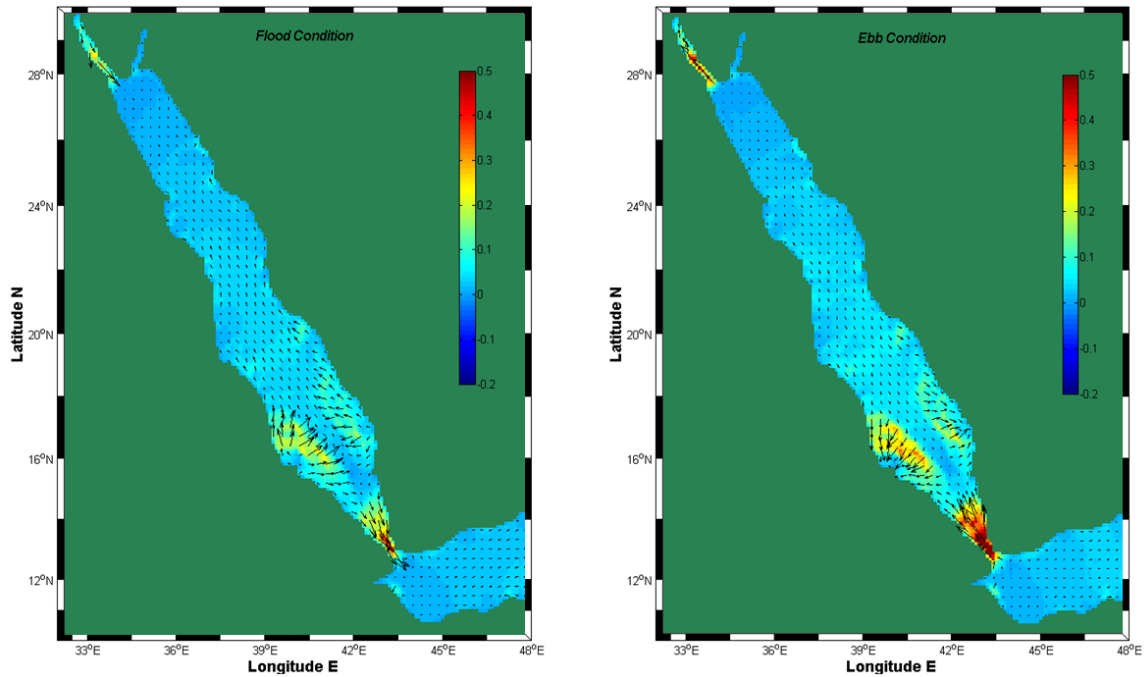


Figure 6.9 Snapshot of the model showing the current velocity field (m/s) for the Flood condition (left panel) and for the Ebb condition (right panel) (depicted by colour size and vector direction) in the Red Sea during spring tide.

6.6 Conclusion

Previous studies of tides in the Red Sea were limited to very few observations. In addition to a few analytical analyses carried out to determine the tides in the strait of Bab el Mandeb and the results were used to explain the tidal dynamics for the whole Red Sea. In the present study, considering the advantages of numerical modelling, the tidal characteristics in the Red Sea region were studied using numerical model. The model was run in two-dimensional mode. The model domain covers the entire Red Sea, the Gulf of Aqaba, and the Gulf of Suez and includes part of the Gulf of Aden with a boundary located at 48° E. The optimal settings were determined based on sensitivity analyses. The model was validated against measured surface elevation at several locations in the model domain. The model is able to reproduce the tidal wave in the Red Sea, reflecting a consistent level of agreement with previous work and field data. At all stations considered in the validation, the tidal amplitudes of M_2 , S_2 , N_2 and K_1 derived from the model agree reasonably well with the values determined from the observations. However, the major discrepancies were observed in relation to phase conditions at stations located near the region of amphidromic point in the central part of the Red Sea.

Based on the model results, the dominant feature of the M_2 , N_2 , and S_2 tide is the existence of the amphidromic systems (anti-clockwise) in the central part of the Red Sea at about 20° N, north the strait of Bab el Mandeb at 13.5° N and in the Gulf of Suez. The distribution of the co-phase of K_1 tide showed the existence of only a single anticlockwise amphidromic system in the southern part of the Red Sea centred around 15.5° N. The amphidromic systems of the

semidiurnal and diurnal constituents in the strait of Bab el Mandeb suggest that the tides include some characteristics of standing waves. Model results of amplitudes and form factor proved that tides in the Red Sea are dominated by the major semidiurnal constituents M_2 , S_2 , and N_2 . However, diurnal character appeared in the central part of the Red Sea and northern part of the strait. In terms of tidal currents, the model results showed that tidal currents in the Red Sea are weak except near the Red Sea entrance where maximum velocity can reach about 0.5 m/s. In summary, additional observations of water levels along the western coastline of the Red Sea are needed for more validation of the model since only one station was used in this study. In addition to that, measurements of currents are needed for validation purposes. Nevertheless, the tidal model is useful and can be used to generate boundary conditions for local models in the Red Sea.

Chapter 7

Simulation of circulation and Thermohaline Structure in the Red Sea

7.1 Introduction

The circulation and thermohaline patterns of semi-enclosed seas such as the Red Sea depend significantly on the magnitude of meteorological and buoyancy forces in addition to the tidal forcing. To study the circulation in the Red Sea, it is very important to take into account the interaction between tides, metrological and buoyancy forces. In this regard, the 2-D RS-Model (tidal model) was extended into 3-D approach and modified to incorporate metrological forcing, temperature and salinity to simulate the circulation and thermohaline structure. This is followed by efficient validation of the model with available measurements. Due to insufficient observational data, another data sources such as satellite technique have also been considered (see Chapter 5).

As already mentioned in Chapter (3) very few attempts were made to study the circulation in the Red Sea. The previous studies on the circulation and hydrographic characteristics in the Red Sea in terms of observational studies were largely limited to the main axis of the basin in addition to few sparse locations inside the domain. On the other hand, numerical modelling studies on the Red Sea circulation are also very limited. It should be mentioned that in the previous studies, the models were driven by monthly mean values of wind fields and thermohaline forcing, and focus was given only on the seasonal patterns (January and July). This means that the high-frequency variability was not taken into consideration. As a result, the current understanding of the circulation in the Red Sea region is still limited. In addition to that, the necessity of numerical modelling approach to advance the basic understanding of the region was clearly stated in the report of the workshop entitled “Arabian Marginal Seas and Gulfs” (William, *et al.*, 1999). In the present study, high-frequency variability of the model forcing is accounted for to deepen our understanding about the processes in question.

This chapter of the thesis focuses on the circulation and thermohaline processes in the Red Sea region using the 3-D RS-Model. Section (7.2) provides a description of the summer circulation and thermohaline characteristics based on the model results. In section (7.3) the hydrographic characteristics at the strait of Bab el Mandeb is described. The full cycle of the Gulf of Aden intermediate water (GAIW) intrusion is studied in section (7.4). Afterwards, the intermediate circulation pattern during the summer season is described in section (7.5). Section (7.6) describes the circulation patterns and thermohaline structure during the winter season. This is followed by investigating the contribution of wind and thermohaline forcing on the key circulation patterns through additional numerical experiments in section (7.7). The mechanisms involved in the water mass formation, possible locations and exact period are investigated in section (7.8).

Model Results and Discussion

In the following, the seasonal circulation patterns and thermohaline structure in the Red Sea are described. In this study we consider the seasonal variability of the circulation and thermohaline processes over the winter and summer seasons. The former is represented by January to March while the latter is represented by June to September. These months were selected taking into account the seasonal patterns of the forcing conditions as well as the exchange flow regime existing at the Bab el Mandeb Strait. Since both wind and thermohaline forcing are highly variable at the seasonal scales, it is expected that the circulation patterns are characterised with strong variations. The features of the simulated-processes are presented in the form of horizontal current fields, zonal and meridional cross-sections of thermohaline processes.

Throughout the course of this study, three different scenarios consisting of numerical simulation experiments are carried out. In the first scenario-I, the RS-Model was run using all forcing conditions mentioned previously in Chapter 5. The purpose of this numerical experiment is on the one hand to reproduce the hydrodynamic conditions and describe the seasonal patterns of the circulation and thermohaline processes, and on the other hand to be used as a reference mode. The aim of the second and third scenarios is to investigate the relative importance of the main forcing mechanisms (wind and heat fluxes) on the key circulation features. This procedure allows investigating the spatial and temporal contributions of the isolated forcing to the general circulation and some of its specific characteristics. For this purpose, two additional numerical simulations consisting of the same model configuration of scenario-I but using different combinations of driving forces are carried out. To determine the effect of wind-stress forcing on the circulation, Scenario-II was performed considering only the thermohaline fluxes. In the third numerical experiment (Scenario-III), the thermohaline fluxes were removed but wind-stress field is included.

7.2 Circulation patterns and thermohaline structure (summer season)

This section presents the predicted circulation features during the summer season. For this purpose, the simulation results over the period from June to September are analyzed.

7.2.1 Horizontal patterns of the circulation

The horizontal distribution of the surface circulation in the Red Sea during the summer is shown in Figure 7.1. In general, the surface circulation field shows variable patterns including series of cyclonic and anticyclonic eddies. To describe the major features of the circulation, we divided the Red Sea basin into two main regions: the northern region (North of 20°N), and the southern region (south of 20°N).

North of 20°N, the surface current field contains a series of organized energetic eddies along the northern part of the Red Sea. They are centered around 27.5°N, 27°N, 26°N, 23°N and 22.2°N respectively. Note that, there are small eddies around 24°N and 20.5 °N located close to the western boundary of the Red Sea. The model results showed that the circulation in the extreme north of the basin is dominated by cyclones while eddies located south of 27 latitude are dominated by anticyclones. The current speeds of these eddies systems are ranging between 0.5-0.9 m/s with exception of the eddy centered at 22.2°N which exceeds 1 m/s. Previous observational studies carried out in the extreme northern part of the Red Sea during the winter season suggest that there is a permanent cyclonic gyre (e.g. Clifford et al. 1997). The model results showed also the existence of such a cyclonic system during summer which is consistent with the modeling studies of Sofianos and Johns (2003) and Yao et al. (2014a); however, the shape of the circulation pattern is different when comparing with the former but almost similar to the latter. The existence of such feature suggests that the northern Red Sea is dominated by the permanent cyclonic system. This cyclonic eddy is one of the essential mechanisms in the RSOW formation processes through an open-ocean convection process that takes place in the northern part of the Red Sea during the winter season (see section 7.8).

The model results also reflect the existence of northward flow (north of 22) along the western coast as a boundary current. It is interesting to note that the strong anticyclonic eddy located in the central basin extends across the entire width of the Red Sea basin with velocities exceeding 1 m/s. This feature produced by the RS-Model is very consistent in size and magnitude with recent observations of Sofianos and Johns (2007). Most importantly, the previous modeling study which is forced by climatological conditions (Sofianos and Johns 2003) showed weaker patterns in both size and magnitude, indicating the important role of account for the high-frequency atmospheric forcing in studying the circulation in the Red Sea region.

South of 20°N, the major features of circulation are the presence of anticyclonic eddies centred around 18°N and 16°N. Quadfasel and Baudner (1993) analysed hydrographic data collected along the central axis of the basin and found an energetic three-dimensional

circulation within the Red Sea basin. Their results showed the presence of a permanent anticyclone located at 23°N, a prevalent anticyclonic feature in the central Red Sea in addition to several quasi-permanent anticyclonic features located near 20-21°N and 17 -18°N. Recently, Sofianos and Johns (2007) conducted salinity-temperature measurements, meteorological and direct current observations along the main axis of the Red Sea during the midsummer of 2001 (from 4 August to 19 August). The major resulting circulation patterns from this survey are three strong anticyclones covering the width of the basin located at 23°N, 21.2°N and 18.5°N respectively, in addition to a cyclone in the extreme northern Red Sea which was not identified in the observations of Quadfasel and Baudner (1993). On the other hand, the satellite data of the sea level anomalies (SLA) also clearly reflects the occurrence of such features (see Chapter 3). The distribution of circulation features predicted by the RS-Model is largely in agreement with these recent studies and SLA data. A maximum velocities magnitude predicted by the model of 1 m/s is observed in the central Red Sea. South of 16°N, the simulation results suggest that the currents in the vicinity of the southern part are in general irregular and mostly directed towards the south following the prevailing wind direction where it reverses during the summer and becomes NNW. The current speeds in the vicinity of the southern part are weaker during this period ranging between 0.1-0.2 m/s as a result of weaker wind and thermohaline forcing. However, according to the model results highest magnitudes of the southward flow occur at the area where the strait is narrowing its land-water boundary. The disappearance of the northwards inflow that takes place during winter season as a result of reversing prevailing wind field is obvious (see section 7.6).

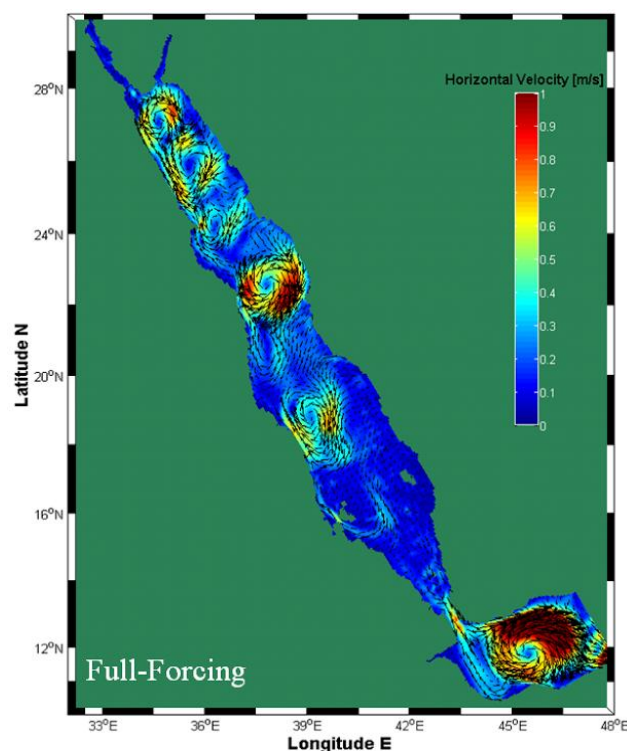


Figure 7.1. Mean surface current velocity field in the Red Sea based on RS-Model over summer months (June-September) [Full forcing].

7.2.2 Horizontal patterns of the thermohaline fields

To represent the horizontal distribution of sea surface temperature (SST) and sea surface salinity (SSS), the simulation results over June to September were averaged. The horizontal distribution of simulated SST and SSS fields during summer season is shown in Figure 7.2. The emerging patterns of SST and SSS over the Red Sea region are highly influenced by the prevailing winds in the region. It is obvious that the entire Red Sea basin during the summer season becomes very warm with meridian gradient over the basin (Figure 7.2-a). Maximum sea surface temperature observed during summer is reaching about 33-34 °C. The major pattern which appeared in this period is that the SST is higher on the western boundary than on the eastern one. Along the eastern boundary of the basin particularly in the middle part of the basin (20° N) and north of 23° N the water temperature is cooler than on the western coast (~ 4 °C), indicating upwelling events associated with the prevailing NNW winds. A similar process is observed in the salinity distribution.

Associated with the prevailing NNW winds during the summer season, we can observe that the surface outflow (RSSW) carries relatively warm and salty waters (~30°C, 37.5 psu) towards the Gulf of Aden. Interestingly higher temperature and salinity associated with the RSSW outflow is concentrated along the western side especially inside the strait, suggesting that the RSSW leaves the strait following its pathway along the western boundary. The horizontal distributions of SSS field in the Red Sea experiences seasonal variations through both wind stress and air-sea buoyancy fluxes. The spatial structure of the SSS in the region increases gradually from the southern part of the Red Sea towards the north reaching about 38.5-39 psu and 40 psu in the middle part and the northern part of the Red Sea respectively (Figure 7.2-b). Similar spatial structure is observed during the winter time (see section 7.6). However, the SSS in the Red Sea is higher in summer than in winter especially in the southern part of the basin where it reaches 37.5 psu. An upwelling process is observed along the northernwest Gulf of Aden at ~12° N. This feature of upwelling processes in the Gulf is consistent with several studies carried out in the Gulf of Aden (e.g Piechura and Sobaih 1986).

7.2.3 Vertical thermohaline structure

To describe the vertical distribution of temperature and salinity, model results along the meridional section were extracted and plotted (see location of the latitudinal section in Figure 3.10). The analysis is focused only on the upper 400 m depth since the thermohaline characteristics below the depth of 300 m in the Red Sea basin are found remarkably homogenous (see Appendix D). The model results clearly showed the significant role played by the atmospheric forcing variations between the two seasons. The stratification characteristics and water masses during both seasons are clearly observed from the latitudinal section of the Red Sea.

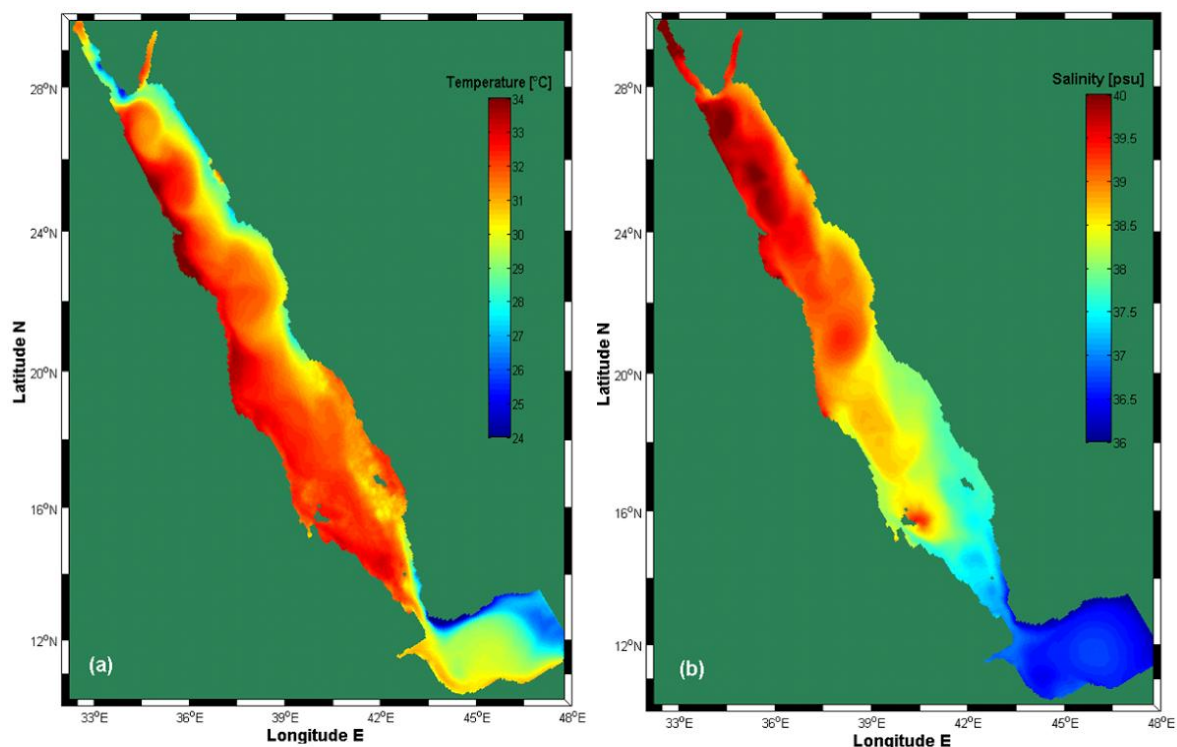


Figure 7.2. Horizontal distribution of simulated (a) sea surface temperature SST ($^{\circ}\text{C}$), (b) sea surface salinity SSS (psu) during summer season (June-September).

The vertical structure of the temperature and salinity respectively during the summer period is shown in Figure 7.3. Higher temperature values ($27\text{-}28^{\circ}\text{C}$) are observed during the winter in the intermediate region ($16\text{-}20^{\circ}\text{N}$) with a gradual decrease towards the southern and northern extremes (see section 7.6) while during the summer (Figure 7.3-a), it is observed that the region of high temperature becomes warmer ($33\text{-}34^{\circ}\text{C}$). Besides due to the influences of the predominant NNW winds extends southwards. The simulation results indicate that the vertical structure is more stratified (unlike the winter situation) and the mixed layer is shallower, comparable with the structure of the summer-2001 observations of Sofianos and Johns (2007). The mixed layer depth extends to 30 m in the northern part and to 50 m between $17\text{-}18^{\circ}\text{N}$. The depth of thermocline layer deepens to 230 m where the temperature decreases from 34°C to $\sim 22^{\circ}\text{C}$. A gradual decrease of the temperature to a minimum of 21.5°C is observed between the depths of 250-300 m.

In terms of salinity (Figure 7.3-b), it is obvious that salinity increases with depth and the depth gradient is larger in the southern Red Sea due to the influence of low salinity water associated with the GAIW. In the southern part mainly south of 16°N , the major pattern is the existence of a 3-layers exchange flow system with the Gulf of Aden which develops during the summer season. This is a well-documented feature during the summer where the minimum temperature and salinity (between the depth 50 to 100 m) associated with the water mass coming from the Gulf of Aden reaches about $16\text{-}17^{\circ}\text{C}$ and 35 psu respectively (e.g. Sofianos and Johns 2007). On top of GAIW layer is the RSSW layer characterized by warmer ($31\text{-}32^{\circ}\text{C}$) and saltier (37.5-38 psu) water. The model results have shown that the thickness of the RSSW is about 20 m which is in agreement with the estimated depth by Murray and

Johns (1997). Underneath the GAIW layer, there are the RSOW and RSDW (More details are given on these water masses in section 7.8).

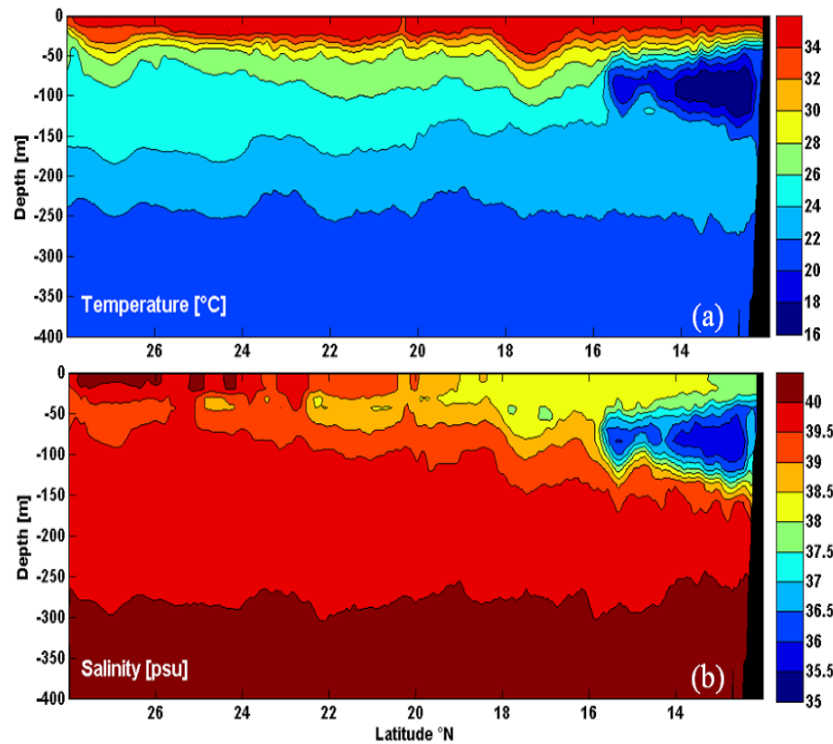


Figure 7.3. Vertical distribution of simulated (a) temperature ($^{\circ}\text{C}$) and (b) salinity (psu) along the main axis during summer season (June-September) based on RS-Model, [Scenario-1: Full forcing].

7.3 Characteristics of the water masses at the Strait of Bab el Mandeb

This section describes the vertical structure of the thermohaline in the southern part of the Red Sea basin. In addition, monthly mean values of the layers transport are described and compared with earlier observations.

As already mentioned in Chapter 3, the southern part of the Red Sea including the strait of Bab el Mandeb and the Gulf of Aden are subject to two annually changing monsoonal events. As a result, there is strong seasonal exchange flow pattern between the Red Sea and Gulf of Aden through the Strait of Bab el Mandeb resulting in a transition from a 2-layer flow regime in winter into a 3-layer exchange system in the summer season. These are represented by the reversal processes of the surface flow (Red Sea Surface Water (RSSW) and Gulf of Aden Surface Water (GASW)), subsurface intrusion of Gulf of Aden Intermediate Water (GAIW) and the seasonal variability of the Red Sea Outflow Water (RSOW).

The vertical distribution of the temperature and salinity at a cross-section located at latitude $\sim 14^\circ\text{N}$ is shown in Figure (7.4). During winter season, it can be seen that the distribution of the temperature in the surface layer is uniform with the western side slightly cooler than the eastern side and the mixed layer extends to about 90 m (Figure 7.4 a). The thermocline layer extends to around 150 m where the temperature values decrease from 26 to approximately 23 $^\circ\text{C}$. Figure (7.4 b) shows the vertical structure of temperature during the summer. As can be seen that the mixed layer reduces to about 20 m and there is small differences between the east and west of the cross-section where the western side is warmer than the eastern side. On the other hand, the salinity distributions (Figure 7.4 c,d) show an increase of salinity values with increasing depth. Beneath the thermocline layer, the GAIW is observed at the depths of about 75 to 100 m. Underlying the GAIW is the warm (22-23 $^\circ\text{C}$) and saline (40 psu) RSOW.

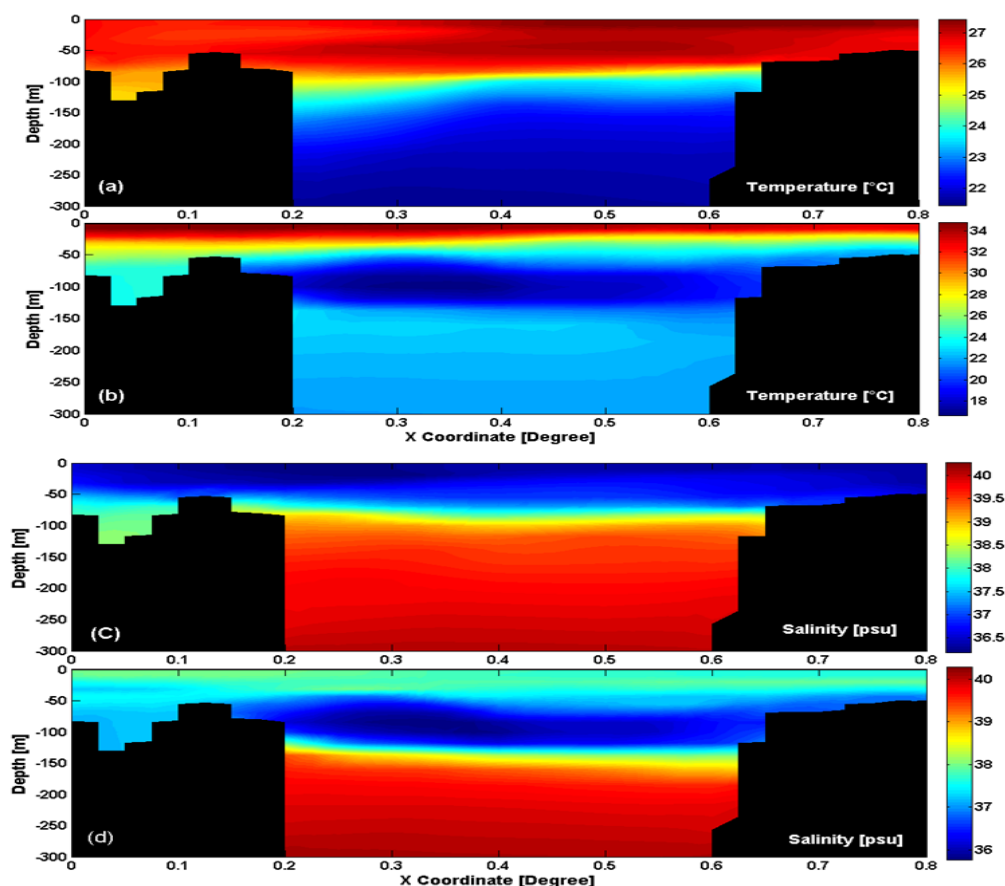


Figure 7.4. Vertical distribution of simulated temperature ($^\circ\text{C}$) (a) winter, (b) summer, and salinity (c) winter and (d) summer [Zonal cross-section in the southern part of the Red Sea along 14°N].

Figure (7.5) shows computed monthly mean values of the layers transport. The analysis over the water column is considered based on the specified water masses. For the winter season, the water column consists of two parts: surface and deep layers. For the summer season, three parts of the water column are considered: surface, intermediate and deep layer. The upper surface layer represents the GASW inflow and RSSW outflow, the intermediate layer

includes the GAIW intrusion and the deep water includes the RSOW towards the Gulf of Aden.

As can be seen in the figure, the RS-Model is able to reproduce the reversal of the surface flow, the intrusion of the GAIW and the RSOW outflow. The calculated mean transports over the summer and winter seasons of the surface outflow/inflow are found to be 0.14 and 0.46 Sv. The intermediate inflow which takes place during the summer is estimated with an average transport of 0.3 Sv. This value is slightly larger than the estimated value of 0.24 Sv by Sofianos et al. (2002). On the other hand, the annual mean transport of RSOW outflow into the Gulf of Aden is estimated at 0.38 Sv with minimums and maximums over summertime and wintertime. Based on velocity data analyses, Murray and Johns (1997) and Sofianos et al. (2002) showed that the annual mean of the RSOW outflow is 0.36 Sv with a large annual cycle ranging from 0.6 Sv in the winter and less than 0.1 Sv in the summer. Although there are discrepancies between the model and previous observations, the model is able to produce the main features of the seasonal cycle of the flow exchange system successfully.

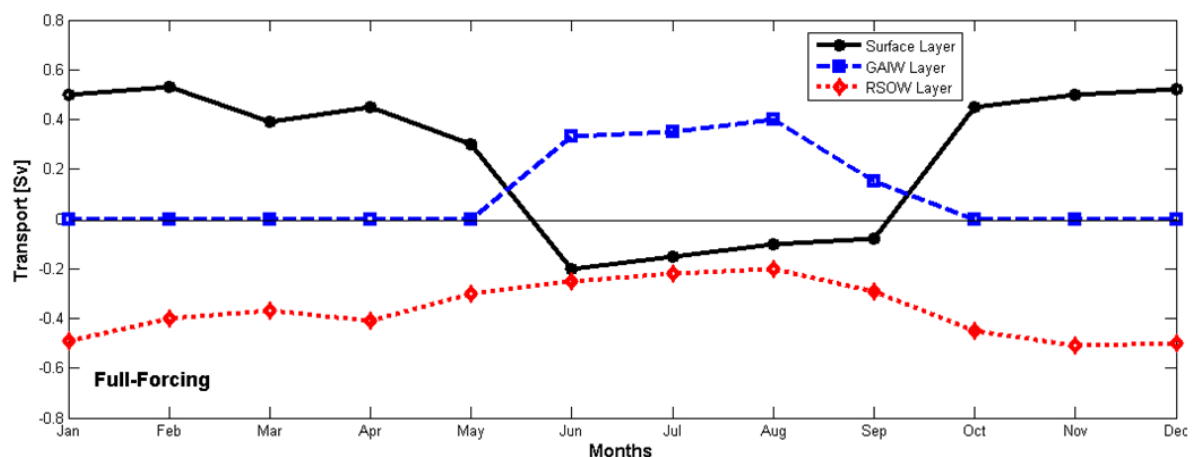


Figure 7.5. Seasonal means of volume transport for Surface, Intermediate and deep layers at a cross-section located at $\sim 12.5^\circ\text{N}$.

7.4 Intrusion of the Gulf of Aden Intermediate Water (GAIW)

This section concerns the subsurface intrusion of the GAIW. Previous studies showed some doubts about the fate and northernmost limit of the GAIW inside the Red sea basin. In this context, the succession of the GAIW intrusion into the Red Sea is investigated. This aims at describing the full cycle of the GAIW structure and determining the northern limit of the intrusion inside the Red Sea basin based on the simulation results. A sequence of the incoming GAIW from June to November represented by the current and salinity fields at 80 m depth is depicted in Figure 7.6. As can be observed, the intrusion of low-salinity associated with the GAIW takes place in June and gradually becomes stronger in July through October.

It is interesting to note the GAIW layer after entering the narrowing strait veers toward the eastern coast inside the southern part of the Red Sea. This is clearly observed in the modelled cross-section at $\sim 16^\circ\text{N}$ in Figure 7.7, where the core GAIW is concentrated at the eastern side between the depths of 50-100 m. This is consistent with Sofianos and Johns (2007) who observed concentrated values of the core during August-2001 along the eastern side at the southern part of the basin, represented by temperature (17°C), salinity (36 psu) and dissolved oxygen ($8.8 \mu\text{mol/kg}$), respectively. Therefore, it is obvious that the GAIW flows into the Red Sea through a pathway mainly along the eastern boundary unlike the RSOW which was observed to flow out the Red Sea basin along the western boundary of the Red Sea. The simulation results also showed that due to an interaction with anticyclones systems present in the southern region, the intrusion propagates to the interior of the southern region.

The model shows that a maximum northernmost limit of the intrusion occurs in August reaching a latitude of $\sim 17^\circ\text{N}$ with current velocity of about 0.5 m/s. Robinson (1973) observed the northernmost limit of the cold subsurface inflow at 18°N in October. On the basis of mean summer inflow rate of Murray and John (1997) (0.22 Sv and 50 m mean layer thickness) it has been suggested that the GAIW intrusion would reach only up to 16°N at the end of August, assuming that little or no mixing process occur (Sofianos and Johns, 2007). Based on historical data, Smeed (1997) estimated the northernmost limit of the intrusion to be occurring in the end of September. Sofianos and Johns (2007) hypothesized the latitude 16°N to be the northernmost limit since temperature and salinity values of the GAIW were not detected north of 22°N latitude. The northernmost limit of the subsurface inflow as observed in Figure 7.6 shrinks to the latitude of 16°N in September lasting up to October. Although the inflow becomes weak in October, it remains flowing northward. In November, the flow direction in the southern portion including the strait becomes reversed; therefore the existing core of the GAIW in the southern part of the Red Sea (at 18°N) is trapped inside the eddy regime and due to mixing processes diminishes gradually. Although the influence of the eddy features present in the surrounding area of intrusion can extend the GAIW further north, the model does not show a signal north of 18°N (Figure 7.6).

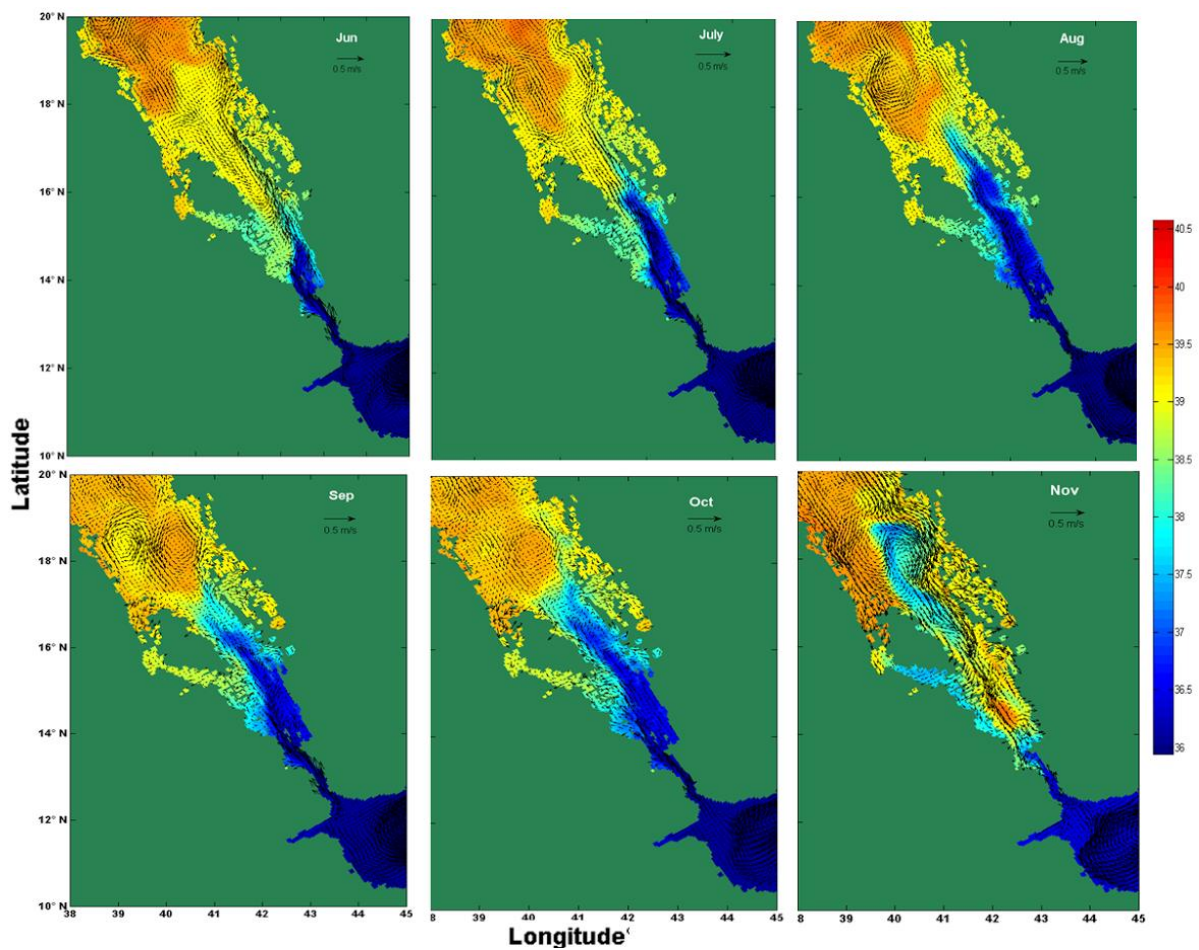


Figure 7.6. Horizontal distributions of salinity field (psu) and currents (m/s) at 80 m depth from June to November representing the full cycle of Gulf of Aden intrusion (GAIW) and its structure of propagation into the Red sea.

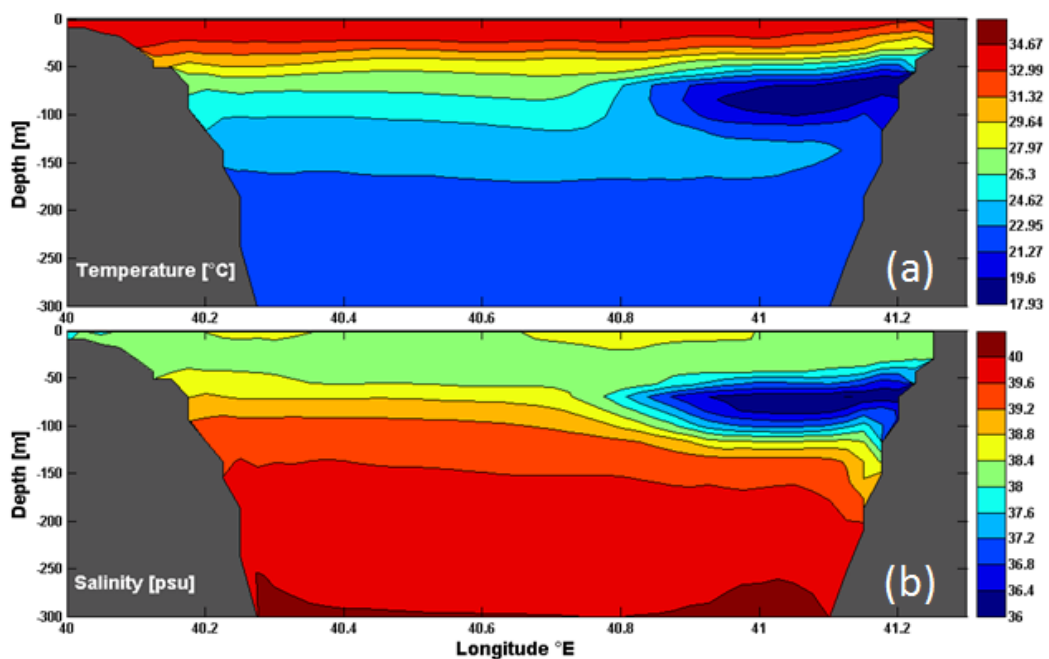


Figure 7.7. Vertical cross-section of (a) temperature and (b) salinity at 16°N based on RS-Model during August-2008.

7.5 Intermediate circulation

In this section, the circulation features associated with the most hypersaline RSOW which flows out the Red Sea basin through the bottom of Bab el Mandeb Strait are described based on the simulation results. Although the circulation at this depth level is much weaker compared with the surface layer, the influence of the surface feature is reaching the depth of RSOW layer. In the north, we can observe that the strong surface anticyclonic eddies located at 27°N, 25°N and 23°N respectively affect the flow at this depth level (Figure 7.8). The influence of the main dynamical feature in the northern part (a permanent cyclonic circulation) is also pronounced. Its signature is acting as a boundary current along the eastern boundary. These coastal currents continue parallel to the eastern shelf following the bathymetry structure and at the extreme north due to the limit of the basin they wrap into the western shelf. Maximum magnitude is achieved with the permanent anticyclonic eddy located at 23°N (> 0.2 m/s). This permanent feature was observed by Quadfasel and Baunder (1993) to penetrate to a depth of 300 m and its maximum velocity was recorded at a depth between 100-150 m.

South of 20°N, the effect of the surface circulation features is obviously much weaker than in the northern part. The general flow is directed southward however, the magnitude of the southward flow between the adjacent layers of the shallow shelves on both sides in the southern Red Sea (16°N and south) is less compared to the winter season, indicating a smaller amount of transport associated with the summer RSOW as discussed in section 7.3. The highest velocities (0.2 m/s) were observed at the area where the strait is narrowing its land-water boundary as a result of topographic restrictions.

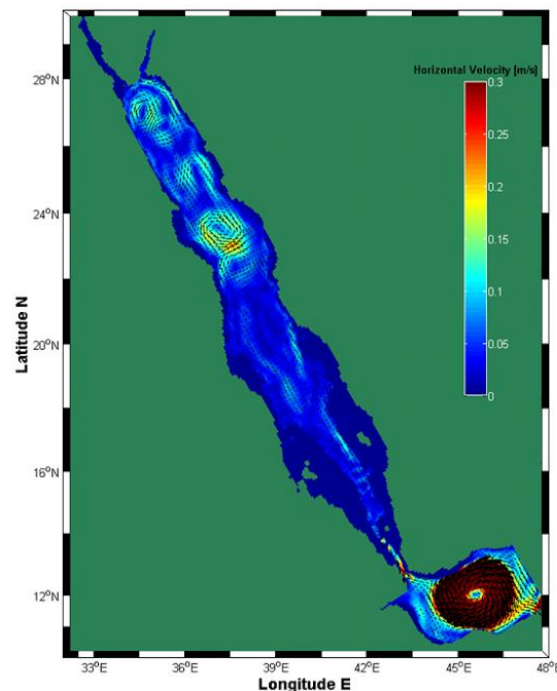


Figure 7.8. Mean current velocity field in the Red Sea at depth 140 m representing the RSOW based on RS-Model over summer season (June-September).

7.6 Circulation patterns and thermohaline structure (winter season)

This section describes the simulated circulation features during the winter season. To represent the patterns of circulation in the Red Sea, the simulation results over January to March are averaged.

7.6.1 Horizontal patterns of the circulation

The simulated surface circulation field in the Red Sea during the winter season is shown in Figure 7.9. The surface current field involves variable patterns including both cyclonic and anticyclonic eddies feature. We note that the resulting mean circulation is rather complex during the winter season unlike the summer season where eddies fields are organized almost along the axis (see section 7.2.1). To explain the major features of the surface circulation, the basin was divided into two regions mainly: the northern region (North of 20° N), and the southern region (south of 20° N).

North of 20 °N, the major patterns observed are series of cyclonic eddies located at ~ 27.5°N, 26°N, 23.3°N and anticyclonic eddies mainly closed to the western boundary centred at 27°N, 25°N, 22.5°N and 21°N respectively. The cyclonic eddy in the extreme north has been identified through previous observational studies to be a permanent feature of the circulation system during winter season. In addition to being observed in our model, such cyclonic system was also observed recently during the midsummer-2001 observations of Sofianos and Johns (2007), in the modelling studies of Sofianos and Jonhs (2003) and Yao et al. (2014b). Accordingly, the northern part of the Red Sea is cyclonically dominated throughout the year. It should be mentioned that the cyclonic eddy produced by the RS-Model is different in shape from the one produced by the former modelling study while somewhat similar with the latter. However, the exact location and strength include some variability.

The simulation results show that the current speeds associated with eddies system is in the range of 0.5-1 m/s (Figure 7.9) with exception of the cyclonic eddy around 23.5°N which involves higher speeds (> 1 m/s) and extends almost across the entire width of the basin. The simulation also shows the presence of a northward-flowing eastern boundary current north of 24° N which eventually interacts with the cyclonic eddy in the extreme north and switches to the western boundary due to the northern limit of the basin.

In the southern portion of the Red Sea, strong northward surface current (NNW) flowing inside the Red Sea from the Gulf of Aden through the strait of Bab el Mandeb with velocities varying with the strength of the inflow are pronounced (Figure 7.9). The obvious dynamical process which derives the inflow through the strait is the wind field where the dominant wind direction is SSE during this period. Inside the strait, as can be seen the inflow magnitude is intense with velocities exceeding 1 (m/s). The inflow enters the southern part of the Red Sea intensified along the western coast (12-15° N) which is in agreement with observational study of Vercelli (1931). At about 16°N, major part of the inflow propagates almost along the main axis of the Red Sea basin and interacts with a cyclonic eddy centred at 18°N. Maximum

velocities attached with the inflow inside the southern part of the basin ranged between 0.5-1 m/s.

In comparison with previous modelling studies carried out in the Red Sea, Sofianos and Johns (2003) found in a 9-year mean winter circulation that the inflow is concentrated along the western boundary and at latitude 16°N it switches to the eastern boundary and continues towards the northern part of the Red Sea as a narrow boundary current. In a numerical experiment driven only by thermohaline forcing they found that the shifting occurs further north at 19°N . They argue that the switching latitude is the latitude beyond which Rossby waves are no longer possible. In the study of Eshel and Naik (1997) a similar feature of shifting boundary currents from the western to the eastern side were observed however at different latitude (25°N). The switching in their study was attributed to the collision of the northward western boundary current with southward flow coming from the eastern boundary. On the other hand, the climatological mean for February in the simulation of the MIT general circulation model (Yao et al. 2014b) showed that the eastward cross-basin current takes place at 24°N . The switching of the western boundary current at this latitude was attributed to the change of the vertical mixing and the resulting change of dynamical balance rather than critical latitude related to Rossby waves.

The picture in our model is not very clear since the results represent only mean winter circulation of a single year which involves several eddies where such feature can be observed clearly through time averaging over several years (e.g. Quadfasel and Baudner 1993; Zhai et al. 2015). In general, the model (scenario-I) shows that at $\sim 16^{\circ}\text{N}$, the inflow deviates into the main axis of the Red Sea and interacts with a cyclonic eddy located around 18.2°N . As a result part of the inflow veers towards the western boundary and part propagates along the main axis which eventually interacts with the eddies in its path. However, as will be shown later in the additional numerical experiments (section 7.7), the surface circulation is mainly wind-driven, and the cyclonic eddy present in the full forcing experiment especially in the southern portion of the basin does not show up in the thermohaline-driven circulation experiment. In the absence of the cyclonic eddy in scenario-II, we note that the western northward inflow reaches almost mid-basin and at $\sim 21^{\circ}\text{N}$ it crosses to the eastern side.

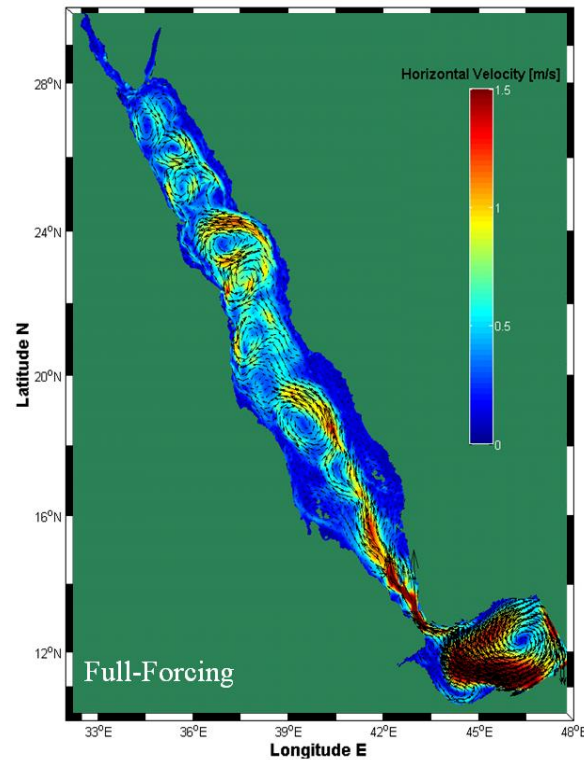


Figure 7.9. Mean surface current velocity field in the Red Sea based on RS-Model over winter months (Jan-March) [Full forcing].

7.6.2 Horizontal patterns of the thermohaline fields

To represent the horizontal distribution of sea surface temperature (SST) and sea surface salinity (SSS), the simulation results over January to March are averaged. Figure 7.10 (a, b) shows the horizontal distribution of simulated SST and SSS fields. As already stated in the summer season, the horizontal patterns of the thermohaline fields are highly influenced by the prevailing wind regime in the Red Sea region. The prevailing wind direction during this period is north-westerly north of 19° N and south-easterly monsoon events dominate south of 19° N. The horizontal distribution clearly reflects that there is a zone in the middle part of the Red Sea (16° N- 21° N) characterized by high SST due to the weak wind velocity in this region where the wind condition is convergent for most of the year (Figure 7.10-a). The major features during this period is a surface inflow of warm water (24 - 25° C) coming from the Gulf of Aden through the Strait of Bab el Mandeb which tends to flow northward. This feature is in agreement with previous observational studies (e.g Maillard and Soliman 1986; Murray and Johns 1997 and Smeed 2004) carried out in the Bab el Mandeb strait. Associated with inflow, SST increases from the southern part of the basin (just north of Bab el Mandeb) towards the north reaching about 27° C at 20° N and above that latitude (20° N) the SST tends to decrease gradually towards the northern part of the Red Sea reaching about 23 - 24° C. Another observed pattern is the downwelling events occurring along the eastern boundary between the Latitudes 16° N and 20° N. Concerning the SSS distribution, the simulation results show that the SSS in the Red Sea exhibits gradual increase from the southern part (36 psu) (near Bab elMandeb Strait) towards the northern part reaching about 38.5-39 (psu) in the

middle part of the basin and maximum values 40 psu are found at the extreme north as a result of high evaporative freshwater loss (Figure 7.10-b).

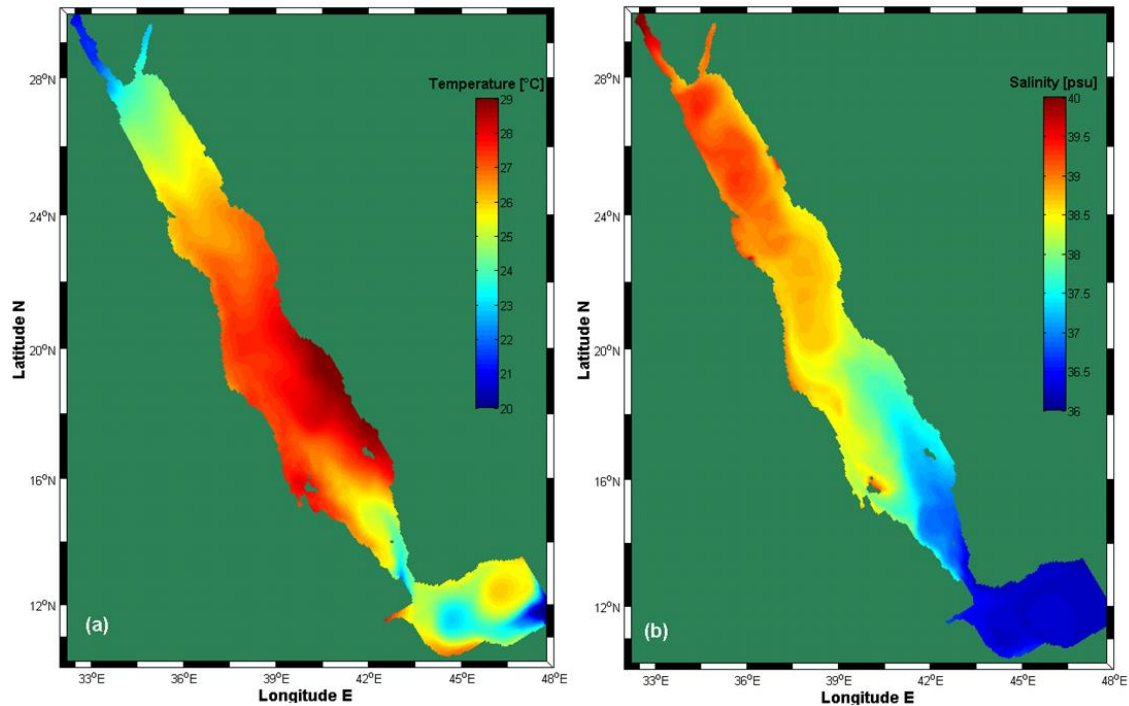


Figure 7.10. Horizontal distribution of simulated (a) sea surface temperature SST ($^{\circ}\text{C}$), (b) sea surface salinity SSS (psu) during winter season (Jan-March).

7.6.3 Vertical thermohaline structure

Figure 7.11 (a, b) shows the vertical structure of the temperature and salinity along the main axis of the Red Sea basin (see location of the meridional section in Figure 3.10). Similar to the summer season, the analysis is focused only on the upper 400 m depth since the thermohaline characteristics below the depth of 300 m in the Red Sea basin is characterized by water of remarkably homogenous temperature ($\sim 21.5^{\circ}\text{C}$), salinity (40.5 psu) and density (28 kgm^{-3}) as observed in the model and also reported by previous studies (e.g. Sofianos and Johns 2007).

In the upper layers, the monsoonal winds blowing over the region, the strong evaporation component and the flow regime existing in the southern part with the Gulf of Aden evidently lead to strong latitudinal gradients in the surface layers. The mixed layer during the winter in the Red Sea basin is found to be deeper unlike the summer season (see section 7.2.2). In the northern part, (north of 24°N), the mixed layer extends to 150 m depth with temperature of 24°C while south of 24°N and towards the southern part of the basin the mixed layer decreases gradually to the depth of approximately 100 m (Figure 7.13-a). Maximum temperature ($\sim 27\text{-}28^{\circ}\text{C}$) is observed in the intermediate region ($16 - 20^{\circ}\text{N}$) that develops only during winter due to the weak NNW winds and the strong SSE winds. The thermocline

layer extends to around 230 m where temperature decreases from 24 °C to 22 °C in the northern part and from 27 °C to 22 °C in the middle and southern part of the Red Sea.

In terms of salinity (Figure 7.11-b), the simulation results indicate that the salinity in the Red Sea increases gradually with depth reaching its maximum at 40.5 (psu). The variation in the deeper layers is neglected due to isolation from the Gulf of Aden by a sill at a depth of 160 m located in the southern part of the Red Sea region. Figure (7.13-b) shows that the upper layer in the northern part of the Red Sea is characterised by high salinities ~ 40 psu while south of 24 °N to 16 °N by less salinity ranging between 37.5-38.5 psu. The simulation results showed that the Red Sea involves highest evaporation heat fluxes in the northern part during winter season, indicating that the salinity is enhanced by the evaporation component significantly unlike the temperature which faces seasonal variability. This is described in more detail in section 7.8 in association with the intermediate water mass formation. The halocline structure during the winter occurs between 100-150 m depth with salinity ranging between 38.5 and 39.5 psu particularly in the middle and southern part. South of 16°N, the existence of a 2 layers flow regime represented by the inflow of fresher surface water 36 psu and hypersaline outflow water (RSOW) present at ~ 160 m depth is obvious.

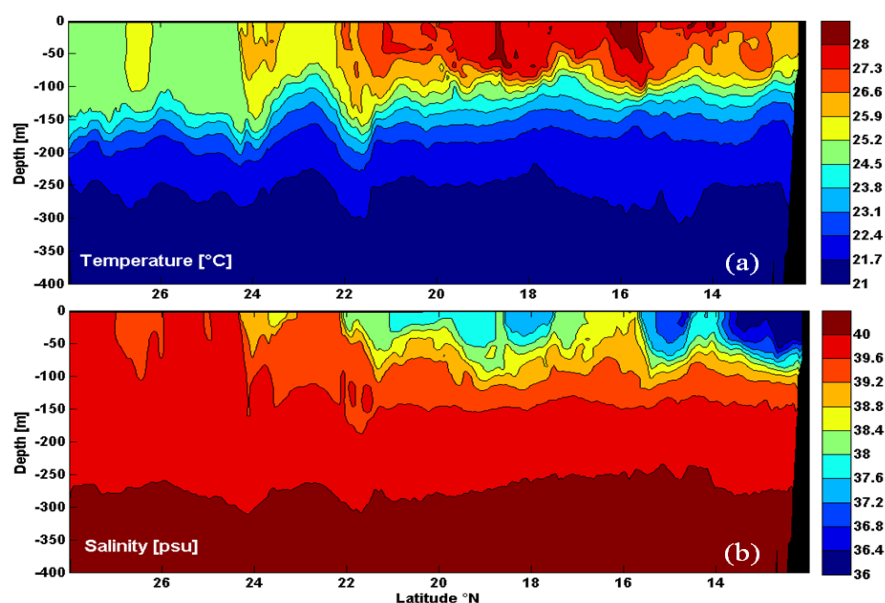


Figure 7.11. Vertical distribution of simulated (a) temperature (°C) and (b) salinity (psu) along the main axis during winter season (June-September) based on RS-Model, [Scenario-1: Full forcing].

7.7 Experiments of Wind and Thermohaline Forcing

As stated previously in Chapter 3, there is a general agreement that the thermohaline and wind forces drive the large-scale two-dimensional circulation in the Red Sea. The RS-Model simulation in addition to the recent observations (Sofianos and Johns 2007) and previous modeling studies showed that the circulation in the Red Sea is rather a complex three-dimensional structure. However, there has been much debate on the relative importance of wind and thermohaline forcing in driving the circulation and stratification in the Red Sea. Several researchers believe that circulation is attributed to thermohaline forcing on the basis of incoming fresh and warm water from the Gulf of Aden into the Red Sea which moves northwards and due to excess of evaporation over precipitation, formation of very saline (> 40 psu) water mass takes place. As a result, the formed dense water sinks and flows out of the Red Sea over the shallow sill at Bab el Mandeb strait (Maury 1855; Phillips 1966; Eshel et al. 1994; Tragou and Garrett 1997). On the other hand, Thompson (1939a); Siedler (1969); Patzert (1974a) argued that wind-stresses are the primary component while the thermohaline forcing plays a secondary role in determining the circulation patterns.

The simulation of 9-year mean circulation (driven by monthly mean climatological conditions of the Red Sea) showed the dominance of the thermohaline forcing over wind-stress forcing in driving the circulation in the Red Sea (Sofianos and Johns 2003). However, the relative contributions of driving forces to the circulation in the Red Sea on seasonal scale are still not clear. Therefore, in this section we investigate the influence of wind and thermohaline forcing and their role on the circulation during the summer (June-Sep) and the winter seasons (Jan-March) respectively.

Buoyancy forcing and the mixed layer depend mainly upon the effect of wind speed and their dynamical interactions play a major role in the final circulation and stratification patterns (Gill 1982). Therefore, it is difficult to separate the thermohaline driven-circulation from the wind-driven circulation since the ocean is not a linear system. Nevertheless, the numerical modelling approach is an appropriate method to investigate different driving forces and their role on the circulation. As such, in this study we carry out additional numerical experiments aiming at defining the relative contributions of wind and thermohaline forcing in driving the seasonal circulation patterns. To achieve the aim, two numerical experiments consisting of the same model configuration of scenario-I but using different combinations of forcing were performed. To determine the effect of wind-stress forcing and its role on the circulation, a numerical experiment (Scenario-II) was performed considering only the thermohaline fluxes. Therefore, no wind is imposed in this scenario. In the third numerical experiment (Scenario-III), the surface heat and salt fluxes were removed but wind-stress field is included.

7.7.1 Horizontal patterns of the circulation (summer season)

To investigate the influences of wind field and thermohaline fluxes and their role on the key features, the results of the two scenarios are analyzed and shall be compared with scenario-1 (section 7.2.1). Figure 7.12 shows the resulting surface layer circulation field from the two numerical experiments over (June-September). The major characteristics features emerging in

the thermohaline experiment are a series of cyclonic eddies located at 27°N, 25.5°N, 23.5°N, 21°N and 18°N respectively (Figure 7.12 left panel). Note that, the cyclonic eddies located at 25.7°N and 23°N involve higher magnitudes compared with the remaining cyclones. The main circulation features appearing in the wind-driven circulation experiment is a chain of anticyclones eddies located around 27°N, 25.5°N, 23.5°N, 22°N, 21°N and 18°N respectively (Figure 7.12 right panel). In addition to that, a western boundary current is observed north of 24°N. The main permanent feature of the circulation is the anticyclone system located around 23.5°N while the features located at 21°N and 18°N are considered as quasi-permanent anticyclonic features as shown previously in section 7.2.1.

It is obvious that the wind-driven circulation achieves higher velocities than the thermohaline-driven circulation. Comparing the resulting features with the surface layer circulation that emerged in Figure 7.1, we observe that the surface patterns in the absence of wind forcing are of cyclonic rotation unlike the combined forcing features. The numerical experiment of scenario-III (wind included) produces similar surface features (anticyclonic eddies) to the circulation patterns obtained from full forcing scenario. This indicates that they are driven by the same physical phenomenon which is the wind-stress forcing. Accordingly, when the two mechanisms compete with each other, the wind-stress forcing dominates the surface circulation. Furthermore, the western boundary current observed in the combined driven circulation is only seen in the wind-driven circulation. Therefore, the general circulation pattern produced by the combined forcing during the summer is largely attributed to the wind-driven experiment. Our model is driven by high-frequency atmospheric forcing. The results are in contrast with the simulation of 9-year mean circulation (driven by monthly mean climatological conditions of the Red Sea) of Sofianos and Johns (2003). They showed that the purely wind-driven circulation produces much weaker circulation than the thermohaline circulation. However, the western boundary current (at 22°N) in their model is observed only in the wind-driven circulation.

The simulated surface gyres of the RS-Model are observed to extend across the entire width of the Red Sea basin (Figure 7.1); in particular north of 20°N, hence an indicative of topographical restriction. As stated in Chapter 3, the wind direction in the Red Sea is parallel to the main axis of the basin and during the summer season the prevailing direction is NNW. The resulting surface circulation feature from a wind-driven circulation scenario evidently show the important role played by the wind-stress field in generating the gyres systems. In a relevant study, Quadfasel and Baudner (1993) investigated the dynamics of the northerly wind case and the resulting circulation during the two monsoon seasons. They used a rather simple rectangular basin and rectangular basin with bathymetry narrows that not taking into account the complicated bathymetry of the Red Sea. The rotation of the wind was observed to cause upwelling along the eastern boundary and downwelling in the western side. The presence of such processes in the northern half of the basin was also observed in our model (Figure 7.2). Furthermore, their results showed the existences of only anticyclonic gyres along the basin during the SW monsoon. The RS-Model in the present study is configured with realistic bathymetry; and its results reflect the distributions of this simple basin considered in their investigation.

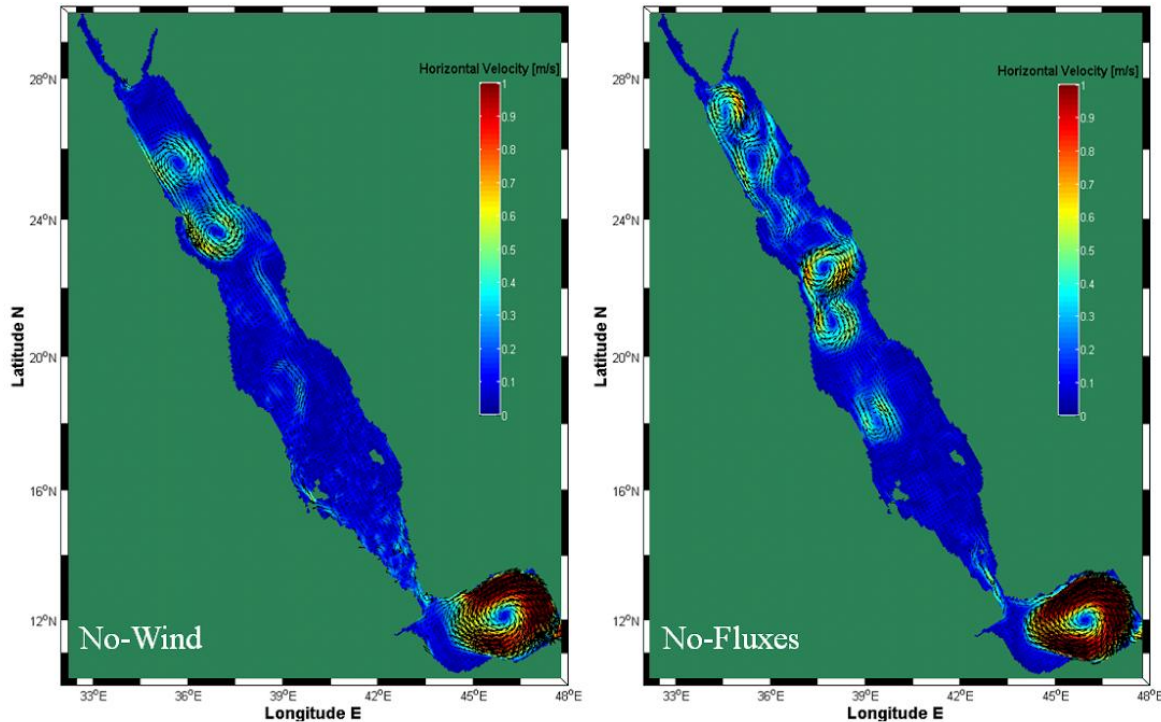


Figure 7.12. Mean current velocity field in the Red Sea based on scenario-II (No-wind) and scenario-III (No-Fluxes) over summer season (June-September).

7.7.2 Horizontal patterns of the circulation (winter season)

To estimate the relative importance of wind field and thermohaline fluxes and their role on the key circulation features, the results of the two scenarios are analyzed and shall be compared with scenario-I (section 7.6.1). Figure 7.13 shows the resulting surface circulation field from the two numerical experiments over the representative period of the winter season (Jan-March).

In general, it is evident that the wind field (Figure 7.13 right-panel) contributes considerably to the surface circulation than the thermohaline forcing. This can be observed when comparing the results of the two scenarios with the surface features resulting from scenario-I which includes all the forcings (Figure 7.9). We observe that the surface patterns in the absence of wind forcing (Figure 7.13 left-panel) are largely differed, unlike the numerical experiment of scenario-III (wind included) which produces similar surface features to the circulation patterns resulting from full forcing scenario-I.

In the removed surface fluxes experiment, we observe for instance that the wind field plays major role in generating the cyclonic feature located at 23°N and involves higher velocities than the thermohaline-driven experiment. The distinguish feature emerging in the numerical experiment of NO-Wind (scenario-II) is that the intensified inflow in the southern part mainly deviates to the western boundary unlike in the wind-driven circulation where it deviates to the main axis of the basin as in scenario-I. This indicates that when the two forcing compete with each other, the wind-stress forcing controls the inflow. It is interesting to note that the

cyclonic eddy located in the extreme north is driven by the thermohaline forcing while in the wind-driven circulation the anticyclonic feature is dominant. Similar fact was also observed in the study of the summer season.

In the modelling study of Sofianos and Johns (2003) (model forced by climatological conditions) the 9-year mean surface circulation produced from the thermohaline forcing experiment was stronger than the wind-driven circulation and in general similar to the circulation obtained from the full forcing experiment, indicating the wind forcing plays a secondary role. Our model is forced with high-frequency atmospheric forcing and suggests that the wind forcing is the primary mechanism deriving the surface circulation. The wind regime in the Red Sea basin is commonly known to be controlled by the high mountain existing on both sides of the basin. Thus the general direction of the monthly mean is mostly aligned along the axis of the basin. However, there are breaks in the topography at few locations which play major role in altering the wind patterns through the gaps. In a relevant study, Clifford et al. (1997) emphasized that the formation of eddies in the Red Sea depends upon the wind direction and there are more eddies when the wind has a cross-basin component while less eddies when the wind is directed along the axis. The importance of mountain gaps along the eastern and western sides of the Red Sea basin has been recently highlighted by Jiang et al. (2009).

Based on a high-resolution regional atmospheric model, two types of cross-basin wind-jets were identified: i) eastward wind-jet originating from the Tokar Gap on the African side (Sudanese coast) at $\sim 19^{\circ}\text{N}$ with velocities of 20-25 m/s during the summer and ii) westward wind-jet bands along the north-western Saudi Arabian coast during winter characterized by wind speeds over 15 m/s. Although the surface circulation produced by the RS-Model is considerably attributed to the wind forcing, the thermohaline forcing experiment shows eddies that are mainly thermohaline driven. For example, the eddy located at 24°N is only emerged in the thermohaline experiment and does not appear either in the wind forcing experiment or in the full forcing experiment.

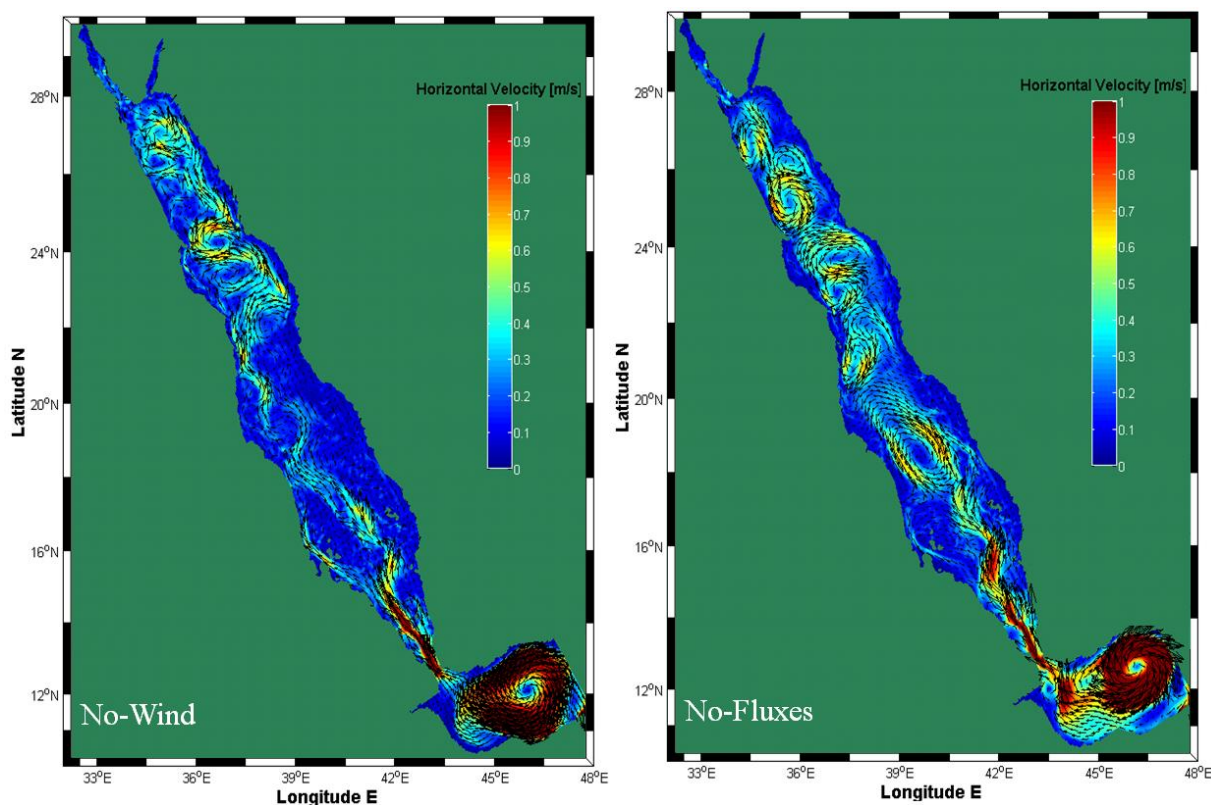


Figure 7.13. Mean current velocity field in the Red Sea based on scenario-II (No-wind) and scenario-III (No-Fluxes) over winter season (Jan-March).

7.7.3 Vertical thermohaline structure (summer season)

Figure 7.14 shows the vertical structure along the main axis of the Red Sea resulting from the two numerical experiments. A comparison between Figure 7.3 and Figure 7.14 leads to recognition of the effect of wind and thermohaline forcing. The change of the interior water mass structure due to separation of both forcing is very obvious. In general, the most important feature is that the wind forcing experiment (Figure 7.14 c,d lower panel) to large extent produces similar strength of the intrusion of GAIW in magnitude to that observed in scenario-I (Figure 7.3), suggesting the important role played by the physical phenomenon in driving the GAIW during the summer.

7.7.4 Vertical thermohaline structure (winter season)

The vertical distribution of temperature and salinity resulting from Scenario-II (upper panel) and scenario-III (lower panel) is shown in Figure 7.15. A general comparison between Figure 7.11 and Figure 7.15 leads to the identification of the effect of wind and thermohaline forcing. The change of the interior water mass structure due to separation of both forcing is very evident. The important role of the wind stress on the upper layers is represented by a dynamic instability which enhances the vertical mixing and increases the surface inflow in the southern part due to the southeasterly wind regime (Figure 7.15 c,d lower panel). However, the thermohaline forcing seems to be stronger than the wind forcing during the winter season. This evident in Figure 7.15 (upper panel (b)) where the inflow magnitude is

increased towards the north reaching latitude of $\sim 18^\circ\text{N}$ unlike the inflow magnitude resulting from the full forcing scenario was observed to reach at 16°N .

However, such a simple comparison does not provide a complete picture on the main mechanism that causes the seasonal cycle. There is incomplete understanding about the role of the seasonal wind and thermohaline forcing and their relative importance. The relative importance of the direct surface wind stress and the indirect effect has been investigated in a modeling study of Sofianos and Johns (2002). Their results suggest that both direct and indirect effects of the surface wind are of similar importance in driving the summer flow. Siddall *et al.* (2002) suggest that the surface wind has minor direct influence on the summer flow. They suggest that the surface temperature plays major role in controlling the exchange system in the strait of Bab el Mandeb. On the other hand, Patzert (1974a) argued that the upwelling process occurring at the northwestern Gulf of Aden (which causes a drop in sea level and produces reversal pressure gradient at intermediate depths) is the main mechanism for the reversal of the summer flow.

A comparison of the mean transport layer values between the three numerical experiments (Scenario-1, Scenario-II and Scenario-III) have been carried out to assess the role played by each forcing mechanisms. Figure 7.16 shows the monthly mean values of the layers transport of the two experiments and shall be compared with scenario-I (section 7.3). It can be seen that in the absence of wind forcing the surface and intermediate layers still include a seasonal cycle (Figure 7.16 upper panel). However, the reversal regime of the surface layer is not observed; indicate the important role of the wind forcing. Moreover, the GAIW inflow exceeds even the summer season and continues into early winter. It is obvious that the RSOW outflow behaves differently where it includes less seasonal cycle unlike the full forcing experiment which showed strong seasonal cycle. The annual mean RSOW outflow is found at 0.395 Sv.

On the other hand, the major difference emerging in the absence of thermohaline forcing (Figure 7.16 middle panel) is the shrink of the RSOW outflow. The annual mean RSOW outflow is estimated at 0.26 Sv. Compared with the first scenario (Full forcing), this value represents about 44%. It is obvious that the flow exchange resulting from this experiment is weaker compared to the full forcing experiment. Unlike the experiment of NO-Wind forcing the seasonal cycle of the exchange system especially the reversal regime of the surface flow is evident. Comparing the first scenario with the sum of the two numerical experiments indicates that the final characteristics of the flow regime in the strait are not a result of a simple linear system of the two forcings (Figure 7.16 bottom panel). The figure shows that the intermediate layer (GAIW) inflow exists while the reversal surface regime disappears. Although the thermohaline-driven experiment (scenario-II) reflects major role in driving the flow exchange, the influence of the wind forcing cannot be neglected since the final characteristics of the exchange system is produced by the interactions of both forcings as revealed in the model.

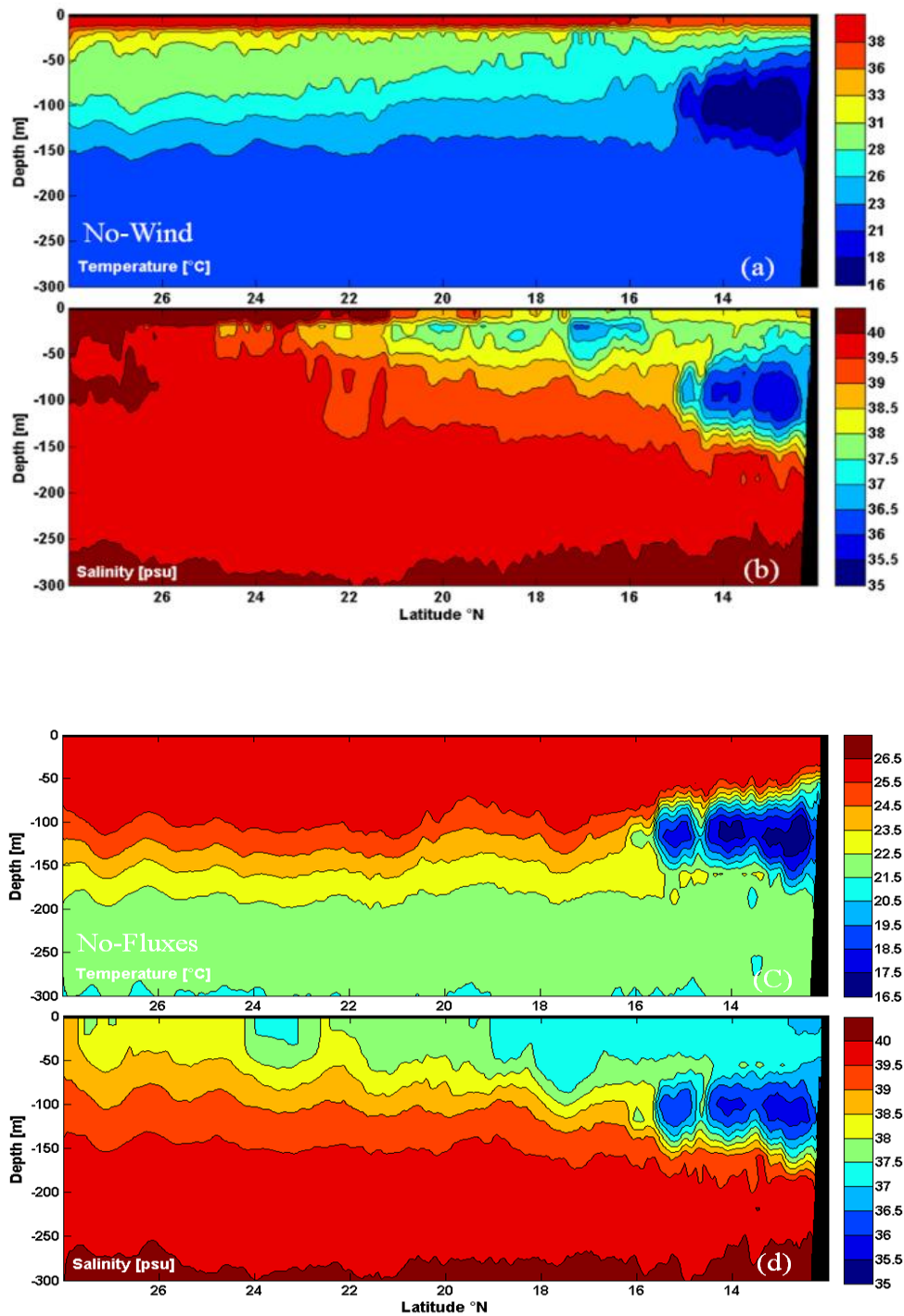


Figure 7.14. Vertical distribution of (a) temperature and (b) salinity during summer season based on scenario-II (No-wind) and scenario-III (No-Fluxes).

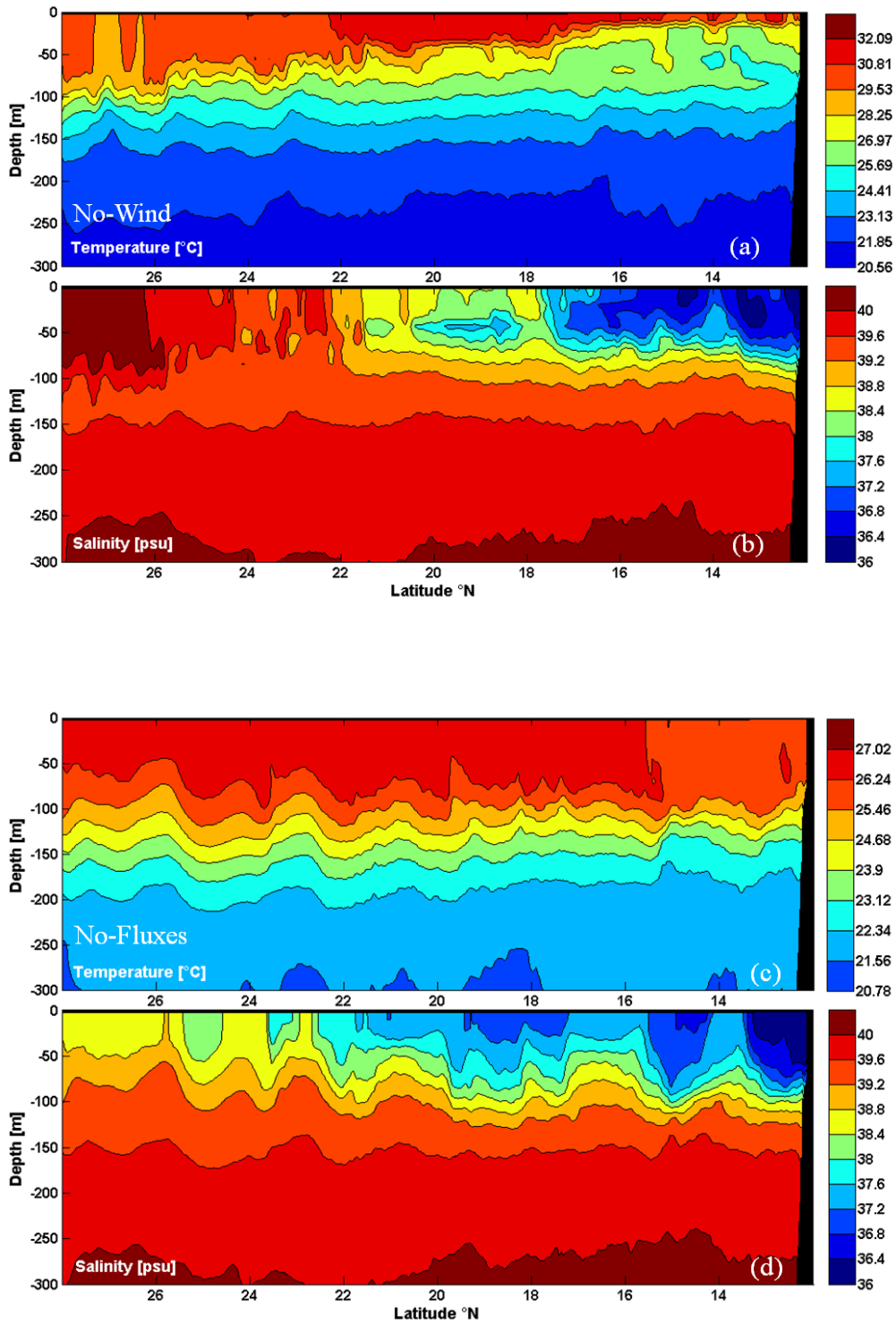


Figure 7.15. Vertical distribution of (a) temperature and (b) salinity during winter season based on scenario-II (No-wind) and scenario-III (No-Fluxes).

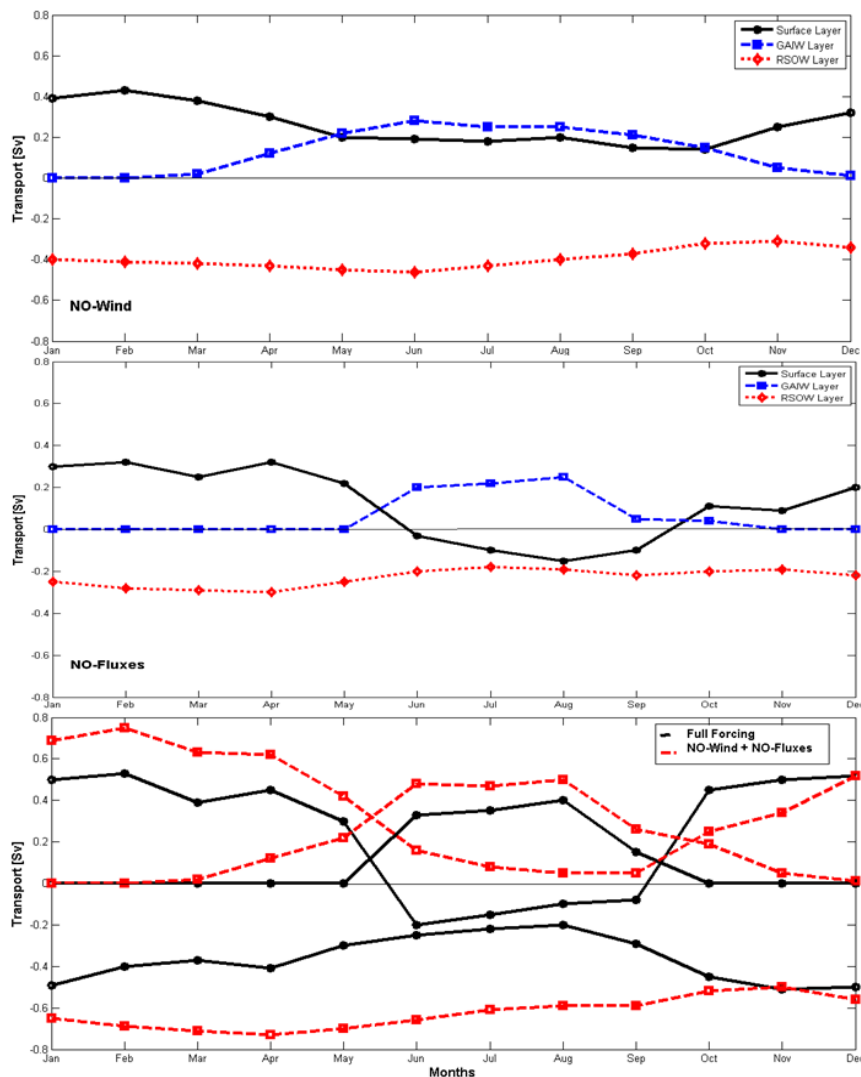


Figure 7.16. Monthly means of transport for Surface, Intermediate and deep layers at a cross-section located at $\sim 12^\circ\text{N}$. top (Scenario-II), Middle (Scenario-III) and bottom (Scenario-I and sum of Scenario-II and Scenario-III).

7.8 Formation of water masses in the Red Sea

As a result of excess evaporation over precipitation and ocean heat loss in the Red Sea, relatively saline intermediate and deep water is formed (Eshel and Naik, 1997; Sofianos and Johns, 2003). The produced dense intermediate or/and deep water masses usually holds distinct water properties. The major source of the information about subsurface and deep circulation in the Red Sea is based on tracer and oxygen observations. Based on geochemical tracer distributions (^{14}C and ^3He), Cember (1988) observed two water masses involving the core of the saline outflow water that leaves the basin through Bab el Mandeb strait and is named Red Sea Outflow Water (RSOW). There has been some ambiguity around the Red Sea Deep Water (RSDW) and the so-called RSOW. The former occupies the Red Sea basin below ~ 200 m to the bottom while the latter just overlies the RSDW layer. Both the RSDW and RSOW share similar temperature and salinity characteristics.

However, recent analysis of oxygen observations (Woelk and Quadfasel, 1996; Sofianos and Johns, 2007) identified the dissimilarity between the deep and intermediate waters where the latter is characterised by high oxygen concentration.

There is a general agreement that the saline deep water mass formation is located in the northern part of the Red Sea predominantly during the winter when air temperatures are comparatively low. However, previous investigations have shown some controversy concerning the sources of the formation in the Red Sea and the exact mechanism of its production. Three different sources have been proposed for the RSDW formation. The relatively shallow Gulf of Suez (~ 50-70 m) was suggested as the main source for the RSDW formation on the basis of the presence of the higher salinities (~41 psu) which eventually sink into the bottom of the Red Sea (Maillard, 1974; Wyrki, 1974; Woelk and Quadfasel, 1996). The deeper Gulf of Aqaba (~1800 m) was proposed as a secondary source on the basis of the outflow of dense water over the shallow sill (300 m) of the strait of Tiran (Wyrki 1974; Murray et al. 1984; Plahn et al. 2002; Manasrah et al. 2004). The open-ocean deep convection mode at the northern part of the Red Sea was also hypothesized (Eshel et al. 1994). Woelk and Quadfasel (1996) claim that the formation is intermittent and does not take place every winter.

Regarding the intermediate water formation, the mechanisms involved in the RSOW formation, potential locations and exact period are still a matter of debate. Neumann and McGill (1962) claimed that the Red Sea outflow originates from intermediate depths. Based on T/S diagrams, Maillard (1974) suggested that the intermediate waters can form at all latitudes and the continental shelves in the southern Red Sea are expected as important formation location. Cember (1988) proposed that the RSOW is injected below the pycnocline layer. Recently, the simulation of Sofianos and Johns (2003) suggested that a large proportion of the hypersaline outflow water through the strait of Bab el Mandeb is formed through open-ocean convection associated with a permanent cyclonic gyre in the northern part of the Red Sea during the peak of the winter season. It should be noted that the model (10 km resolution) in their study was forced by monthly mean climatological conditions while the influences of high-frequency atmospheric conditions must be considered in order to capture such processes properly. According to Schott and Leaman (1991), in most of the known cases of open-ocean deep or intermediate water formation, the associated processes occur on shorter timescales, during events of strong atmospheric forcing.

7.8.1 Red Sea Outflow Water Mass (RSOW)

In this study, the mechanism involved in the RSOW formation including the period and possible locations are investigated. There are several mechanisms involved in the water mass formation. Open-ocean deep or intermediate convection is one of the most important mechanisms involved in the water mass formation in the ocean. It occurs usually in few regions of the world ocean mainly during winter season. As mentioned earlier in Chapter 2 several cases of deep water formation through convection process has been observed in the western Mediterranean e.g. the Gulf of Lion, the eastern Mediterranean Sea, the Labrador

Sea, the Greenland Sea ; Weddell Sea and it is believed to be main mechanism driving the thermohaline circulation.

Three widespread phases of convection have been identified earlier by MEDOC-Group (1970) and are used in all studies involving deep water formation through deep convection processes: the preconditioning phase, the violent mixing phase and the sinking plus spreading phase. There are three conditions required for open-ocean convection to take place: i) the water column is largely homogenized or weakly stratified, ii) the cyclonic gyre with a doming of isopycnals towards the surface at the centre of the gyre and iii) strong sea surface buoyancy loss to the atmosphere due to cooling and evaporation (MEDOC-Group 1970; Swallow and Caston, 1973). An example of such case is the eastern Mediterranean Sea where the formation of the Levantine Intermediate Water is localized winter process in the region of the Rhodes Gyre in the Levantine basin. Once, these conditions are fulfilled, strong vertical mixing occurs in the preconditioned area. In the violent mixing phase, convection is observed in the centre of the convective area, leading to strong mixing and deepening of the mixed layer. In the last phase “the sinking and spreading” the mixed water sinks and spreads away from the formation site horizontally.

In addition, there are studies that throw light on the baroclinic instability mechanism and its important role during the deep convection process especially in the Mediterranean Sea. It has been suggested that the spreading of dense water occurs through the action of eddies, i.e. believed to be produced at the edge of the convective patch by baroclinic instability mechanism of the rim current (Gascard, 1978; Herrmann et al., 2008; Lascaratos, 1998). Gascard (1978) proposed that the role of baroclinic instability mechanism can be at any instant including the preconditioning phase. The important role of baroclinic instability is represented by the strong atmospheric forcing scenarios that triggers deep convection in the centre of the preconditioned area. As a result a stationary “chimney” of mixed and dense waters is formed. When the atmospheric forcing weakens significantly or ceases, the chimney becomes highly unstable baroclinically and eddy shedding occurs quickly. This is followed by a breakup process of the chimney on a time scale of few weeks (Testor and Gascard 2006). Gascard (1978) observed eddies of about 5 km radius associated with a baroclinic wave-like pattern at the periphery of the convection area in the north-western Mediterranean and the Labrador Seas. In addition, a coherent eddy associated with deep convection in the Weddell Sea which remained for several months was observed by Gordon (1978). The researchers also highlighted that the preexisting eddies generated earlier by a large scale baroclinic instability of the main flow during the preconditioning phase may contribute to the formation of chimney. These “mesoscale” eddies characterized by uplift of isopycnals toward the surface would precondition for local deep convection at a smaller scale than large scale preconditioning which arises within a gyre circulation (Gascard 1978; Killworth 1979).

It can be concluded from the above mentioned that preconditioning is a primary requirement for open-ocean convection to take place. Considering the fact that the Red Sea basin is characterized by net buoyancy loss to the atmosphere due to heat and fresh water fluxes, the model results suggest that the formation process of RSOW occurs in the northern part of the

Red Sea. This can be explained on the basis of the strongest evaporation heat flux (averaged during winter) that exists in the northern Red Sea as shown in Fig. 7.17-a. The prevailing wind during winter period is north north-west (NNW) in the northern Red Sea which carries dry air to the sea. Simultaneously high wind velocity eliminates more heat and freshwater from the sea surface.

The simulated spatial distribution along the axis of the Red Sea shows that the largest evaporation heat flux takes place north of 24°N, and both the evaporation heat flux (Q_{ev}) and the total heat flux (Q_{tot}) decrease gradually from 20 °N southward. The heat loss due to evaporation is lower over the southern part with mean magnitudes around 75 W/m², whereas significantly higher evaporation heat fluxes with mean magnitudes around 200 W/m² is observed in the northern Red Sea. The free convection of latent and sensible heat also shows higher magnitudes north of 24 °N and lower values over the southern Red Sea (Figure 7.16-b). The intensive net of atmospheric forcing in this regard enhances the vertical mixing in the weakly stratified layer and therefore convection process takes place.

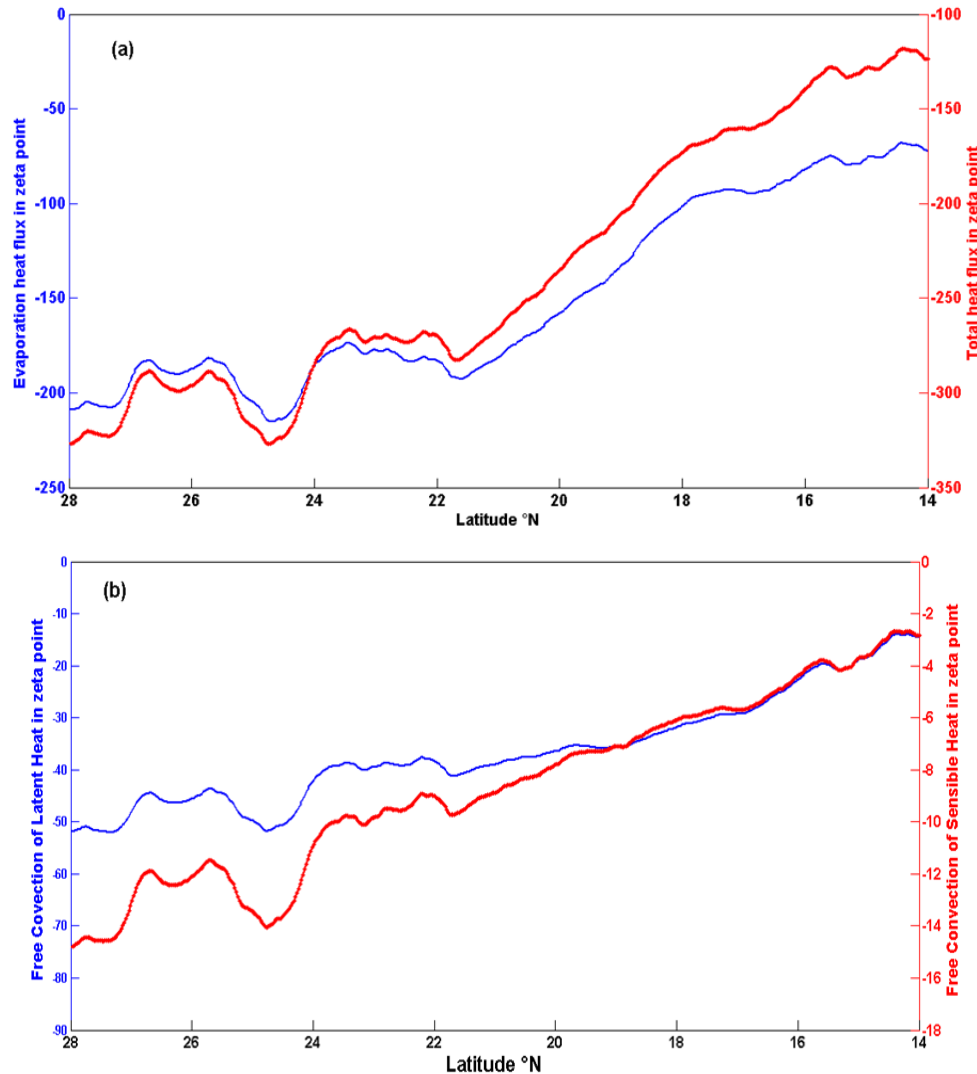


Figure 7.17. Axial distribution of (a) Evaporation heat flux and Total heat flux, (b) Free convection of Latent and Sensible Heat (average during Jan-March) based on the RS-Model.

Open-ocean convection process requires also cyclonic gyre with weak stratification features. Previous observational studies carried out in the northern Red Sea emphasized that there is a permanent cyclonic gyre located in the northern part of the basin (e.g. Morcos and Soliman 1974). Simulations of the RS-Model showed that the surface circulation in the northern Red Sea involve intense eddies activities (Figure 7.9). There is a cyclonic eddy in the extreme north of the Red Sea close to the eastern wall at $\sim 27.5^\circ\text{N}$ in addition to other cyclonic eddies further south. According to the model results, the diameter of the eddies range between 80 to 100 km. These features are indicative that the Red Sea experiences similar process of open-ocean convection. Therefore, it should be emphasized that the RSOW formation mainly occurs in the northern part of the Red Sea.

In order to investigate the phases of convection and the formation periods, the model results for a sequence months were plotted. Figure 7.18 depicts the average surface current velocity field superimposed on the density north of 20°N representing the period from October to March. The influence of strong atmospheric forcing on the surface waters is evident as indicated by high density values north of 24°N . This suggests that the densest intermediate water formed in the Red Sea is largely connected with the cyclonic eddies which carry the denser water from deeper depth to the surface through weak stratification. Figure 7.18 shows that water of higher density occupies the northern portion of the Red Sea basin (north of 25°N) in early winter. Maximum density value close to the RSOW is observed in the northern Red Sea during February and March respectively, giving indication about the period of production. The cyclonic eddy forms surface water with a temperature of about 23°C and salinity of 39.8-40 psu, giving a typical density 27.5 kgm^{-3} which is almost consistent with the density value of 27.7 kgm^{-3} observed at the strait of Bab el Mandeb by Sofianos et la., (2002).

To study the vertical structure and reflect the features associated with convection process, a Meridional transect of density structure along the main axis of the northern part (21.5°N to 27°N) representing the period from October to May is considered (Figure 7.19). The transect location is marked in Figure 7.18 (Feb). Figure 7.19 presents a sequence of the convection phases showing the erosion upper layer stratification cycle associated with influences of surface fluxes and the formation period of the intermediate water. In general, the erosion of the upper surface layer stratification seems to fulfil the convection process requirements. During the preconditioning phase, the role played by the cyclonic eddies is represented markedly by a doming of isopycnals towards the surface layers in the northern basin which makes the weakly stratified waters exposed to local cooling and evaporation processes. Therefore, the saline waters are brought close to the surface to be exposed to entrainment with mixed layer. This creates favorable conditions for deep convection since the surface water remains in the same depth level exposed to strong atmospheric forcing (Swallow and Caston, 1973). The strong atmospheric forcing in November dissipates the stratification in the extreme north (north of 26.5°N) and mixed the water to about 100 m depth. In December, strong atmospheric forcing events take place almost at all the northern part of the basin in which the mixing reaches down to ~ 150 m as reflected by homogenization of the water at this depth level.

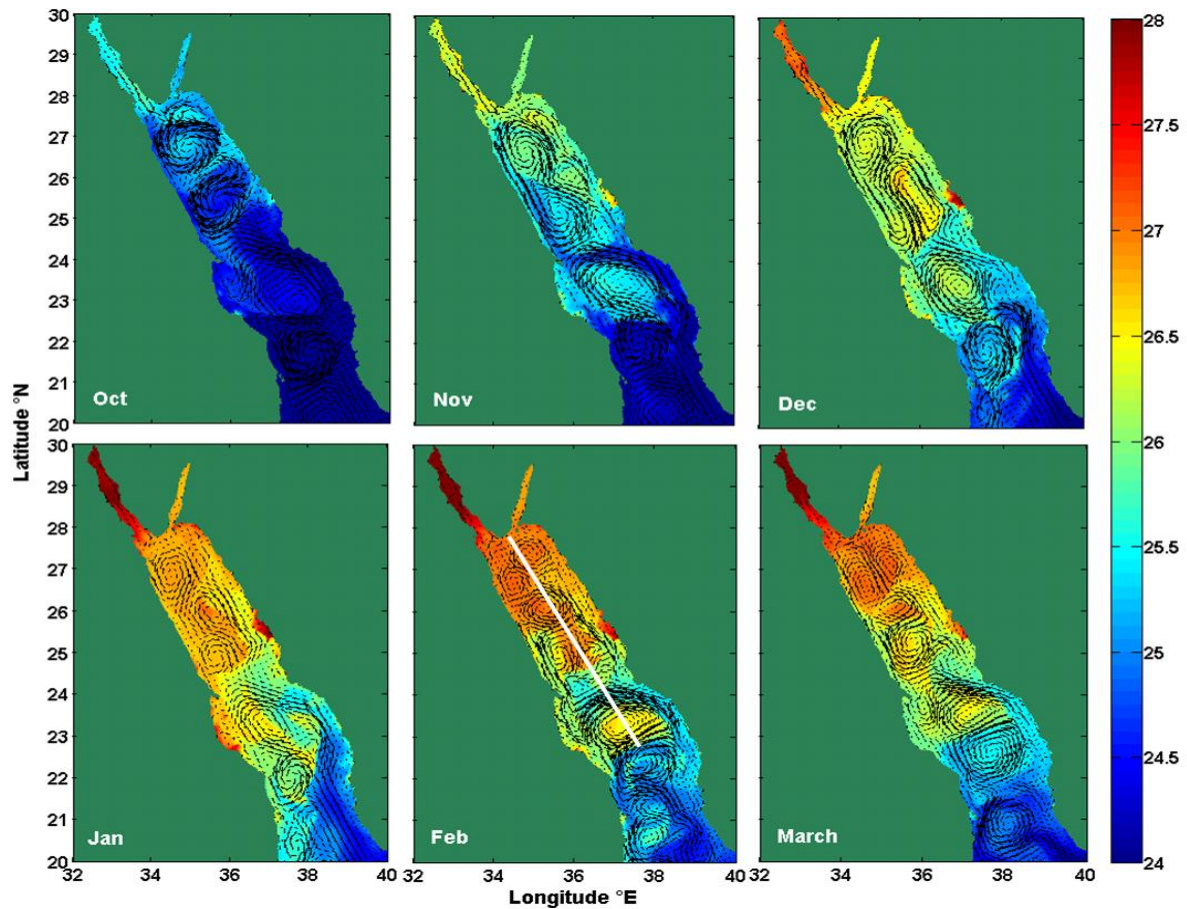


Figure 7.18. Simulated horizontal current field and density from the period October to March.

It can be seen that the strong surface cooling and evaporation processes with favorable preconditions trigger deep convection in January (Figure 7.19). Relevant studies of intermediate/deep water formation showed that convection depth might reach hundreds or thousands of meters (e.g. Levantine Sea 300 m; Gulf of Lion > 1000 m). In view of the fact that the RSOW moves towards the Gulf of Aden over a shallow sill (Hanish Sill) with depth of ~150 m depth, it is expected that the depth of convection in the Red Sea case may reach in the range of this depth level.

The simulation results show that in January, a narrow chimney of mixed, dense water (located at ~ 25.8°N) spans from the surface down to about 150 m depth is formed, where intense vertical mixing takes place under atmospheric forcing acting on the surface. As a result of atmospheric forcing fluctuations, the convective chimney becomes unstable baroclinically in February and March with vary widths, reflecting the important role of the baroclinic instability mechanism found in the Mediterranean Sea. The simulation also shows that there two major convective chimneys are formed in February and March with larger width centred around 26.5°N and 27.3°N. The density values inside these chimneys are related to the RSOW values, suggesting substantial production of dense intermediate waters

occurs during February and March. The deepening of the mixed-layer of both convective columns has similar depth reaching to the depth level where the RSOW is found and which is occupied within the depth between ~ 150 m and 200 m in the whole Red Sea basin. During spring (April), the chimneys feature starts to disappear and are followed by a collapse of the chimneys. As can be observed, the homogenous water layer remains as intermediate water below the surface after strong atmospheric forcing events ceases. The re-stratification phase of the mixed layer occurs very quickly and stratification conditions return during May.

The spreading pathway of the formed RSOW is investigated through the simulated flow field at 160 m depth (Figure 7.20), the typical depth of RSOW. Evidently the influence of the surface circulation features reaches this level depth. However, the magnitude is weaker compared with the surface circulation. The simulation shows a pronounced intensified southward boundary current along the western boundary (African boundary). The source of the southward western boundary current originates mainly from the edge of the baroclinic eddies, and also the crossing zonal currents from the eastern side to the western boundary around 21°N respectively. At 21°N and southward, the crossing-basin western boundary drives the hypersaline water along the western boundary and on its way it interacts with two cyclonic eddies centred around 20°N and 18°N respectively. This suggests that the hypersaline water moves towards the strait of Bab el Mandeb mainly along the western boundary. In fact, there are no observational studies to support the model results in this regard. However, similar general results for the spreading pathway have been presented in recent modelling studies. The 9-year simulation of Sofianos and Johns (2003) suggests that the RSOW is carried out towards the Gulf of Aden by a southward undercurrent intensified along the western coast. The results of the modelling study of Yao et al. (2014b) suggest also a southward subsurface western boundary current generated by a cyclonic rim current through the northern limit of the basin and westward cross-basin currents from the eastern boundary south of 26°N which is mainly consistent with our simulation. Our simulation indicates that the magnitude of the southward flow increases to the south particularly between the adjacent layers of the shallow shelves on both sides (eastern and western along 16°N - 14°N). The highest velocities occur at the area where the strait is narrowing its land-water boundary as a result of bathymetric restrictions and the effect from the adjacent layers.

In summary, the high-resolution (5 km) RS-Model with high-frequency atmospheric forcing reflects the involvement of the important role of the baroclinic instability mechanism in the RSOW formation process. In the Mediterranean Sea, the use of both high-resolution numerical models and high-frequency atmospheric forcing in studying the intermediate/deep water formation was found to be essential approach compared with low-resolution models forced by monthly conditions. For instance, Lascaratos (1998) simulated the intermediate water formation in the Levantine basin (the easternmost part of the Mediterranean Sea) using low (11 km) and higher resolution (5.5 km) models. The use of high-resolution approach allowed the study of the role of baroclinic eddies which were not resolved in the low-resolution model. He found that the convection area as well as the duration of the formation is controlled mainly by a large number of small baroclinic eddies formed at the periphery of the cyclone. Two major differences were emerged between the two models. In the high-

resolution model the convection area is smaller and the restoration of stability is faster. The opposite applies for the low-resolution model. The role played by these baroclinic eddies is to transfer buoyancy horizontally toward the centre of the chimney which partially compensates for the surface buoyancy loss and therefore shrinks both the horizontal and vertical extent of the convection area. Accordingly he emphasized that baroclinic eddies formed at the periphery of the convection area in the Levantine control the formation process. The spreading of the newly formed intermediate water was also due to the baroclinic eddies that dominate the flow at intermediate depths. On the other hand, the use of realistic atmospheric conditions was found to be important mainly in correctly reproducing the observed convection depths and formation rates.

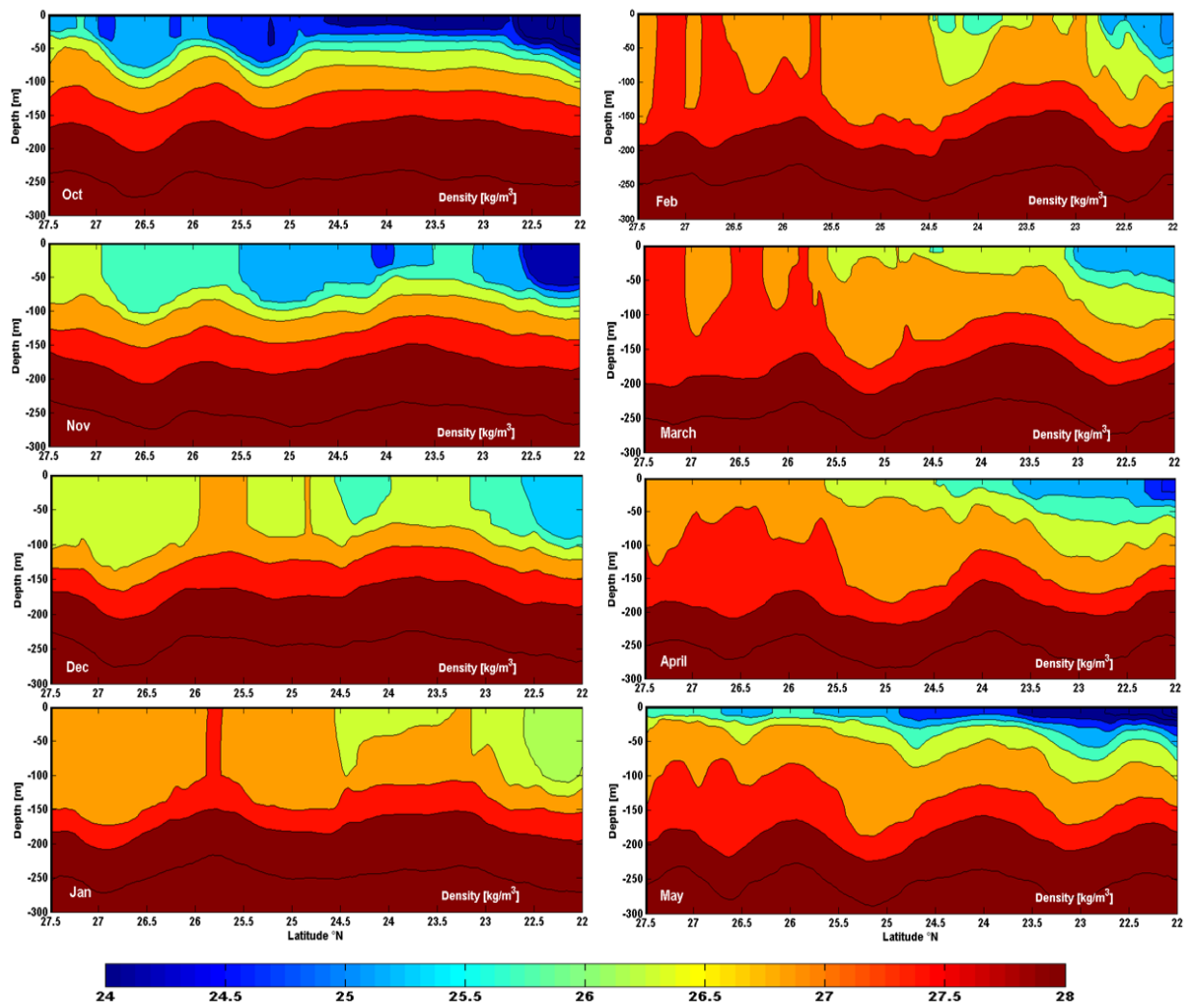


Figure 7.19. Vertical distribution of simulated density from the period October to May, representing the sequence of formation and re-stratification of the mixed layer phases. [Meridional section along the main axis of the northern Red Sea].

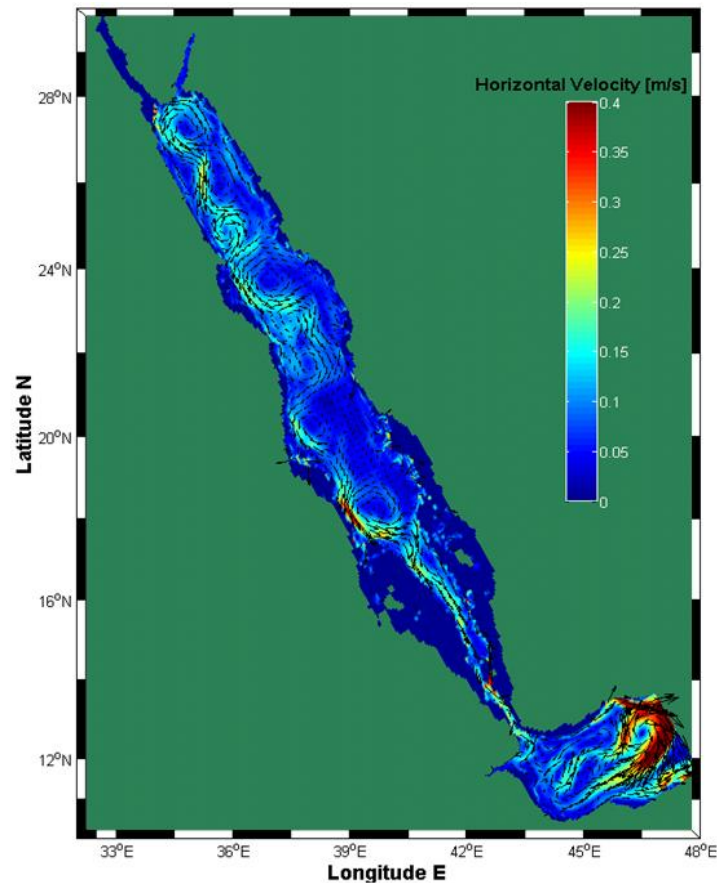


Figure 7.20. Mean current velocity field in the Red Sea at depth 160 m, typical depth of the RSOW based on RS-Model.

7.8.2 Red Sea Deep Water (RSDW)

The RSDW layer is found beneath the RSOW and occupies the RS basin below ~ 250 m to the bottom. As stated previously, most researchers agreed that deep water formation (RSDW) originates mainly from Gulf of Suez and the Gulf of Aqaba. The former is characterized by its shallowness, with depths ranging between 50-70 m, which is shallower than the depth of the thermohaline in the Red Sea. The latter is a miniature of the Red Sea with maximum depths > 1800 m. In addition, the open-ocean deep convection mode was also hypothesized as a third source of formation.

In general, it is proposed that the formation occurs during the peak of winter as a result of strong evaporation and surface cooling process. To investigate the water mass characteristics of the two Gulfs, the simulation results during the winter period were analysed. Figure (7.21 left panel) shows the vertical distribution of salinity (psu) along the main axis and cross-section of salinity (psu) and temperature ($^{\circ}\text{C}$) across the mouth of the Gulf of Suez.

The simulation results indicate that the salinity in the head of the Gulf of Suez reaches 41.0 psu. However, these higher salinities do not extend to the entrance of the Gulf. At the mouth of the Gulf (Figure 7.18 B Left panel), the characteristics of the bottom water in the Gulf for salinity is > 40.0 psu while temperature value is 23.7 °C. On the other hand, the salinity values in the Gulf of Aqaba (Figure 7.21 right panel) exceed 40.1 psu only in the head of the Gulf while down the axis it is found to be in the range of 39.9 psu. At the mouth of the Aqaba Gulf salinity and temperature values are 39.95 psu and 21.0 (°C) respectively.

Previous observational studies of Maillard (1974) and Wyrski, (1974) indicated that the salinity values down the axis of the Gulf of Suez exceed 41 psu while at the Gulf of Aqaba salinities range between 40.5-40.8; these values are slightly larger than the model predictions. Such discrepancies are expected since the salinity values of the deep water in the Red Sea are underestimated by the RS-Model, where it was found to be ranging between 40.0-40.3 psu whereas observed values of the deep water are in the order of 40.5-40.6 psu (Sofianos *et al.*, 2002). On the other hand, higher temperature values observed at the bottom at the mouth of the Suez Gulf is mainly attributed to the fact that in the Delft3D-Flow system the heat exchange at the bed is assumed to be zero. This leads to over-predicted temperatures in shallow areas.

Although some discrepancies do exist, the Gulf of Suez can be a first source of dense water formation contributing to the RSDW formation. This is probably justified on the basis of its shallowness where the bathymetry is characterized by bottomed flat with maximum depth of about 70 m. This in turn is shallower than the depth of the thermocline layer in the Red Sea basin. Such bottom depth is considered the limiting depth of influence of the air-sea heat and salinity fluxes (Clifford *et al.*, 1997). On the other hand, considering underestimation of the model predictions, the water mass properties in the Gulf of Aqaba are close to those of the deep water in the Red Sea. Concerning the open-ocean convection mode source, as shown previously the results suggest the formation process of the open-ocean convection does not involve deep penetrative convection and maximum depth of convection is observed at about 150 m. This depth level is related to the intermediate layer where the RSOW is found. Therefore, on the basis of the model results it can be concluded both the Gulf of Aqaba and Gulf of Suez contribute significantly to the RSDW formation.

Previous estimation of the RSDW formation rate at the Gulf of Suez during late winter (1971-1972) found to be 0.082 Sv ($1 \text{ Sv} = 10^6 \text{ m}^3/\text{s}$) (Maillard, 1974). Based on a one-dimensional plum model, the estimated outflow from the Gulf of Suez (over 7 months) was found to be 0.058 Sv. On the other hand, the estimated winter outflow from the Gulf of Aqaba to the Red Sea was 0.069 Sv (Klinker *et al.*, 1976) while the transport outflow was estimated at 0.029 Sv over a period of two weeks in February (Murray *et al.*, 1984). Recent numerical model studies have shown that the annual mean outflow from the Gulf of Aqaba was estimated in the order of 0.0185 Sv. The calculated mean outflow over winter (Jan-March) from the RS-Model is found to be 0.079 Sv and 0.017 Sv at the Gulf of Suez and the Gulf of Aqaba respectively.

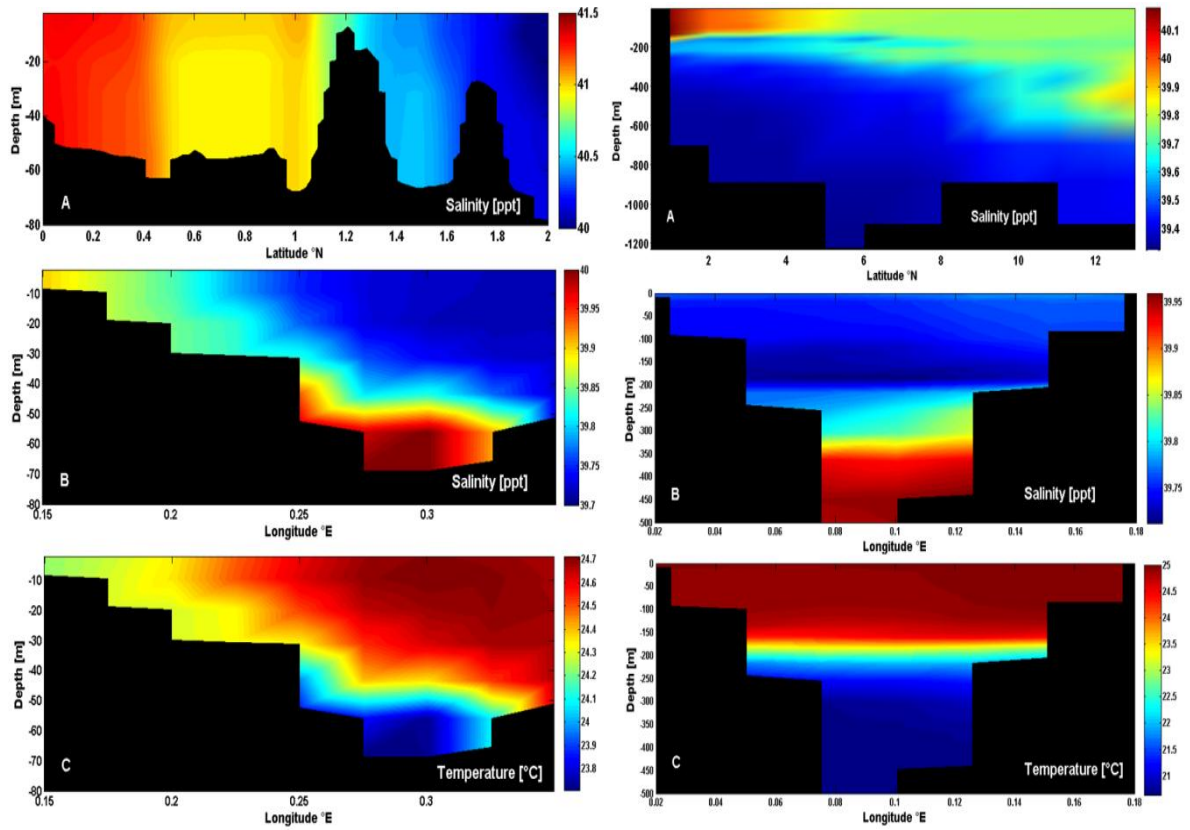


Figure 7.21. Vertical distribution of simulated averaged salinity [psu] and temperature over winter season at the Gulf of Suez (Left) and the Gulf of Aqaba (Right), As: Longitudinal section along the main axis, Bs and Cs: cross-sections across the mouth of the two Gulfs.

Chapter 8

Conclusion and Recommendations

8.1 Conclusion

In the present thesis, the tidal characteristics, the seasonal thermohaline structure and the circulation patterns in the Red Sea region are studied. Detailed literature survey has shown that very few attempts were made regarding physical processes in the Red Sea region. Consequently, the aim of this study is to improve our understanding about the hydrodynamic processes in the region.

The concerns processes are studied mainly by a combination of a very few available observations (water levels and oceanographic data), remotely sensed data as well as with major focus by means of using a numerical modelling and a realistic high-frequency atmospheric forcing approach. The field data and remotely sensed information were mainly used on the one hand to acquire more information on the hydrodynamic features in the region and on the other hand to be used as a benchmark to evaluate the performance of the numerical simulations. The use of numerical modelling approach provides more insight on the tidal characteristics as well as the physical processes that control the circulation and water mass characteristics in the Red sea. Using both high-resolution model and high-frequency atmospheric conditions indeed served to increase and improve our understanding of the underlying processes in the region.

Eight tidal gauge stations at different sites along the eastern boundary and only one station positioned at the western boundary of the Red Sea, CTD observations distributed along the main axis of the basin, satellite data AVHRR / Pathfinder datasets (Advanced Very High Resolution Radiometer) and climatological information (Sea Level Anomalies, SLA) were made available during the course of this study. The specific model used in the current investigation is based on Delft3D modelling system, developed by Delft Hydraulics in the Netherlands. Initially the model was set up, calibrated and validated in 2-Dimensional mode to investigate the tidal characteristics in the Red Sea region. Afterward, the validated 2-D model was extended into 3-D mode in order to study the three-dimensional circulation processes in the region.

The computational domain of the Red Sea Model (RS-Model) was configured to cover the entire Red Sea (Lon 32° to 48°E & Lat 10° to 30°N) including the Gulf of Aqaba and Gulf of Suez in the northern part. The model was extended to include also part of the Gulf of Aden in the southern part of the basin. The model domain was schematized on a rectilinear mesh oriented (NNW and SSE) following the main axis of the Red Sea, with a horizontal uniform grid spacing of approximately $\Delta x = \Delta y = 5$ km. The vertical grid discretization was implemented using z -coordinate system. The water column was resolved by unequally 30 vertical layers with 15 of these layers concentrated in the upper 200 m, thus keeping the higher resolution at the surface in order to capture the dynamic of the upper ocean. The bathymetric data of the RS-Model were sourced from the global bathymetry dataset for the world ocean “GEBCO_08 Grid” at a 30 arc-second horizontal resolution (~ 1 km). Due to insignificant artificial contact between the Red Sea basin and the Mediterranean via Suez Canal, the model has only one open boundary which was set at the Gulf of Aden at longitude (48° E). The ocean open boundary was forced by the main eight semidiurnal and diurnal (M_2 , S_2 , N_2 , K_2 , K_1 , O_1 , P_1 , and Q_1) tidal constituents. In terms of transport forcing, the eastern open boundary is controlled by temperature (T) and salinity (S) and velocities components (u , v) obtained from Simple Ocean Data Assimilation (SODA) at every five days intervals. The 3-D RS-Model was initialized with SODA data. The surface boundary of the RS-Model was forced by realistic high-frequency atmospheric forcing (i.e. winds and surface heat fluxes) derived from DWD at temporal resolution with 6 hourly intervals.

The optimal settings of the numerical model were determined based on sensitivity analyses. The model was validated against the available measured surface elevation in addition to summer CTD observations. Discrepancies between the model results and available observations have been determined qualitatively and statistically. It was observed that the model predictions and observations of water levels are in good agreement. The performance of the model in terms of temperature and salinity vertical profiles was assessed using measurements of temperature and salinity at a number of sites along the main axis of the Red Sea. The simulation results are consistent with the measurements reasonably well. On the other hand, in order to assess the model on temporal and spatial scale, the satellite data (AVHRR / Pathfinder datasets) was considered. It was observed that there is a good agreement between the simulation results and the satellite data, reflecting a consistent level of agreement (see Chapter 5). Although the measurements used in the validation processes are quite scarce, other data sources such as satellite data were helpful, increasing our confidence in the model results.

Further evaluation was conducted to test the ability of the hydrodynamic RS-Model in reproducing the seasonal variability especially in the southern part of the Red Sea at the strait of Bab el Mandeb, the area where the most consistent observations were carried out. It was found that the model is able to reproduce the documented hydrodynamic features at the strait quite well. These features are the reversal processes of the surface flow (Red Sea surface water (RSSW) and Gulf of Aden surface water (GASW), subsurface intrusion of Gulf of Aden intermediate water (GAIW) and the seasonal variability of the Red Sea outflow water

(RSOW). The incoming surface water from Gulf of Aden has an average of 36.0 psu, 24.0 °C and an average transport of 0.46 Sv while the outflow of the Red Sea water has an average salinity and temperature of 39.6 psu and 22.0 °C. In the summer season, conditions of exchange flow experience a warm, saline thin surface outflow (30.0 °C, 37.5 psu); a cooler and fresher inflow from the Gulf (17.0 °C, 36.0 psu, with an average transport of 0.3 Sv) and a saline weaker outflow (RSOW). The annual mean transport of the RSOW outflow is estimated at 0.38 Sv with minimums and maximums over summertime and wintertime. Besides, the permanent cyclonic gyre observed during winter period in the extreme north of the Red Sea by several investigators (e.g. Clifford et al. 1997) and the anticyclonic eddy feature observed recently in the central part of the Red Sea (~ 23°N) by Bower et al. (2013) are also predicted by the RS-Model. The RS-Model is also able to predict the large anticyclones which exist in the Gulf of Aden as was reported by previous studies (e.g. William et al. 1999). These major features in addition to the previous comparisons reflected the predictive capability of the RS-Model.

Accordingly, the validated RS-Model is used to describe the seasonal variability of the circulation features and thermohaline structure in the Red Sea. Moreover, the relative importance of the main mechanisms in driving the circulation and stratification processes in the Red Sea is investigated. For this purpose, the RS-Model was used to conduct a number of numerical experiments aimed at determining the role of each mechanism in driving the key features of the circulation produced by the RS-Model. The model was also used to investigate the involved processes in the hypersaline RSOW outflow formation, the RSDW in the Red Sea basin.

Tidal Characteristics in the Red Sea region

The tidal analyses of the available coastal water level measurements showed that the major semidiurnal and diurnal constituents that have relatively higher amplitudes are M_2 , N_2 , S_2 and K_1 respectively. To describe the tidal characteristics in the region, the RS-Model was set up, calibrated and validated in a 2-Dimensional mode. Subsequently, two scenarios of numerical simulations were carried out to describe the tidal characteristics in the Red Sea. In the first scenario, separate simulations of each individual constituent to generate Co-tidal and Co-range charts for the Red Sea region were carried out. The results showed that the dominant feature of the M_2 , N_2 , and S_2 tide is the existence of the amphidromic systems (anticlockwise) in the central part of the Red Sea at about 20° N, north the strait of Bab el Mandeb at 13.5° N and in the entrance of the Gulf of Suez. The distribution of the co-phase of K_1 tide showed that only a single anticlockwise amphidromic system exists in the southern part of the Red Sea centred around 15.5° N. The amphidromic systems of the semidiurnal and diurnal constituents in the strait of Bab el Mandeb suggest that the tides include some characteristics of standing waves. Model results of amplitudes and form factor proved that tides in the Red Sea are dominated by the major semidiurnal constituents M_2 , S_2 , and N_2 . However, diurnal character appeared in the central part of the Red Sea and northern part of the strait. In the second scenario, the model was forced on the ocean open boundary with the amplitudes and phases of the primary semidiurnal and diurnal constituents (Q_1 , O_1 , P_1 , K_1 , N_2 , M_2 , S_2 and K_2).

The purpose of this simulation was to reproduce the tidal currents that are generated by a combination of the primary constituents at moments of extreme conditions, ebb and flood phases during spring and neap tidal cycles. The RS-Model results suggest that tidal currents in the Red Sea are in general quite weak in the order of 0.1 m/s except near the Red Sea entrance where maximum velocity was observed to be up to about 0.5 m/s.

Circulation patterns in the Red Sea

To investigate the three-dimensional circulation features in the Red Sea, three different scenarios of numerical simulations consisting of the same model configuration but using different combinations of forcing were carried out. The first numerical experiment (scenario-I) including all the forcing conditions mentioned above is carried out to reproduce the circulation processes in the Red Sea region. Scenario-II and Scenario-III consist of the same model configuration of scenario-I but using different forcing mechanisms aiming at determining the role of each mechanism in driving the key features. To determine the effect of wind-stress forcing and its role, a numerical experiment (Scenario-II) was performed considering only the thermohaline fluxes. Therefore, no wind is imposed in this scenario. In the third numerical experiment (Scenario-III), the surface heat and salt fluxes were removed but wind-stress field was included.

The simulation results revealed several interesting features of the circulation in the region. The results of the first numerical simulation (scenario-I) indicate that the Red Sea basin shares several aspects with other semi-enclosed marginal seas such as the Mediterranean Sea, in which the general circulation is a result of combined effect of the wind-driven and thermohaline-driven flow, complex meoscale eddy fields and water exchange with the open ocean. The seasonal circulation patterns produced by the RS-Model not only confirms some of the earlier description in the region but also provides new insights. The major features predicted by the RS-Model include the existence of several cyclonic and anticyclonic gyres; small eddies as well as intensified boundary currents at both boundaries. The most important features are the eddy activities located in the northern part of the Red Sea that contributes significantly to the RSOW formation; permanent energetic anticyclonic gyre system in the middle Red Sea around (23°N) which extends almost over the entire width of the basin, and the stronger seasonality of the flow in the southern part of the Red Sea.

In fact, using both high-resolution model (5km) and high frequency atmospheric conditions, yielded some different results compared with the low-resolution (10 km) climatological modeling study of Sofianos and Johns (2003). It is worth mentioning that large part of our results share three-dimensional analytical models carried for idealized marginal seas (e.g. McCreary *et al.*, 1986).

The model results (combined with previous observations and numerical modelling studies) suggest that the circulation regime in the southern part of the basin is a robust feature during both summer and winter seasons. This is characterized by the existence of a 2-layer circulation system (inverse-estuarine) in the winter, which is replaced by a 3-layer exchange

flow system at the strait of Bab el Mandeb during the summer months. The effect of the wind forcing was observed to be an essential factor in controlling the seasonal variability. This was evident in the southern Red Sea where for instance it influences strongly the reversal of the surface exchange flow at the strait of Bab el Mandeb. Furthermore, the model results (shared with the previous observations carried out particularly in the northern part of the basin) suggest that the existing circulation feature in the northern part is a permanent regime. This is represented by the cyclonic eddies in the extreme north of the basin which are driven mainly by the thermohaline forcing as shown in the numerical experiment driven only by thermohaline fluxes. The simulations suggest also that the surface circulation under combined forcing over the winter season consists of alternating cyclones and anticyclones eddies. In contrast, the simulation results showed that the surface current field during the summer season contains a series of organized energetic eddies with speeds ranging between 0.5 to 1 m/s. The influence of such eddies was observed to extend to depths exceeding 200 m in some parts of the Red Sea basin especially in the extreme north of the basin.

The exchange flow regime at the strait of Bab el Mandeb seems to be not a result of a simple linear system of the wind and thermohaline forcing. Although the thermohaline-driven experiment (scenario-II) shows major role in driving the flow exchange, the influence of the wind forcing cannot be neglected since the final characteristics of the exchange system is produced by the interactions of both forcings as revealed in the model. The full cycle of the Gulf of Aden intermediate water (GAIW) was studied in order to determine the northern limit intrusion inside the Red Sea basin. Consistent with recent observations, the model results suggest that the subsurface GAIW layer enters the narrowing land-boundary of the strait and banks toward the eastern coast inside the southern part of the Red Sea following a pathway mainly along the eastern boundary. The full cycle of the GAIW structure showed that the intrusion takes place in June and become stronger gradually in July. A maximum northern limit of the intrusion was found to establish in August reaching latitude of 17 °N with current velocity of about 0.5 m/s. The northern limit of the subsurface inflow shrinks to the latitude of 16°N in September and lasts up to October with the inflow ceasing in November.

Based on additional numerical experiments (separating wind and thermohaline forcing), the wind-stress field was observed to be the main mechanism generating the key surface features produced by the RS-Model. Major features observed from the numerical experiments (scenario-II and scenario-III) are that the thermohaline forcing drive the circulation in the extreme northern part cyclonically while the wind-drives the circulation anticyclonically. The recent modeling study of Sofianos and Johns (2003) under climatological forcing suggest that the wind forcing has less effect on the surface circulation of the Red Sea region and that the eddies generation more related to thermohaline forcing. In their thermohaline-driven circulation experiment, they found that the mean circulation is in general similar to the features of the full forcing experiment. Although in our model the few eddies are mainly thermohaline-driven, the effects of the wind field was observed to play a primary role. Our model results are in agreement with a conclusion drawn by Clifford et al. (1997). They confirmed the importance of the cross-basin component of the wind which produces wind stress curl and consequently more eddies. The importance of the wind-stress field is also

evident at the southern part of the Red Sea where the winds have their greatest variability and become very strong during winter.

Thermohaline structure in the Red Sea

Distributions of horizontal and vertical thermohaline have shown very interesting patterns. Horizontal distribution of surface temperature and salinity was observed to be highly associated with the wind patterns in the Red Sea. The patterns of the thermohaline structure was observed to exhibit strong latitudinal gradients in the surface layers due to the monsoonal winds blowing over the region, the strong evaporation component and the flow regime existing in the southern part with the Gulf of Aden.

During the winter season, sea surface temperature (SST) horizontally increases from the southern part of the basin (just north of Bab el Mandeb) towards the north reaching about 27 °C at 20°N and above that latitude (20 °N) it tends to decrease gradually towards the northern part reaching about 23-24 °C. On the other hand, sea surface salinity (SSS) exhibits gradual increase from the southern part 36 psu (near Bab elMandeb Strait) towards the northern part where maximum values reach about 40 psu are found at the extreme north. Vertically, the mixed layer during the winter extends to 150-200 m depth in the northern part while it reduces gradually to about 100 m in the middle and southern parts of the basin. The thermocline layer extends to around 250 m with temperature ~ 22 °C. Salinity on the other hand increases gradually with depth reaching its maximum at 40.5 psu. The halocline structure occurs between 100-150 m depth with salinity ranging between 38.5 and 39.5 psu particularly in the middle and southern part of the Red Sea.

In contrast, the simulation results showed that the entire Red Sea basin becomes very warm during the summer season with a meridian gradient over the basin and maximum SST of about 33-34 °C. The major pattern of observed SST is higher on the western boundary than the eastern one. Upwelling events were observed to occur along the eastern coastline particularly in the middle part of the basin of about 20 °N and north of 23 °N while downwelling occurs on the western boundary. Salinity distribution showed an increase of salinity gradients from the south towards the northern end of the Red Sea. In the vertical direction, the significant role played by the atmospheric forcing variations between the two monsoon seasons was clearly observed. The vertical structure during the summer is more stratified unlike the winter situation. The mixed layer depth during summer decreases to about 30 m in the northern part and to 50 m between 18-16 °N. The depth of thermocline layer deepens to 200 m where temperature decreases from 34 °C to become 23-24 °C. In terms of salinity, there is an increase in values with depth and the depth gradient is larger in the southern Red Sea due to the influence of low salinity water associated with the intrusion of Gulf of Aden Intermediate Water (GAIW). Underneath 300 m depth, the Red Sea is filled by water of remarkably homogenous temperature; salinity and density of about 21.5-21.6 °C, 40.5 psu and 28.6 kg m⁻³ respectively.

Red Sea Outflow Formation

The involved mechanisms in the RSOW formation, periods and possible locations have been investigated. The use of both high-resolution model and high frequency atmospheric forcing showed interesting results that are different from the previous model study of Sofianos and Johns (2003) particularly regarding the formation period and mechanism involved in the formation. Our model suggests that the Red Sea experiences similar processes of formation that were observed in the Mediterranean Sea. The simulation suggests that the northern part of the Red Sea is the only dominant area for intermediate water formation justified by several factors. The simulation showed that the heat loss due to evaporation is significantly higher in the northern Red Sea compared with other parts of the Red Sea basin. The presence of cyclonic eddies is indicative of precondition for the formation of RSOW where their role is represented markedly by a doming of isopycnals towards the surface layers in the northern basin which makes the weakly stratified waters exposed to local cooling and evaporation processes. It was observed that the strong atmospheric forcing events triggering deep convection in the preconditioned area produced three chimneys of mixed dense waters. The depth of the convection columns reaches to the level depth where the intermediate water mass is found. Maximum convection depth is observed at the level of about 150-200 m. The model results suggest that baroclinic instability mechanism plays major role in the formation process. The convection events include period of 3-months (January-March) where three convective chimneys are formed. The formed RSOW with homogeneous characteristics remained below the surface water after convection process ceases. The simulation showed also that the formed RSOW is carried away from the formation site by southward currents, mainly intensified along the western boundary, generated from the edge of the eddies, and also the crossing eastward currents to the western boundary.

8.2 Recommendations

The circulation in the Red Sea presents an interesting challenging subject for oceanographers. The model results showed that the circulation in the Red Sea is not simple, and complicated on the one hand by the presence of eddies embedded in them, and on the other hand by the buoyancy loss which plays a significant role in Red Sea circulation.

The RS-Model simulations have successfully reproduced the basic documented features of the seasonal exchange at the strait of Bab el Mandeb as well as the few identified circulation features through the previous and recent observational studies inside the Red Sea domain. They also provided more insight on the circulation in the Red Sea. However, there are still a number of issues that need to be considered for future modelling studies. The validation of the model can be improved with measured data. These would include current measurements; more water level observations since few available data were used covering the eastern boundary of the Red Sea and only one tidal station located on the western coastline of the basin. Measurements of temperature and salinity covering the winter time are necessary since only summer CTD measurements were found available during this study for validation purposes. Furthermore, salinity and temperature time series measurements are also of the

most important needs for further validation to check the more reliability of the model on temporal scale. Observational evidences without doubt could help further validate the performance of the model. Therefore the model can be used for more investigations such as the influence of the permanent eddies on the water properties.

The RS-Model results showed many interesting findings that can be used as a guide for future observations such as the intermediate water formation and sinking processes places where there is still much debate concerning these processes. Such measurements would on the one hand verify the model results and on the other hand increase our understanding about the hydrodynamic conditions especially the RSOW formation. In addition to that, measurements of currents near the boundaries are also necessary since our model as well as previous modelling studies highlighted the existence of boundary currents. However, such measurements are not an easy task and thus, it needs collaboration with the countries surrounding the Red Sea basin. Observations in particular on the export path of the outflow along the western boundary to the strait of Bab el Mandeb are needed.

The use of high-frequency atmospheric forcing approach was observed to be quite relevant. This was evident in the surface circulation features where the RS-Model showed features consistent both in size and magnitude with recent summer observations unlike the previous modelling study of Sofianos and Johns (2003) (forced by climatological conditions) showed weaker patterns in both size and magnitude. Therefore, more modeling studies using high-frequency atmospheric forcing should be carried out. Our simulations also showed that combination of wind and thermohaline forcing leads to the generation of maximum current speed. Therefore, it is very important inserting both forcing fields for any future numerical studies of circulation in the region.

References

- Abbott, M.B., Damsgaard, A. and Rodenhuis, G.S., 1973, A design system for two-dimensional nearly-horizontal flows. *Journal of Hydraulic Research*, Vol. 1, pp. 1-28.
- Adkins, G. and Pooch, U.W., 1977, Computer simulation: a tutorial. *Computer*, vol. 10, pp 12 - 17.
- Ahmad, F. and Sultan, S.A.R., 1989, Surface heat fluxes and their comparison with the oceanic heat flow in the Red Sea. *Oceanology Acta* 12, 33–36.
- Ahmad, F. and Sultan, S.A.R., 1987, on the heat balance terms in the central region of the Red Sea. *Deep-Sea Res.* 34: 1757-1760.
- Al-Barakati, A.M.A., 2012, The Flushing Time of an Environmentally Sensitive, Yanbu Lagoon along the Eastern Red Sea Coast, *International Journal of Science and Technology* Vol No. 1. Pp. 53-58.
- Al Barakati, A.M.A., James, A.E., and Karakas, G.M., 2002, A Three-dimensional Hydrodynamic Model to Predict the Distribution of Temperature, Salinity and water Circulation of the Red Sea, *J. KAU: Mar. Sci.*, vol. 13, pp. 3-17.
- Anderson, R.J. and Smith, S. D., 1981, Evaporation coefficient for the sea surface from eddy flux measurements. *J. Geophys. Res.* 86: 449-456.
- Apel, J.R., 1987, *Principles of Oceans Physics*, Academic Press, London, England.
- Arakawa, A. and Lamb, V.R. (1977) Computational Design of the Basic Dynamical Process of the UCLA General Circulation Model. *Methods Computational Physics*, 17, 173-265.
- Black, K.P., 1995, The numerical hydrodynamic model 3D and support software, Occasional Report No.19, In: Department of Earth Sciences, Waikato, N.Z. (Eds.), University of Waikato, 69 pp.
- Boon, J.D., 2004, *Secrets of the Tide: Tide and Tidal Current Analysis and Predictions, Storm Surges and Sea Level Trends*, Horwood Publishing, Chichester, U.K, 212 p.
- Bower, A.S., Swift, S.A., Churchill, J.H., McCorkle, D.C., Abualnaja, Y., Limeburner, R., and Zhai, P., (2013), New Observations of eddies and boundary currents in the Red Sea. *Geophysical Research abstracts*, Vol. 15, EGU2013-9875
- Bleck, R. and Smith, L.T. (1990). A wind driven isopycnic coordinate model of the north and equatorial Atlantic Ocean. 2. Model development and supporting experiments. *J. Geophys. Res.*, 95, 3273-3285.

- Blindheim, J., and S. Østerhus, 2005: The Nordic Seas, Main Oceanographic Features, in AGU Geophysical Monograph Series, pages 11-38, American Geophysical Union, Washington, DC.
- Bryan, K. (1969). A numerical method for the study of the circulation of the world ocean, *J. Comput. Phys.*, 4, 347-376.
- Budyko, M. I., 1963, Atlas of the heat balance of the earth. Glabnaia Geofiz. Observ. 5 pp.69 plates.
- Bunker, A.F., Charnock, H. and Goldsmith, R. A., 1982, A note on the heat balance of the Mediterranean and Red Seas. *J. Mar. Res.* 40 (Suppl): 73-84.
- Carton, J. A. and Giese, B. S., 2008, "A reanalysis of ocean climate using Simple Ocean Data Assimilation (SODA)." *Monthly Weather Review* 136(8): 2999-3017.
- Casey, K.S., T.B. Brandon, P. Cornillon, and R. Evans., 2010, "The Past, Present and Future of the AVHRR Pathfinder SST Program", in *Oceanography from Space: Revisited*, eds. V. Barale, J.F.R. Gower, and L. Alberotanza, Springer. DOI: 10.1007/978-90-481-8681-5_16.
- Cember, R. P., 1988, On the source, formation and circulation of Red Sea deep-water. *Journal of Geophysical research*, 93, 8175-8191.
- Chassignet, E.P., Arango, H., Dietrich, D., Ezer, T., Ghil, M., Haidvogel, D.B., Ma, C.-C., Mehra, A., Paiva, A.F. and Sirkes, Z., 2002, DAMEE-NAB: the base experiments. *Dynamics of Atmospheres and Oceans* 32, 155–183.
- Chen, C., Ruixiang. Li., Larry Pratt., Richard Limeburner., Robert, C.B., Amy Bower., Houshuo Jiang., Yasser Abualnaja., Qichun, Xu., Huichan Lin., Xuehai Liu., Jian Lan and Taewan Kim., 2014 , Process modelling studies of physical mechanisms of the formation of an anticyclonic eddy in the central Red Sea, *J. Geophys. Res. Oceans*, 119, Doi:10.1002/2013JC009351.
- Clarke, R. A., and J. C. Gascard, 1983, The formation of Labrador Sea Water, I, Large-scale processes, *J. Phys. Oceanogr.*, 13, 1764– 1778.
- Clifford, M., Horton, C., Schmitz, J. and Kantha, L. H., 1997, An oceanographic nowcast/forecast system for the Red Sea, *J. Geophys. Res.*, 102, 25,101– 25,122.
- Cromwell, D. and Smeed, D. A., 1998, Altimetric observations of sea level cycles near the Strait of Bab al Mandeb. *Int. J. Remot Sens.*, 19, 1561-1578.
- Defant, A., 1961, *Physical Oceanography*, Vol. No. 2, pergamon Press, Oxford, 598p.

- Deltares, 2011. Delft3D-FLOW User Manual Simulation of Multi-dimensional Hydrodynamic Flows and Transport Phenomena, Including Sediments, User Manual, Hydro Morphodynamics, Version: 3.15.
- De Goede, E.D., Roozekrans, J.N., De Kok, J.M., Vos, R.J. and Uitten bogaard, R. E., 2000, REST3D-Remot Sensing Sea Surface Temperature for 3D North Sea Modelling. WL | Delft Hydraulics Report, NRSP – 00-16.
- Denner, w.w., 1989, Measuring and understanding coastal processes for engineering purposes, National Academies Press, 119 pp.
- Dongeren, Ap. Van., 2009, Delft3D-Modelling of Hydrodynamic and Water Quality Precesses in San Diego Bight, Report, Deltares, MH Delft, the Netherlands.
- Drake, C. L. and Girdler, R. W., 1964, A geophysical study of the Red Sea: Roy. Astron. Soc Geophys. J., v. 8, p. 473-495.
- Edwards, A.J. and Head, S.M. (1987) Red Sea, Key Environments Series. Pergamon Press, Oxford, 42-78.
- Egbert, G.D. and Erofeeva, S.Y., 2002, Efficient inverse modelling of barotropic ocean tides, J. Atmos. Oceanic Technol., 19(2), 183-204.
- ELias, E.P.L., Walstra, D.J.R., Roelvink, J.A., Stive, M.J.F. and Klein, M.D., 1998 Hydrodynamic validation of Delft3D with field measurements at Egmond.
- Eshel, G., and N. H. Naik 1997, Climatological coastal jet collision, intermediate water formation, and the general circulation of the Red Sea, J. Phys. Oceanogr., 27, 1233–1257.
- Eshel, G., Cane, M. A. and Blumenthal, M. B., 1994, Modes of subsurface, intermediate and deep water renewal in the Red Sea. Journal of Geophysical Research, 105, 28, 585-28, 593.
- Fares, Y.R., 1997, Hydrodynamic modelling of water circulation in the Red Sea. Transaction on the Built Environment Vol. 27, 1743-3509.
- Furbringer, J.M. and Roulet, C.A., 1999, Confidence of simulation results: put a sensitivity analysis module in your mode, The IEAECBCS annex 23 experience of model evaluation, Energy and Buildings, vol. 30, pp 61–71.
- Furumai, H., 2010, Significance of Advanced Monitoring and Application of environmental Numerical Simulation, In: Advanced Monitoring and Numerical Analysis of Coastal Water and Urban Air Environment, H. Furumai, S. Sato, M. Kamata and K. Yamamoto (Eds.), vol. 3, pp 1 - 11.
- Gascard, J. C., 1978, Mediterranean deep water formation, baroclinic instability and oceanic eddies, Oceanologica Acta, 1, 315–330.

Gill, A.E., 1982, Atmosphere-Ocean Dynamics. International Geophysical series, Vol. 30 Academic Press.

Gordon, A. L., 1978, Deep Antarctic convection west of Maud Rise, *J. Phys. Oceanogr.*, 8, 600– 612.

Grignon, L., Smeed, D. A., Bryden. H. L., and Schroeder, K. 2010, Importance of the variability of hydrographic preconditioning for deep convection in the Gulf of Lion. *Ocean Sci.*, 6, 573-586.

Haney, R.L., 1991, On the pressure gradient force over steep topography in sigma coordinate ocean models. *J. Phys. Oceanogr.*, 21 , 610-619.

Hardisty, J., 2007, Estuaries: Monitoring and Modelling the Physical System. Malden, M.A.: Blackwell.

Hastenrath, S. and Lamb, P.J., 1979, Climatic Atlas of the Indian Ocean. University of Wisconsin Press, Madison.

Herrmann, M., Somot, S., Sevault, F., and Estournel, C., 2008, Modeling the deep convection in the northwestern Mediterranean Sea using an eddy-permitting and an eddy-resolving model: Case study of winter 1986–1987, *J. Geophys. Res.*, 113, C04011, doi:10.1029/2006JC003991.

Hsu, M. H., Kuo, A. Y., Kuo, J. T. and Liu, W. C., 1999, Procedure to Calibrate and Verify Numerical Models of Estuarine Hydrodynamics. *Journal of Hydraulic Engineering*, Vol. 125, No. pp. 162-182.

Institute of Hydrological and Oceanic Sciences National Central University, Taiwan.
http://cmtt.tori.org.tw/data/App_map/maplist.htm

Jiang H, Farrar JT, Beardsley RC, Chen R, Chen C (2009) Zonal surface wind jets across the Red Sea due to mountain gap forcing along both sides of the Red Sea. *Geophys Res Lett* 36, L19605

Ji, Z. G., 2008, Hydrodynamics and water quality; modeling rivers, lakes and estuaries, Wiley Interscience., 704 pp.

Klinker J, Reiss Z, Kropach C, Levanon I, Harpaz H, Halicz E, Assaf G (1976) Observations on the circulation pattern in the Gulf of Elat (Aqaba), Red Sea. *Israel J Earth Sci* 25:85–103

Killworth, P. D., 1976, The mixing and spreading phases of MEDOC. I. *Progress in Oceanography*, Vol. 7, Pergamon, 59–90.

Knolt, S. T., Bunce, E. T. and Chase, R. L., 1966, Red Sea seismic reflection studies. In *The world rift system: Canada Geol. Surv. Paper 66-14*, p. 33-61.

Lascaratos, A., 1993, Estimation of deep and intermediate water mass formation rates in the Mediterranean Sea, *Deep sea Res.*, 40, 1327– 1332.

Lascaratos A (1998) A high-resolution three-dimensional numerical study of intermediate water formation in the Levantine Sea, *J Geophys Res* VOL. 103, NO. C9, PAGES 18,497-18,511.

Law, A.M. and Kelton, W.D., 1982, *Simulation Modeling and Analysis*, New York: McGraw Hill Co.

Leaman, K. D., and F. A. Schott, 1991, Hydrographic structure of the convection regime in the Gulf of Lions: Winter 1987, *J. Phys. Oceanogr.*, 21, 575– 598.

Manasrah RS, Badran M, Lass HU, Fennel W (2004) Circulation and the winter deep-water formation in the northern Red Sea. *Oceanologia* 46:5–23.

Manins, P. C., 1973, A filling box model of the deep circulation of the Red Sea. *Mémoires Sociéte Royale des Sciences de Liége*, 6, 153-166.

Martin, J. L. and McCutcheon, S. C., 1999, *Hydrodynamics and Transport for Water Quality Modeling*. Lewis Publications, Boca Raton, Florida.

Maillard, C. and Soliman, G., 1986, Hydrography of the Red Sea and exchanges with the Indian Ocean in summer. *Oceanologica Acta*, 9, 249-269.

Maillard, C., 1974, Eaux intermediaires et formation d'eau profonde en Mer Rouge, in *L'oceanographie physique de la Mer Rouge*, pp. 105– 133, Cent. Natl. pour l'Exploitation des Oceans.

Maury, M. F., 1855, *The Physical Geography of the Sea and its Meteorology*, 432 pp., Harvard Libr., Cambridge, Mass.

McAnally, W. H. and Letter, J. V. & Thomas, W. A., 1986, Two and Three- Dimensional Modelling Systems for Sedimentation. *Proc. Third Int. Symp., River Sedimentation*, Jackson, USA.

McCreary, J. P., S. R. Shetye, and P. K. Kundu (1986), Thermohaline forcing of eastern boundary currents—with application to the circulation off the west-coast of Australia, *J. Mar. Res.*, 44, 71–92.

MEDOC-Group, 1970, Observation of formation of deep water in the Mediterranean Sea, 1969, *Nature*, 227, 1037-1040.

Metha, U.B., 1995, *Guide to Credible Computational Fluid Dynamics Simulations*, AIAA Paper 95-2225.

- Moffatt and Nichol., 2000, hydrodynamic modelling tools and techniques.
- Moore, A. M., Arango, H. G., Lorenzo, E. Di., Cornuelle, B. D., Miller, A. J. and D. J. Nelson, 2004, A comprehensive ocean prediction and analysis system based on the tangent linear and adjoint components of a regional ocean model, *Ocean Modelling*, 7:227-258.
- Morcos, S. A., 1970, Physical and chemical oceanography of the Red Sea, *Oceanography Marin Biology. Annual Review*, 8, 73–202.
- Morcos, S. and Soliman, G. F., 1974, Circulation and deep water formation in the Northern Red Sea in winter (based on R/V Mabahiss sections, January– February, 1935), in *L’oceanographie physique de la Mer Rouge*, pp. 91– 103.
- Morley, N.J.F., 1975, 'The coastal waters of the Red Sea'. *Bulletin of Marine Research Centre, Saudi Arabia*, No. 5. pp. 8-19.
- Muench, R. D., 1988, Relict convective features in the Weddell Sea, in *Deep Convection and Deep Water Formation in the Oceans*, edited by P. C. Chu and J. C. Gascard, pp. 53– 67, Elsevier Sci., New York.
- Maury, MF. 1855, *The Physical Geography of the Sea and its Meteorology*, 432 pp., Harvard Libr., Cambridge, Mass.
- Murray, S. P. and Johns, W., 1997, Direct observations of seasonal exchange through the Bab El Mandeb Strait. *Geophysical Research Letters*, 24, 2557-2560.
- Murray S, Hecht A, Babcock A., 1984, On the mean flow in the Tiran Strait in winter. *J Mar Res* 42:265–284
- National Geophysical Data Centre, (NOAA) (<http://www.ngdc.noaa.gov/mgg/coast/>).
- Nansen, F., 1906, Northern waters. *Videnskabs-Selskabets Skrifter, I. Matematisk Naturvidenskabelig Klasse*, 3, 145 pp.
- Nghiem, T.L., Marcel, J. F., Stive Zheng, B.W., Verhagen, H.J. and Vu Thi Thu T., 2008, Hydrodynamic and morphodynamics of a seasonally forced tidal inlet system. *Journal of Water Resources and Enviromental Engineering*, No. 23.
- Open University, 1989, Open University. 1989. *The Open University: Ocean Circulation*. Pergamon Press.
- Palacio, C., Mayerle, R., Toro, M. and Jiménez, N., 2005, Modelling of Flow in a Tidal Flat Area in the South-Eastern German Bight, *Die Küste*, Heft 69, pp 141-174.

Patzert, W. C., 1974a, Wind-induced reversal in Red Sea circulation, *Deep Sea Research.*, 21, 109– 121.

Patzert, W. C., 1974b, Volume and heat transports between the Red Sea and Gulf of Aden, notes on the Red Sea heat budget, in *L’océanographie physique de la Mer Rouge*, pp. 191–201, Cent. Natl. pour l’Exploitation des Océans, Paris.

Paul, R. P., 2003, *Invitation to oceanography*. COLGATE UNIVERSITY, Third Edition

Pedgley, D. E., 1974, An outline of the weather and climate of the Red Sea, in *L’Oceanographie Physique de la Mer Rouge*, pp. 9 – 27, Cent. Natl. Pour l’Exploitation des Océans, Paris, 1974.

PERSGA (Regional Organization for the Conservation of the Environment of the Red Sea and Gulf of Aden), 2006, the State of the marine Environment. Report for the Red Sea and Gulf of Aden.

Phillips, O. M., 1966, On turbulent convection currents and the circulation of the Red Sea, *Deep Sea Res.*, 13, 1149– 1160.

Phillips, N. A., 1957, A coordinate system having some special advantage for numerical forecasting, *Journal of Meteorology*, Vol. 14, pp 184-185.

Piechura, J. and Sobaih, O. A. G. (1986) Oceanographic conditions of the Gulf of Aden. In *Scientific investigation of the Gulf of Aden Series A Oceanography*, 2, pages 1–26. Marine Science and Resources Research Centre, Aden Republic of Yemen.

Plahn, O., Baschek, B., Badewien, T.H. and Walter, M. & Rhein, M., 2002, Importance of the Gulf of Aqaba for the formation of bottom water in the Red Sea. *Journal of Geophysical Research- Oceans* 107: 1–18.

Pugh, D.T., 1987, *Tides, Surges and Mean Sea-Level*. John Wiley and Sons, 472 pp.

Pugh, D. (2004) *Changing Sea Levels-Effects of Tides, Weather and Climate*. Cambridge University Press, Cambridge. 265 pp.

Quadfasel, D. and Baudner, H., 1993, 'Gyre-scale circulation cells in the Red Sea'. *Oceanologica ACTA*, 16, No. 3, pp. 221-229.

[Rahmstorf, S., 2006, Thermohaline circulation: The current climate.](#) *Nature* 421, 699.

Reeve, D., Chadwick, A. and Fleming, C., 2004, *Coastal engineering-processes, theory and design practice*: Spon Press, New York.

- Robinson, G.D., 1966, another look at some problems of the air-sea interface. *Q.J.R. Meteorol. Soc.* 92: 451-465.
- Robinson, A.R, Leslie, W.G, Alexander T., and Alex, L., 2001, Mediterranean Sea Circulation, Academic press, doi:10.1006/rwos.2001.0376
- Saad, M.A. and Ahmad, F., 1995, Red Sea Surface Heat Fluxes and Advective Heat Transport through Bab AlMandab. *JKAU: Mar. Sci.*, Vol. 6, pp. 3-13.
- Saad, M.A., 1997, Seasonal Flucuation of Mean Sea Level at Jizan, Red Sea. *Journal of Coastal Research*, Fort Lauderdale, Florida. Vol 13, 4, 1166-1172 pp.
- Schott, F., M. Visbeck, and J. Fischer, 1993, Observations of vertical currents and convection in the central Greenland Sea during the winter of 1988– 1989, *J. Geophys. Res.*, 98, 14,401–14,421.
- Schwartz, M.L., (Ed.), 2005. *Encyclopedia of Coastal Science*, Springer-Verlag, The Netherlands,1211 pp.
- Sheppard, C. and Price, A. & Roberts, C., 1992, *Marine Ecology of the Arabian Region: patterns and processes in extreme tropical environments*. Academic Press, London.
- Siedler, G., 1969, General circulation of the water masses in the Red Sea, in *Hot Brines and Recent Heavy Metal Deposits in the Red Sea*, edited by E. T. Degens and D. A. Ross, pp. 131–137, New York.
- Sisson. M., Wang, H., Li, Y., Shen, J., Kuo, A., Gong, W., Brush, M. and Ken Moore., 2010, Development of hydrodynamic and water quality models for the Lynnhaven River System, Special Report No. 408 In *Applied Marine Science and Ocean Engineering*.
- Smeed, D., 2004, Exchange through the Bab el Mandeb, *Deep-Sea Research*, 51, 455-474 pp.
- Sofianos, S. S. and Johns, W. E., 2007, Observations of the summer Red Sea circulation. *Journal of Geophysical Research*, 112, doi: 10.1029 - 2006JC003886.
- Sofianos, S. S., and W. E. Johns (2002), An oceanic general circulation model (OGCM) investigation of the Red Sea circulation: 1. Exchange between the Red Sea and the Indian Ocean, *J. Geophys. Res.*, 107, 3196, doi:10.1029/2001JC001185.
- Sofianos, S. S. and Johns, W. E., 2003, An Oceanic General Circulation Model (OGCM) investigation of the Red Sea circulation, *Journal of geophysical research*, Vol. 108, NO. C3, 3066, Doi:10.1029/2001JC001185.
- Sofianos, S. S., Johns, W. E. and Murray, S. P., 2002, Heat and freshwater budgets in the Red Sea from direct observations at Bab el Mandeb. *Deep-Sea Research Part II: Topical Studies in Oceanography*, 49, 1323-1340.

- Souvermezoglou, E., Metzl, N. And Poisson, A., 1989," Red Sea budgets of salinity, nutrients and carbon calculated in the strait of Bab-el- Mandab during the summer and winter seasons ". *Journal of Marine Research*, 47: 441-456.
- Sultan, S.A.R., Ahmad, F. and Nageb, M.E., 1995, Sea Level variability in the central part of the Red Sea. *OCEANOLOGICA ACTA – Vol. 18 N 6*.
- Swallow, J. C., and Caston, G. F., 1973, The preconditioning phase of MEDOC 1969, I, Observations, *Deep Sea Res.*, 20, 429–448.
- Swapna, P., 2005, dynamics of large scale 3-Dimensional circulation of the Indian Ocean, PhD thesis.
- Testor, P. and Gascard, J. C., 2006, Post-convection spreading phase in the Northwestern Mediterranean Sea, *Deep-Sea Res. Part IOceanographic Research Papers*, 53, 869–893, doi:10.1016/j.dsr. 2006.02.004.
- Tevfik K. C., 2006, Simulation of Hydrodynamic and sediment Transport Patterns in Delaware Bay, PhD thesis.
- Thompson, E. F., 1939, The exchange of water between the Red Sea and the Gulf of Aden over the “sill”. *John Murray Expedition 1933-34 Scientific Report*, 2, 105-119.
- Tragou, E. and Garrett, C., 1997, The shallow thermohaline circulation of the Red Sea, *Deep Sea Res.*, Part I, 44, 1355– 1376.
- Tragou, E., Garrett, C., Outerbridge, R., and Gilman, C. (1999). The heat and freshwater budgets of the Red Sea. *Journal of physical oceanography*, 29(10):pp. 2504-2522.
- Vercelli, F., 1927, The Hydrographic Survey of the R. N. Amrairaglio Magnaghi in the Red Sea. *Annual Hydrographic* 2, 1 -290.
- Vercelli, E., 1931, Nuove ricerche sulli correnti marine nel Mar Rosso, *Ann. Idrograf.*, 12, 1-74.
- William, E.J., Gregg, A.J., John, C.K., Steven, P.M. and Mike, C. (1999) Arabian Marginal Seas and Gulfs, Report of a Workshop Held at Stennis Space Centre, Mississippi, University of Miami RSMAS, Technical Report 2000 01.
- Woelk, S. and Quadfasel, D., 1996, Renewal of deep water in the Red Sea during 1982-1987, *J. Geophys. Res.*, 101, 18,155-18,165, 1996.
- World Oil Transit Chokepoints, 2012. Report, U.S. Energy Information Administration

Wyrтки, K., 1974, On the deep circulation of the Red Sea, in *L'oceanographie physique de la Mer Rouge*, pp. 135–163, Cent. Natl. pour l'Exploitation des Oceans, Paris.

Yegorov, N. I., 1950, Calculation of the heat balance of the Red Sea. *Meteorologia idrologia*, 3, 49-56.

Yao, F., I. Hoteit, L. J. Pratt, A. S. Bower, P. Zhai, A. Köhl, and G. Gopalakrishnan (2014a), Seasonal overturning circulation in the Red Sea: 1. Model validation and summer circulation, *J. Geophys. Res. Oceans*, 119, 2238–2262, doi:10.1002/2013JC009004.

Yao, F., I. Hoteit, L. J. Pratt, A. S. Bower, A. Köhl, G. Gopalakrishnan, and D. Rivas (2014b), Seasonal overturning circulation in the Red Sea: 2. Winter circulation, *J. Geophys. Res. Oceans*, 119, 2263–2289, doi:10.1002/2013JC009331

Zhai, P., Pratt, L.J., Bower A., 2015, On the Crossover of Boundary in an Idealized Model of the Red sea, *Journal of Physical Oceanography*. doi: 10.1175/JPO-D-14-0192.1.

Appendix A: Individual terms of the total heat flux equation

Short wave radiation

The ocean heat flux model calculates the short wave flux based on the geographical position and the local time. The incoming shortwave flux at the water surface depends on the declination between the Sun and the Earth's surface. Based on these parameters the solar elevation angle γ is calculated. Assuming the incoming short wave solar radiation through a clear sky at ground level is 76% of the flux incident at the top of the atmosphere and an average solar flux S (the solar constant), the total short wave flux at the surface is calculated by:

$$Q_{s0} = \begin{cases} 0.76S \sin(\gamma) & \sin(\gamma) \geq 0 \\ 0 & \sin(\gamma) < 0 \end{cases} \quad [W/m^2] \quad (4-12)$$

Long wave radiation

The sea radiates heat back into the atmosphere at longer wavelength the incident shortwave radiation. Part of this long-wave radiation is absorbed and re-emitted by the atmosphere. Therefore, the effective long-wave radiation flux Q_{eb} from the sea surface is expressed as back radiation from the sea Q_{br} minus the long-wave atmosphere radiation Q_{an} . In the ocean heat flux model the effective back radiation is calculated as a product of the radiation by a black body at sea surface temperature, the emissivity of water, a correction factor for cloud cover and the amount of water vapour in the air:

$$Q_{eb} = Q_{br} - Q_{an} = \epsilon \sigma T_s^4 (0.39 - 0.5\sqrt{e_a})(1 - 0.6F_s^2) \quad [W/m^2] \quad (4-13)$$

In equation (4-13), e_a is actual vapour pressure formulated as a function of relative humidity (r_{hum}) and air temperature (T_a).

Evaporation heat flux

Evaporation is a process that takes place at the surface between water and the air. It depends on the conditions in the immediate vicinity of the free surface and occurs until the air above the sea surface is saturated. The transport of the water vapour into the air proceeds by turbulent exchange which depends on the wind velocity.

In the ocean heat model, the evaporation flux is calculated using a so-called bulk formula which is based on empirical relations. It is assumed that the heat loss of sea water due to evaporation depends on the difference between the specific humidity ($q_a(T_a)$) and the specific humidity of saturated air ($q_s(T_s)$) at a prescribed atmospheric state, the air density (ρ_a), the latent heat of evaporation (L_v), and the entrainment rate $f(W)$:

$$Q_{ev} = L_v \rho_a f(U_{10}) (q_s(T_s) - q_a(T_a)) \quad [\text{W/m}^2] \quad (4-14)$$

$f(U_{10})$ is a wind speed function defined as :

$$f(U_{10}) = c_e U_{10} \quad (4-15)$$

Where:

U_{10} is the wind speed 10 meters above the water surface and c_e is a dimensionless constant called the Dalton number. The Dalton number is an input parameter of the ocean heat flux model and is used to tune the magnitude of the evaporative flux.

Convective heat flux

The ocean heat flux model calculates the convective heat exchange through the water atmosphere interface using a bulk formula. It assumes that the heat loss of sea water due to convection depends on the entrainment rate $g(W)$, the temperature difference between the air (T_a) and the sea (T_s) and the heat capacity of the air (c_a):

$$Q_{co} = \rho_a c_a g(U_{10}) (T_s - T_a) \quad [\text{W/m}^2] \quad (4-16)$$

$g(U_{10})$ a wind speed function defined as:

$$g(U_{10}) = c_h U_{10} \quad (4-17)$$

Where:

U_{10} is the wind speed 10 meters above the water surface and c_h is a dimensionless constant called the Stanton number. The Stanton number is an input of the ocean heat flux model and is used to calibrate the magnitude of the convective flux.

Vertical Temperature transport

In Delft3D-Flow, temperature is transported by advective and diffusive processes. Heating entering or leaving at the open model boundaries (due to the heat flux at the free surface or prescribed transport at the lateral boundaries) is transported to other regions of the model

domain by these processes. In Cartesian coordinates the transport equation for temperature can be expressed as:

$$\frac{\partial T}{\partial t} = advection + D_h \left(\frac{\partial^2 T}{\partial x^2} + \frac{\partial^2 T}{\partial y^2} \right) + D_v \left(\frac{\partial^2 T}{\partial z^2} \right) + Q_t \quad (4-18)$$

Where:

D_h and D_v are the horizontal and the vertical eddy diffusivity coefficient, and Q_t is the net heat flux calculated by the heat flux model. In Delft3D-Flow system D_v is defined as $D_v = D_{3D} + D_{mol}$.

D_{3D} is referred to as the three-dimensional turbulence and is related to the turbulent eddy viscosity, which is determined by a turbulent closure model. D_{mol} represents molecular diffusion.

It has been reported by (De Goede et al., 2000), that in strongly stratified flows problems appear when using the definition of D_v . That is, the turbulent eddy diffusivity at the bottom of the mixed layer reduces to zero and the vertical mixing reduces only to molecular diffusion. This causes too much heat remains trapped in the models top layers. This is physically not realistic due to internal wave which cause additional mixing through the interface. There are two possible approaches are suggested to account for this process. The first one is a background mixing coefficient D_{back} can be specified to prescribe a minimum vertical diffusivity which account for all unresolved forms of mixing:

$$D_v = D_{mol} + max(D_{back}, D_{3d}) \quad (4-19)$$

De Goede et al., (2000) had used a background eddy diffusivity of $7 \times 10^{-5} \text{ m}^2/\text{s}$ in modelling stratified flow in the North Sea.

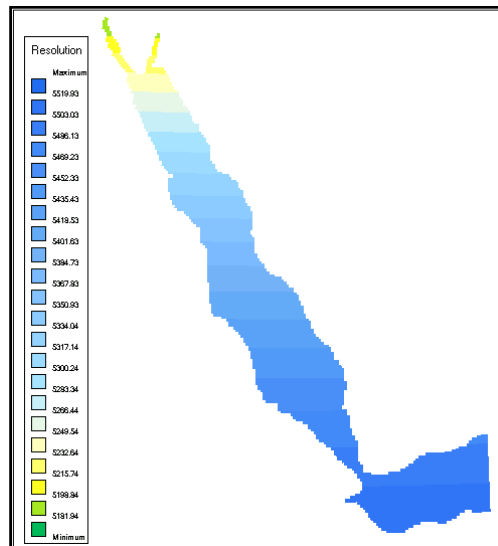
The second approach is that the minimum diffusivity can be specified by the Ozmidov length scale L_∞ , which prescribes mixing caused by internal waves calculated by the Brunt Väisälä frequency (it is also known as the buoyancy frequency, since it produces a vertical oscillation caused by buoyancy force which induces vertical mixing):

$$D_v = D_{mol} + max \left(0.2 L_\infty^2 \sqrt{\frac{-g}{\rho} \frac{\partial \rho}{\partial z}} D_v \right) \quad (4-20)$$

Appendix B: Grid Requirements

B-I Grid Resolution of the RS-Model

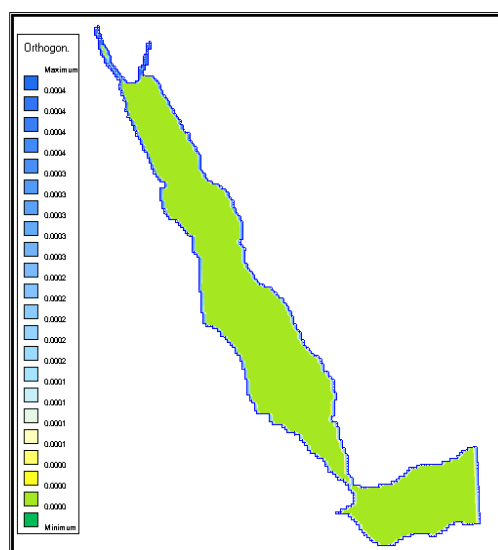
The final grid resolution chosen based on the sensitivity tests carried out during the development procedures.



Distribution of Grid resolution [m] - **RS-Model**

B-II Grid Orthogonality of the RS-Model

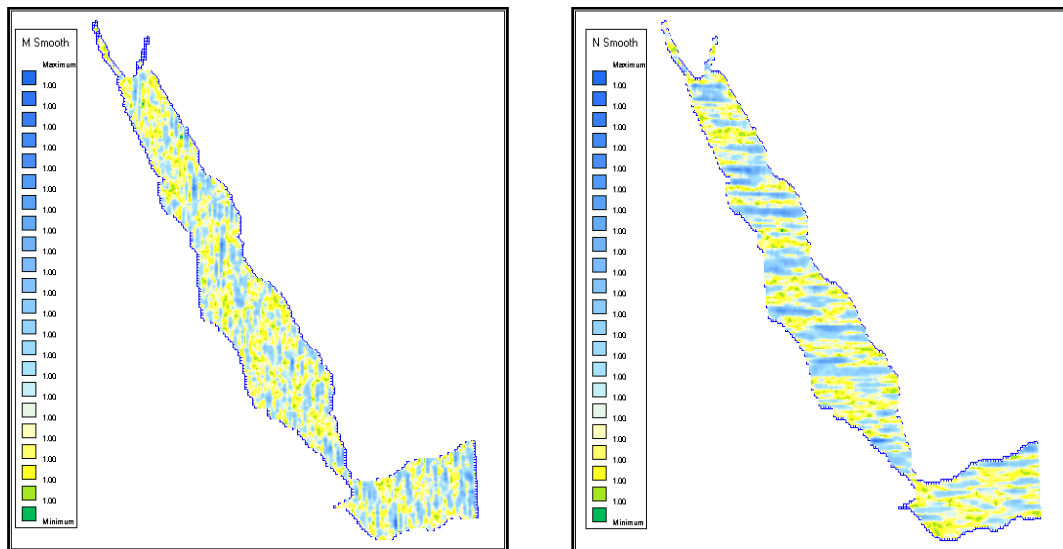
The order of the orthogonality of a grid is determined by the point centred cosine value. The below Figure depicts the orthogonally of the RS-Model grid, it is clear by looking to the scale that the values in agreement with the requirements where the values close to zero.



Distribution of Grid Orthogonality- **RS-Model**

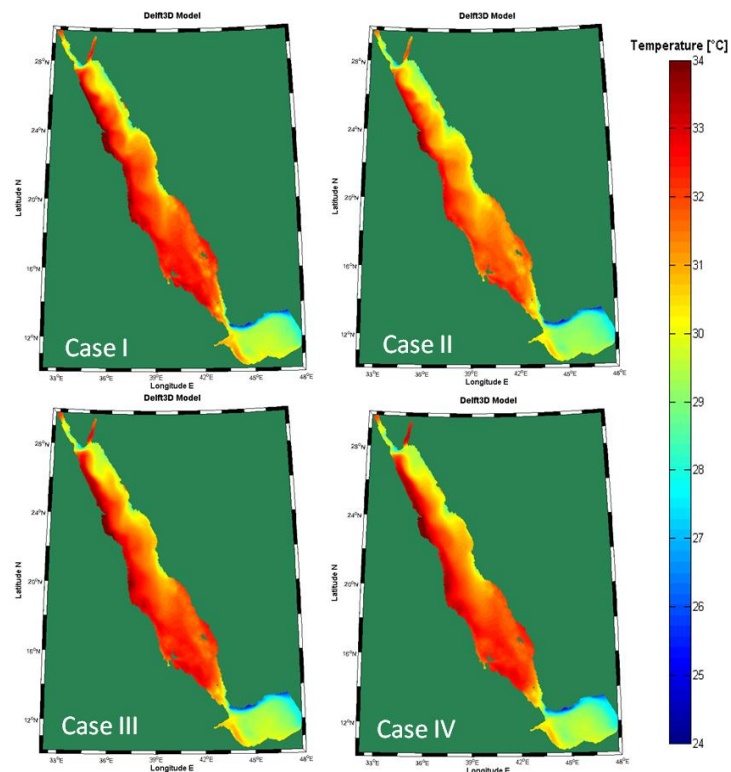
B-III M & N Smoothness of the RS-Model

The factor of smoothness is defined as the ratio between adjacent grid cell lengths. The recommended value of smoothness in the area of interest is 1.2. The below Figure shows the distribution of M (left panel) and N (right panel) smoothness in the entire model domain. It is obvious that they meet the allowable range as can be seen in the scales.

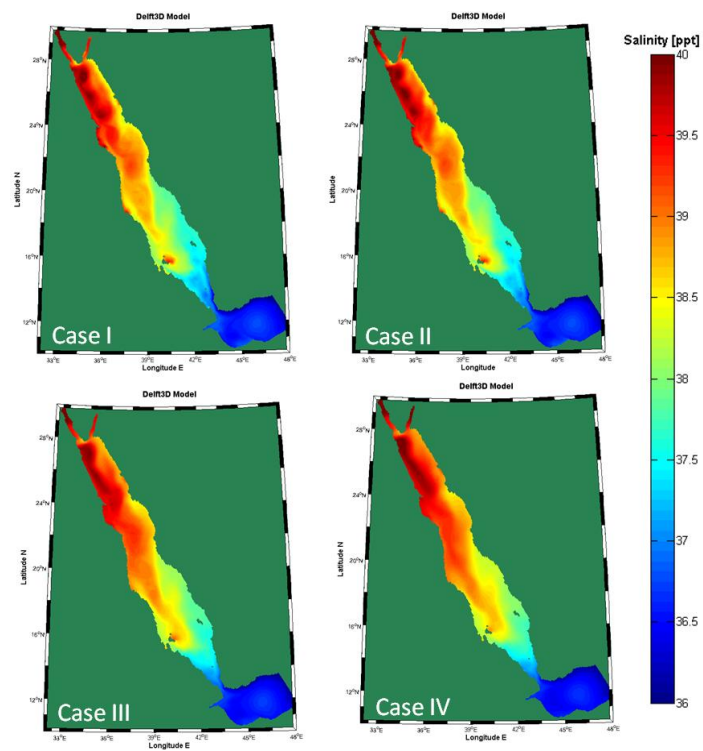


Distribution of Grid smoothness in M-direction-Left and N-direction-Right, **RS-Model**

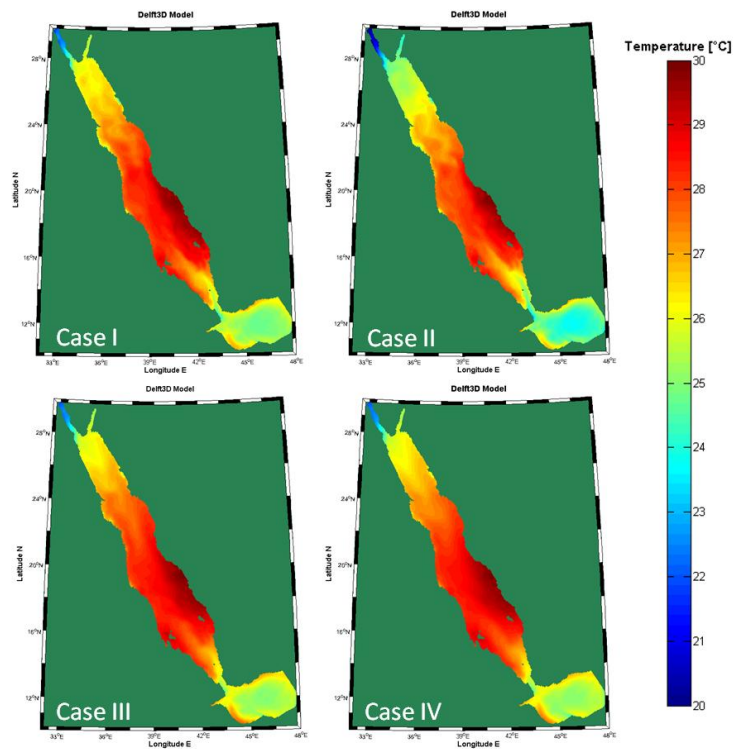
Appendix C: Sensitivity analysis on Horizontal Eddy Diffusivity



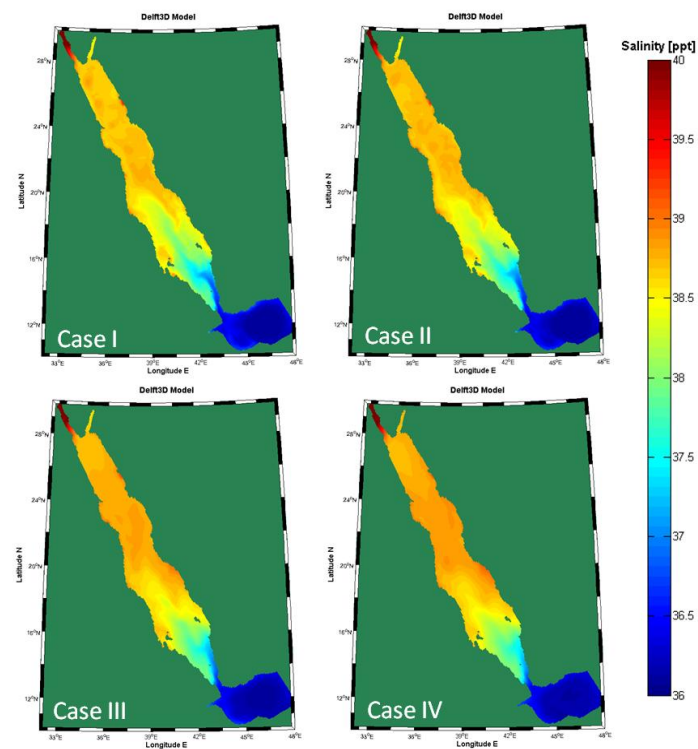
Effects of Horizontal Eddy Diffusivity on surface temperature during summer (Jun-September).



Effects of Horizontal Eddy Diffusivity on surface salinity during summer (Jun-September).

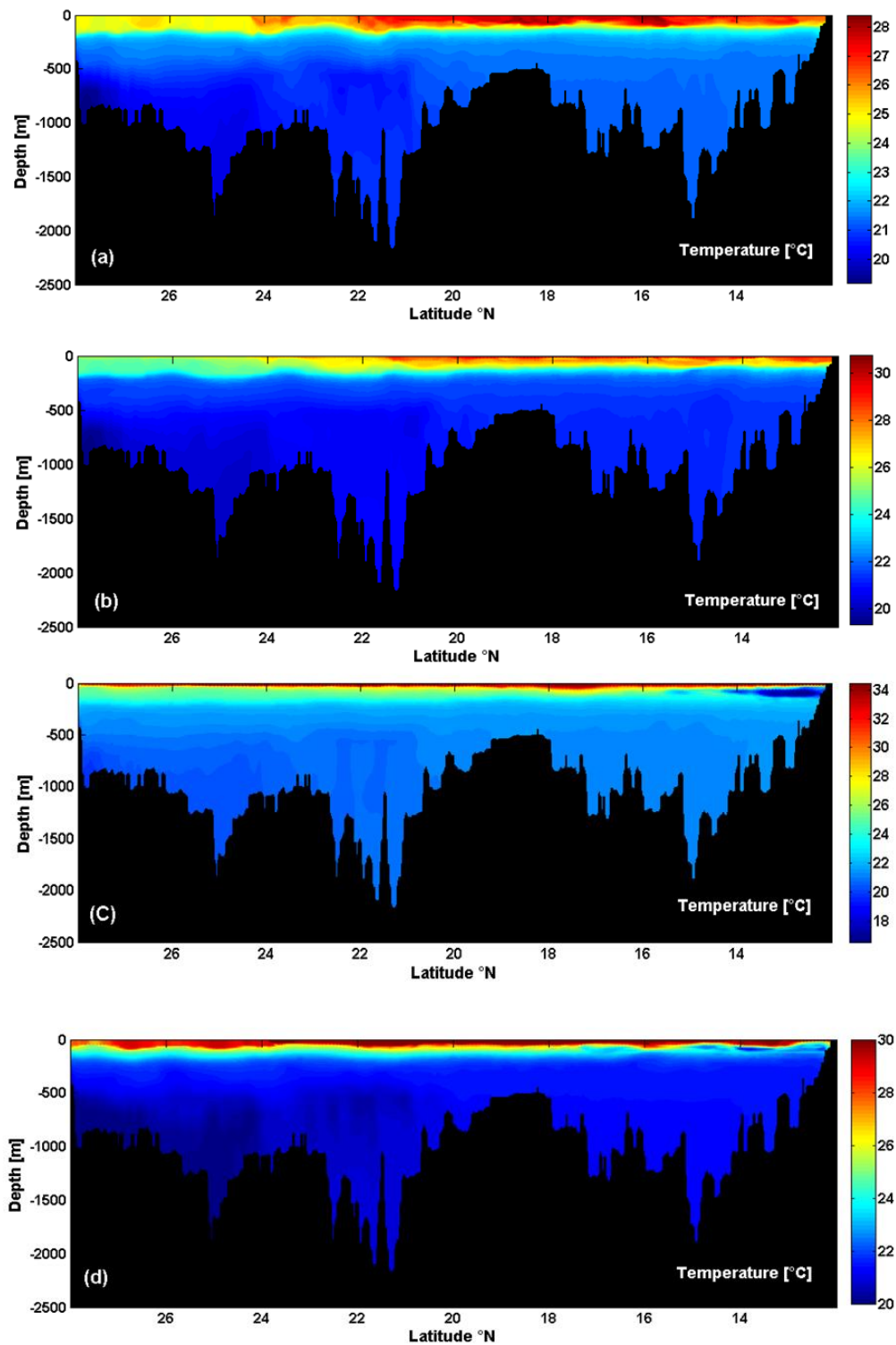


Effects of Horizontal Eddy Diffusivity on surface temperature during winter (December-March).

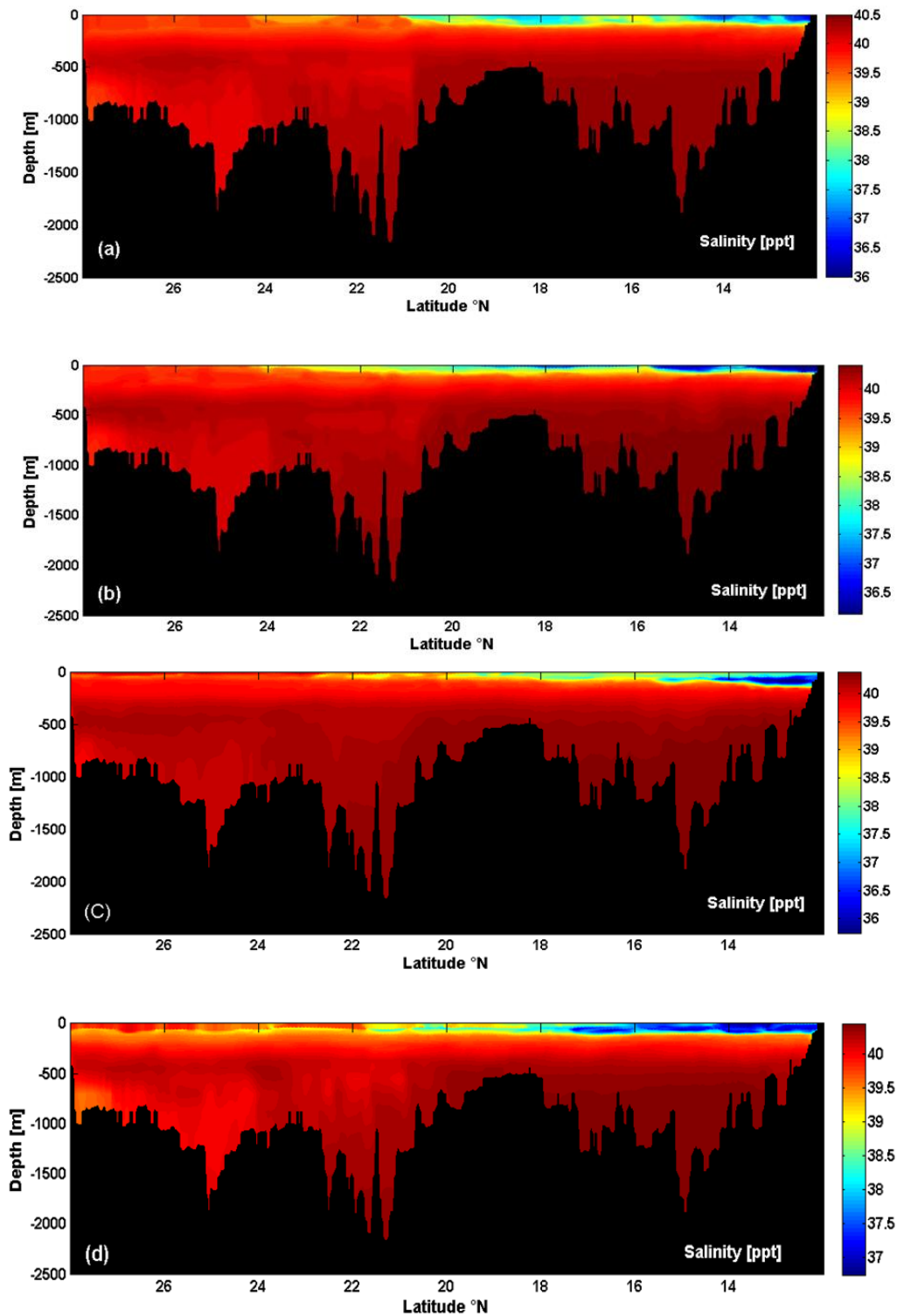


Effects of Horizontal Eddy Diffusivity on surface salinity during winter (December-March).

Appendix D: Vertical distribution of Potential Temperature ($^{\circ}\text{C}$) and Salinity (psu) along the main axis of the Red Sea.



Vertical distribution of simulated potential temperature ($^{\circ}\text{C}$) on (a) January, (b) April, (c) July and (d) October -2008. [Meridional cross-section along the main axis of the Red Sea].



Vertical distribution of simulated salinity field (psu) on (a) January, (b) April, (c) July and (d) October -2008. [Meridional cross-section along the main axis of the Red Sea].

Erklärung

Hiermit erkläre ich, dass die Abhandlung – abgesehen von der Beratung durch meine akademischen Lehrer, nach Inhalt und Form meine eigene Arbeit ist. Diese Arbeit hat an keiner anderen Stelle im Rahmen eines Prüfungsverfahrens vorgelegen. Außerdem erkläre ich, dass dies mein erster Promotionsversuch ist.

Declaration

- I. That apart from the supervisor's guidance the content and design of my thesis is all my own work.
- II. The thesis has never been submitted either partially or as a whole as part of a doctoral degree to another examining body.
- III. That my thesis has been prepared subject to the Rules of Good Scientific Practice of the German Research Foundation.

Kiel, den 21. March 2017

Fawaz Abdulwahab Madah

Curriculum Vitae

Personal details

Name: Fawaz Abdulwahab Madah
Date of birth: 29 July 1976
Place of birth: Jeddah, Saudi Arabia
Nationality: Saudi
Sex: Male
Marital status: Married
Address: Olshausenstr. 79, 24106 Kiel, Germany
Phone: +49 431 880
Fax: +49 431 880 7303
Email: fmadah@corelab.uni-kiel.de

Academic qualification

2007: M.Sc. degree, Applied Marine Science, Faculty of Science, School of Earth, ocean & environmental science, Plymouth University, Plymouth, United Kingdom.

2002: Diploma in Applied computer, Al-alamiah institute, Jeddah, Saudi Arabia.

2001: B.Sc. Marine Physics, Faculty of Marine Science, King Abdul-Aziz University, Jeddah, Saudi Arabia.